A STUDY OF THE STRUCTURE OF THE TURBULENT BOUNDARY LAYER WITH AND WITHOUT LONGITUDINAL PRESSURE GRADIENTS

By

F. A. Schraub and S. J. Kline

Prepared from work done under
NSF Grants G14535 and GP2720,
Mechanics Division AFOSR Grant AF-136-63,
and Mechanics Division AFOSR Contract AF-49(638)-1278

Report MD-12

Thermosciences Division
Department of Mechanical Engineering
Stanford University
Stanford, California

March 1965

F

Department of Mechanical Engineering
Stanford University
Stanford, California 94305

October, 1966

ERRATA FOR MD-12 BY F. A. SCHRAUB AND S. J. KLINE

Page 22, line 5: "Craemer [1954]" should be "Craemer [1955]".

Page 24, line 10: "Taylor 1938 " should be "Taylor [1938]".

Page 24, next to last line: "$x = t/\bar{u}$" should be "$x = \bar{u} \cdot t$".

Page 29, Figure 2.4: Label on abscissa should be "E_{30}".

Page 36, 3rd paragraph, 2nd line: "region is subject" should be "region are subject".

Page 36, equation six lines from bottom should read:

$$U^+ = 5.6 \log_{10} y^+ + 4.9 .$$

Page 45, first line of last paragraph: "wall is both spatially and time" should read "wall is both space and time".

Page 58, last line: "end vie. of" should read "end views of".

Page 72, 4th paragraph, 3rd line: "In veiw of" should read "In view of".

Page 86, Figure 3.15b: Ordinate label should be: $u_{\tau g}/u_\infty$.

Pages 95 and 96, Figures 3.25-3.28: reference is made to a value of $G = 6.1$ for "Const. Press." Flows. G should be 6.7 for constant pressure flow.

Page 97, Figure 3.29: Ordinate label should be $\dfrac{\sqrt{\overline{u^2}}}{(u_\tau)_{\text{profile method}}}$.

Page 97, Figure 3.29: The words "present data" are superfluous.

Page 97, Figure 3.29: Subscript on "Re" on last data identification should be "Re_D", not "Re_0".

Page 100, Figure 3.33: The words "positive skewness" and "negative skewness" written in the two sketches are mixed up. The left figure should read "negative skewness", the right one "positive skewness".

Page 101, Figure 3.35: Title should read: λ_{visual} versus U_∞ .

Page 114, Figure 3.48: Curve which passes through origin and lies about all other curves for $\bar{x} < 35$ should be labeled: "Runstadler curve [1963]".

Page 114, Figure 3.48: Abscissa label should read: $\bar{x}$ [inches x 10^1].

(over)

Page 117, Figure 3.53: Abscissa label should read:
F [bursts/sec-in].

Page 117, Figure 3.53: Equation identifying upper curve should be:

$$F = (8.14 \times 10^{4})\, u_{\tau}^{3} .$$

Page 118, Figure 3.55: Label on curve should be:

$$U^{+} = 5.6 \log_{10} y^{+} + 4.9 .$$

Page 120, Figure 3.57: Abscissa label should be: x [feet].

Page 121, Table 3.1: Repeated twice on same page.

References omitted:

Abbott, D. E. and Kline, S. J. [1961], "Theoretical and Experimental Investigations of Flow over Single and Double Backward Facing Steps", Report MD-5, Thermosciences Division, Stanford University, June 1961.

Kline, S. J. and Runstadler, P. W. [1959], "Some Preliminary Results of Visual Studies of the Wall Layers of the Turbulent Boundary Layer", ASME Paper No. 58-A-64, Journal of Applied Mechanics, June 1959.

Ling, S. C. [1955], "Measurement of Flow Characteristics by the Hot-Film Technique", Ph.D. Thesis, Iowa State University, 1955.

Roshko, A. [1954], "On the Development of Turbulent Wakes from Vortex Streets", NACA Rept. 1191.

Runstadler, P. W. [1962], "An Experimental Investigation of the Flow Structure of the Turbulent Boundary Layer", Ph.D. Thesis, Thermosciences Division, Stanford University, 1962.

Runstadler, P. W., Kline, S. J., and Reynolds, W. C. [1963], "An Investigation of the Flow Structure of the Turbulent Boundary Layer", Report MD-8, Thermosciences Division, Stanford University, June 1963.

A STUDY OF THE STRUCTURE OF THE TURBULENT BOUNDARY LAYER WITH AND WITHOUT LONGITUDINAL PRESSURE GRADIENTS

By

F. A. Schraub, Research Assistant†

and

S. J. Kline, Professor

Prepared from work done under
NSF Grants G14535 and GP2720,
Mechanics Division AFOSR Grant AF-136-63,
and Mechanics Division AFOSR Contract AF-49(638)-1278

Report MD-12

Thermosciences Division
Department of Mechanical Engineering
Stanford University
Stanford, California

March 1965

†Presently employed at General Electric Company, Atomic Power Equipment Division, San Jose, California.

BLANK PAGE

ACKNOWLEDGMENTS

The assistance of Messrs. A. B. Cocanower, H. T. Kim, and C. K. Liu with computer programming and data reduction is gratefully acknowledged.

The financial support of the National Science Foundation and the Mechanics Division of the Air Force Office of Scientific Research made this study possible.

ABSTRACT

The flow structure of the turbulent boundary layer with and without arbitrary streamwise pressure gradients has been studied experimentally. The structure picture for the $dp/dx = 0$ case found by Runstadler, Kline and Reynolds [1963] has been (i) confirmed, (ii) further verified using improved experimental techniques, and (iii) extended to pressure gradient cases.

The existence of three regions of the turbulent boundary layer, each correlating with a distinct part of the non-dimensional mean velocity profile, was confirmed; these are:

(a) wake or intermittent region

(b) fully turbulent region

(c) wall layer region.

Details of the flow structure of these regions were further verified using a new hot-wire anemometer and an improved combined-time-streak marker hydrogen-bubble technique. Instantaneous spanwise velocity profiles over a large extent of the flow at many fixed y-positions across the layer have been obtained. The wall-layer region streaky pattern is thus shown beyond any reasonable doubt to be due to spanwise variations in the x-component of velocity. Spatial spectral analyses of these spanwise profiles verify the existence of a fundamental structural scale in the wall layer; it corresponds to that observed by viewing dye patterns by eye.

The study of the flow structure was extended to include both positive and negative pressure gradient flows, including a relaminarization flow. The basic turbulent flow structure under moderate pressure gradients is not significantly changed from the zero pressure gradient cases. For example, the non-dimensional sublayer structure parameter, $\lambda^+ = \frac{\lambda u_\tau}{\nu}$, was found to be constant for all the turbulent flows studied.

Relaminarization was shown to occur for values of the pressure gradient parameter, $K = \frac{\nu}{u_\infty^2} \frac{du_\infty}{dx}$, greater than

3×10^{-6} . An essential feature of the relaminarization process is the cessation of turbulent bursting from the low-speed streaks of the sublayer region. This reduction in turbulence production helps to explain the reduction in heat transfer at the same value of K observed by other independent investigators.

The hot-wire anemometer provided a means of obtaining detailed mean velocity profiles well within the sublayer region. The existence of a linear mean velocity profile in the sublayer is clearly shown. When the wall shear is determined by the slope of the linear profile near the wall, non-universal profile behavior is observed in the logarithmic region for pressure gradient flows. Thus, reasonable doubt is raised as to the true universality of "the law of the wall" in pressure gradients.

The hydrogen-bubble combined-time streak marker visualization technique was shown to be a useful tool for quantitative measurement of time-dependent velocity fields. It is an excellent supplement to the hot wire.

TABLE OF CONTENTS

LIST OF FIGURES

LIST OF TABLES

NOMENCLATURE

English Letters

C_f	$= \tau_w \Big/ 1/2\rho U_\infty^2$
d	= diameter of hot-wire
E_{30}	= voltage accumulated by anemometer integrator for 30 seconds
e	= voltage output of anemometer
EBW	= Equivalent Band Width
F	= Burst rate in Bursts/sec/in.
F	= flatness factor $= \overline{u^4} \Big/ \left(\overline{u^2}\right)^2$
$f(y^+)$	= functional form of the "law of the wall"
G	= shape parameter $= \int_0^\infty \left(\frac{u_\infty - u}{u_\tau}\right)^2 dy/\Delta$
H	= shape parameter $= \delta^*/\theta$
i	= summation index
K	= pressure gradient parameter $= \frac{\nu}{u_\infty^2} \frac{dU_\infty}{dx}$
k_1	= wave number in 1 or x-direction
k	= thermal conductivity
K_o	= square root of hot wire correction factor
ℓ	= hot-wire length
N	= number
N_{St}	= Stanton number
P	= absolute value of total velocity vector
p	= pressure
q	$= (u^2 + v^2 + w^2)^{1/2}$
R	= result for which uncertainty band is desired
Re	= Reynolds number; e.g., $Re_\theta = u\theta/\nu$
$R_{xx}(z_o)$	= correlation coefficient $= \dfrac{\overline{u(z)\, u(z + z_o)}^{\,z}}{\overline{u^2}^{\,z}}$
$R_{11}(z_o)$	$= R_{xx}(z_o)$
s	= sample standard deviation

s_w = velocity profile slope at the wall = $\partial u/\partial y\big]_{wall}$

S = skewness = $\overline{u^3} \Big/ \overline{u^2}^{3/2}$

t = time

T = time difference; e.g., $t - t_{ejection}$

T.I. = Turbulence Intensity

u = fluid velocity in x-direction

u' = velocity fluctuation in x-direction; $u' = u - \bar{u}$

$u_{fil.}$ = x-component of velocity of ejected filament

u_τ = shear velocity = $\sqrt{\tau_w/\rho}$

$(u_\tau)_{log\ cross\ plot}$ = shear velocity determined by method of cross plotting data against logarithmic region of u^+, y^+ universal velocity profile

$(u_\tau)_{wall\ slope}$ = shear velocity determined by method of determining slope of velocity profile at the wall or near the wall in linear region

$\bar{u}(E_{30})$ = velocity from hot-wire calibration as a function of E_{30}

u^+ = u/u_τ

u_∞ = Freestream Velocity

U(ν) = Fourier coefficient

v = velocity fluctuation in y-direction

V_i = variable

VAR[U(ν)] = estimate variance in distribution of magnitude of U(ν)

w = velocity fluctuation in z-direction

$W_{(\ )}$ = uncertainty interval in ( ); e.g., W_u

x = spatial Cartesian coordinate in mean streamwise direction

y = spatial Cartesian coordinate normal to the wall

z = spatial Cartesian coordinate in spanwise direction; i.e., parallel to the wall but perpendicular to streamwise direction

z_o = lag length in correlation calculation in z-direction

$\overline{(\,)}^{t}$ = time average; i.e., = $\frac{1}{T}\int_{o}^{T}(\,)dt$

$\overline{(\,)}^{z}$ = space average in z-direction = $\frac{1}{L}\int_{o}^{L}(\,)dz$

$\triangleq$ = equal to, by definition

Greek Letters

α = acute angle between incidence and reflection for H_2-bubble illumination

β = probability density function of velocity distribution

γ = intermittency factor = % of time flow is turbulent at a point

δ or $\delta_{0.99}$ = boundary layer thickness where $u = 0.99\ U_\infty$

δ^* = displacement thickness = $\int_{o}^{\infty}(1 - u/U_\infty)dy$

Δ = thickness = $\int_{o}^{\infty}\left(\frac{U_\infty - u}{u_\tau}\right)dy = \frac{\delta^* U_\infty}{u_\tau}$

η = similarity parameter = $y\sqrt{\frac{U_\infty}{\nu x}}$

θ = momentum thickness = $\int_{o}^{\infty}\frac{u}{U_\infty}\left(1 - \frac{u}{U_\infty}\right)dy$

λ_v = spacing between low velocity streaks in sublayer determined by visual counting method

λ = spatial wavelength

λ_o = wavelength determined as ensemble average of individual frame spectral analyses

$\lambda_{R_{11}}$ = wavelength determined as lag length to first maximum in R_{11} (other than that maximum at $R_{11}(0)$)

λ_U = wavelength determined as wavelength where $U(\lambda)$ is maximum

μ = fluid dynamic viscosity

ν = fluid kinematic viscosity = μ/ρ

ν = $1/\lambda$ = spatial frequency

ρ = fluid density

τ = lag time in auto-correlation function

τ = time constant of hot-wire response

τ_{yx} = part of total shear stress tensor corresponding to shear in a plane normal to the y-direction, acting in the x-direction

τ_w = local wall shear

ϕ = probability density distribution of trajectory position for y-coordinate direction

ψ = probability density distribution of trajectory position for x-coordinate direction

ω_o = $1/2\pi\tau$ "Break-off" frequency

GLOSSARY

Flow Structure - The mechanics of the fluid motion; the flow patterns or types of fluid motions that comprise the flow field.

Laminar-like - The rectilinear motion of fluid particles. The term as used in this text refers to such particle motions very near the wall over distances of the order of the boundary layer thickness.

Fully Turbulent - Fully turbulent is used to denote the pattern of the flow over a specified region of space where the flow structure is completely turbulent. The term is also used to describe that state of boundary layer development sufficiently far downstream of the boundary layer transition region where the fluctuation quantities (as usually measured experimentally) agree with the values generally accepted as being characteristic of the type of boundary layer development called turbulent.

Turbulent Eddy Structure - A somewhat unclearly defined turbulent region in which the turbulent motions bear some relation to each other; a region of more or less coherent motion.

Viscous Stresses - The ordinary viscous stress terms associated with laminar flow.†

Reynolds Stresses, Turbulent Stresses - Apparent additional stresses which appear in the time-averaged Navier-Stokes equations when fluctuation quantities are considered and the equations are reduced to the same form as those satisfied by laminar flow.†

---

†The viscous terms under consideration here are those appearing in the Navier-Stokes equations, which involve certain basic assumptions regarding the nature of the fluid. These assumptions and the derivation of the Navier-Stokes equations are adequately considered elsewhere (see Schlichting [1960] and Hinze [1959]).

Wall Layers - The layers of fluid within the constant stress region (immediately adjacent to the wall). The region is not sharply defined but can be taken to be the region within which the mean viscous stress is nearly constant, i.e., what is generally referred to as the "laminar sublayer", $y^+ = y\, u_\tau/\nu < 10$.

Wall Layer Structure or Pattern - The distinct and relatively regular flow structure found in the wall layers of the boundary layer.

Longitudinal Streaks - That part of the wall layer structure consisting of alternating regions in the transverse direction of fast and slow moving fluid. Tracer particles introduced into the fluid to visualize the flow accentuate the slow moving regions of fluid and these regions are called low velocity streaks or dye concentrations. The term streaks refers to both high and low velocity regions whereas low velocity streaks and dye concentrations refer only to the low speed regions.

Ejection, Burst - The expulsion of part or all of the wavy part of the streaks away from the wall in a swirling or chaotic eddy motion.

Intermittency - The phenomenon occurring in some turbulent flows where the flow is non-turbulent for a portion of the time and for the rest of the time is turbulent. The ratio of the portion of the time the flow is turbulent to the total time is termed the intermittency factor. (See Hinze [1959]).

Longitudinal - In the stream or x-direction.

Normal - Away from the plate or in the y-direction.

Transverse - Across the plate perpendicular to the flow; in the span or z-direction.

Relaminarization - The process of reverse-transition of a boundary layer from a fully turbulent boundary layer to a laminar boundary layer.

Laminarescent - A boundary layer in the process of relaminarization.

Relaminar - The laminar condition of a boundary layer which has undergone the relaminarization process.

BLANK PAGE

I. INTRODUCTION

Turbulent boundary layer flow under arbitrary flow boundary conditions of pressure gradient and wall surface conditions is one of the most important unsolved problems of fluid mechanics. Boundary layer properties control such important phenomena as heat transfer and mass transfer coefficients as well as drag and separation characteristics in both internal and external flow. The rate of boundary layer growth controls entirely the performance of most short ducts, nozzles and diffusers. Proper design in innumerable applications thus requires ability to predict boundary layer properties including both thickness parameters and the flow conditions very close to the wall.

Boundary layer flow without turbulence (laminar flow) is well understood. There is also a great deal of knowledge of turbulence for the special case of homogeneous, isotropic turbulence where there is no mean rate of shear such as is present with the turbulent boundary layer. However, the fully developed turbulent boundary layer cannot be successfully analyzed by simply combining the laminar boundary layer solutions with the present understanding of homogeneous, isotropic turbulence. What is apparently missing is a physical model which correctly describes the generation and hence the maintenance of turbulence in a boundary layer flow.

A significant contribution toward understanding of this underlying physical structure was made by Runstadler, et al, [1963]. Using both visual and quantitative techniques, Runstadler gave a new, descriptive physical picture of the turbulent boundary layer flow on a smooth, flat plate. Runstadler, et al, [1963] describe the boundary layer as consisting of three zones, each having distinctive physical characteristics; each zone has a one-to-one correspondence with the well known regions of the u^+ , y^+ non-dimensional mean velocity profile. A <u>wall-layer</u> region is shown to

exist below $y^+ = 8$. A fully turbulent region exists corresponding to the logarithmic "law of the wall", i.e., y^+ from about 8 to 300 (the latter value depending upon the Reynolds number). An intermittent zone appeared to correspond to the "wake" or deviation region. Figures 1a through 1d (from Runstadler, et al, [1963]) show the relationship of the different structural zones to the u^+ , y^+ plot; also shown are photographs of hydrogen bubble sheets which are distorted by the flow to give visual pictures of the structure in the different regions.

The delineation of structural details in the wall layer region is particularly important because this is the region of highest mean shear and most wall influence. The only observations available for this zone prior to the study of Runstadler were a few point measurements of mean velocity and in direct data such as mass transfer, heat transfer, and shear coefficients at the wall. This wall region was shown to consist of a relatively regular structure of low and high velocity fluid streaks alternating in the span direction. For the flat plate case studied by Runstadler, the averaged distance between low speed streaks was shown to correlate with wall shear velocity such that $\lambda^+ \approx 80$ $(\lambda^+ \triangleq \frac{\lambda u_\tau}{\nu})$ (figure 1.2), where λ is average distance between low speed streaks, u_τ friction velocity, and ν is the kinematic viscosity. The most observable interaction between the wall layers and the rest of the boundary layer was the ejection of low momentum fluid from the slow speed streaks of the wall layers into the outer flow regions. The trajectories of this ejected fluid and the frequency of ejection were observed; the non-dimensional results are shown in figures 1.3 and 1.4. Much additional quantitative description of the flow structure in the wall layer region and the other regions are also given by Runstadler, et al.

Runstadler's experimental study provides much valuable

information about the physics of the turbulent boundary layer which was not previously available. However, the picture of the flow details is not yet complete enough to build a mathematical model linking the turbulent motions to the gross mean-flow parameters nor to fully explain the creation and maintenance of the turbulence in a bound shear layer.

However, after careful study of these flow structure details Runstadler, et al, proposed the "wall layer hypothesis": the wall layer structure and its interaction with the outer flow play a dominant role in creating and maintaining the structure of the entire turbulent shear layer. This study begins with the belief that this hypothesis is correct. Its primary objective is to gain more knowledge of the structure details, and to extend the type of observation reported by Runstadler, et al, to a wider range of flow conditions.

The main purpose of this study, then, is to extend the physical picture of the flow mechanics of the turbulent boundary layer given by Runstadler, et al, [1963].

In particular, the present work is an experimental investigation of the flow structure details of the turbulent boundary layer over a smooth plate under the influence of five different streamwise pressure gradients. The pressure gradient flows range from a strong favorable gradient which caused "relaminarization" to a relatively strong adverse gradient (with no local separation) and includes a zero pressure gradient case. Using both improved hot-wire anemometry and new hydrogen-bubble flow visualization techniques, additional details of the zero pressure gradient or "basic" flow structure were disclosed, and the effects of non-zero pressure gradients upon this structure were investigated.

The application of non-zero pressure gradients did not drastically change the basic nature of the structure from that observed in the zero pressure gradient flow as long as the layer remained a steady, two dimensionally, fully developed

turbulent boundary layer. In fact, clarification of the zero pressure wake structure was obtained as a result of observation of the thick wake regions of adverse pressure gradient cases.

However, deviations from fully developed turbulent boundary layer behavior (such as relaminarization) were accompanied by drastic changes in the flow model details. This correlation between the flow structure details observed and the overall behavior of the layer adds new support to the belief that the observed flow models are an essential part of a turbulent boundary layer (and to the wall layer hypothesis).

Much of the discussions and interpretations found here are necessarily based upon detailed descriptions or similar discussions given by Runstadler, et al, [1963]. A familiarity with this earlier work and with the descriptive terms defined there is suggested before proceeding with what follows here.

A description of the experimental techniques and equipment appears in Chapter 2. Particular emphasis is given to the combined time-streak-line hydrogen bubble technique for quantitative determination of time-dependent velocity fields. The experimental flows and data obtained are then described; the resulting data are interpreted generally in two ways: clarification and extension of the "basic" zero pressure gradient flow structure details; and new features or distinct changes in the basic structure associated with pressure gradient effects.

The present study is a portion of a longer range research program in the mechanics of turbulent boundary layers in the Thermosciences Laboratory, Department of Mechanical Engineering, Stanford University under joint financial support of U.S. Air Force Office of Scientific Research and the National Science Foundation. The ultimate objective of this program is the construction of improved prediction theories based upon the observed flow models. The present study does not reach this

final goal. However, parameters which appear to govern the pressure gradient effect are established, and a mathematical expression constructed for the probability density of trajectories of outgoing eddies from the wall layers. Correlations of some of the important statistical properties of eddy formation and streak spacing within the wall layers are also established. A relation giving the effect of velocity on eddy burst frequency is found and verified. With these data in hand, it should be possible to design experiments that will give in much clearer form the underlying equilibrium properties of turbulent shear layers and the rate of relaxation toward these local dynamic equilibrium states. It should also be possible to begin attempts to construct improved predictive treatment of the turbulent boundary layer under general flow conditions.

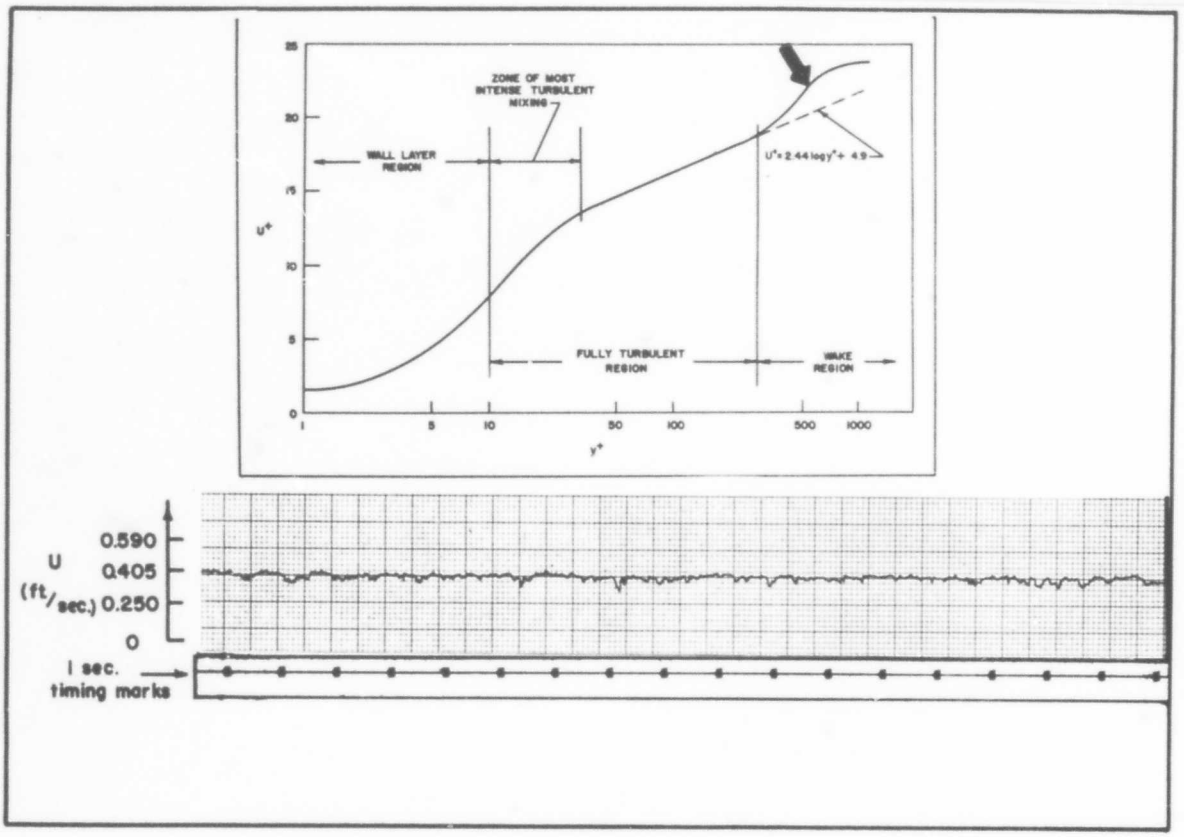

Fig. 1.1a Turbulent boundary layer flow structure $u_\infty = 0.430$ ft/sec., $y = 3.25$ in., $y^+ = 5.31$; Runstadler [1963].

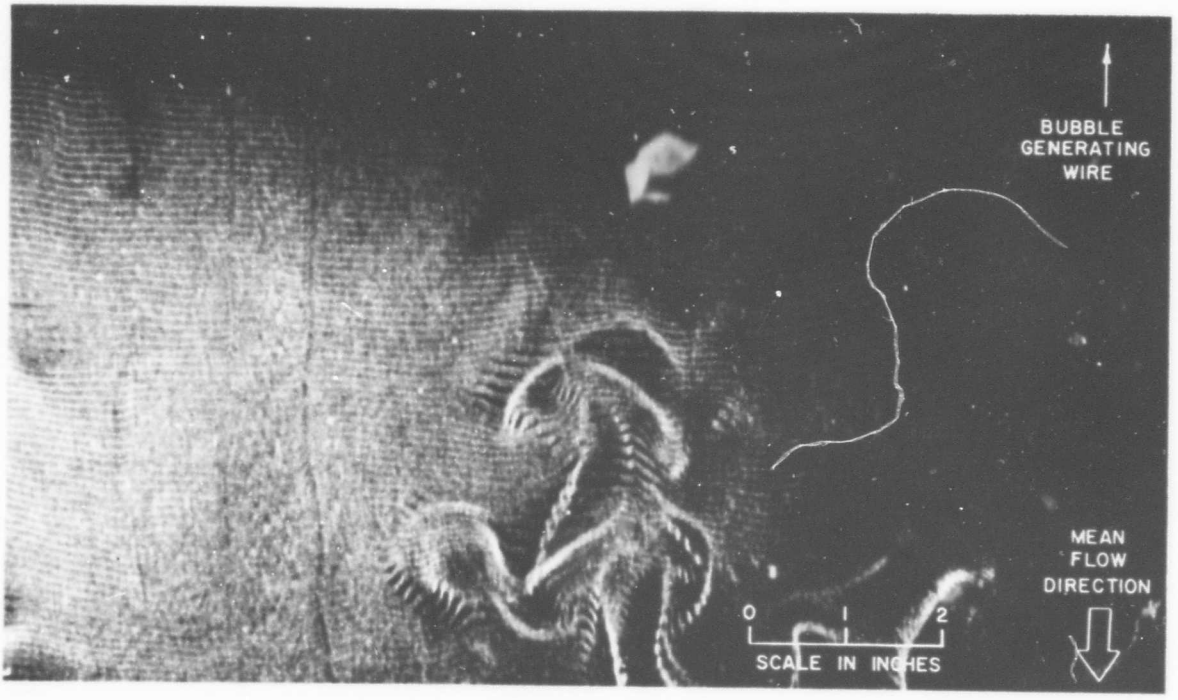

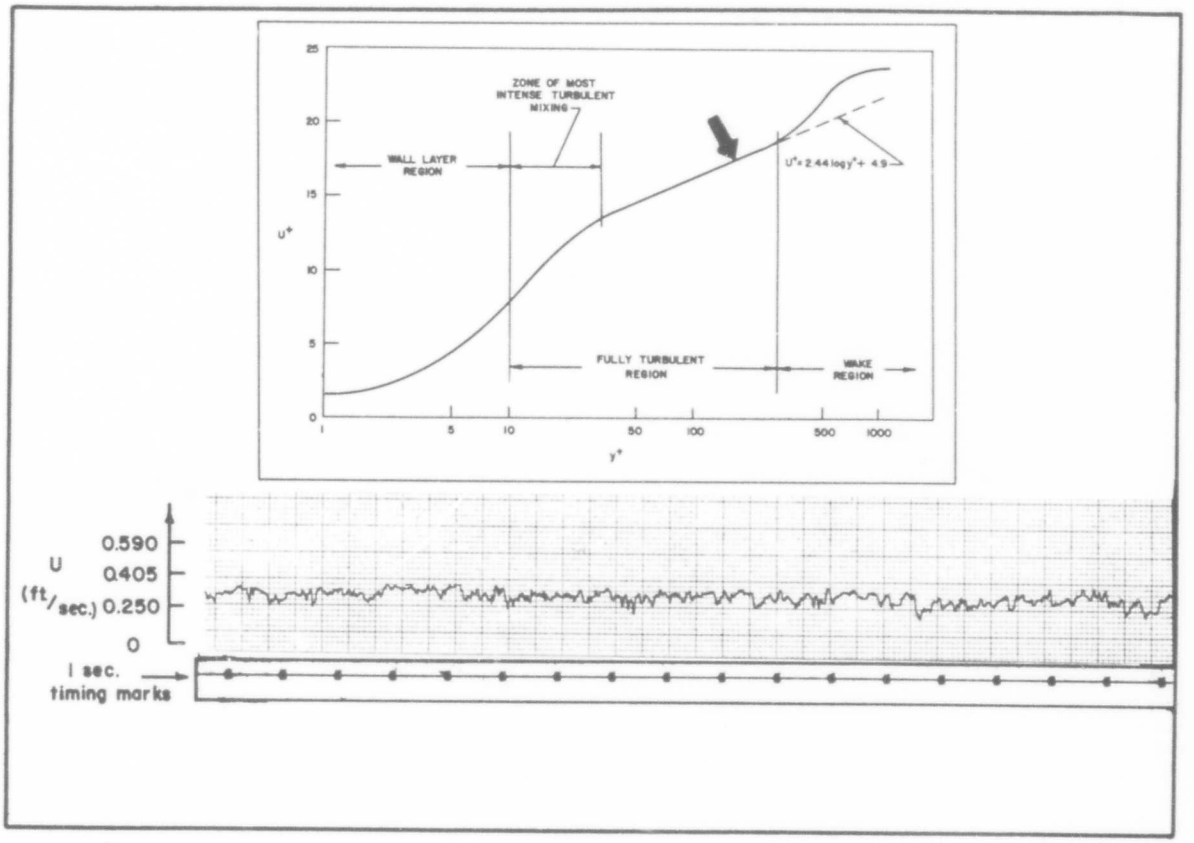

Fig. 1.1b Turbulent boundary layer flow structure u_∞ = 0.430 ft/sec., y = 1.00 in., y^+ = 164; Runstadler [1963].

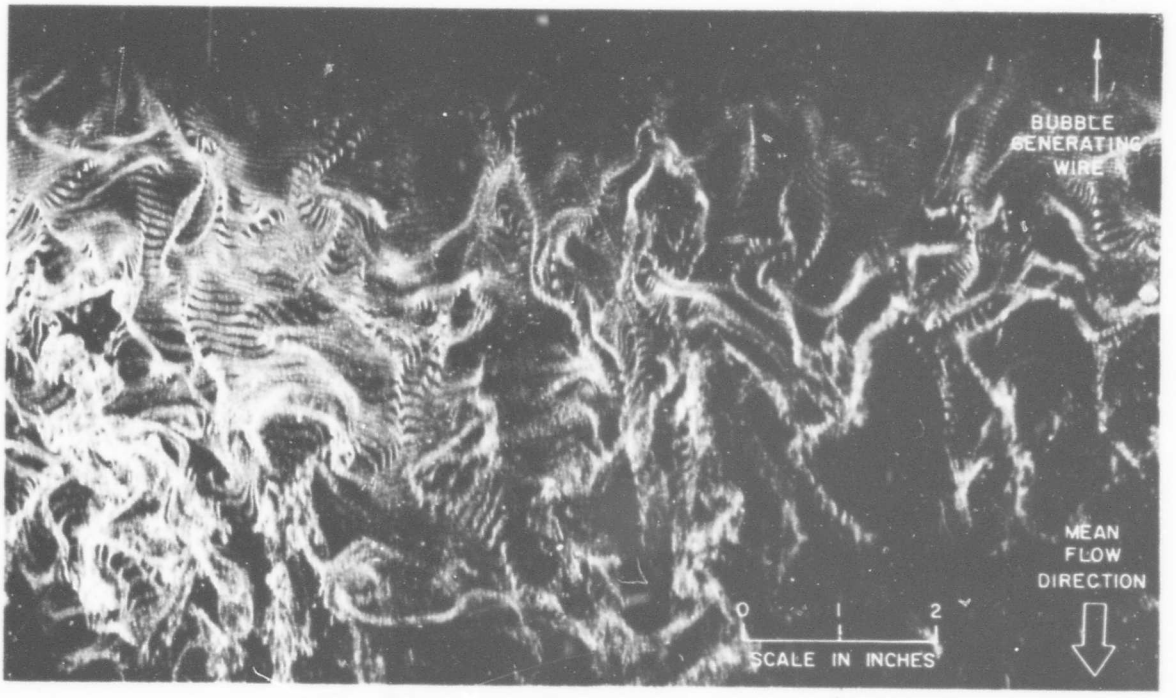

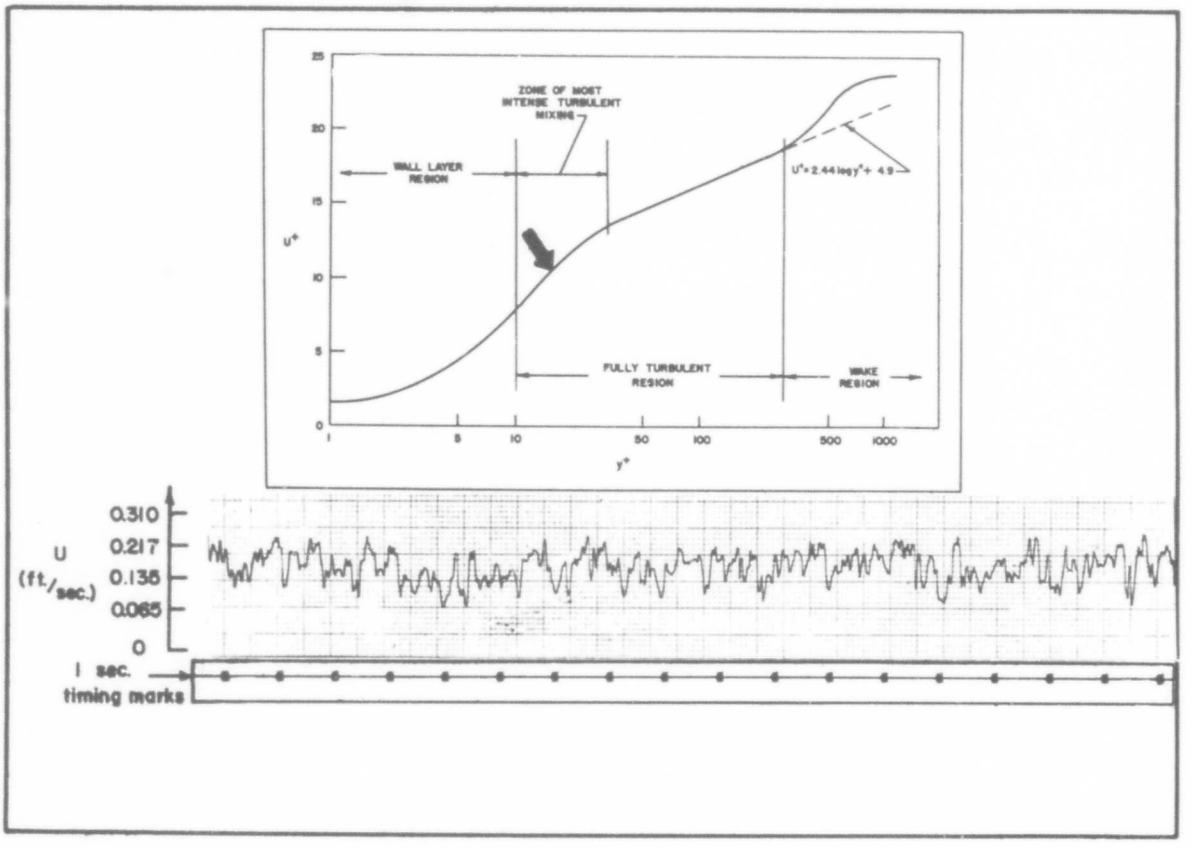

Fig. 1.1c Turbulent boundary layer flow structure $u_\infty = 0.430$ ft/sec., $y = 0.100$ in., $y^+ = 16$; Runstadler [1963].

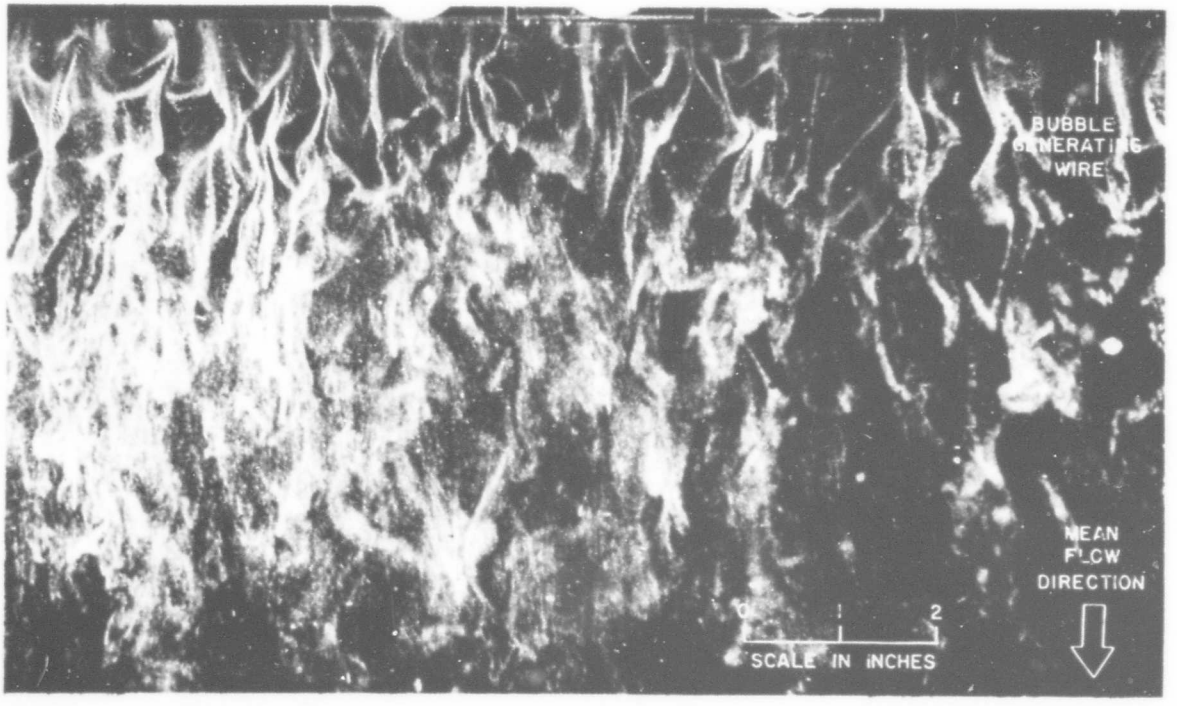

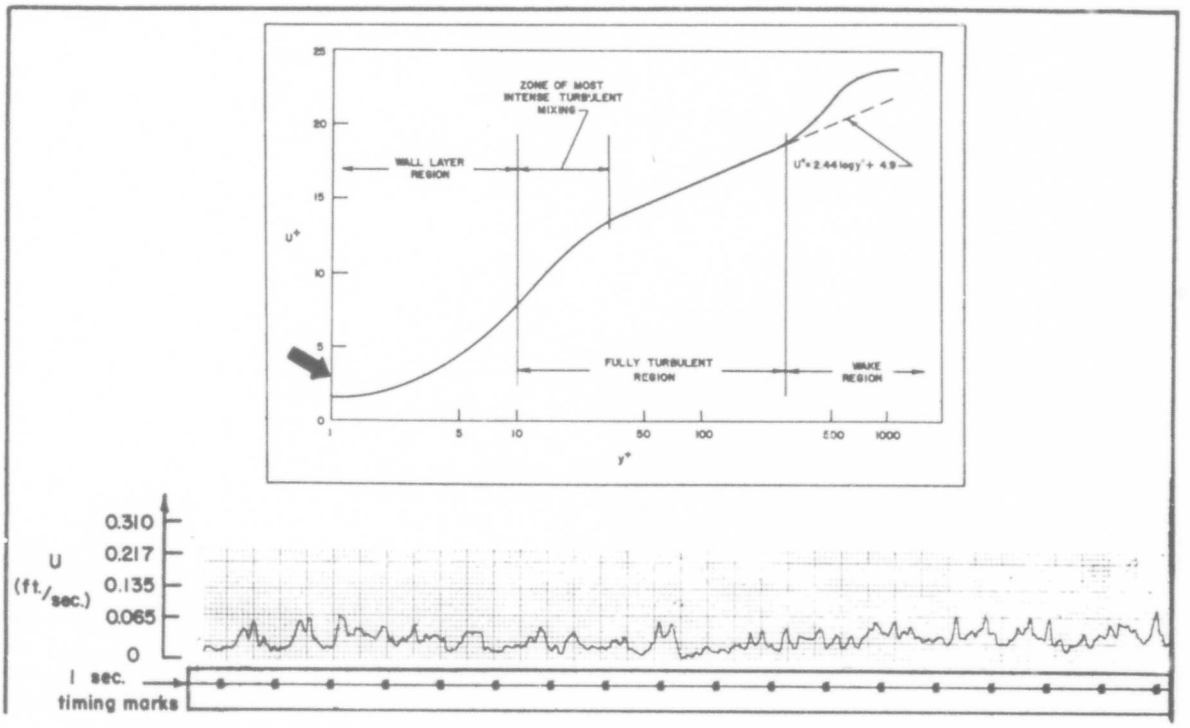

Fig. 1.1d Turbulent boundary layer flow structure $u_\infty = 0.430$ ft/sec., $y = 0.001$ in., $y^+ = 0.16$; Runstadler [1963].

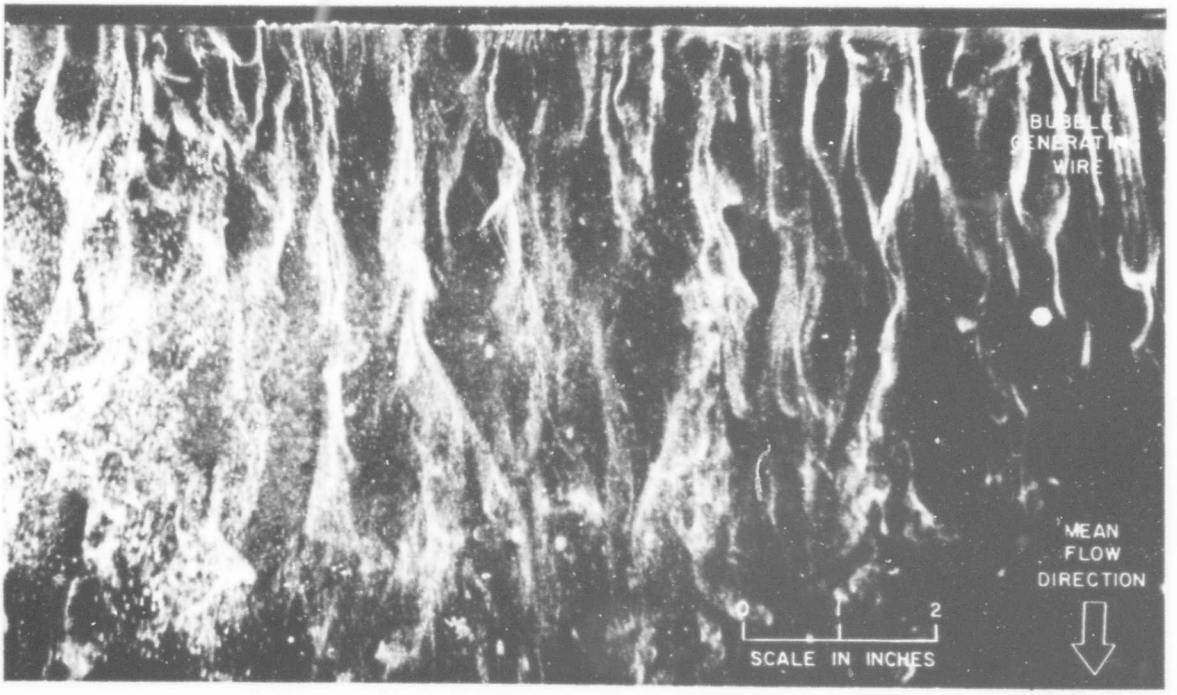

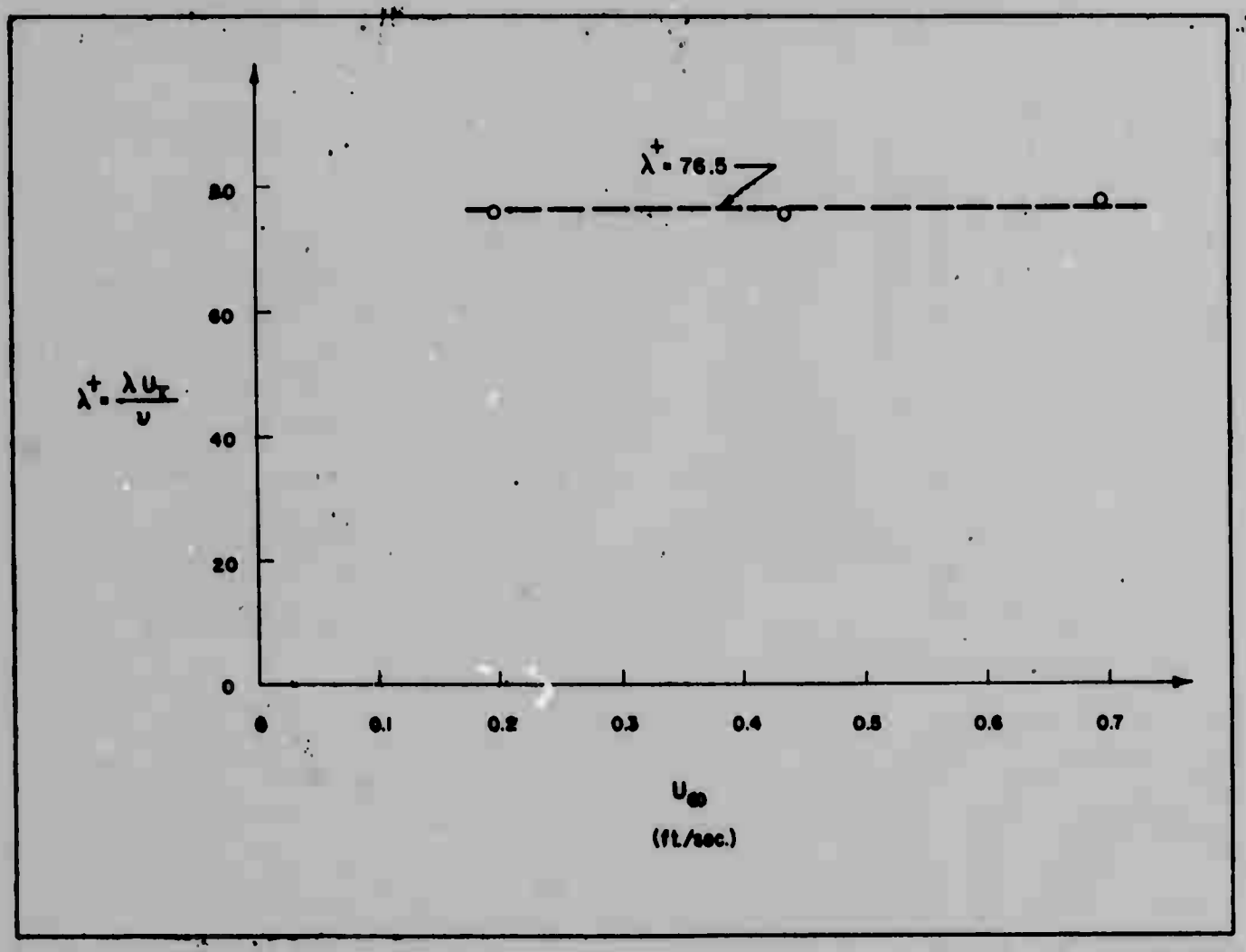

Fig. 1.2 λ^+ vs. u_∞ ; Runstadler [1963].

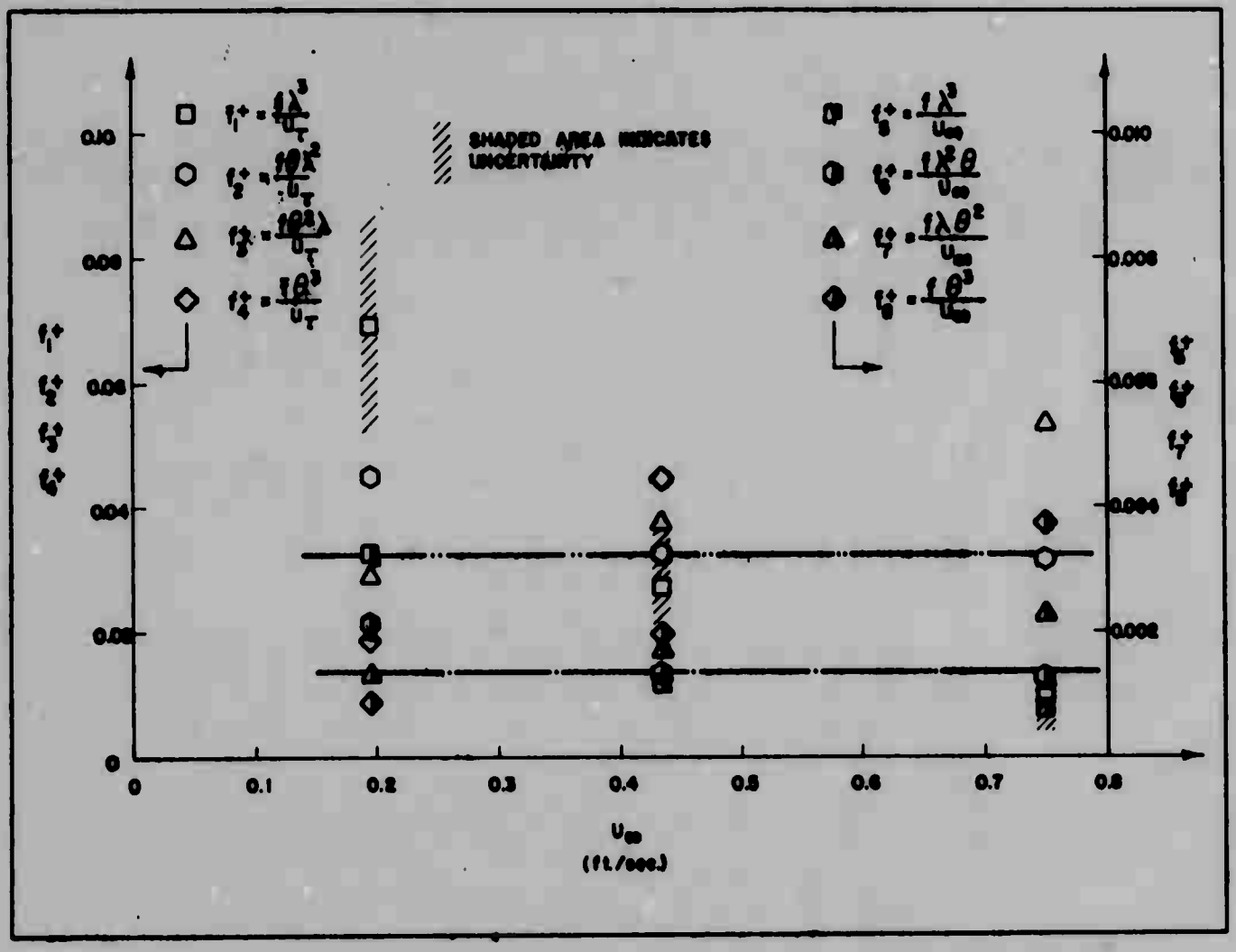

Fig. 1.3 f^+ vs. u_∞ ; Runstadler [1963].

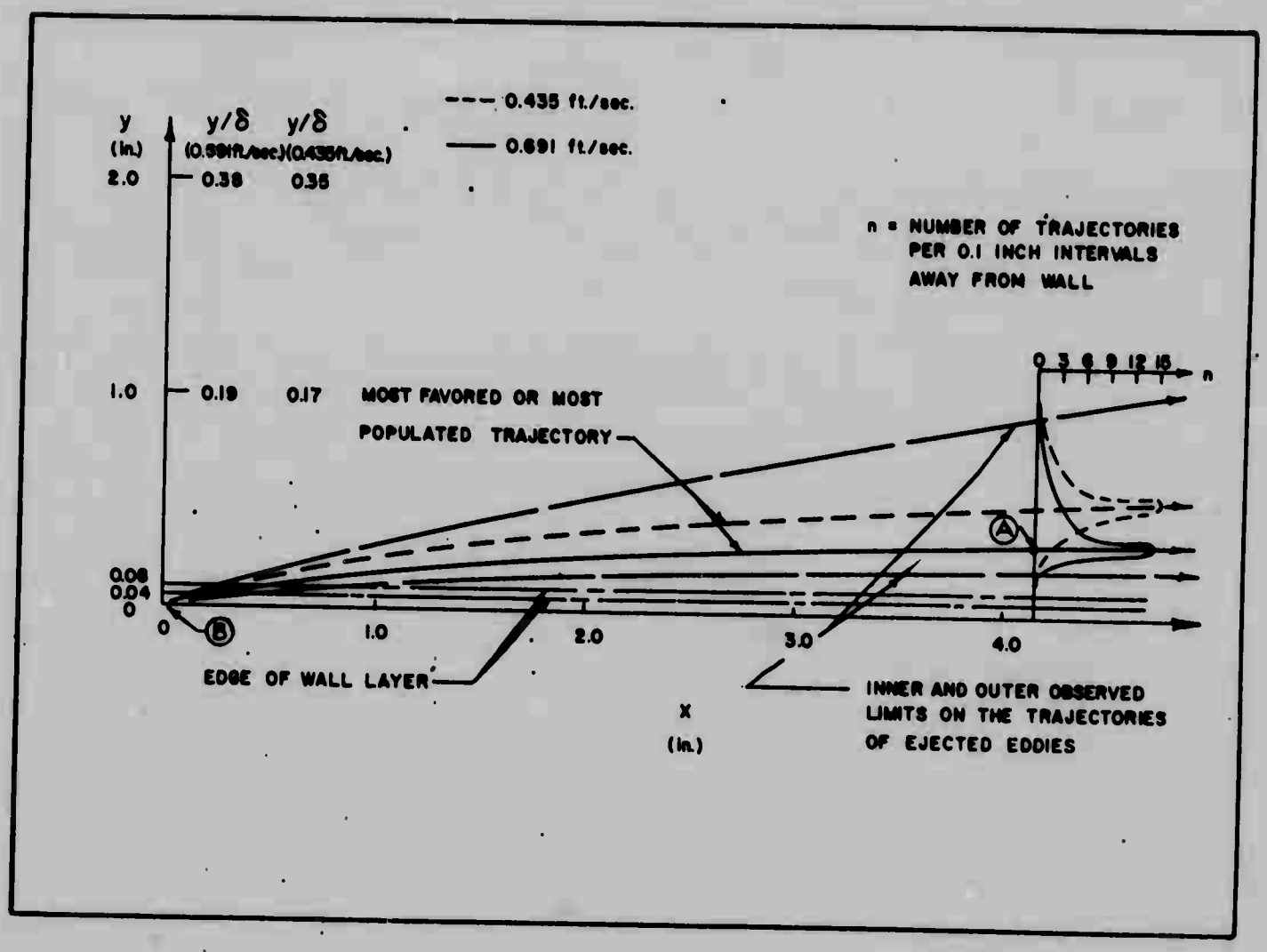

Fig. 1.4a Trajectories of approximate "centers" of ejected streaks. y/δ vs. x ; Runstadler [1963].

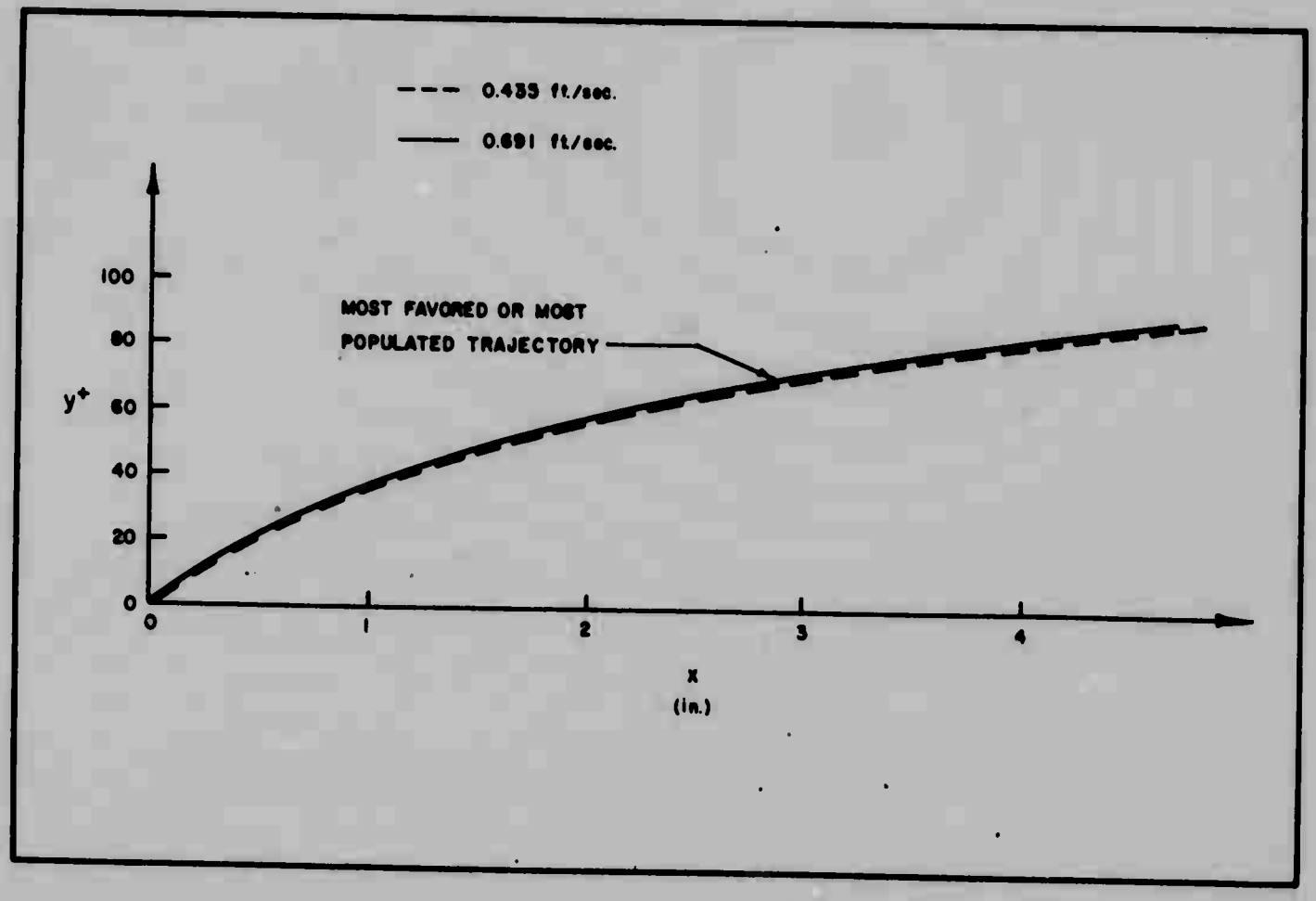

Fig. 1.4b Trajectories of approximate "centers" of ejected streaks. y^+ vs. x^+; Runstadler [1963].

II. APPARATUS, INSTRUMENTATION, DATA REDUCTION PROCEDURES

In order to carry out the experimental objectives, boundary layer flows under arbitrary streamwise pressure gradients were established in a low-speed (0.2 - 0.8 ft/sec) recirculating water channel system. The system is located in the Thermosciences Laboratory, Department of Mechanical Engineering, Stanford University.

A combination of quantitative and visual techniques were used to obtain data on the flow structure. This study incorporates several new techniques. The most important are the use of a combined time-streak-marker hydrogen-bubble technique to obtain instantaneous velocity profiles in the z(or spanwise) direction and the application of spectral analysis procedures to investigate fundamental spatial frequencies of the spanwise velocity profiles.

In this chapter, procedures are described for obtaining the following information:

1. Mean velocity profiles normal to the wall and mean velocity distribution in the flow direction.
2. Qualitative pictures of the physical structure.
3. Instantaneous velocity profiles across the flow (spanwise) at fixed x and y positions.
4. Statistical data on velocity variation:
   a. velocity probability density distributions
   b. higher moments of the velocity distribution: rms, skewness, flatness.
5. Average spacing between low speed streaks (λ) in sublayer.
6. Rate of turbulent bursting (F) from sublayer.
7. Velocity, average trajectory path, and downstream distribution of ejected (burst) fluid.

A. Water Channel System and Flow Conditions

Low speed water-flow is used for this study in order to obtain very thick fully turbulent boundary layers which make possible good resolution of structural details using the

visual techniques to be discussed below. For example, viscous sublayer thicknesses of 0.050 - 0.100" are obtained; thus, their structure can be examined in considerable detail using 0.001" diameter hot wire or hydrogen-bubble generation wire.

The water channel system used in these investigations has been previously described in detail by Runstadler [1963] and by Abbott [1961]. The following description will, therefore, emphasize only the modifications made for the purpose of obtaining the necessary pressure gradient flows for this study.

The water channel shown in figures 2.1 and 2.2 is part of the Stanford recirculating water system. It uses domestic water softened by a commercial ion exchange unit as a working fluid. Deaeration of the water to 80% of saturation is obtained by a by-pass loop containing a deaerator. Water depth and flow rate in the channel are controlled by valves in the recirculation system and by screens at the end of the channel which act as porous weirs. Vibrational disturbances in the flow system were shown by Runstadler [1963] to be unimportant for this type of study.

The boundary layers investigated were developed on a straight vertical side-plate placed inside the water channel. The plate is a smooth, 18' long, 10" wide, 1/2"-lucite sheet, which has a rubber seal along the bottom to eliminate leakage between it and the channel floor. Ten 0.003 inch dye slots for dye marker investigation have been placed in the plate at one foot intervals along the test section.

The streamwise pressure gradient is controlled by adjustment of the opposing vertical wall which is flexible. This second control-wall is 1/8" thick lucite and is designed so that the distance between it and the test wall can be varied smoothly in any manner along the flow direction. Thus the flow cross-sectional area can be made an arbitrary smooth function of the streamwise coordinate, x . The free stream

velocity can then be made any function of x by trial and error adjustment of the wall shapes. The boundary layers are thin compared to the channel width so that there is a well-defined free-stream in the center of the channel. The pressure gradient on the flat wall is a unique function of the free-stream velocity gradient as given by Bernoulli's equation:

$$\frac{dP}{dx} = - \rho \, u_\infty \frac{du_\infty}{dx}$$

Two-dimensionality of the mean flow was ascertained by hot-wire measurements of the mean velocity profiles. These profiles are presented in figures 3.5-3.9. The flow over the test plate is not two dimensional over its entire width due to the growth of a floor boundary layer and to open water surface effects. Data were considered only over that portion of the test plate where the flow was two dimensional; i.e., where profiles at different span stations differed (at any y-height) by less than 5 percent. This region of acceptable two-dimensionality was usually from 3 to 9 inches from the channel floor when the water depth was 10.5 inches.

Inlet free-stream turbulence intensities of below 1% were obtained by using a combination of screens, vanes, honeycomb and a converging nozzle in the entrance region. Careful adjustment of the turning vanes and the use of the honeycomb section were necessary in order to avoid introduction of large scale disturbances by the entrance section.

Laminar to turbulent boundary layer transition was effected by placing a 0.125 inch diameter wire across the test plate at x-station 3.5 as a tripping device. X-stations refer to the distance in feet measured arbitrarily from the honeycomb section in the entrance section.

The temperature of the recirculating water was kept relatively constant by bleeding in a small amount of cold tap water. Kinematic viscosity as a function of temperature was taken from Schlichting [1955].

B. Data Gathering Techniques

1. Hot-wire and hot-film anemometer systems

Two constant temperature anemometers were used for measuring mean and fluctuating velocity. A commercially available Lintronic Laboratories' hot-film anemometer with a wedge probe was used to take mean velocity data for the zero pressure gradient flow. This unit is described in detail by Ling [1955]; problems associated with its use in low-speed water flows are discussed by Runstadler [1962].

All other flow setups were studied with the use of a hot-wire anemometer which was built by C. M. Sabin at Stanford University as the result of experience with a modified hot-wire anemometer from Lewis Flight Propulsion Laboratory; see Sabin [1963] for a description of this anemometer. The new Stanford water hot-wire anemometer will be described in detail in a later paper by Sabin, Schraub, et al.

Both anemometers consist of electronic feedback circuitry which supplied current to the sensing probe and maintains the probe at a fixed temperature above the temperature of the water. The operation is similar to the familiar hot-wire anemometers used in air except for several modifications required to obtain usable results in water flows. Both units provide a voltage output which is linearized to be directly proportional to the fluid velocity. This constant-temperature linearized operation is required for measurements where large velocity fluctuations occur as in wall shear flows. These instruments have been shown to have virtually flat response curves from 0 to about 1,000 cps in the velocity range of interest (see Ling [1955] and Appendix A).

The hot-wire anemometer was used for all data except the zero pressure gradient flow. The hot wire unit is somewhat superior to the hot-film unit in its ease of operation, lower scatter, and lesser calibration drift. The scatter of the two systems are illustrated in figure 2.3 by a comparison of data

for a laminar boundary layer on a flat plate taken by each of the two instruments with the theoretical solution due to Blasius as tabulated by Schlichting [1955].

The hot-film probe used is a commercially available wedge probe with a 1 mm by 0.2 mm platinum film as a sensing film. Its characteristics are described by Ling [1955] or Runstadler [1963].

The hot-wire probe is a specially designed hot-wire for low-speed water flow. An 0.0008 inch diameter platinum wire about 0.2 inches long is resistance welded to pure platinum leads 0.025 inches in diameter which are enclosed in a holder of glass and epoxy resin. See Sabin [1963].

The probes are rigidly held and accurately positioned with respect to the test wall by means of the traversing apparatus. A probe is mounted on an airfoil-shaped holder. This is held by a microscope stand mounted on a compound-head from a lathe which is mounted on a cross bar bolted to the channel. Using this mechanism, six degrees of freedom are available for placement of the wire perpendicular to the flow direction and parallel to the wall. Initial placement of the wire with respect to the wall is measured using a magnified optical-comparison to feeler guages of known dimension. In this manner, the zero position is determined to $\pm$ 0.0015 inches. Relative movement perpendicular to the wall is shown by a dial indicator-guage which reads to $\pm$ 0.00025 inches.

The anemometers were calibrated from determination of the Strouhal number of a stable Kármán-vortex street behind a circular cylinder in a uniform low turbulence flow. This method which is based upon the empirical relationship between Strouhal number and Reynolds number given by Roshko [1954] is believed to be accurate to 1%. A detailed description of the calibration procedure is given by Runstadler [1963].

Both anemometers suffer from some long-term calibration drift. A discussion of the factors effecting this drift is

given by Runstadler [1962] and Sabin, Schraub, et al [to be published]. The calibration was checked in detail before and after each data run and against a known velocity point during the run in order to avoid errors due to drift.

The hot-wire anemometer calibrations are reproducible within about 3%. A typical calibration curve is shown by figure 2.4.

The output of the anemometer was processed in two ways. The primary scheme for determining the mean-velocity profiles was to pass the signal into an analog-computer circuit which computed the time-integral of the signal. At the low velocities employed in this study, integration times of three to five minutes were necessary to obtain stable mean velocity values in the boundary layer flows.

A second scheme was to record the velocity data on a Sanborn strip-chart recorder whose frequency response is flat from zero to 50 cps. Mean and rms velocities are then determined by sampling the record at discrete time intervals and processing with a digital computer. The permanent velocity record is useful for qualitative study as well.

2. Hydrogen-bubble techniques

A significant contribution was made to the development of the hydrogen-bubble flow visualization technique as a part of this work. This development arose because an instrument capable of quantitative measurement of the instantaneous velocity field in a plane as a function of time was needed. The dye-slot injection techniques used successfully in earlier discovery of the complicated wall-flow structures of the turbulent boundary layer (Kline and Runstadler [1959]) gave primarily qualitative results. Extraction of quantitative features of the flow structure such as low speed streak spacing in the sublayer from the dye patterns necessarily involved some subjective bias of the observer. Neither single-point probe instruments nor any other previously

existing visual techniques were satisfactory.

The combined-time-streak marker hydrogen-bubble technique allows simultaneous determination of the velocity field over the six inch center span of the flow in planes at any distance from the wall. A permanent movie-film record of the flow structure allows both detailed qualitative and quantitative study of the flow structure using special film analyzing projectors such as the L-W PhotoOptics' Model 224-A.

A detailed description of several hydrogen-bubble techniques and of some operating experience with them as well as an extensive consideration of the uncertainties of the method are given in a separate paper by Schraub, Kline, et al [1964]. The basic method of visualization is shown in figure 2.5. A fine wire, usually of the order 0.0005 - 0.002" diameter, is employed as an electrode of a direct current circuit in the water tunnel. Hydrogen bubbles, formed at the wire are swept off and follow the flow. The bubbles are made visible by intense lighting at an oblique angle (65°) to the view direction. The wires have short sections coated with insulation at regular intervals; these insulation marks provide dark streaklines when the rest of the wire is producing bubbles. The wire is then pulsed at regular intervals of time to provide time lines. Motion picture photography of the combined-time-streak markers thus produced, allows nearly instantaneous determination of the streamlines and velocity patterns over the finite spatial extent of the boundary layer.

Figure 2.6 illustrates the determination of velocity at an instant over a large extent of the flow in the complicated flow of the sublayer of the turbulent boundary. Another example of combined-time-streak markers shown in figure 2.7 is taken from a teaching movie entitled "Flow Visualization".†

---

†Made under auspices of National Committee for Fluid Mechanics Films with Grant funds by National Science Foundation. Copies obtainable from Educational Services, Inc., 47 Galen Street, Watertown 72, Massachusetts.

Two film reading procedures were used to transfer the velocity data from movie film to IBM cards where it could be analyzed with digital computer facilities. At first, discrete data points were written by hand from the dial readout of a Vanguard Film Reader. This system is tedious and too slow for the quantity of data required. A more efficient system was designed and built specifically for this data reduction process: the projected film image is scanned (manually) with a device which produces a frequency proportional to velocity; the time of span is proportional to the spanwise spatial coordinate. This signal was then recorded on magnetic tape and sampled electronically as often as desired.

Figure 2.8 presents a direct comparison of mean velocity data (for a turbulent boundary layer) taken by the hot-wire anemometer and data obtained by the H_2-bubble technique and reduced using the specially designed film-reading system.

3. Wall-slot dye-injection technique

Side views of the flow patterns near the wall are made visible by seeping small quantities of food-coloring dye into the flow through 0.003 inch slots placed at one-foot intervals in the walls. Runstadler [1963] describes this technique in detail and has shown that the basic flow patterns are not disturbed by the visualization technique.

Dye marked at the wall in fully turbulent boundary layers is seen to move away from the wall in intermittent bursts which carry distinguishable filaments of lower momentum fluid well out into the logarithmic region. The bursting frequency and the actual trajectories and velocities of the tops of the marked filaments are determined by the analysis of movie records of this process. Data of this type are described in Chapter III, section B2.

C. Statistical Data Analyses

1. Averaging procedures

Turbulent fluid motion is an irregular condition of flow in which the velocity is a random function of both time and space. For an ensemble of experiments with the same boundary conditions, the trace of any velocity component will be a different function of space and time for each realization. So statistical averages must be defined in turbulence studies which have the same values for identical experiments.

Probably the most fundamental average is the "ensemble" average taken at the same relative time and position over an ensemble of identical experiments. When a flow is stationary, ensemble averages are independent of time; and when the flow is homogeneous in a given direction the ensemble average is independent of that direction.

For the steady, two-dimensional boundary layers of this study, the flow is stationary and is homogeneous in the z- or spanwise direction parallel to the wall. For this case, it is normally assumed that the time average at a point is the same as the ensemble average (an ergodic hypothesis) and that space averages in the z-direction are the same as the ensemble averages (another ergodic hypothesis). Thus, time averages and averages in the z-direction are assumed to be identical. This assumption is shown to be correct for the two-dimensional boundary layer by experimental verification of the equality of the time-averaged and space-averaged moments of the velocity distribution. For example, for the zero pressure gradient flow at the x-station of 13 feet and y^+ of 12, using H_2-bubble technique:

$$\bar{u}^{\,z} = 0.203 \text{ ft/sec}$$

$$\bar{u}^{\,t} = 0.196 \text{ ft/sec}$$

The velocity at this point determined by the hot-film was 0.20 ft/sec.

The experimental apparatus has a finite flow width of only 10 inches in the z-direction; thus averages in the z-direction could not be well defined at an instant by just one data sample. To provide z-averages, several data samples taken at long time separations were combined. The time separation was long enough so that any two samples were not correlated in time. Thus a combined spatial-ensemble average is obtained.

Averages are represented by an overbar, i.e., $\overline{(\ )}$. For hot-wire data this average was always taken with respect to time. For the H_2-bubble data, averages are usually taken with respect to z. Where necessary time averaged are denoted: $\overline{(\ )}^t$, and space averages: $\overline{(\ )}^z$.

2. Velocity probability density function

The probability density function, $\beta(x, y, z, t; u)$, of the x-component of velocity, u, provides all the meaningful information about u at a point in space and time (Lumley, [1964]).

β has the properties

$$\beta(x, y, z, t; u) \geq 0$$

$$\int_{-\infty}^{\infty} \beta(x, y, z, t; u)\, du = 1$$

$\beta(x, y, z, t; u)$ may be interpreted as the <u>probability</u> that the velocity at x, y, z, t has a value between u and $u + du$. <u>All</u> the mean powers (or central moments) of u are given by β:

$$\overline{u^n}(x, y, z, t) = \int_{-\infty}^{\infty} u^n \beta(x, y, z, t; u)\, du$$

For the two-dimensional, steady turbulent boundary layer at fixed x_o and y_o, $\beta = \beta(x_o, y_o; u)$ because of stationarity and homogeneity in the z-direction.

Histogram approximations of $\beta(u)$ for this case are calculated by simply counting the number velocity values in certain interval Δu about u. These distributions are compared to the Gaussian Distribution by the Chi-Squared "Goodness of Fit" test (Craemer [1954]), and by calculation of Skewness, S, and Kurtosis or Flatness, F.

$$S \triangleq \overline{u^3}^z \Big/ \left|\overline{u^2}\right|^{3/2}$$

$$F \triangleq \overline{u^4}^z \Big/ \left|\overline{u^2}\right|^{2}$$

Near the wall these probability density distributions show significant deviations from the Gaussian distribution. The Gaussian is that distribution approached by the sum of a large number of independent, random samples. Deviations from Gaussian are due to a correlation or statistical relation between velocity values: i.e., the velocity samples are not completely independent random variables.

Skewness different from zero (see data in Chapter III, figures 3.31 and 3.32) is indicative of the turbulent transport of turbulent energy. (See e.g., Townsend [1956] or Lumley [1963]). In this case $\overline{u^3}$ represents the transfer of the intensity of the x-component of velocity in the x-direction. The term associated with turbulent transport in the turbulence-energy equation (e.g., Hinze [1959]) is:

$$\text{transport} = \frac{\partial}{\partial x_i} \overline{u_i (p/\rho + q^2/2)}$$

The x-component of transport of the turbulence energy portion of this term is thus:

$$-\frac{\partial}{\partial x}\overline{u^3} = -\frac{\partial}{\partial x}\left(S \cdot \left|\overline{u^2}\right|^{3/2}\right)$$

So S is indicative of transport of $\overline{u^2}$ away from the point of measurement.

Flatness less than Gaussian distribution value of 3 is indicative of a structure in which there are less velocity values concentrated close to the mean than the Gaussian; i.e., the distribution is "flatter" than normal. The data on these statistical measures are given in figure 3.32.

3. Spatial spectral analysis

A spatial spectral analysis was applied to the spanwise velocity patterns obtained using the H_2-bubble technique. This was undertaken in order to ascertain whether or not the structure of relatively regular patterns of low speed streaks observed by eye in the wall layers corresponds to an underlying spatial wavelength which can be extracted by objective statistical means.

The spatial spectral-analysis procedures used here to analyze the velocity patterns are an extension of the results of time-series spectral analyses commonly used by workers in communications theory and statistical turbulence theory. See, for example: Hinze [1959], Parzen [1963], Lin [1959], Jenkins [1961], Blackman and Tukey [1958], Lumley and Panofsky [1964].

The method of determining the underlying spatial frequencies in the spatial velocity variation is to represent the correlation coefficient, $R_{11}(z_o)$, by a Fourier integral representation. The magnitude of the Fourier Transform coefficient, $U(\nu)$, of this representation is proportional to the relative presence of the ν(cycles/inch) frequency in the velocity pattern.

$$R_{11}(z_o) \triangleq \frac{\overline{u(z) \cdot u(z + z_o)}^{\,z}}{\overline{u^2}^{\,z}} \qquad (1)$$

where u is the fluctuation velocity in the x or "1" direction.

The Fourier representation of the velocity correlation

coefficient is given by:

$$R_{11}(z_o) = \int_o^\infty U(\nu) \cos 2\pi \nu z_o \, d\nu \qquad (2)$$

and its Fourier transform is:

$$U(\nu) = 4\int_o^\infty R_{11}(z_o) \cdot \cos 2\pi \nu z_o \, dz_o \qquad (3)$$

$R_{11}(z_o)$ satisfies the requirements for Fourier cosine integral representation (Sneddon [1951]). Physical intuition and experience show that $R_{11}(z_o)$ is an even function, is absolutely integrable, and will contain only a finite number of discontinuities and maxima in a given interval of z_o.

It was shown by Taylor 1938 that $\overline{u^2}\, U(\nu)$ is the contribution to the kinetic energy† of the turbulent u-velocity fluctations per unit mass from the frequencies between ν and $\nu + d\nu$. So that:

$$\int_o^\infty U(\nu) \, \overline{u^2} \, d\nu = \overline{u^2}$$

---

† $\overline{u^2}_t$ is interpreted as a kinetic energy per unit mass by many authors (e.g., Hinze [1959]). They are considering u in the Eulerian sense as the velocity at a point in space and with averaging over time. However, this average is actually performed over different fluid particles which happen to occupy that spatial point as a function of time. For the present case under consideration, $\overline{u^2}_z = \overline{u^2}_t$ by the assumptions of stationarity, homogeneity, and the ergodic hypotheses discussed above. $\overline{u^2}_z$ is averaged over different fluid particles which happen to lie in a line in the z-direction at a fixed time; but it may also be interpreted as kinetic energy of turbulence. Since turbulence is a random function of time and space, the analysis of $\overline{u^2}$ into its spatial frequencies is as valid an analysis as the "usual" analysis into time frequencies (or into x-direction wave numbers using Taylor's Hypothesis of $x = t/\bar{u}$ or $k_1 = \frac{2\pi\bar{u}}{t}$ where k_1 is wave-number).

$R_{11}(z_o)$ is calculated from (1) and $U(v)$ from (3) using the u versus z data from the hydrogen-bubble technique. These functions provide information indicative of the spatial structure of the turbulent flow. However, the inference of a specific flow structure from a given or calculated correlation coefficient is a difficult if not impossible process, since more than one flow structure can give the same correlation coefficient. But when the flow pattern itself is also available for detailed observation, as is the case in this study†, then the correlation gives very meaningful results. For example, in the sublayer region of the turbulent boundary layer, dye patterns and hydrogen-bubble pictures qualitatively show a relatively regular pattern of high and low fluid velocity streaks; when the statistical analysis indicates the existence of dominant wave lengths at about the streak-pattern spacing, then the existence of an ordered structure of this wave length is established beyond reasonable doubt. Data of this type are presented in Chapter III.

Several features of correlations are helpful in obtaining information about turbulent structure. A definable turbulent structure (or eddy) is the persistence of a fluid pattern over which the turbulent velocity bears some relationship or is correlated. The correlation at two points will be unaffected by structural features with length scales smaller than the separation distance, but positive contributions will be made by fluid motions with scales larger than the separation distance. Thus, at the largest separation distances where the correlation is non-zero, the behavior of the correlation provides direct information about the structure.

It may be shown (Townsend [1956]) by continuity requirements that the correlation between velocity components normal

---

†Here the flow pattern is available in visual form as a function of time on movie film and also as samples of velocity.

to a plane containing the two points must be negative for some values of the separation distance. $R_{11}(z_o)$ falls into this category. Negative correlation infers that the velocity at the two points is on the average in opposite directions (i.e., back flow is occurring†). Thus, where passage from positive to negative $R_{11}(z_o)$ occurs at large z_o, qualitative and some quantitative information about the largest structural features is provided by the correlation. Coincidence of such length scales with those of the visual observations lend support to the validity of both methods of investigation and to validity of the proposed flow structure.

Such results will be presented below. $U(\nu)$ will sometimes be presented $U(1/\nu)$ or $U(\lambda)$ where $\lambda = 1/\nu$. $U(\lambda)$ is useful for physical interpretation since λ is a physical length dimension (usually given in inches).

---

†Here u is measured relative to the mean speed $\bar{u}^z$ so that backflow in laboratory coordinates is not necessarily implied.

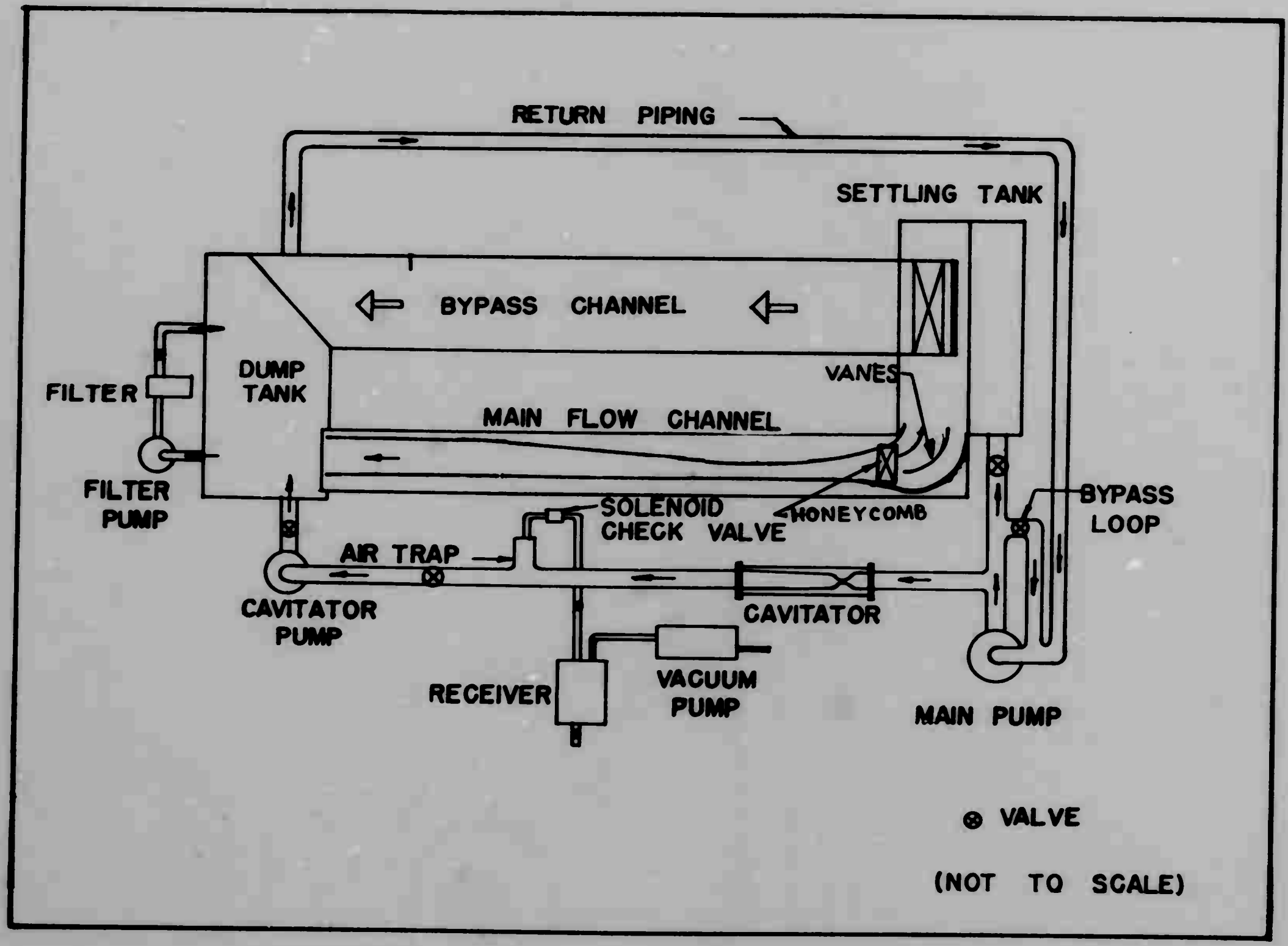

Fig. 2.1 Diagrammatic plan view of flow channel, recirculation system, and associated apparatus.

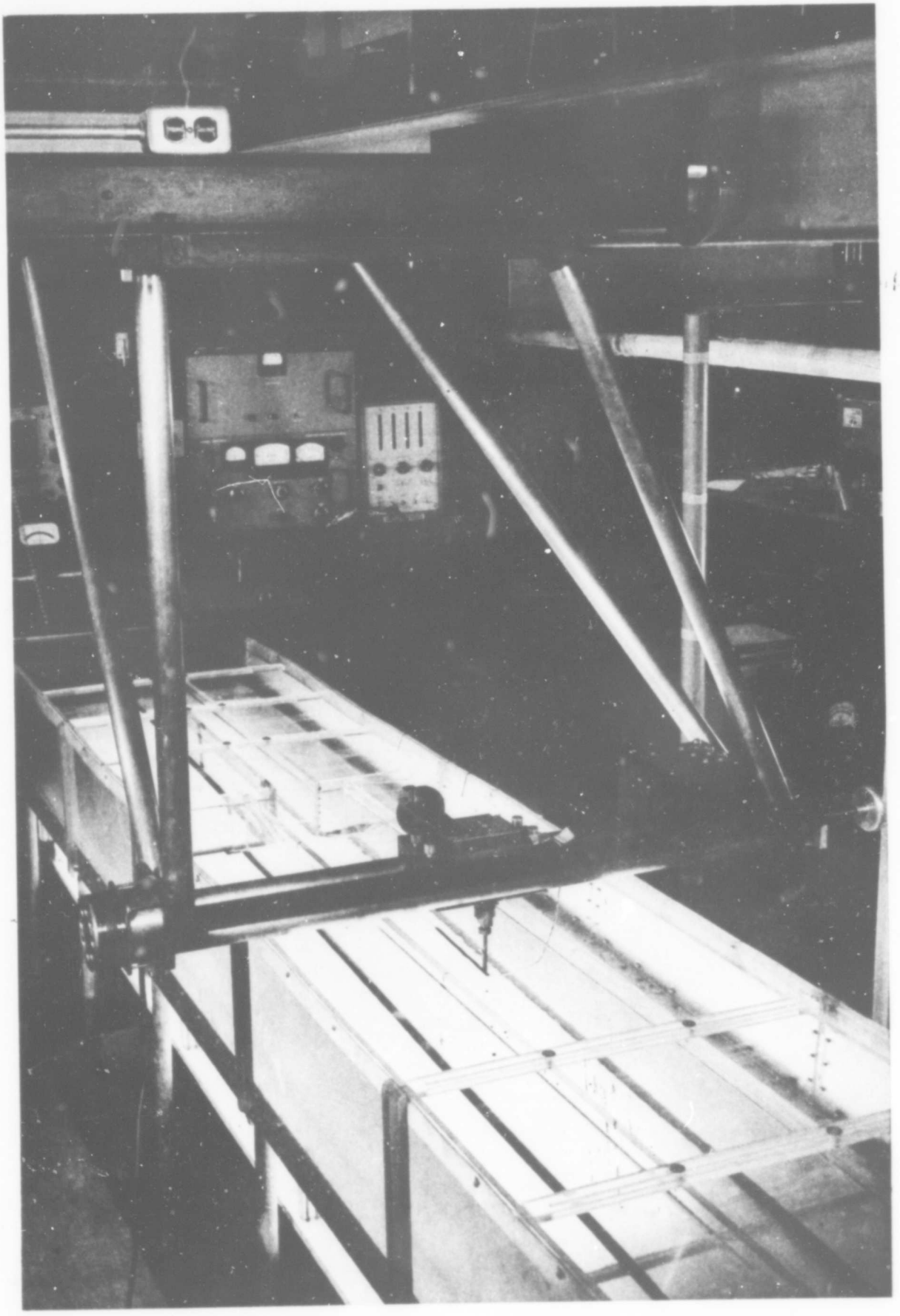

Fig. 2.2 Water channel and traversing equipment.

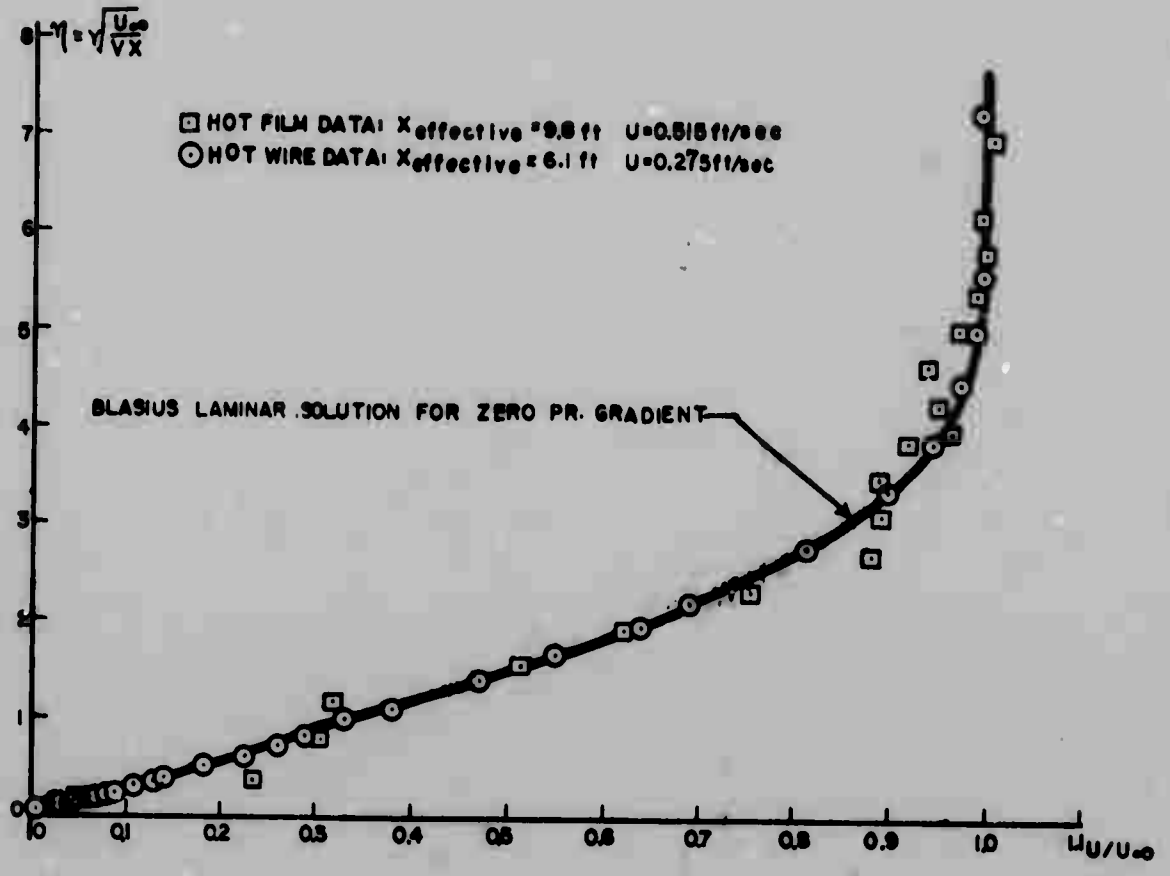

Fig. 2.3 Hot-wire, hot-film data comparison for laminar profile.

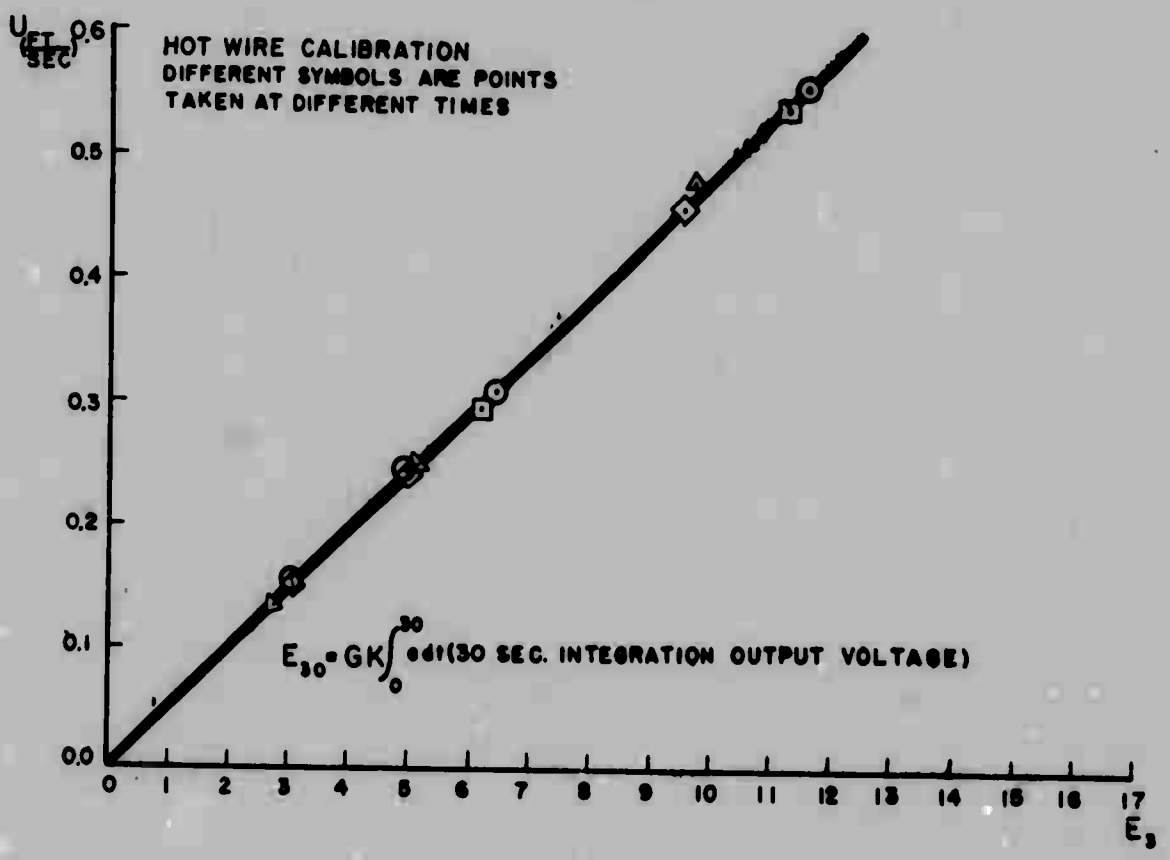

Fig. 2.4 Typical hot-wire calibration.

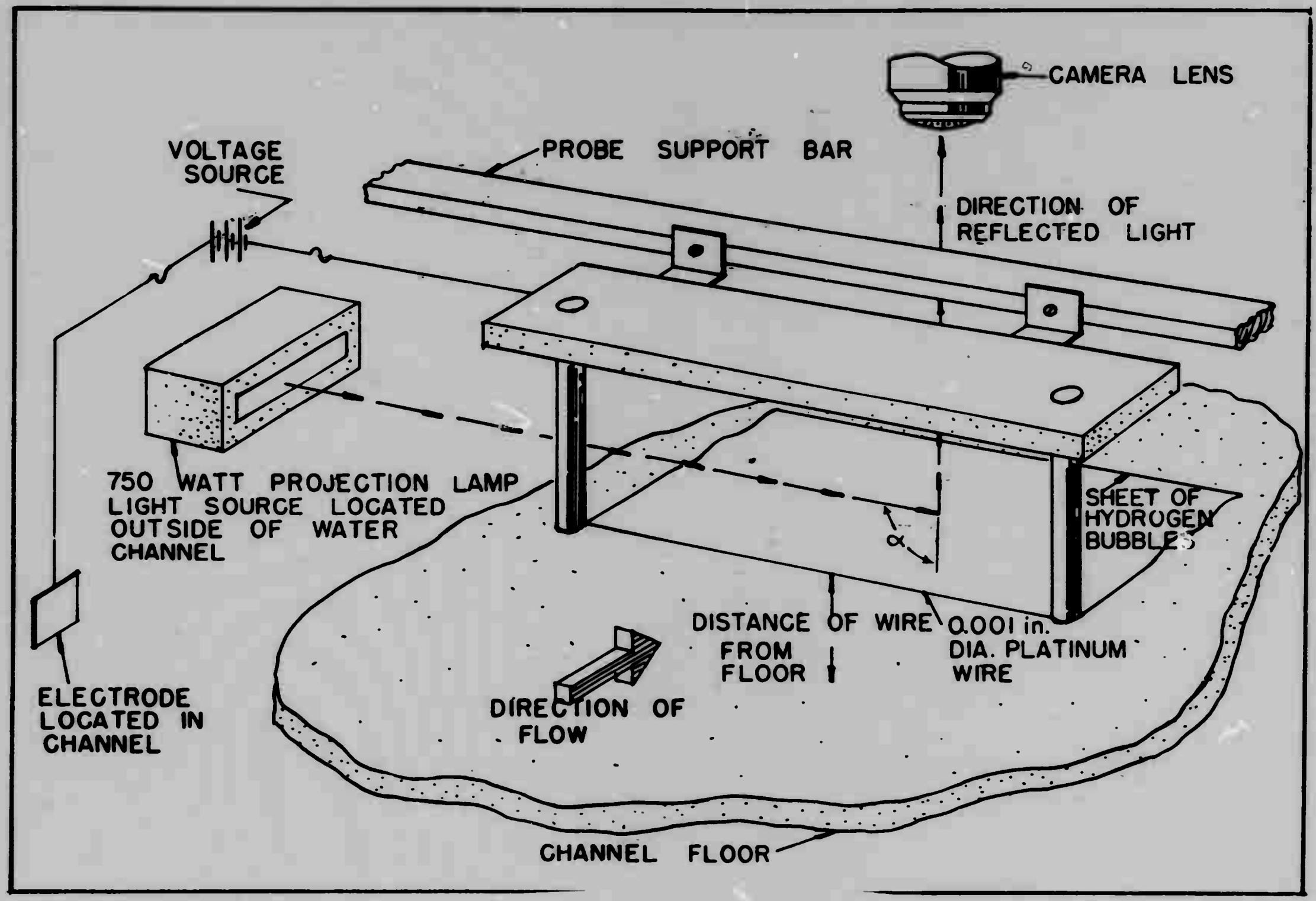

Fig. 2.5 Schematic of a typical bubble-lighting equipment.

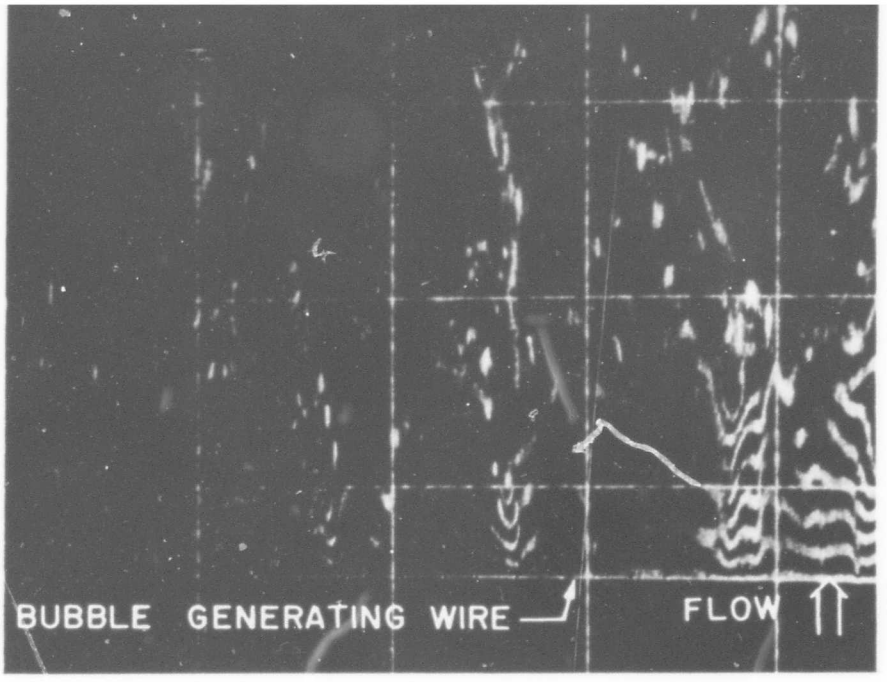

Fig. 2.6a Eddy structure of turbulent boundary layer on a flat plate (u_∞ = 0.5 ft/sec, Re = 5 x 10^5, y^+ = 11) observed with combined-time-streak markers with short time lines. Grid is made of one inch squares.

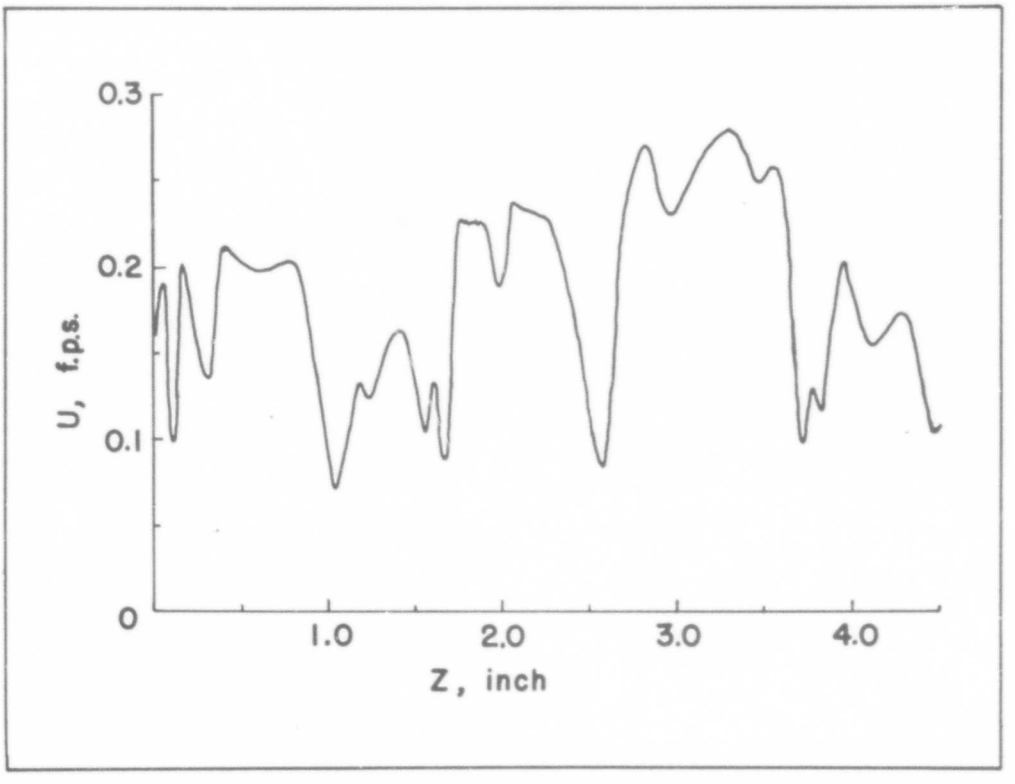

Fig. 2.6b Spanwise velocity profile taken from figure 2.6a (x-component of velocity versus z). z = 0 corresponds to grid line furthest to the left in figure 2.6a.

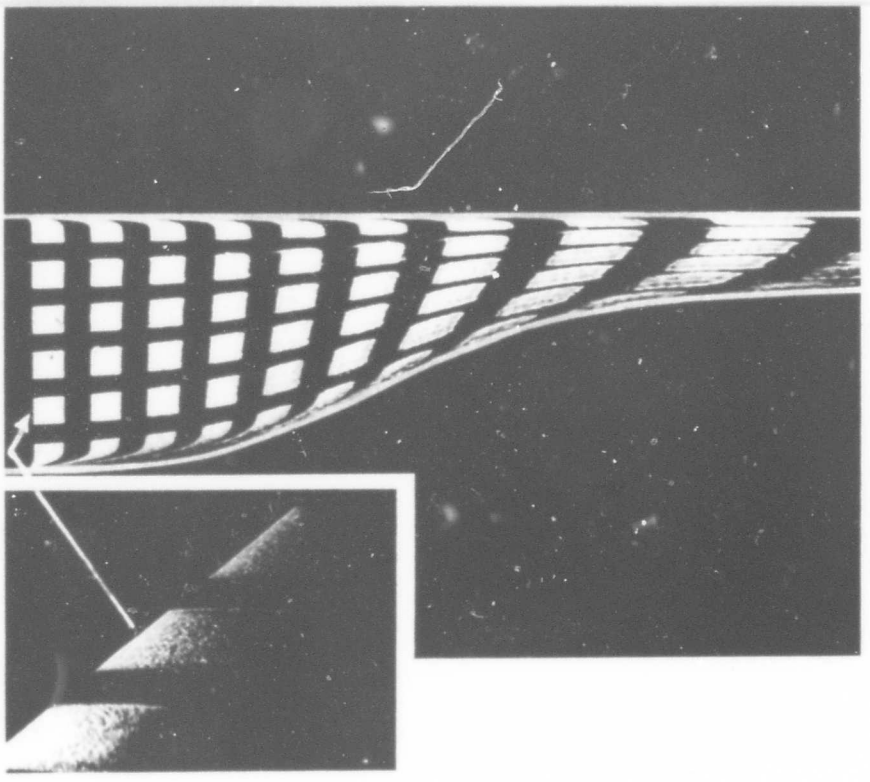

Fig. 2.7 Hydrogen bubble streak-squares in contraction; and close up of wire making streak squares.

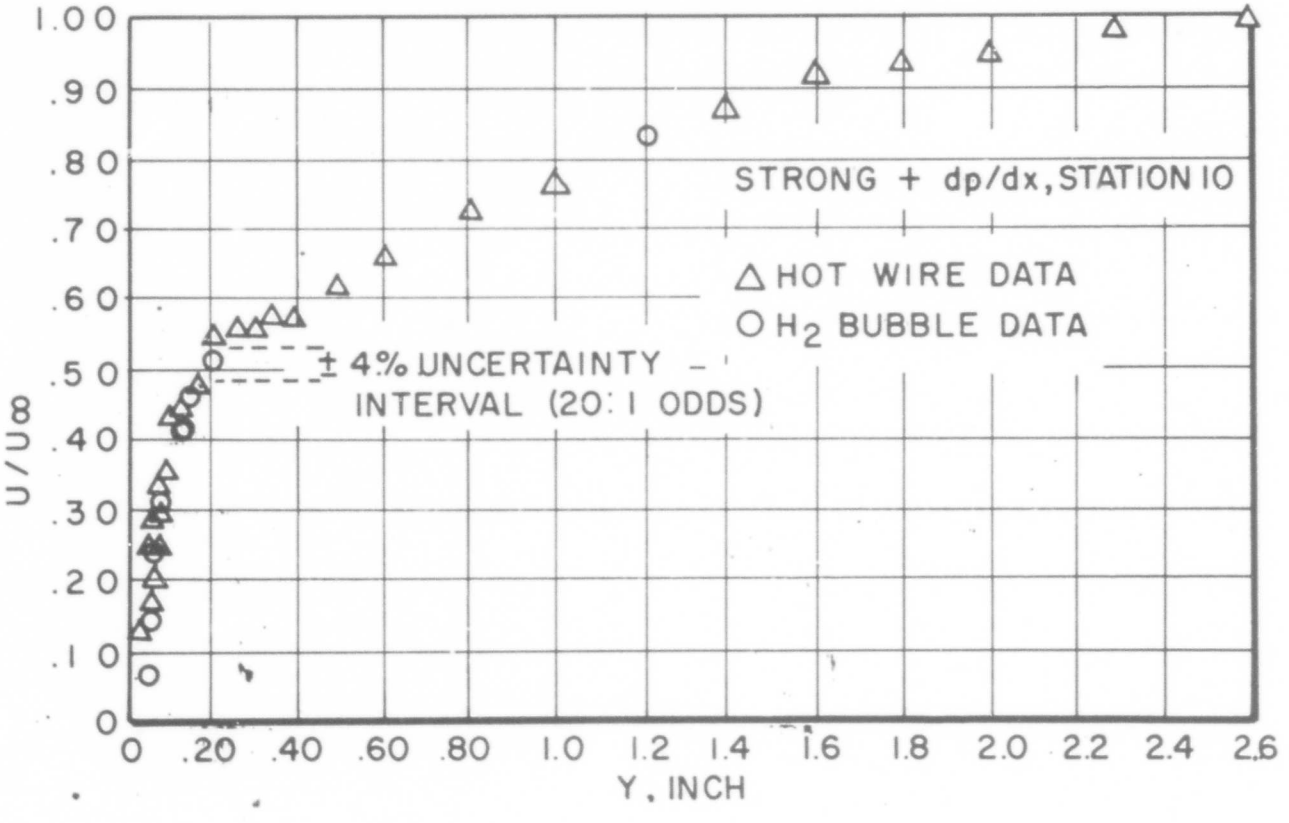

Fig. 2.8 Comparison of velocity measurements by hot-wire anemometer and H_2-bubble-film reading system.

III. EXPERIMENTAL RESULTS

A. Mean Flow Data

Five different flows were studied experimentally:

1. Zero pressure gradient: dp/dx = 0
2. Mild positive pressure gradient: mild + dp/dx
3. Mild negative pressure gradient: mild - dp/dx
4. Strong positive pressure gradient: str + dp/dx
5. Strong negative pressure gradient: str - dp/dx

The various data presented below are generally given for the different flows in the order listed above. The different flows will be referred to as the mild - dp/dx flow, the str + dp/dx flow, etc. for brevity.

1. Wall shapes and velocity distributions

The dp/dx = 0 flow was established experimentally by adjusting the flexible wall to allow for the displacement thickness effect of the growing boundary layers until constant free-stream velocity of 0.5 $\pm$ 0.01 ft/sec was attained from x-station 6 to x-station 14 (feet). The velocity distributions were determined using the constant-temperature anemometer.

The mild + dp/dx flow was obtained by fixing the flexible wall into a straight, flat surface at 1° divergence angle to the straight test wall. The mild - dp/dx flow was established by fixing the flexible wall straight and flat at 1° of convergence to the test wall. These wall shapes and resulting velocity distributions are given in figures 3.1 and 3.2, respectively.

The flexible wall shapes for the str+ dp/dx was formed by arbitrarily moving the wall to a steeper and steeper velocity gradient position until a small transitory stall (see Kline [1959] for definition of stall regions) appeared on the flexible wall. The flow on the flexible wall was then tripped with a 0.100" diameter wire, and the increased mixing which resulted provided a steady, non-stalled flow with the steep velocity gradient illustrated in figure 3.3.

The str - dp/dx flow configuration was established by moving the flexible wall into a shape which gave a negative pressure gradient strong enough to cause cessation of turbulent bursting from the sub-layer region or "relaminarization".† The wall shape and resulting velocity distribution are shown in figure 3.4.

The mean velocity data given in figures 3.5 through 3.9 were taken in conjunction with the velocity distribution data of figures 3.1 through 3.4 and show the degree of two-dimensionality of the flows at each test station.

2. Mean velocity profiles normal to wall

A velocity profile at the entrance to the test region (x-station 6) was taken with no trip wire in place. This profile (figure 2.4) is of standard laminar boundary layer form and agrees well with the Blasius flat plate solution (non-dimensionalizing with an adjusted or "effective" x-length). The excellent agreement of the hot-wire data to the theoretical curve (all data points are within 2% of the theoretical curve) shows that standard flow conditions are obtained with the channel and that the instrumentation is able to measure these flows correctly.

With the boundary layer trip in place across the test plate at x-station 3, mean velocity profiles were taken at various positions along the length of the test section for each of the five pressure-gradient flow setups. These profiles are presented in figures 3.10 through 3.14.

The dp/dx = 0 flow profiles (figure 3.10) were measured with the hot-film anemometer; all other data were taken with

---

†"Relaminarization" will be employed here as the word most descriptive of the phenomena of the regression of a fully turbulent boundary layer toward a layer with laminar characteristics. Other authors have used the expressions reverse-transition or laminarization; see, e.g., Launder [1963]. The terminology used here is consistent with Moretti and Kays [1964].

the hot-wire.† The smaller inherent scatter of the hot-wire unit is apparent in the results.

Displacement thickness, δ^* , and momentum thickness, θ , were calculated by integrating the velocity profiles. The values for the selected test stations for each flow are found in Table 3.1. From these data, the shape factor H and Re_θ have been determined and are presented in Table 3.1.

The values of Re_θ at the inlet are low compared to much of the air tunnel data in the literature. However, they are all above 500, and the shape of the profiles are typical of turbulent flow; it is therefore felt that the results will apply in general to turbulent boundary layer flows at higher Re_θ . The shape factors, H , are 1.4 for the zero pressure case and vary from 1.35 (strong negative dp/dx) to 1.66 (strong positive dp/dx) for the entire range of pressure gradient profiles. These values are indicative of non-separating fully-turbulent flows.

3. Wall shear and the "law of the wall"

The "law of the wall" is an hypothesis which states that there exists a region near a smooth wall where the mean velocity data from all turbulent boundary layers fall on one universal curve even when pressure gradients are present. The law of the wall provides a method of indirectly determining the wall shear.

If $u^+ = f(y^+)$ is the universal relationship where $u^+ \triangleq u/u_\tau$ and $y^+ \triangleq yu_\tau/\nu$, and $u_\tau \triangleq (\tau_w/\rho)^{1/2}$, then u_τ can be determined by cross-plotting the data with f . It is essential in what follows to note that u_τ is determined such that the data is forced to fit the "universal" curve over at least the "fitted" portion by this procedure.

---

†The hot-wire unit became available after the flat plate data had been taken. Separate tests for the flat plate using the hot wire are under way by C. K. Liu at Stanford University.

The "cross plot of log-region" procedure used in this study will now be described. Using the universal function $u^+ = f(y^+)$, another universal function $u_g^+ = g(u^+ \cdot y^+) = g(uy/\nu)$ was formed (Figure 3.15). Then for each raw data point, $u(y)$, $u \cdot y/\nu$ was formed and a u_g^+ determined from $g(uy/\nu)$; u/u_g^+ then gives a $(u_\tau)_g$ for each data point; the average $(u_\tau)_g$ should be the u_τ for that profile. $(u_\tau)_g$ versus y will be a constant (u_τ) over the entire range where the law of the wall is universal. Note that the data need not be matched to a slope over just the logarithmic region to determine u_τ .

However, if there are regions near the wall where the data does not have the behavior predicted by $f(y^+)$ - i.e., where the law of the wall is not universal - then the u_τ determined by this method depends upon which part of $f(y^+)$ the data is forced to fit!

Since most data very close to the wall in the sub-layer region is subject to relatively large experimental uncertainties, most recent investigators† using this cross-plot procedure match only the data in the logarithmic or fully-turbulent region to the logarithmic portion of the universal relationship. Well defined logarithmic regions are observed for most of the profiles of this investigation (see figures 3.16 - 3.20). Thus wall shear may be determined by the "cross-plot of log region" procedure, using the universal logarithmic relation given by Clauser [1954]: $u^+ = 5.6 \log_{10} y^+ = 4.9$. The method is illustrated by figure 3.15.

This "cross-plot of log region" is the primary method of determining u_τ for the data of this investigation. Non-dimensional u^+ , y^+ mean velocity profiles based upon u_τ determined by this method are given by figures 3.16a - 3.20a.

---

†For example: Clauser [1954], Launder [1963], Runstadler [1963].

In this form, the data have "standard" fully turbulent boundary layer profile shapes. There is a well defined logarithmic region near the wall. This logarithmic profile extends from y^+ of about 40 out to the section where the profile deviates from the logarithmic curve and from that point out a typical "wake" profile is seen (Coles [1956]). The point of deviation depends upon the Reynolds number and pressure gradient history and varies from y^+ of 80 to 200. Below y^+ of 40 the data blend gradually toward a linear (u = constant y) curve as the wall is approached.

The profile at station 12 in the str - dp/dx flow is an exception. For this case, the boundary layer has no linear region near the wall and no logarithmic region. The detailed structure is, correspondingly, seen to be of a non-fully-turbulent nature. For this case, the application of the strong negative pressure gradient so altered the flow that the mean profile is not the standard fully turbulent form. This "relaminarization" of the flow will be discussed in greater detail below in section C.

A secondary method of wall shear determination will now be discussed.

Using the hot-wire anemometer, considerable data (such as shown in figure 3.21) obtained between y^+ of 1 and 8 clearly indicate the existence of a linear mean velocity profile region near the wall (i.e., $u = cy$). The presence of this linear region very near the wall suggests that this is the $u^+ = y^+$ region of the universal law of the wall and that wall shear can be determined by forcing these data into $u^+ = y^+$ form. This is equivalent to determining wall shear from the slope of the mean velocity profile in this linear region near and at the wall, i.e., $\tau_w = \mu \left(\frac{\partial \bar{u}}{\partial y} \right)_{y=0}$. Figure 3.21 illustrates this method of shear determination.

These data are felt to be the most complete and reliable

so far obtained for the sub-layer region. The probe is very small compared to the sublayer thickness.† The hot-wire diameter, nondimensionalized on a typical value of wall shear, is only $d^+ = \frac{du_\tau}{\nu} = 0.10$. The consistent linearity observed is strong experimental evidence in support of the theories of Prandtl [1933] and others which predict linear behavior of the mean velocity profile very near the wall.

However, these theories are based upon a completely viscous or laminar flow model for this wall region under zero pressure gradient conditions. For the flows studied here, not only are pressure gradients present, but time-dependent motions are always observed in this wall region when the boundary layer is turbulent (see next section). Nevertheless, a linear profile is observed near the wall. This may be interpreted as experimental evidence that turbulent shear‡ is negligible and that viscous shear dominates this region. Thus this wall-slope method of determining wall shear rests not only upon the assumption that the pressure gradient has

---

†Instruments are of typical size, but the sublayer is roughly 10 times thicker than in previous studies due to the very low speeds employed in water flow.

‡The important term in the turbulent shear is $-\rho\overline{uv}$. That is, an apparent shear is caused by momentum interchange between fluid layers by turbulent motions in the x and y directions giving rise to a finite $-\rho\overline{uv}$. The existence of large time-dependent fluctuations in the x-component, u , which are observed in the sub-layer region are not necessarily indicative of large momentum interchange between adjacent fluid layers. The following simple experiment gave qualitative (but not conclusive) evidence that turbulent momentum interchange is small in the sublayer. A H_2-bubble wire was placed perpendicular to the wall and pulsed so that instantaneous velocity profiles in the sublayer were made visible. The u versus y profiles at an instant were linear (within the resolution). The slope changed continuously as a function of time, but the profiles remained smooth; i.e., no small scale mixing was observed between fluid layers which would indicate significant "turbulent shear" at $y^+ < 7$. This was in contradistinction to the motions observed in the same experiment for $y^+ > 10$.

negligible effect upon the universal profile in this region (as does the cross-plot method) but also upon the assumption of negligible turbulent shear in this region. For this reason the wall-slope method is considered less dependable and is a secondary method.

The shear velocity obtained by the two methods (cross-plot of log region and wall-slope) do not coincide in general. Table 3-1 and figure 3.22a present a summary of the shear velocities determined by the two methods. Differences of up to 20% exist between u_τ determined by the two methods. The uncertainty of determining the shear velocity for each method separately is estimated to be $\pm$ 7% at 20:1 odds.

The differences between u_τ determined by each method is $7\sqrt{2} \approx 10\%$.† Thus, while the magnitude of the differences is not known with certainty, a real difference is observed in some cases.

In the u^+, y^+ mean velocity profiles of figures 3.16a - 3.20a, the data were non-dimensionalized using wall shear determined by the cross-plot of logarithmic region method. Thus, the data are "forced" to fall on: $u^+ = 5.6 \log y^+ + 4.9$; deviation from the $u^+ = y^+$ in the sublayer is observed.

In figures 3.16b - 3.20b, the same data are presented in the $u^+ - y^+$ form but non-dimensionalized using wall shear by the wall-profile method. The result is agreement with the $u^+ = y^+$ curve near the wall and deviations from universality in the logarithmic region.

A trend in the direction and magnitude of deviation from universal behavior is shown by the $u^+ - y^+$ data plots of figures 3.16 - 3.20. These trends are more clearly shown by plotting the ratio ($u_{\tau\ \text{wall}} / u_{\tau\ \text{log plot}}$) as a function of x-station for the different pressure gradient flows; (figure 3.22b). Only if the ratio is a constant, can a universal

---

†Method of estimation due to Kline and McClintock [1953].

velocity profile for the wall and logarithmic regions exist simultaneously.

For fully turbulent boundary layers, u_τ wall slope/u_τ log c.p. is observed to <u>increase</u> smoothly for positive pressure gradients and <u>decrease</u> smoothly for negative gradients† (figure 3.22b). Comparing the strong and mild positive gradient behavior, it appears that the magnitude of the effect is generally proportional to the magnitude of the pressure gradient applied. Notice that the ratio is not simply directly proportional to the magnitude of the local pressure gradient but is also dependent upon the pressure gradient history; i.e., the ratio continues to rise (or fall depending upon the sign of the applied pressure gradient) after the local pressure gradient is relieved (see Table 3.1 for pressure gradient parameter as function of x).

The shape and even the existence of a truly universal law of the wall have been questioned on theoretical grounds by several workers (see e.g., Mellor [1963], Einstein and Li [1956]...). Smith and Walker [1959], for example, have given convincing evidence of a dependence of the constants in the logarithmic portion of the correlation upon Reynolds number. The "pressure gradient" deviations observed in this study are not due to a Reynolds number effect, since the Reynolds number is very nearly the same for all pressure gradient flows considered. However, the value of $\left[u_\tau \text{ wall}/u_\tau \text{ log}\right]$ at the inlet station (which is about 0.8 from figure 3.22b) depends upon the constants in the logarithmic correlation. The constants used here are from Clauser [1956]; they correlate data for higher Reynolds number flows very well, but are not as satisfactory for the low Reynolds number flows of the present study. The constants in the logarithmic correlation <u>could</u> be

---

†The relaminarization flow (str - dp/dx) is considered separately below since these layers are not fully turbulent.

chosen to make $[u_{\tau\ wall}/u_{\tau\ log}]$ equal to one at the inlet stations where $dp/dx \approx 0$, but this was not done.

Very little experimental data have been obtained by previous investigators in the sub-layer region. Figure 3.23 illustrates some of the early data of Ludweig and Tillman [1949] and others upon which the concepts of the law of the wall were founded. Notice that there are no data at $y^+ < 10$ (that is closer to the wall than the region blending between the sublayer and fully turbulent regions). More recent investigators have obtained some data in the wall region (figure 3.24).

Even these later data have usually consisted of just a few points in the outer portion of the wall region usually with higher uncertainty than data in the outer regions. No clear conclusions on mean profile in the wall layer can be drawn from these older data. The present hot-wire data is significant in that a large number of measurements are available in the sublayer for several profiles under a variety of flow conditions. The above mentioned lack of universality of the "law of the wall" is observed. The data were not taken for the purpose of investigating the "law of the wall" in detail. And although they are much more detailed than previous data they are still not sufficiently complete to allow generalizations to be made at this time as to the amount of deviations or for the suggestion of a new law for the wall region. However, these results do add new evidence to the proposition that the "law of the wall", while a reasonable first approximation, is not an accurate "universal" expression in pressure gradient flows.

4. Non-dimensional velocity defect profiles

Velocity profile data are given by figures 3.16 - 3.20 by the "law of the wall" (u^+ vs y^+) type of non-dimensional plot. Another common non-dimensionalization used to compare turbulent boundary layer data is the velocity defect plot.

Figures 3.25 - 3.28 present the data of this investigation as $\frac{u_\infty - \overline{u}}{u_\tau}$ vs. $\frac{y}{\Delta}$. Δ is an integral boundary layer thickness defined by $\Delta \triangleq \int_0^\infty \frac{u_\infty - \overline{u}}{u_\tau}\, dy = \delta^* \frac{u_\infty}{u_\tau}$. The curves of constant shape parameter, G , of Clauser [1954] are given on these curves for comparison; where: $G \triangleq \int_0^\infty \left(\frac{u_\infty - \overline{u}}{u_\tau}\right)^2 d(\frac{y}{\Delta})$.

An <u>equilibrium</u> flow is defined by Clauser [1956] to be one in which the profiles at all x-stations have the <u>same</u> profile in these non-dimensional coordinates; thus, in an equilibrium flow, all profiles have the same value of G . G is, however, different for each equilibrium flow; for the special equilibrium case of zero pressure gradient, Clauser [1956] gives a value of $G = 6.8$.

The flows of this investigation are not, in general, equilibrium flows, and G changes for each profile. Only the zero pressure gradient flow is an equilibrium case in the flows reported. A constant value of $G \cong 6.7$ was obtained for this flow. (The difference between the present value of G for zero gradient and that of Clauser may be due to Reynolds number differences.) For the pressure gradient flows G varies in an arbitrary manner.

A cumulative effect of the application of the pressure gradients is shown by examination of the velocity defect profiles (figures 3.25 - 3.28). The strongest gradients produce the most deviation from zero gradient shape; and positive and negative gradients have a clearly different effect. The flows are clearly <u>not</u> equilibrium flows.

5. <u>Longitudinal velocity fluctuation measurements</u>

Accurate measurement of turbulent fluctuations is difficult for the low velocity flows of this investigation because the low temporal frequencies involved require averaging times of several minutes and make analog calculation difficult. Data obtained by sampling the velocity trace which was recorded

on a Sanborn strip recorder and then calculating $\sqrt{u^2}$ by digital computer are presented in Figure 3.29 as $\sqrt{u^2}/u_\tau$ versus y^+ . One data profile (strong + dp/dx, sta 10) derived by the H_2-bubble technique is also given in figure 3.29.†

Data of Runstadler [1963] and Laufer [1954] for zero pressure gradient boundary layer and pipe flows respectively are also given for comparison. The trends in the present data are observed to be the same as those of these other authors: $\sqrt{u^2}/u_\tau$ increases nearly linearly from zero at the wall to a maximum of between one and three in the vicinity of y^+ of 10 to 20 (the buffer region) and then gradually decreases with increasing y^+ .

The data show that the applied pressure gradients do not drastically alter the shape of the intensity profile from that of the zero pressure gradient case. However, the pressure gradient does change the magnitude of intensity; in particular, the positive gradient increases the intensity, and the negative gradient decreases it. In the positive pressure gradient flow, intensity increases from zero at $y^+ = 0$ to a maximum which is about the same or slightly above the zero gradient data and then decreases with y^+ more gradually. The negative gradient flow (relaminarization flow) has a maximum intensity which is considerably less than the zero case (by 50% for these data) and the level appears generally lower for all y^+ .

Free-stream turbulence intensity at the inlet to the test section is observed to be 1-2% for all flows.

---

†Better data can be obtained for this type of flow by FM recording and playback through analog-to-digital converter and electronic counter. Such a system hopefully will be available at a later date.

B. Flow Structure Details and Pressure Gradient Effects

This chapter contains the central results of the present study on the structure of the turbulent shear layer in the presence of longitudinal pressure gradients.

The fully turbulent boundary layer consists of three distinct layers with different structural features: (a) a sublayer or wall region, (b) a fully turbulent or core region, (c) an outer or wake region. Runstadler, et al [1963] showed the relationship of these regions to the mean velocity profile in u^+ , y^+ coordinates and presented considerable information describing the detailed structure. Summaries of Runstadler's previously reported structural features are included at appropriate places below.

The flow patterns are strongly three-dimensional and time-dependent, making observation of the structure difficult and complete understanding of all details probably impossible. Nevertheless, using better techniques of visualization, (see Chapter II), considerable new structural detail has been recognized in the present investigation and is presented below.

These results are in good general agreement with Runstadler's [1963] picture of the flat plate boundary layer flow structures. However, new information on the details of the bursting phenomena from the sublayer and a wider range of observed pressure gradients make revisions of a few of Runstadler's detailed conclusions necessary.

A major result of this study is that turbulent boundary layers under pressure gradients have all the same major structural features of the zero pressure gradient layers. Regions across the layer defined by structural details have the same one-to-one correspondence with the regions defined by the $u^+ - y^+$ mean velocity profile (wall, logarithmic, wake) as in the zero gradient flows. The growth and extent of these regions are, however, strongly dependent upon the

applied pressure gradients.

Evidence of this general result is given by figure 3.42 where a pictorial survey at 11 y positions across a layer with positive pressure gradient is given. The qualitative features of the structure are identical to the zero gradient flow in corresponding regions: i.e., wall, buffer, turbulent core, and wake; these features correspond to those given by Runstadler [1963] for zero pressure gradient flows. Figure 3.43 gives a direct comparison of pictures taken in the wall layer region for zero, positive and negative pressure gradient flows. The general features are identical.

1. Sublayer or wall region

The sublayer or wall region extends from the wall out to $y^+ \approx 7$. This is the region of strong wall effect; viscous forces dominate; the mean velocity profile is linear.

The flow structure in the wall region† is a highly ordered turbulent structure. The velocity variations in the spanwise direction form a rather regular pattern of high and low velocity streaks. Thus, when the fluid is marked across the flow with a uniform line of dye or bubbles, the trace does not proceed downstream in a uniform manner (such as it does in truly laminar flow). Instead, the trace is observed to change very rapidly to a rather regular "streaky" pattern of dye or bubble concentrations stretched in the longitudinal direction. The low-velocity streaks are the order of 10 times longer in the flow direction than in the transverse or lateral directions.

The entire flow near the wall is both spatially and time dependent in contrast with a truly laminar flow. Nevertheless, the particles move in rectilinear motions (over distances the order of the boundary layer thickness) in contrast to the random, erratic motion usually attributed to turbulent motions. (This was called "laminar-like" motion by Runstadler.) The

†Most features of this summary description are from Runstadler [1963] but are given in the present author's wording.

spatial dependence arises from the relatively regular pattern of spanwise variation over the wall surface described above. The time dependence arises because: (i) the pattern "waves" gently back and forth in the spanwise direction; (ii) a streak exists for a period of time and then washes out or breaks up (see section on interaction of wall region and outer layer); (iii) the entire streaky wall structure moves slowly in the downstream direction with the mean flow.

a. Instantaneous spanwise velocity profiles

The most striking feature of this wall region ($o < y^+ \leq 8$) is the nearly regular spanwise structural variations which cause the pattern of dye streaks or "islands of hesitation" reported by Kline and Runstadler [1959] and Runstadler, et al [1963]. The combined-time-and-streak markers of the H_2-bubble technique provide instantaneous velocity images over the entire span of the flow at any x-station. In this manner the somewhat regular "streaky pattern" (figure 1.1a) has been conclusively† shown to be a variation of the x-component of velocity, u , in the z-direction (figure 2.7). The z-component, w , may also be obtained (with greater uncertainty; see Appendix) and shows a corresponding regular pattern of z dependence.

For example, in figure 3.30 a typical wall layer pattern and the u and w traces derived from it are shown. The u and w are determined by the pathline or frame-to-frame method of velocity determination (see Schraub, Kline, et al, [1964]). There is some evidence (see footnote in section A.3) that not only is the mean velocity near the wall linear, but that the instantaneous velocity profile (u vs y) is smooth

†While Runstadler, et al [1963] clearly indicates the variations in u(z) at fixed y, x and t using timelines alone, the present study established this point beyond any reasonable doubt using the improved combined-time-streak marker technique.

and nearly linear. In this case, u vs. z given at an instant and at a fixed distance from the wall is proportional to the local wall shear; i.e. $u(z)$ is proportional to $\tau_w(z)$, and the $u(z)$ plots are indicative of the variation of τ_w with z at an instant. Instantaneous local wall shear is thus both time and space dependent in a turbulent boundary layer.

The spanwise u-velocity variations are typically observed to be the order of 40-50% of the local mean velocity in the wall regions. This large variation gives rise to significant $\frac{\partial u}{\partial z}$ shearing components. $\frac{\partial u}{\partial z}$ often reaches 10% of $\left.\frac{\partial \bar{u}}{\partial y}\right|_w$ locally; the root mean square value of $\frac{\partial u}{\partial z}$ is the order of 1% of $\left.\frac{\partial \bar{u}}{\partial y}\right|_w$ at $y^+ = 8$.

The combined-time-streak H_2-bubble technique provides a method for obtaining instantaneous velocity profiles over a large extent of the flow; this makes possible more systematic statistical analysis of the flow structure than was previously possible.† The next several sections discuss and present some of the results of these statistical analyses applied to these velocity profiles.

b. Velocity probability density histograms

The velocity probability density function of the longitudinal component of velocity (see example in figure 3.31) resembles the Gaussian or normal distribution. However, in the wall layer regions, the distributions differ significantly (in statistical sense) from Gaussian as determined by the Chi-squared "goodness of fit" test at 5% significance level (Craemer, [1955]).

The variation of the skewness and flatness factors of the

†Runstadler used hydrogen bubble timelines. However, timelines alone are not sufficient to provide accurate instantaneous spanwise velocity profiles. The combined-time and streak marker system used here provides this information (see Schraub, Kline, et al [1964]).

city fluctuation probability density functions as a
tion of y-position in the region near the wall was
stigated for one profile. Figure 3.32 compares the
ent data with that of Comte-Bellot [1963] for a channel
. Qualitative agreement is good.

The monotonic decrease in skewness from positive values
ugh zero to negative values across the sublayer region
be given a simple physical interpretation in terms of
observed flow patterns. In the regions nearest the wall,
relatively low-speed regions are wider than the fast
ons; i.e., a greater extent of the flow has values less
the average velocity and these will be balanced by
r relatively higher velocity points which will produce a
tive skewness. This is the case for $y^+ < 10$. Further
the wall ($y^+ > 10$), the relatively low-speed streak
ons are narrow compared to the higher speed regions giving
to negative skewness. This correspondence between the
itative features of the structure and the statistical
ysis of the structure is illustrated by a sketch in
re 3.33.

No conclusive pressure gradient effect is discernible
the velocity distributions from the limited data. How-
, all the positive pressure gradient distributions have
ness and flatness factors below those of the zero and
tive gradient flows (at the same y^+) of the present data
those of Comte-Bellot [1963]. This trend corresponds to
qualitative observation of wider low-speed regions and
accentuated streaks in the wall region of the positive
ient flows (compared to the zero pressure gradient
vior).

c. Low-velocity streak spacing

(1) Visual streak counting

Runstadler [1963] suggested a parameter, λ^+,
h successfully correlated the average low-speed streak

spacing in the sublayer. $\lambda^+ = \frac{\lambda u_\tau}{\nu}$, where λ is the average distance in the span direction between centers of low velocity streaks, u_τ is the local shear velocity, and ν is kinematic viscosity of the fluid. Runstadler showed that for zero pressure gradient flow conditions λ^+ = constant for a wide range of free stream velocities (figure 1.2) at a fixed x-station. λ was determined by measuring the distance between streaks in a large number of still photographs of the wall structure; the structure was made visible by dye injection through a dye slot or by the bubble timelines. This method of finding λ is called the "visual counting" method.

The zero pressure gradient flow setup of the present investigation was established in order to investigate the behavior of the boundary layer structure at <u>different</u> x-stations at a fixed free-stream velocity. Using the same methods as Runstadler, λ^+ was determined at three x-stations and was found to be constant. The actual value of the constant is dependent upon the "ground rules" of the observer who counts the streaks by eye. The difficulty is discussed at length by Runstadler [1963]. Using Runstadler's ground rules $\lambda^+ \approx 80$ was obtained (Runstadler found $\lambda^+ = 76.5$), but using other reasonable counting rules λ^+ as high as 110 were obtained. This difficulty gave the major incentive toward development of the statistical procedures for structure analysis which are discussed in the next section.

The "ground rules" adopted for visual determination of λ for the present data are slightly different than those used by Runstadler, et al [1963]; the present rules give consistently higher values of λ (see figure 3.35). Runstadler "counted" streaks several inches <u>downstream</u> of the marking point as well as near the marking point; thus a streak which had washed slightly downstream from the marking point was "counted" as well as those streaks near the wire. For the present data, low-velocity streaks were "counted" only when present at or

very near the marking point. The reason for adopting this procedure is that streaks are then counted at a discrete x-station only; also, this method is expected to give results more consistent with the statistical procedures which analyze the actual velocity profile, $u(z)$, at a fixed x-station very near the marking point.†

The visual count data for the various pressure gradient and zero-pressure-gradient flows of the present study are plotted versus the pressure gradient parameter K in figure 3.34. The primary conclusion to be drawn from the data is that λ^+ is not a function of pressure gradient and λ^+ is a constant: $\lambda^+ \approx 102 \pm 10$ (at 10:1 odds).

This result is based on the turbulent boundary layer data of this report where: $560 \leq Re_\theta \leq 1700$ and $-2 \leq K \leq 4$.‡

In the case where relaminarization took place (strong - dp/dx flow), the boundary layer was not a turbulent layer, and this results in values of λ^+ very much larger than 100 (see figure 3.34).

The results of the visual streak counting are generally borne out by the statistical analysis which is described in the next section. However, the visual count data has the advantage of simpler physical interpretation since λ is simply the average distance between low u-velocity streaks in the wall layer region. The statistical results, while more elegant in principle, have no such obvious physical meaning and, in addition, have larger uncertainties: λ_{visual} is in general about 20% less than λ determined by the

---

†For the H_2-bubble marking technique, velocity measurements in the sublayer are of least uncertainty when taken from about 40d to 240d, where d is the H_2-bubble generating wire and d = 0.001 inches; see Schraub, Kline, et al [1964].

‡$K \triangleq \frac{\nu}{u_\infty^2} \frac{du_\infty}{dx}$; K is the pressure gradient parameter used in this study; it is developed and discussed in detail in section C of this chapter.

statistical procedures; a direct comparison of λ_v to $\lambda_{R_{11}}$ † is given by figure 3.35.

(2) Correlation coefficients and spatial analysis

Definitions and discussions of $R_{11}(z_o)$, $U(\nu)$ and $U(\lambda)$ are found in Chapter II, section C3. A discussion of the interpretation of these results is also found there. A discussion of the uncertainty and resolution is given in the Appendix.

When spectral analysis procedures are applied to a single realization of $u(z)$ (i.e., one frame of motion picture of the flow) very striking results are obtained. (See figure 3.36.) The velocity trace shown in figure 3.36 has been obtained using the Vanguard film reader from a single frame of a motion picture. The flow structure was made visible by illumination of H_2-bubbles in the wall layer of a zero pressure gradient turbulent boundary layer.

The near-periodicity of the $u(z)$ trace (streaky structure) is reflected as near periodicity in $R_{11}(z_o)$. The transform function $U(\lambda)$ shows a corresponding peak at the dominant wavelength of this periodicity. This wavelength, λ_U, corresponds closely to the average spacing between low-speed streaks as determined by the visual method. This λ_{visual} (or λ_v) is 0.67 inches whereas λ_U is 0.73 inches. The agreement is encouraging since it shows that completely objective statistical methods indicate the existence of a dominant wavelength which corresponds quite closely to the average spacing the subjective human viewer perceives. The peak at $U(\lambda_o)$ implies that the largest contribution to $\overline{u^2}^z$ is made by spatial wavelengths near λ_o.

Expanding the analysis to include six different $u(z)$ traces taken at different times from the same flow, $R_{11}(z_o)$

---

† $\lambda_{R_{11}}$ is the distance (in inches) of the wavelength where $R_{11}(z_o)$ peaks; (see next section).

and $U(v)$ were calculated by ensemble-averaging over the individual results of the six frames (figure 3.37). The traces analyzed were separated in time by intervals which are long compared to the maximum correlation time (at fixed z). Again the analysis indicates a dominant wavelength approximately equal to the visual estimate of average low-speed streak spacing. However, each of the six traces of this example were hand-picked for better-than-average uniformity of streak spacing.

Figure 3.38 shows the results of analysis of 31 frames of another data film (str + dp/dx , sta. 10) which was sampled at regular time intervals in the film; i.e., the frames were <u>not</u> chosen for analysis because they "looked" well ordered. The ensemble-averaged spectrum (figure 3.38c) shows a much less pronounced peak for this more general example - but a peak nevertheless. Six samples of individual frame spectrums are shown in figure 3.38a. The six samples of figure 3.38a are carefully selected from a much larger population of 31 frames to be a representative sampling so that a true impression of the data can be formed by the reader without the necessity for scanning a large number of samples. Note that about four out of six frames show marked periodicity, one shows little periodicity and one shows extreme periodic characteristics. As in the example of figure 3.36, any individual frame analysis yields well defined peaks for <u>that frame</u>. However, due to the turbulent nature of the flow, the details of the velocity patterns are constantly changing; and so each individual frame analysis, although showing a peak in the spectrum, gives somewhat varying value in the magnitude and location of the peak (figure 3.38a). Because of the variation in the location of the peak in individual frames, the ensemble-average result, which averages all the individual spectrums, is considerably smoothed (figure 3.38c). So much does the averaging smooth out the spectrum that the basic and

striking ordered patterns seen in the velocity patterns and reflected in the individual frame analysis (3.38a) are masked.

If the spatial spectrum results are viewed as if they were response characteristics, one would say the system responds to a band of frequencies rather than a sharply defined critical frequency or wave length. The data of figure 3.38 show again the inherent difficulties of deducing the structure just from total average data† and show the importance of direct structure pictures for accurate interpretation.

Figure 3.38b illustrates an alternate procedure used to determine underlying spatial wavelengths of the structure without the loss of information inherent in the averaging procedure. In figure 3.38b, a histogram of the distribution of individual frame spectrum peaks distances are shown. Since the distribution is relatively peaked, the mean position, λ_o, of the individual peaks gives a useful measure of the spanwise structural scale. (The major peaks and the secondary or long-wavelength peaks are plotted separately on figure 3.38b; i.e., where two peaks occur in $U(\lambda)$, both the highest (major) and second highest (secondary) are recorded.)

It is apparent that several different lengths can be obtained from these spectral analysis procedures which can be used to give statistical estimates of the spanwise structural scale. In addition to the two mentioned above (λ_v and λ_o), $\lambda_{R_{11}}$, which is defined as the distance from zero to the first major peak in $R_{11}(z_o)$, is a useful length. (See definition in figure 3.35.) Since this length is nearing the largest separation at which $R_{11}(z_o)$ is non-zero, this length bears direct resemblance to the structure scale of the largest eddies. (See discussion in Chapter II.)

---

†Townsend [1956] discussed the inherent difficulties of such statistical inferences.

Figure 3.35 compares the lengths $\lambda_{R_{11}}$, from the statistical analysis, to λ_{visual}. $\lambda_{R_{11}}$ is definitely the same order of magnitude as λ_{visual} and exhibits the same trends but is generally higher than λ_{visual} by up to 35%.

A typical comparison of four spanwise structure length scales follows for station 10.13 of the strong + dp/dx :

λ_{visual} = 0.88" $\pm$ 5% (at 20:1 odds)
λ_{v} = 0.72 - 0.92" (Range given because of flat peak)
$\lambda_{R_{11}}$ = 0.70" $\pm$ 10%
λ_{o} = 0.61" $\pm$ 10%

(3) Streak spacing, λ, versus distance from the wall

No mention has been made of the y-position in presenting λ data in the sublayer. This is because λ is approximately constant with y^+ out to $y^+ \approx 7$. Figure 3.39 presents visual data for dp/dx = 0 flow. Statistical data, which can be obtained from data further from the wall even where no definite streaky structure is seen by eye is also shown for station 10 of the str + dp/dx flow.

λ is essentially constant from the wall out to $y^+ \approx$ 6-8. λ then begins to increase sharply outside the wall layer with increasing y^+ and then a monotonic increase in $\lambda_{R_{11}}$ with y out through the logarithmic region is indicated by the results of this single case which was analyzed in detail.

d. Temporal spectral analysis

For purposes of comparison to the spatial spectral analyses results, a spectral analysis of the velocity trace at a fixed point in space as a function of time was made using the combined-time-streak marker H_2-bubble technique. The correlation coefficient calculated, $R_{11}(\tau)$ is

$$R_{11}(\tau) = \frac{1}{T}\int_{o}^{T} u(x_o,y_o,z_o,t) \cdot u(x_o,y_o,z_o,t+\tau)dt$$

This is the auto-correlation (at a single point in space) calculated by many workers in turbulence using hot-wires; it is not the same as $R_{11}(z_o)$ presented in the previous section.

The finite averaging times required by the hydrogen bubble technique make the effective frequency response quite low. (See uncertainty analysis.) The correlation results shown (figure 3.40) are from a movie taken at 8 frames per second. These results are for precisely the same data (i.e., the same movie film) as that of figure 3.37 which illustrated the spatial analysis.

The two correlations (spatial and temporal) show distinct differences. While the spatial correlation passes down through zero to negative values and then rises positive again, the temporal correlation is always positive and approaches zero asymptotically. This difference indicates that the temporal velocity fluctuations are not simply the regular movement of a fixed spatial velocity pattern over one point. The temporal and spatial fluctuations are fundamentally different. Since $R_{11}(0,0,z_o;0)$ and $R_{11}(0,0,0;\tau)$ are different, it follows from Taylor's hypothesis† that $R_{11}(0,0,z_o;0)$ has a fundamentally different shape from $R_{11}(x_o,0,0;0)$. This difference has been observed by other investigators: e.g., Grant [1958] or Comte-Bellot [1963]. It is thus clear that, even aside from spatial resolution problems that would occur with typical hot-wire length dimensions in air, the "usual" hot-wire autocorrelation measurements cannot reveal the actual spatial structure in the sublayer region. Only two-point space correlations would do so, and these have not been available for the region $y^+ \leq 7$ prior to this study.

The knee in the temporal correlation is interpreted by Townsend [1956] to be indicative of two distinct eddy sizes. That is, the sharp initial slope indicates a range of small

†Taylor's hypothesis relating small changes in x-position to small changes in time.

eddies and the more gradual slope at larger separations indicates the existence of a larger eddy structure. This would be consistent with the present view of the structure in this sublayer region: the large scale being associated with the ordered streaky structure and the small scale with eddies formed in the breakup process.

e. Random location of low-speed streaks

The positions of the low-velocity streaks in the wall region are shown to be randomly distributed over long times in the spanwise direction by counting the number of streaks in small intervals across the flow as a function of time. A histogram of the spatial distribution of low velocity streaks is illustrated by figure 3.41b. The standard deviation of the distribution is seen to approach zero asymptotically as a function of sampling time-indicating an even distribution of streaks across the plate (3.41a). The structure is thus not tied to any irregularities in the apparatus such as uneven entrance screens or bumps on the plate. The nearly regular structure is an inherent characteristic of the flow and not the result of the specific apparatus.

Notice, however, the rather long time scale over which the flow must be observed to ascertain this random streak distribution.† Even after one minute of observation the standard deviation of the distribution is still 5% of the mean. Casual observation by an observer for a few seconds may lead to the erroneous conclusion that streaks are fixed in space. They are not, but the time scales for their movement are relatively long compared to the other observed time scales of the motion. This long time scale explains why very long integration times are required to obtain stable mean values when taking data in the wall region.

---

†An experimental curve may be fitted to the curve of sample standard deviation. For this case the time constant is about 10 seconds. The curve of figure 3.41a may thus be approximated by $e^{-t/10}$.

2. Interaction of wall layers with the outer layer

A major part of this investigation is focused upon extending the present knowledge of the flow structure in the sublayer or wall region. This concentration of effort was made because the wall region is felt to be a very important, but the least understood, region of turbulent boundary layer flow. The present techniques allow detailed investigation closer to the wall (in non-dimensional sense) than had previously been possible. However, the wall region is not an isolated layer. In fact, the interaction of the sublayer region with the rest of the layer is felt to be essentially related to the behavior of the entire boundary layer. (See Runstadler's "Wall Layer Hypothesis" [1963]). A brief summary of Runstadler's [1963] observations of this interaction follows below.

The predominant feature of the observable interaction between the wall layer and the rest of the flow is the ejection of low u-velocity fluid away from the wall. This ejected fluid takes the form of loops or long filaments which lift away from the wall with a swirling motion. As the filaments move upward into regions of higher velocity in the buffer region, they form a low-momentum disturbance to the higher velocity fluid. Severe interactions occur which stretch and distort the filaments tending to diffuse them as they move downstream and outward into the turbulent core region. The trajectories of the heads of these filaments are observed to vary widely but average and "most populated" trajectories can nevertheless be defined (figure 1.4). Non-dimensionalizing the y-coordinate of the trajectory path by forming a y^+ vs x successfully brought the most populated trajectory into a single curve for the $dp/dx = 0$ layers studied by Runstadler.

These ejections or bursts are observed to occur randomly over the wall as a function of time and space. The ejection rate per unit wall area was studied by Runstadler (figure 1.3);

however, the experimental uncertainty is large, and Runstadler did not find a conclusive correlating parameter for bursting frequency.

The trajectory paths and ejection rate are two aspects of the wall layer interaction which can be measured quantitatively. The results of such measurements will be presented for the flows of the present study. The displacement of the ejected fluid as a function of time is also studied in the present work and the fluid is traced several inches further from the point of ejection than in Runstadler's study.

a. Visualization of flow structure details

Details of the interaction are observable by eye and in motion pictures when the flow structure is suitably illuminated. Better qualitative pictures of the flow structure obtained with newer visualization techniques are an important part of the present work. These qualitative descriptions are often at least as useful in gaining understanding of the flow model as a multitude of isolated quantitative measurements.

Several visualization techniques are useful, each giving a clearer picture of different aspects of the complicated flow structure. Dye injection through wall slots and hypodermic needles and H_2-bubble generating wires oriented at various angles to the wall were used to study various flow features.

An excellent means of observing the flow is to produce and illuminate bubbles from a wire parallel to the plate and to view their motion from an oblique overhead view by eye (see sketch in figure 3.44). In the sublayer region, when u_∞ is less than 0.5 ft/sec, the local velocity is sufficiently low that the three-dimensional patterns may be clearly seen by eye when properly lighted. There is no substitute for viewing the actual flow by eye from this angle. Much of the visualization is lost in two-dimensional photography.

End view of H_2-bubble wires normal to the mean flow vector

and parallel or perpendicular to the wall also give useful but somewhat limited views of the bursting. The parallel wire shows the concentration of bubbles in the low-speed regions and the vortex-like swirling motion of the bursts (figure 3.44). The perpendicular wire appears to show a correlation between fluid movement in one z-direction at the edge of the sublayer with fluid movement in the opposite direction in the buffer region (figure 3.44).

An improved picture of the "typical" ejection process has been obtained from these qualitative observations. The ejection of sublayer fluid appears to be usually initiated by the sudden spreading or widening of a relatively high u-velocity region. This faster fluid then "interacts" with the slower fluid on both sides as it spreads. The faster fluid appears to undermine the slower fluid. That is, faster fluid spreads against the adjacent low u-velocity streaks and a sharp line of high shearing ($\frac{\partial u}{\partial z}$) is formed. This high velocity gradient† is relieved by the upward movement of the low u-velocity fluid and a filament is ejected from the sublayer.

The net result is the upward movement of low-momentum fluid on one or both sides of the fast u-velocity region. The ejected fluid tends to swirl back in the direction of the fast region as it is caught up in the higher velocity fluid further from the wall. (See figure 3.44.) The result is a vortex-like motion along either side of the fast regions with the rotation in opposite directions on each sie. The spreading fast fluid sometimes results in the simultaneous ejection of counter-rotating filaments, but more often this interaction occurs first on one side and then on the other at a later time.

b. Burst trajectory data

Data on the movement of marked fluid which is ejected

†$\frac{\partial u}{\partial z}$ sometimes is as high as 10% of $\left.\frac{\partial u}{\partial y}\right|_{wall}$ as determined by actual measurement from u versus z profiles. (See figure 3.30.)

from the wall layer region are given in table 3.2 and figures 3.46 through 3.52. Figure 3.45 defines the coordinates used and shows a typical ejection. X is the distance in the flow direction between the head of the diffusing filament and the point where the marked fluid was first observed to be moving up out of the wall layer. Y is the distance from the wall to the highest part of the filament. T (time) is referenced from the time each filament first lifts up from the wall layer.

The trajectory paths vary rather widely for a given flow position as shown by the sample trajectories of figure 3.46. The occasional upward and then downward motion is consistent with the vortex-like motion of ejected fluid observed in the end views of the interaction process (figure 3.44).

The trajectory data are obtained by recording the coordinates, X and Y , at discrete time intervals from the point of ejection. Thus, distribution curves (e.g., figure 3.44) of x and y position are obtained at each recording time. These distributions approximate the probability density distribution for the trajectory positions. The central tendency of the distributions are indicated by mean positions† , $\bar{X}$, $\bar{Y}$. The dispersion of the distributions are given by sample standard deviations, S_x , S_y (see table 3.2).

The $\bar{Y}$ versus T and $\bar{X}$ versus T data (such as that of figures 3.47a and 3.47b) are combined in figure 3.48 as $\bar{Y}^+$ versus $\bar{X}$. Non-dimensionalizing Y into Y^+ brings the curves from 3 x-positions into near coincidence. (The wide distribution of trajectory paths about these mean paths should be recalled when comparing curves from different positions and different flows.)

The typical trajectory can be divided into two parts: an

†Runstadler [1963] used the mode or most populated trajectory as an indicator of central tendency. Due to the finite skewness of the distributions the mean and mode do not coincide; however, the discrepancy is small. The means gave better statistical correlations, i.e., smoother trajectory curves for the present data.

"acceleration" region nearest the wall ($12 < y^+ < 50$) where the trajectory has a parabolic shape - concave toward the wall; and an outer "linear" portion ($y^+ > 50$) where the average path ($\bar{Y}$, $\bar{X}$) is linear within the uncertainty. The acceleration region corresponds approximately with the buffer region of the u^+ , y^+ mean velocity correlation, and the linear average trajectory region with the logarithmic correlation region.

The acceleration portion of the trajectory is the combination of an initially high upward velocity (dY/dt in figure 3.47a) compared to the upward velocity further out and an initially low downstream velocity (dX/dt in figure 3.47b). Thus, the typical ejection is pictured as fluid given† an initial upward velocity component away from the sublayer which is then accelerated downstream as a result of the forces arising from the interaction with the higher x-velocity flow in the buffer layer.

The acceleration of the low-momentum filaments in the flow direction is clearly shown by plotting $\bar{u}_{filament}/\bar{u}_{local}$ versus y^+ (figure 3.49). $\bar{u}_{filament}/\bar{u}_{local}$ increases from a low value upon ejection up to nearly unity at $y^+ = 50$, then decreases with y^+ , apparently approaching an asymptotic value of about 0.80. Since $\bar{u}_{fil.}$ is approximately constant, the decrease of $\frac{\bar{u}_{fil.}}{\bar{u}_{local}}$ in the logarithmic region is given by $\frac{\bar{u}_{fil.}/u_\tau}{A+B \log Y^+}$ where for the $dp/dx = 0$ data of this study, $\frac{\bar{u}_{fil.}}{u_\tau} = 13.85$. That is, with the single experimental constant, $\bar{u}_{fil.}/u_\tau$, determined by one data point all other data in the log region are well represented by the above relation (see figure 3.49).

†See discussion on further details of ejection process in first part of section B2, Chapter III.

The observation that the ejected fluid approaches $0.8\ \overline{U}_{local}$ (figure 3.49) is entirely consistent with the hot-wire observations of Klebanoff [1954] in the wake region. Klebanoff observed that in the intermittent region: "The turbulent regions travel with a velocity lower than that of the free-stream." This connection with Klebanoff's observations is useful for two reasons. First it suggests that the flow at the rather low unit Reynolds numbers necessary for the present type of study have at least some of the same quantitative properties as turbulent flows at higher unit Reynolds numbers. Second, if the association with Klebanoff's observations are accepted, and there seems to be no reason why they should not be, then supporting evidence is given for the wall layer hypothesis of Runstadler, et al [1963]. One of the hardest questions to answer regarding this hypothesis is whether the eddies in the outer flow are in part or in whole the observed low speed ejected filaments. The agreement of the asymptotic speed of these filaments with the eddy measurements of Klebanoff lends considerable credence to the idea that the eddies and the low speed ejected filaments are indeed the same.

For the flows studied, the effect of pressure gradient upon the trajectory is indicated by figures 3.50 and 3.51. Figure 3.50 shows that the bulk of the pressure gradient trajectory data fall within the limits of the zero pressure gradient results (figure 3.48) and the trajectory shapes are similar. The notable exception is the strong - dp/dx flow where relaminarization occurs. For this latter case, the trajectories are shallower than the others.

The plot of $\overline{u}_{fil.}/\overline{u}_{local}$ (figure 3.51) shows considerably more variation from station to station for the pressure gradient flows than for the zero gradient data of figure 3.49. The general trends are similar, but for $dp/dx > 0$ the difference between $\overline{u}_{fil.}$ and $\overline{u}$ appears

larger and for $dp/dx < 0$ the peak in $\overline{u}_{fil.}/\overline{u}$ occurs at larger y^+. The uncertainty in these data is unfortunately large; no highly accurate conclusions seem possible without additional data on the exact effect of pressure gradient on trajectory.

The S_x and S_y data which indicate the dispersion of the distribution of trajectory position show the following behavior: $S_y/\overline{Y}$ versus $\overline{Y}$ shows no definite trends with $\overline{Y}$ and can best be represented for <u>all</u> flows studied by $\frac{S_y}{\overline{Y}} = 0.35 \pm 0.10$ at 10:1 odds. (The zero pressure gradient alone data are better represented by $\frac{S_y}{\overline{Y}} = 0.40$.) $\frac{S_x}{\overline{X}} = 0.30\ (\overline{X})^{-1/2}$ gives best correlation of S_x for all flow data, whereas $\frac{S_x}{\overline{X}} = 0.325\ (\overline{X})^{-1/2}$ is best for zero pressure gradient alone.

These dispersion correlations can now be used to form analytical models for the distributions which incorporate the major trends of the data.

The distribution of trajectory paths across the layer in the y-direction is of most interest. Figure 3.52 shows the analytical model for $dp/dx = 0$ flow compared to data. Considering the limited number of trajectories observed which results in a ragged histogram, the agreement between model and data is excellent.

The model is a Gaussian Distribution: $e^{-1/2\left(\frac{Y-\overline{Y}}{S_y}\right)^2}$, modified by $\left[1 - e^{-4(Y/\overline{Y})^2}\right]$ to account for the presence of the wall by making the distribution go to zero at the wall. S_y is replaced by $0.40\ \overline{Y}$ (above result) and the resulting distribution is

$$\phi(Y) = \frac{0.80}{\overline{Y}} \left[1 - e^{-4(Y/\overline{Y})^2}\right] e^{-3.13(Y/\overline{Y}-1)^2}$$

where the constants are chosen so that $\int_0^\infty \phi(Y) = 1$.

The distribution has the similarity feature that $\overline{Y}\phi(Y)$ is a <u>universal</u> function of $Y/\overline{Y}$ (given in figure 3.52). Thus, for zero pressure gradient flows (and to good approximation for the pressure gradient flows studied, as well) where $\overline{Y}$ is a known function of $\overline{X}$, the distribution may be given as $\phi(\overline{X})$. For example, the mean trajectories can be approximated by a straight line over most of the observed motion; figure 3.52 illustrates this approximation by example.

$\phi(Y)$ represents the frequency distribution of y-position of ejected fluid after it has proceeded a definite time, T. However, $\overline{X}$ and T are nearly linear and so $\phi(Y)$ is a good approximation to the distribution over y of bursts after having proceeded downstream a fixed x-distance as well.

So $\phi(\overline{X})$ (where $\overline{Y}$ vs $\overline{X}$ is approximated by straight line, for example) provides a statistical prediction of the downstream position of fluid ejected from the wall at any x-station. This information should be useful for studying the influence of bursting from the sublayer on boundary layer <u>history</u> phenomena.

The distribution of X about $\overline{X}$ is modeled by the Gaussian distribution; but no <u>universal</u> distribution function can be given since $S_x = 0.30\, X^{1/2}$. The approximate zero pressure gradient representation is:

$$\psi(x) = \frac{1.23}{x^{-1/2}}\, e^{-4.72x^{-1/2}\left(\frac{x}{\overline{X}}-1\right)^2}$$

c. <u>Burst rate</u>

The frequency of ejection of low velocity filaments away from the wall layer (bursts) per unit area per unit time was investigated by examining the side view motion pictures of the ejection process. The procedure was to introduce dye through a wall slot over a known width of injection (one inch) and then count the number of ejections per second over a given downstream distance (about 10 inches).

The ejection process is an intermittent process; but when viewed for a time long compared to the time for formation and breakdown of streaks the bursts occur uniformly over the plate, i.e., at random locations.

However, the introduction of dye at a discrete x-station and its subsequent diffusion into the sublayer necessarily gives non-uniform observation with respect to the x-direction; that is, upstream of the dye slot no bursts are observed, and far downstream (12 inches) of the slot the dye is sufficiently diffused that the bursts which occur cannot be observed. Between these limits the percentage of actual bursts which are observed varies in some unknown manner with x. This "marking distribution" probably depends upon dye injection flow rate and to some degree upon flow conditions as well. Unfortunately, no better technique for measuring burst rates is currently known.

For this reason the burst rate data are given as total number of bursts per inch of spanwise dye ejection; the number is not divided by some ill-defined x-dimension. For observing the trends in the data, the effect of non-uniform marking distribution is removed by referencing the burst rate, F, to $\bar{F}$ at the inlet station, F_{inlet}.

The ejection rate magnitudes (see Table 3.3 for tabular presentation) should be considered as only approximate estimates of the actual bursts/sec over about 6 in^2 of plate area. However, valid indications of the functional dependence of the burst rate with x-position, freestream velocity, and applied pressure gradient are given by figures 3.53 and 3.54. The dependence of burst rate upon known sublayer-model variables is given by the following plausible argument: Assume that for $dp/dx = 0$ flows, the volume of fluid ejected per square inch of plate area is constant; moreover, $\frac{vol}{in^2} = \frac{vol}{burst} \times \frac{burst}{in^2}$ and volume/burst is assumed proportional to λ^3. But

$\lambda^+ = \frac{\lambda u_\tau}{\nu}$ = constant (see figure 3.34); hence λ is proportional to $\frac{1}{u_\tau}$ and $\frac{\text{vol}}{\text{burst}} \sim \frac{1}{u_\tau^3}$. So for $\frac{\text{vol}}{\text{in}^2}$ to be constant, burst/in^2 must be proportional to u_τ^3; or since for $dp/dx = 0$, $u_\tau \sim u_\infty^{9/10}$, burst/in^2 must be proportional to $u_\infty^{2.7}$.

F versus u_τ and u_∞ are plotted in figure 3.53; the burst data for the zero pressure gradient are seen to correlate very well with u_τ^3 or $u_\infty^{2.7}$ independent of the x-station.

The effect of pressure gradient upon the burst rate is shown by plotting $\frac{F}{F_{in}}\left(\frac{u_{\infty in}}{u_\infty}\right)^{2.7}$ (figure 3.54) against K, where $K = \frac{\nu}{u_\infty^2}\frac{du_\infty}{dx}$.† On this plot all zero pressure gradient data fall at one point: $K = 0$, $\frac{F}{F_{in}}\left(\frac{u_{\infty in}}{u_\infty}\right)^{2.7} = 1$. Deviations from 1 for $K \neq 0$ are due to pressure gradient effects. It is shown that positive gradients increase the bursting rate over that of zero gradients at the same velocity, and negative gradients accordingly decrease the bursting. In fact, strong enough negative pressure gradients (such as the strong - dp/dx flow of this study) can cause complete cessation of bursting from the sublayer. The bursting phenomena is felt to be the essential feature of turbulence production in the boundary layer, and its cessation quickly leads to a marked departure from typical turbulent boundary layer characteristics. This change in behavior is called "relaminarization" in this report and is discussed more fully in the separate section on relaminarization (Chapter III, section B4).

3. Outer flow regions

The flow structure of a turbulent boundary layer has been conveniently divided into three distinct regions: (a) sublayer

†See section on relaminarization for a discussion on the use of K as pressure gradient parameter.

or wall region, (b) fully turbulent region, (c) wake or intermittent region.

The major effort of this investigation is spent studying flow details in the sublayer region (section B1) and the interaction region between the sublayer and the outer regions (B2).

However, visual images of the structure in the fully turbulent and wake regions have also been obtained for each flow test station using the hydrogen bubble technique. For the fully turbulent pressure gradient flows studied, the qualitative structural features observed are those expected from many prior investigations, particularly Runstadler, et al [1963].

The fully turbulent region extends from $y^+ = 40$ out to a value which depends upon the Reynolds number and pressure gradient history; it is characterized by a very complicated pattern of random turbulent motions over the entire plane of the flow (for example, see photograph in figure 3.42-F). The turbulent motions have no apparent order. Erratic lateral turbulent motions are seen; these lateral motions become more intense in the presence of positive pressure gradients, and they are diminished in negative pressure gradients.

The fully turbulent region gradually blends into the intermittent region as y^+ increases. This latter region is characterized by filaments of turbulent fluid which project up out of the fully turbulent region causing intermittent turbulent-and-potential velocity measurements in time at any fixed point in this region of the flow. Runstadler et al [1963] observed a one-to-one correspondence between the extent of the logarithmic portion of the u^+ , y^+ velocity profile and the extent of fully turbulent structure. Runstadler reported that the intermittent region began at the y-position where the profile deviates from the log region, and that intermittency extends out to $y/\delta \approx 1.2$, when δ is taken

as the point at which $u_{local} = 0.99\ u_{\infty}$.

The present pressure gradient studies indicate that the structure is fully turbulent beyond the point where the profile deviates from logarithmic dependence and that the inflection point in the profile - the point in the wake region where the curve becomes concave downward - is where intermittency begins. See, for example, positions G, H, and I in figure 3.42.

Since this behavior was observed in both positive and negative pressure gradient profiles, the zero pressure gradient case was reexamined. For the zero pressure gradient flows at the relatively low Re_{θ} of this and Runstadler's investigation, the point of deviation from the logarithmic region and the point of inflection in the wake-like outer profile are very nearly the same. In the hot-film data profiles of Runstadler, et al [1963] the two distances are indistinguishable due to the scatter. Thus, in Runstadler's data it is difficult to distinguish the difference between the point of deviation from the log curve and the point of inflection, let alone to determine at which point the intermittency factor begins to be less than one.

In view of the pressure gradient results and after closer examination of the zero pressure gradient results of this and Runstadler's [1963] study, it now appears that a fully turbulent structure (with intermittency factor of one) exists not only in the portion of the layer corresponding to the logarithmic portion of the profile but also out to the point of inflection in the wake profile.

C. Relaminarization

Relaminarization is the "reverse-transition" of a fully turbulent layer to a laminar boundary layer. Just as natural transition from laminar to turbulent flow is a gradual succession of stages (Meyer and Kline, [1961]), relaminarization

occurs gradually rather than suddenly. However, the details of this relaminarization process are not yet fully understood in spite of significant recent contributions by Launder [1963], Moretti and Kays [1964], Steinberg [1954], Sergienko and Gretsov [1959], Sebulkin [1962] and others. To avoid confusion a boundary layer undergoing relaminarization will be called "laminarescent"; and it will be called "relaminar" when the transition is complete - i.e., when the flow has entirely laminar characteristics except for, perhaps, a high residual fluctuation level.

The "point" of relaminarization is arbitrary since it is a gradual process and it must be carefully defined. In this report the "point" of relaminarization will mean the position where the production of turbulent kinetic energy becomes zero. As will be discussed below, this point does not coincide either with the beginning of relaminarization or with the point of reaching a relaminar state (both of these latter definitions are difficult to define accurately and unambiguously.)

The strong negative pressure gradient flow of the present study produces laminarescent boundary layers.† The accompanying structure studies add significant understanding to the relaminarization process. However, this aspect of the study was undertaken to investigate the behavior of turbulent boundary layers under negative pressure gradients, and a relaminarization study, per se, was not originally intended. Just one laminarescent flow is considered and it does not carry the flow completely to a relaminar state. More complete relaminarization structure studies are contemplated as future work at Stanford University.

The point of relaminarization probably depends upon most

---

†Laminarescent boundary layers may be formed by other means than application of severe negative pressure gradients (see discussion by Moretti and Kays [1964]), but this means alone is considered here.

of the same things as the point of natural (forward) transition: Reynolds number, pressure gradient, free-stream turbulence, Mach number, wall curvature, etc. This study does not encompass all these effects. The only variable which undergoes significant variation in the present study is the pressure gradient. A non-dimensional parameter which predicts the effect of pressure gradient upon relaminarization under the given limitations of incompressible, subsonic, moderate turbulence freestream flow over a flat plate for Re_θ around 600 was sought.

Since the point of relaminarization has been arbitrarily defined as the point where the production of turbulent energy becomes zero, a reasonable parameter may be obtained by setting the production terms in the turbulent energy differential equation equal to zero.†

In Cartesian coordinate the turbulence production‡ term is (for example see Hinze [1959]):

$$- \overline{u_i u_j} \frac{\partial \bar{u}_j}{\partial x_i}$$

This term may be expanded using the continuity equation, yielding (in x, y, u, v coordinates) for a two-dimensional, steady mean flow:

$$- \overline{u_i u_j} \frac{\partial u_i}{\partial x_i} = \left(\overline{u}^2 - \overline{v}^2\right) \frac{\partial \bar{u}}{\partial x} + \overline{uv} \left(\frac{\partial \bar{u}}{\partial y} + \frac{\partial \bar{v}}{\partial x}\right)$$

For the production to be zero, where $\frac{\tau_{yx}}{\mu} = \frac{\partial \bar{u}}{\partial y} + \frac{\partial \bar{v}}{\partial x}$

$$\frac{\overline{u^2} - \overline{v^2}}{\overline{uv}} \left(\frac{\mu}{\tau_{yx}}\right) \cdot \frac{\partial \bar{u}}{\partial x} = - 1$$

---

†A more general argument can be given since the same parameter will also be obtained if the production terms are set equal to any non-zero value.

‡Or destruction if negative.

This grouping may be put into a more useful form by arguing that $\frac{\overline{u^2} - \overline{v^2}}{\overline{uv}}$ is a function only of y^+ ; also $\tau_{yx} = \tau_{wall} x(\text{function of } y^+)$. Now the region just outside the wall layer (i.e., $y^+ \cong 15$) is known to be the region of highest turbulent production (Klebanoff [1954]). Further, the present study shows that the laminarization phenomena caused rapid changes in the mean velocity profile and diminishing of turbulent bursting in the same y^+ region. (See below.) Thus, consideration of the pressure gradient parameter at a fixed y^+ should not limit its usefulness for predicting relaminarization. Thus,

$$\frac{\mu}{\tau_w} \frac{\partial \bar{u}}{\partial x} = f(y_o^+) = \text{constant}$$

Since $\tau_w = C_f \, 1/2 \, \rho \, u_\infty^2$ (defines C_f), $\frac{1}{C_f} \frac{\nu}{u_\infty^2} \frac{\partial \bar{u}}{\partial x} = \text{constant}$

$\frac{\partial \bar{u}}{\partial x}$ may be expressed in terms of $\frac{du_\infty}{dx}$ in the following manner:

$u = u_\tau \cdot f(y^+)$. Therefore, $\frac{\partial \bar{u}}{\partial x} = \frac{\partial u_\tau}{\partial x} f(y^+)$

$$\frac{\partial u_\tau}{\partial x} = \sqrt{\frac{C_f}{2}} \frac{du_\infty}{dx} + \frac{u_\infty}{2\sqrt{2}} \frac{1}{\sqrt{C_f}} \frac{C_f}{dx}$$

$$\frac{\partial u_\tau}{dx} \approx \sqrt{\frac{C_f}{2}} \frac{du_\infty}{dx} \quad \text{when} \quad \frac{1}{u_\infty} \frac{du_\infty}{dx} > \frac{1}{2C_f} \frac{dC_f}{dx}$$

For large applied pressure gradients such as are required for relaminarization this is a fair assumption (e.g., at x-station 12, τ_r - dp/dx flow, $\frac{1}{u_\infty} \frac{du_\infty}{dx} = 3.5 \left[\frac{1}{2C_f} \frac{dC_f}{dx}\right]$.)

Substituting this simplification the constant grouping becomes:

$$\sqrt{1/C_f} \cdot \frac{\nu}{u_\infty^2} \frac{du_\infty}{dx} = K \Big/ \sqrt{C_f} \quad \text{(defines } K \text{)}$$

K alone or K in some other combination with C_f or Reynolds number has been suggested by several other workers. Back, et al [1964] using nearly the same argument as above suggests the parameter K/C_f .

Back [1962] in an earlier analysis of the momentum integral equation suggests: $K/C_f^{3/2}$.

Moretti and Kays [1964] suggest K alone based upon a consideration of the momentum integral equation. A common prediction of pressure gradient effect upon the critical Reynolds number for natural transition (laminar-to-turbulent) (Schlichting [1960]) correlates $Re_{critical}$ against $\frac{\delta^2}{\nu}\frac{du_\infty}{dx} = K(Re_\delta)^2$.

Thus, it appears that K is a useful parameter, but in what combination with C_f or Re is "best" is not clear. In veiw of the conflict, K alone will be used to represent pressure gradient magnitude in the present report. K is simple and correlates the present results adequately. Moreover, since C_f is a slowly varying function which normally does not vary as much as a factor of 2 for turbulent boundary layers, $\sqrt{C_f}$ is almost a constant factor, and its omission in correlations has a slight effect.

In a logical but not strictly rigorous manner, a non-dimensional parameter, expected to be useful for predicting relaminarization, has been derived. The parameter should also be useful for correlating pressure gradient results different from the relaminarization flow. The basic assumption in the derivation was that turbulent energy production by the mean velocity gradients in the flow directions was set equal and opposite to the production arising from the gradient normal to the wall. In cases other than relaminarization, the ratio of these terms will have some value other than -1, but the parameter should still be a generally useful one.

1. Structure results

The most striking structural feature of laminarescent flow is a decrease in turbulent bursting from the wall layer region. Figure 3.57 shows the channel shape and the burst rate and pressure gradient parameter, K, as functions of x-station down the channel (the free-stream velocity distribution is given by figure 3.4, and Table 3.1 gives other pertinent data).

As the flow accelerates downstream and K increases, the bursting rate decreases to a minimum of nearly zero for K above about 3.5×10^{-6}, and then the bursting begins again as K decreases below about 1×10^{-6}. The region where $K > 1 \times 10^{-6}$ ($9 \leq$ x-station ≤ 12), where the bursting is lessened is a region of laminarescent flow. From x-station 13 downstream, the flow changes back from the partially laminarized state toward turbulent flow; in this region one observes isolated "spots" of turbulence typical of the later stages of natural transition (Meyer and Kline [1961], Emmons [1951]).

The burst data are plotted as $\frac{F}{F_{in}} \left(\frac{u_{\infty\, in}}{u_\infty} \right)^{2.7}$ versus K in figure 3.54. These coordinates separate changes in the burst rate due to pressure gradient from those due to velocity variations alone, since in a zero pressure gradient $F = c_1 u_\infty^{2.7}$ (figure 3.53). The high positive K data shown is for the relaminarizing flow. The decrease in bursting for large positive K is approximately linear with K for the laminarescent flow (upper linear curve in figure 3.54). The apparent hysteresis and low burst values as K approaches zero on lower curve is explained by the retransition of the flow. That is, only isolated areas of the wall layer are turbulent and although the burst rate from these patches is very high, the total burst rate appears low because only a portion of the flow contains turbulent spots in time and space. Unfortunately the test section was not long enough to

actually observe whether the burst rate further downstream returns to the higher value predicted by the zero gradient correlation, but there seems to be no reason why it should not. A special study to further define these effects is needed.

Corresponding to the drastic reductions in burst rate, other structural changes were observed. Figures 3.55 and 3.56 show still photographs taken from plan-view hydrogen bubble movies of the flow at several y-positions across the laminarescent layers at x-stations 10.25 and 12.18 feet. Smoothed curves of the respective velocity profile data in u^+,y^+ coordinates are also shown.

At x-station 10.25 (figure 3.55), where the flow has begun to accelerate ($K = 2.8 \times 10^{-6}$) changes away from the typical fully turbulent velocity profiles occur in the wake region and in the wall layers. The mean profile near the wall becomes nonlinear. When plotted in u^+,y^+ coordinates based upon wall shear determined by the wall slope method, the deviation from linearity shows as a deviation from the $u^+ = y^+$ curve (figures 3.20 and 3.55).

While the sublayer structure at station 10.25 has the general appearance of the typical turbulent streaky structure (picture A, figure 3.55), several changes have occurred. Occasional spots of laminar-like (quiescent) flow are observed in the wall layer region. Picture B, $y^+ = 9.9$, shows an example of the laminar-like spot of wall flow which occurs intermittently at this point in the wall layers at this x-station. The right-center part of picture B (figure 3.55) is the laminar-like spot; the left side is typically turbulent.

The spacing, λ, between the streaks at x-station 10.25 is not correlated by $\lambda^+ = \text{constant}$ for laminarescent flow. A high value of $\lambda^+ = 170$ (figure 3.34) is obtained whereas all the turbulent layers have $\lambda^+ \approx 105$. The spacing between streaks does not decrease in proportion to the increase of u_τ

for this flow to keep $\lambda^+ \approx 105$ in the strong pressure gradient region.

A clearly defined logarithmic profile region still exists and the flow structure is accordingly unchanged, i.e. fully turbulent. Picture C, figure 3.55, at $y^+ = 33$ shows the typically fully turbulent eddy structure of this region for x-station 10.25.

The acceleration of the free-stream tends to quickly eliminate the "defect" portion of the profile.† However, that the outer profile nearly coincides with the logarithmic curve of the turbulent core is a coincidence. From $y^+ = 130$ outward, typical wake-intermittency structure is observed (see picture D, figure 3.55).

Transferring attention now to <u>x-station 12.2 feet</u> (refer to figure 3.56), all characteristics of fully turbulent boundary layer profile and structure have vanished; no ejections or burst from the wall layers are seen; the wall layer profile is not linear; no logarithmic section exists in the mean profile; no part of the mean profile obeys the "law of the wake". The flow structure pictures show spanwise variations in the x-component of velocity which extend from the wall outward nearly to the outer edge of the layer. But note that no fully turbulent core region exists; the spanwise pattern simply extends well out into the layer (see picture C at $y^+ = 66$). The outermost portions (picture D) show an essentially laminar structure with some residual fluctuations.‡ The spanwise

---

†The Bernoulli equation shows why: since dp/dx is the same for all streamlines (for negligible streamline curvature) then $du/dx = (-\frac{1}{\rho} dp/dx) \frac{1}{u}$. That is, fluid with lower velocity is given proportionately higher acceleration, tending to flatten the outer profile.

‡We distinguish here between coherent (i.e., laminar-like) fluctuations and "usual" turbulence which is unsteadiness containing all sizes of eddies (wave numbers). The distinction is qualitative but nevertheless very clear and significant in both direct observation and movies.

velocity patterns are much more fixed in space than turbulent "streaks" and these patterns extend for 10δ or more downstream, whereas turbulent streaks break up in about one δ . This structure near the wall is strongly reminiscent of the peak-valley structure (stage III) described by Meyer and Kline [1961] in an investigation of the later stages of natural transition on a flat plate. The spacing between these span-wise velocity variations yields a $\lambda = 240$ (figure 3.34) which is measurably different from the turbulent layer correlation of $\lambda^+ \cong 100$.

The sudden change (in terms of x-length) from typical turbulent profiles at x-station 10.25 makes the determination of wall shear by the cross-plot-of-the-wall-region invalid. On the other hand, determination by the slope of the mean velocity profile at the wall is inaccurate because no well-defined linear profile exists. Figure 3.20 plots the data in u^+, y^+ coordinates using both methods. The wall slope method is felt to be the better evaluation of wall shear for this strong - dp/dx flow. The degree of discrepancy between wall shear determined by the cross-plot method and the wall slope method is shown by figures 3.22a and 3.22b. The relaminarization data are seen to be not only quite different but also to exhibit a trend contrary to that found in the fully turbulent data. The 50% discrepancy between $\tau_{\text{(cross plot of log region)}}$ and $\tau_{\text{(wall profile slope)}}$ (figure 3.22b) is indicative of the possible error if the cross-plot method is used to determine wall shear in a region of relaminarization.

Distributions of the longitudinal (x) component of velocity fluctuation for laminarescent flow (str - dp/dx) (figure 3.29) show values of $\sqrt{\overline{u^2}}/u_\tau$ of 40-50% less than the zero pressure gradient values over the entire profile. These results are consistent with the observations of decreased bursting and lessened mixing described above.

In summary, the flow undergoes the following succession of stages in relaminarization. At the entrance (x-station 8) the boundary layer has a typical zero-pressure-gradient, fully-developed turbulent structure. As the walls converge and the flow begins to accelerate, the first stages of laminarescence are observed as K rises to about 0.5×10^{-6} at x-station 9. The bursting rate drops some 20% from the zero gradient correlation (figure 3.54) at this point, but very little structural or profile changes are expected (no profiles were actually taken at this x-station). Relaminarization continues to progress in the direction of relaminar flow. At x-station 10, where $K = 2.8 \times 10^{-6}$, the defect region is eradicated. At this station the burst rate is down to 40% of the zero gradient correlation, and the wall layer region is non-linear. Spots of laminar-like flow are observed, and λ^+ is 60% higher than the typical turbulent correlation (figure 3.34). The "point of relaminarization", defined as the point where the production of turbulent energy reaches zero, is apparently reached at about x-station 11, or at $K = 3.5 \times 10^{-6}$. The profiles at x-station 12 where K is about 3.25×10^{-6}, show no characteristics of the earlier turbulent condition; the laminarescent profile is in transition between turbulent and laminar. A moderate fluctuation level remains (figure 3.29), but the character of the structure is 3-dimensional-laminar-unsteady rather than turbulent (see figure 3.56). At x-station 13.5, K drops back below 0.5×10^{-6} (figure 3.57) and turbulent bursting begins again from isolated spots of wall turbulence. As K drops to zero the flow apparently returns to turbulent flow by the usual mechanisms observed in natural transition.

The response of the boundary layer to <u>local</u> changes in pressure gradient as measured by the parameter $K \triangleq \frac{\nu}{u_\infty^2} \frac{du_\infty}{dx}$ are surprisingly rapid in this flow. However, certain

"delays" are known to exist which make the description of the stages of relaminarization by a local pressure gradient parameter incomplete. For example, the viscous damping of small scale turbulence during relaminarization, and the movement of ejected turbulent fluid outward during the retransition involve delays of several boundary layer thicknesses at least. Nevertheless, during the initial relaminarization stages of this flow, figure 3.57 indicates that K provides good correlation of the decrease in bursting and the onset of retransition.

Within these limitations and with due respect for the lack of experimental variation of variables other than pressure gradient (note, for example, (Table 3.1) that Re_θ was very nearly constant during relaminarization), the following stages of relaminarization are tentatively suggested as functions of K :

$K \leq 0.5 \times 10^{-6}$ Turbulent flow

$0.5 < K < 3 \times 10^{-6}$ 1st Stage: Laminarescent; lessening of burst rate from sublayer and lower turbulence intensity; sublayer becomes quiescent, streak spacing parameter, λ^+ , rises rapidly; defect region disappears; slow decay of turbulence core.

$K \approx 3 \times 10^{-6}$ Point of Relaminarization: As evidenced by cessation of bursting and low turbulence activity, production of turbulent energy is presumed zero or very near zero.

$K > 3 \times 10^{-6}$ 2nd Stage: Bursting has ceased, layer is in transition from turbulent to laminar with characteristics of neither. (laminarescent boundary layer)

$K > 3 \times 10^{-6}$

3rd Stage: Continuing $K > 3 \times 10^{-6}$ will result in a relaminar boundary layer with high turbulence level which will be damped out, finally resulting in a true laminar boundary layer.

This relaminarization structure study provides considerable physical insight into the mechanism. The results, while they are limited to just one flow of short pressure gradient application (layer just reached stage 2 before retransition), generally agree with more detailed relaminarization studies of Launder [1963] and Moretti and Kays [1964]. Figure 3.58, taken from Moretti and Kays [1964] shows the reduction in heat transfer from that predicted for turbulent flow due to relaminarization of the boundary layers. A gradual relaminarization process such as suggested by the present results, is shown by the gradual reduction of heat transfer with increasing K. Moretti also suggests the point of laminarization occurs at $K \approx 3 \times 10^{-6}$. The coincidence of this value and the similarity of conclusions reached as a result of heat transfer studies on the one hand and the present structure studies on the other, gives more confidence in both results. Many applications of relaminarization including prediction of heat transfer coefficients, and hence also estimates of C_f, are given by Moretti and Kays [1964] and are not repeated here.

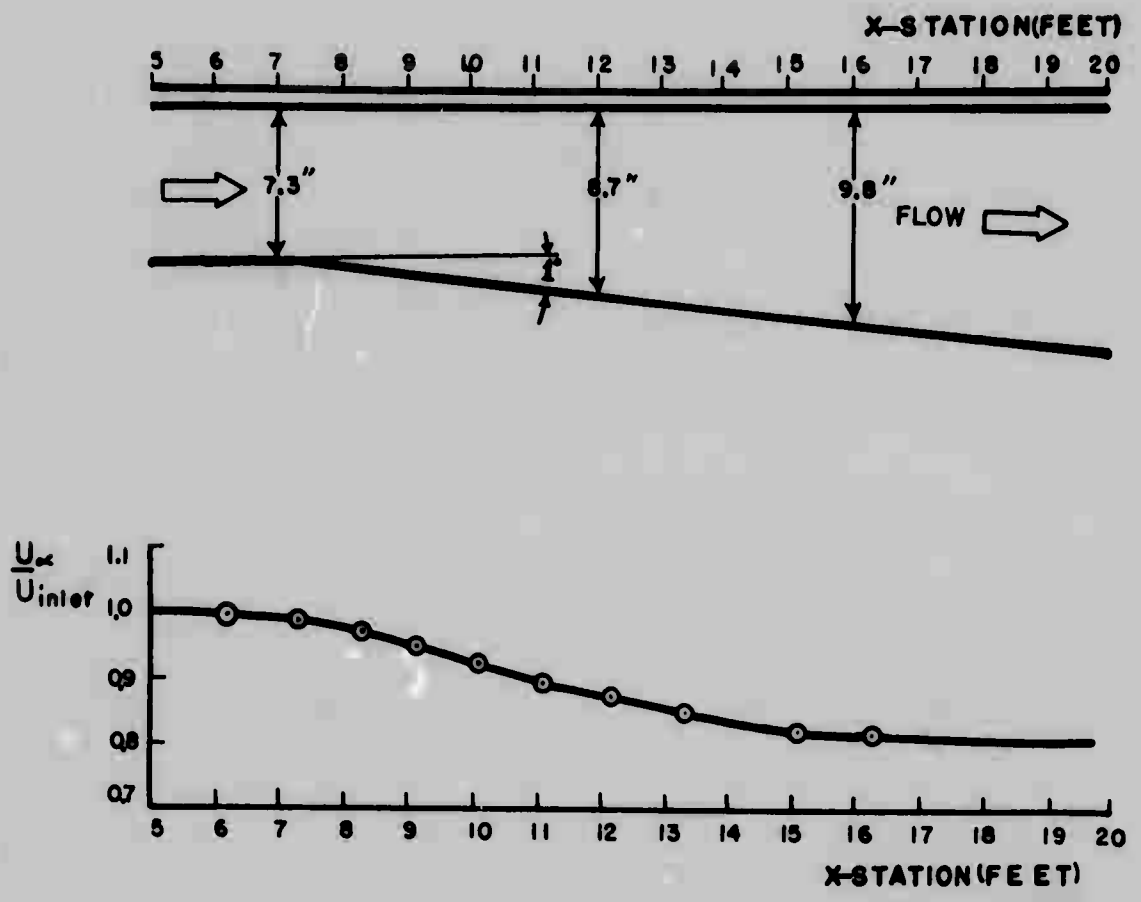

Fig. 3.1 Wall shape and free-stream velocity distribution for mild positive pressure gradient flow.

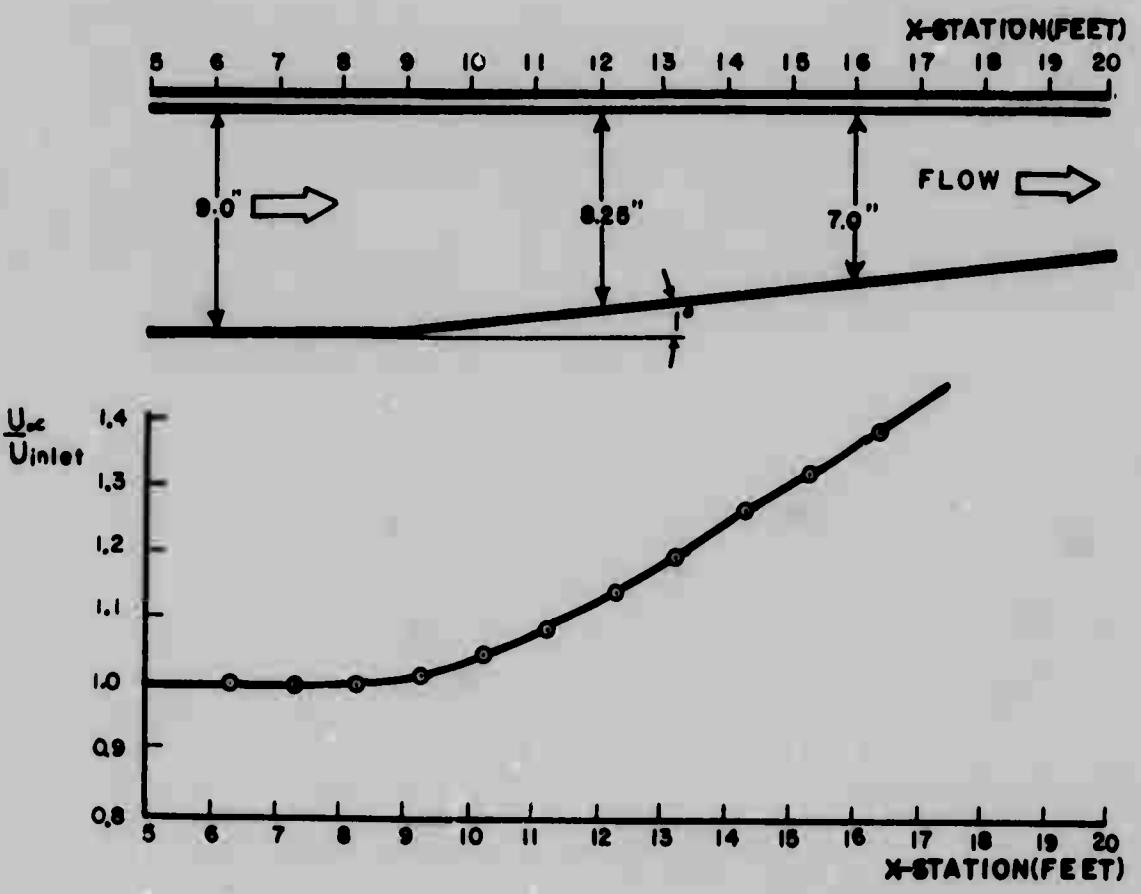

Fig. 3.2 Wall shape and free-stream velocity distribution for mild negative pressure gradient flow.

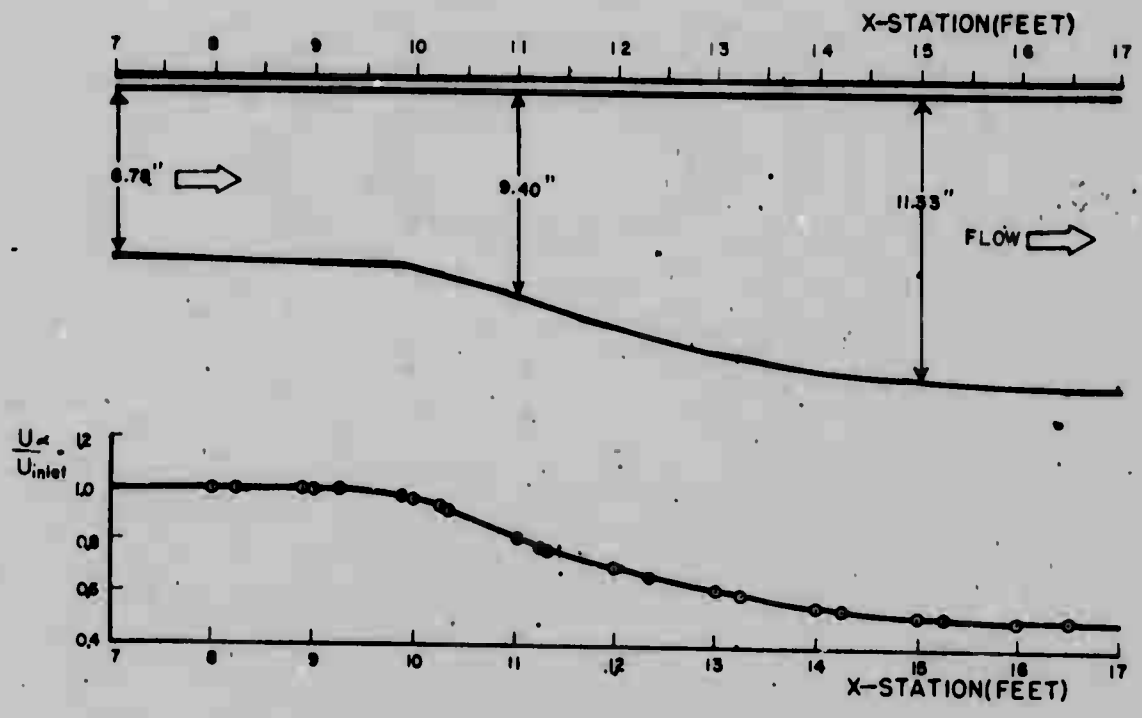

Fig. 3.3 Wall shape and free-stream velocity distribution for strong positive pressure gradient flow.

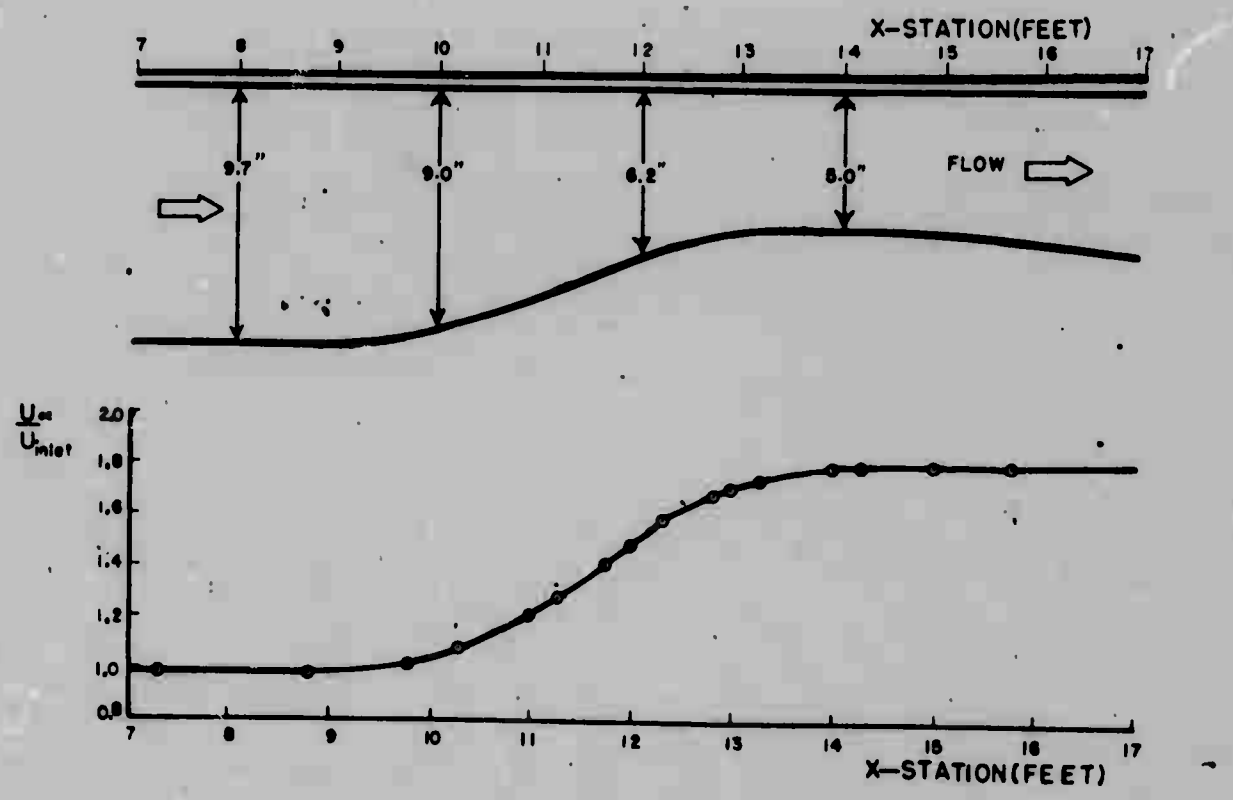

Fig. 3.4 Wall shape and free-stream velocity distribution for strong negative pressure gradient flow.

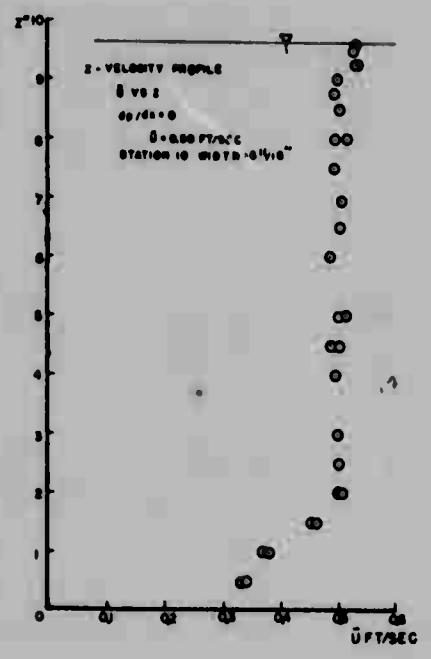

Fig. 3.5 Mean velocity profile illustrating degree of two-dimensionality for zero pressure gradient flow, x-station 10.

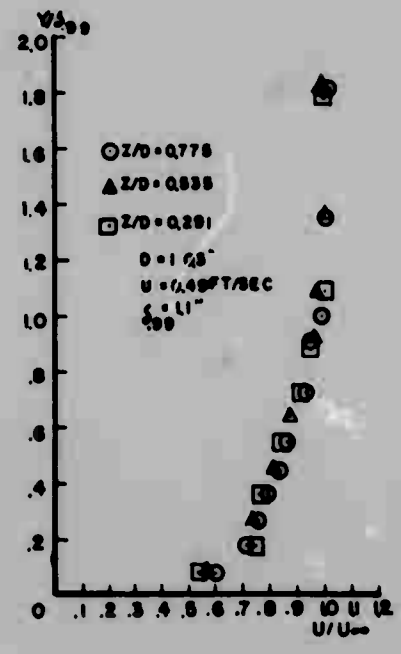

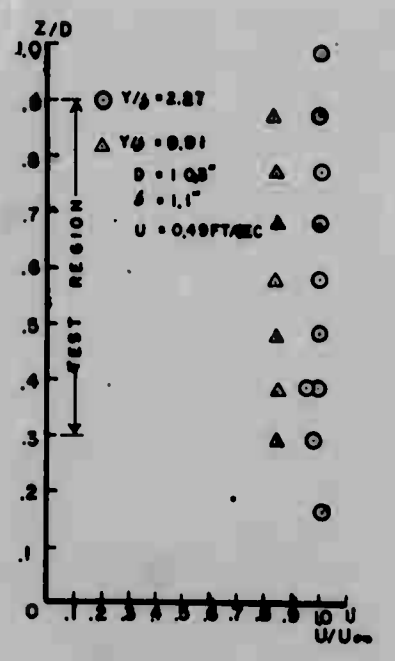

Fig. 3.6 Mean velocity profiles illustrating degree of two-dimensionality for mild positive pressure gradient flow, x-station 6.

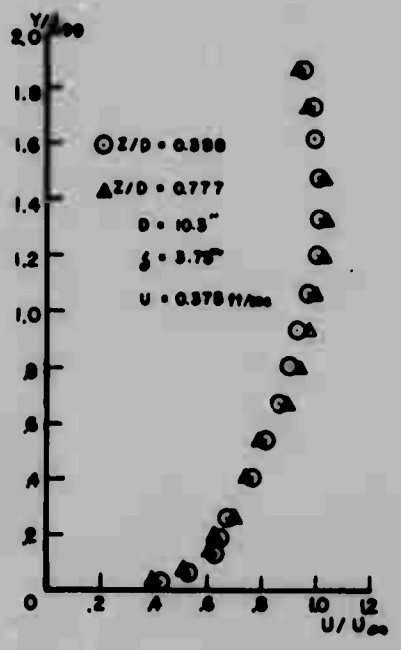

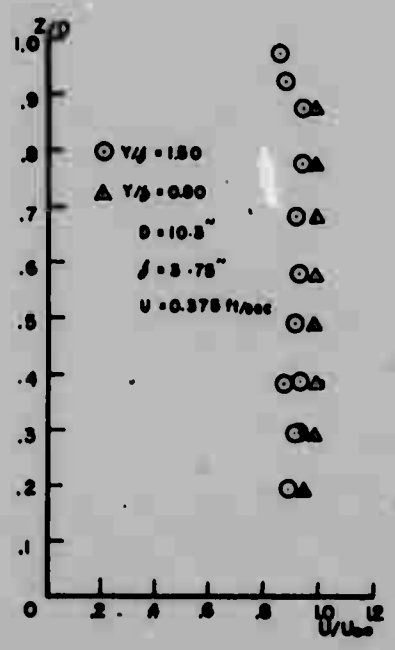

Fig. 3.7 Mean velocity profiles illustrating degree of two-dimensionality for mild positive pressure gradient flow, x-station 15.

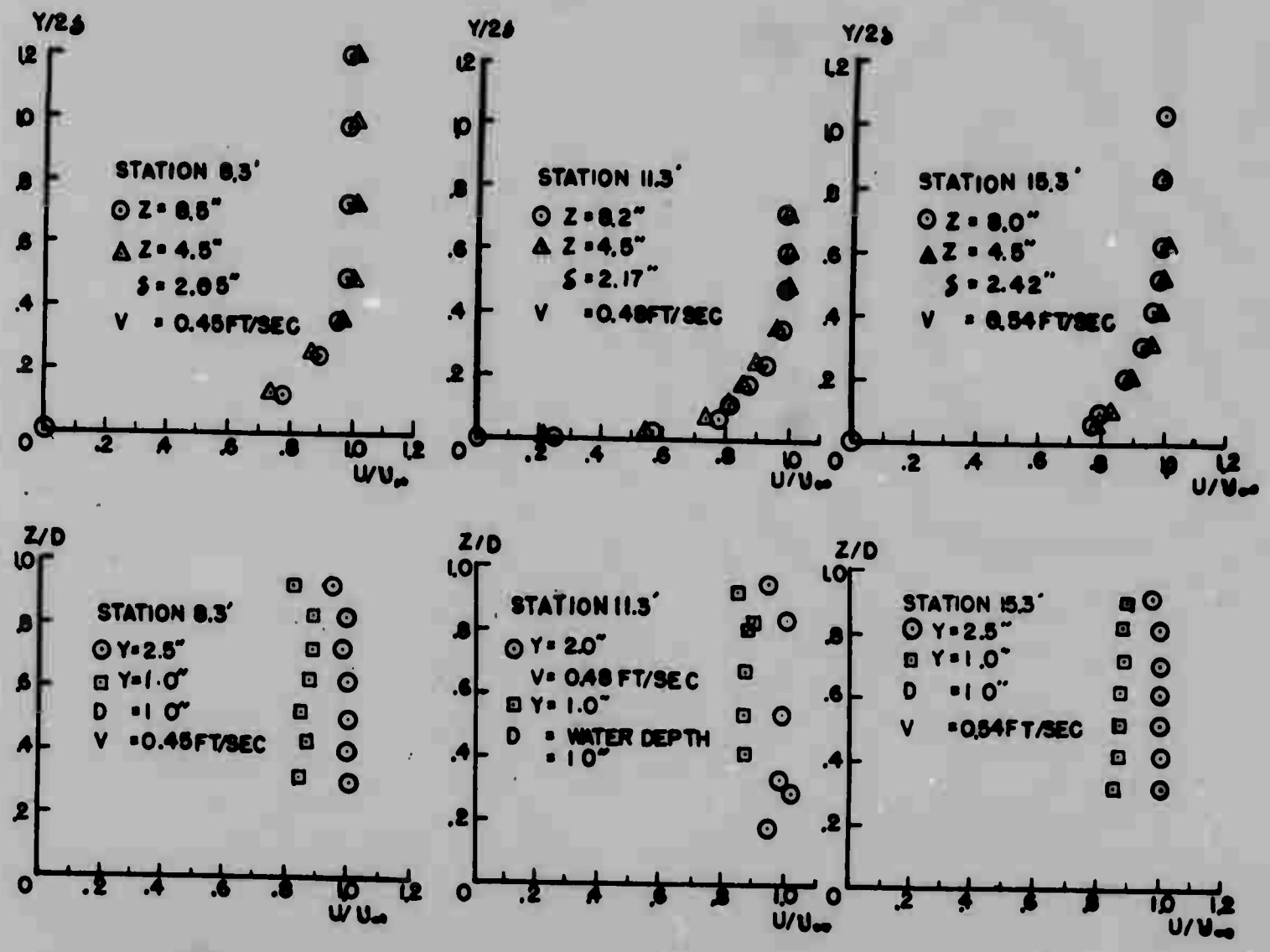

Fig. 3.8 Mean velocity profiles illustrating degree of two-dimensionality for mild negative pressure gradient flow.

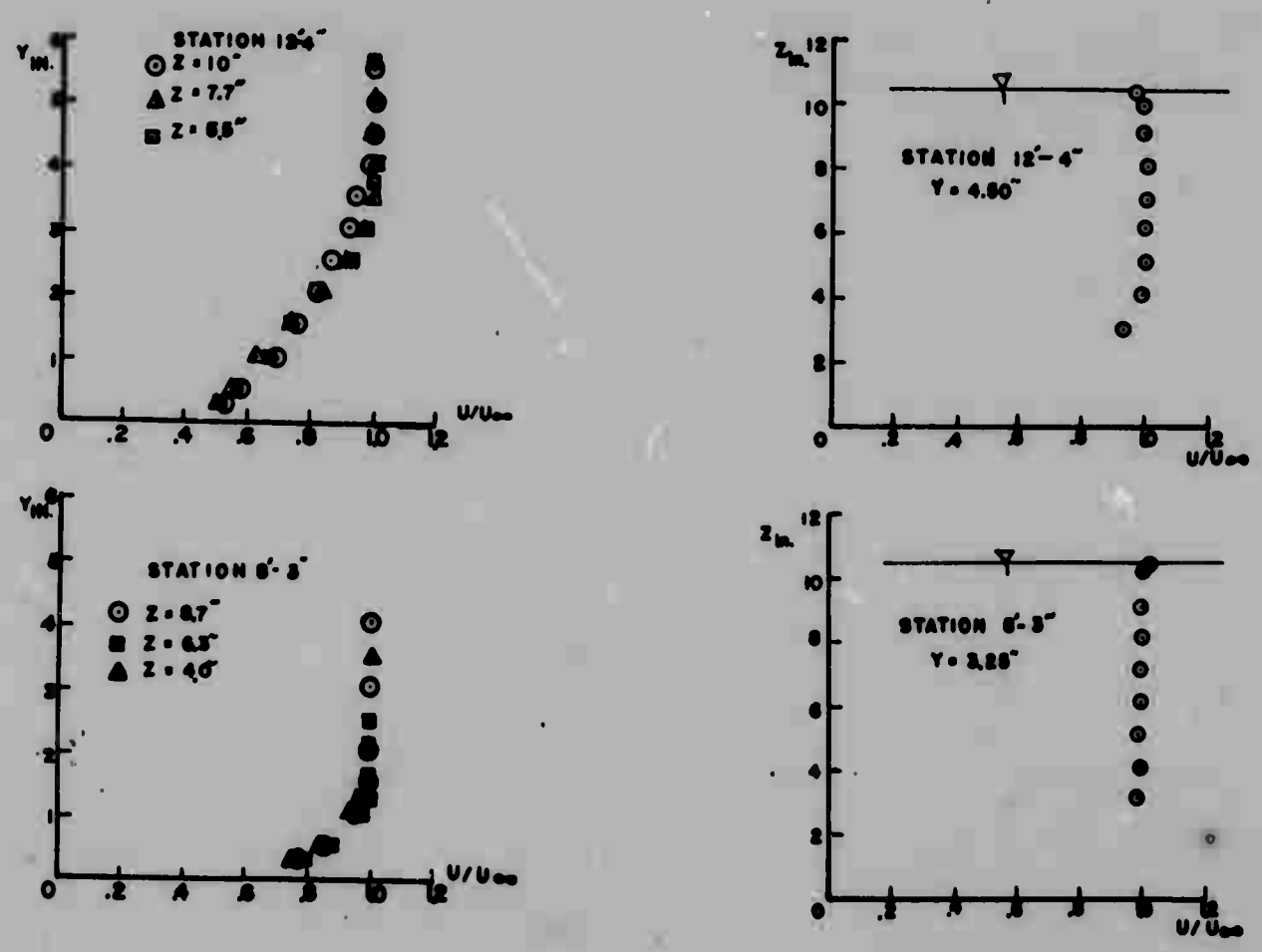

Fig. 3.9 Mean velocity profiles illustrating degree of two-dimensionality for strong positive pressure gradient flow.

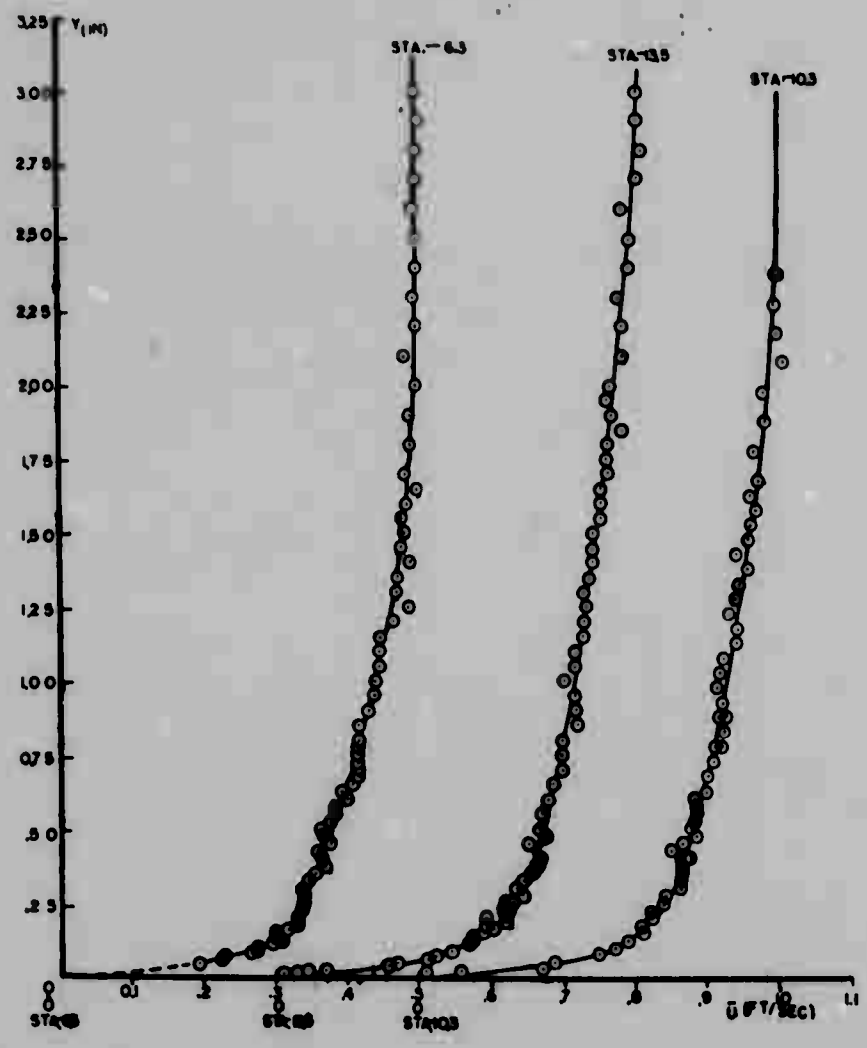

Fig. 3.10 Mean velocity profiles (u vs. y): zero pressure gradient flow.

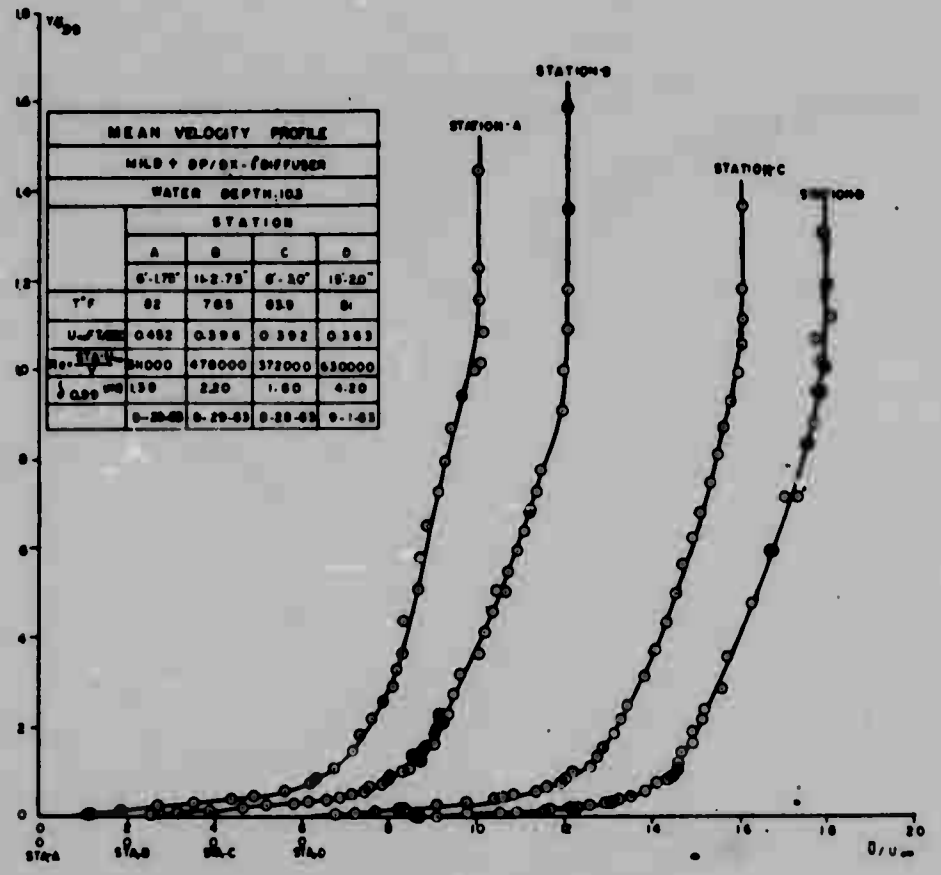

Fig. 3.11 Mean velocity profiles (u vs. y): mild positive pressure gradient flow.

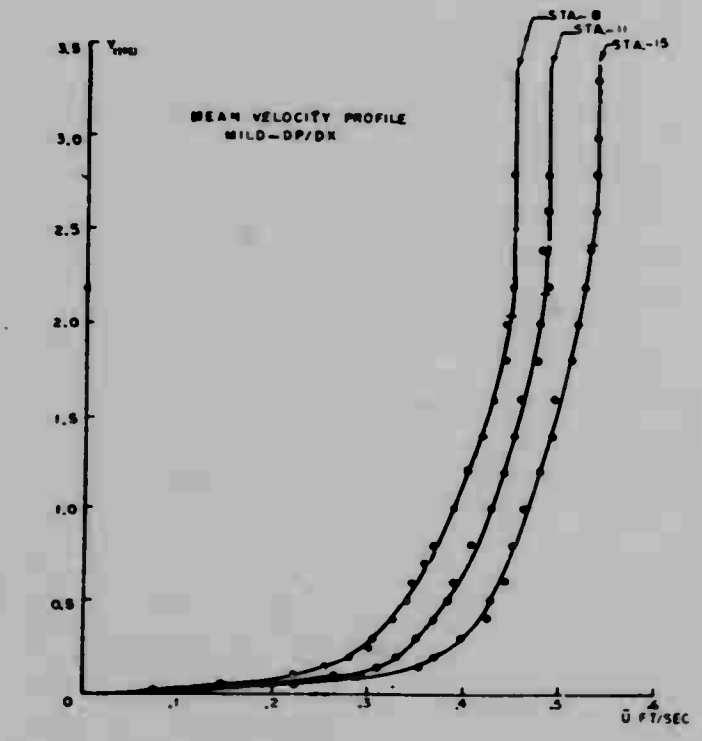

Fig. 3.12

Mean velocity profiles (u vs. y): mild negative pressure gradient flow.

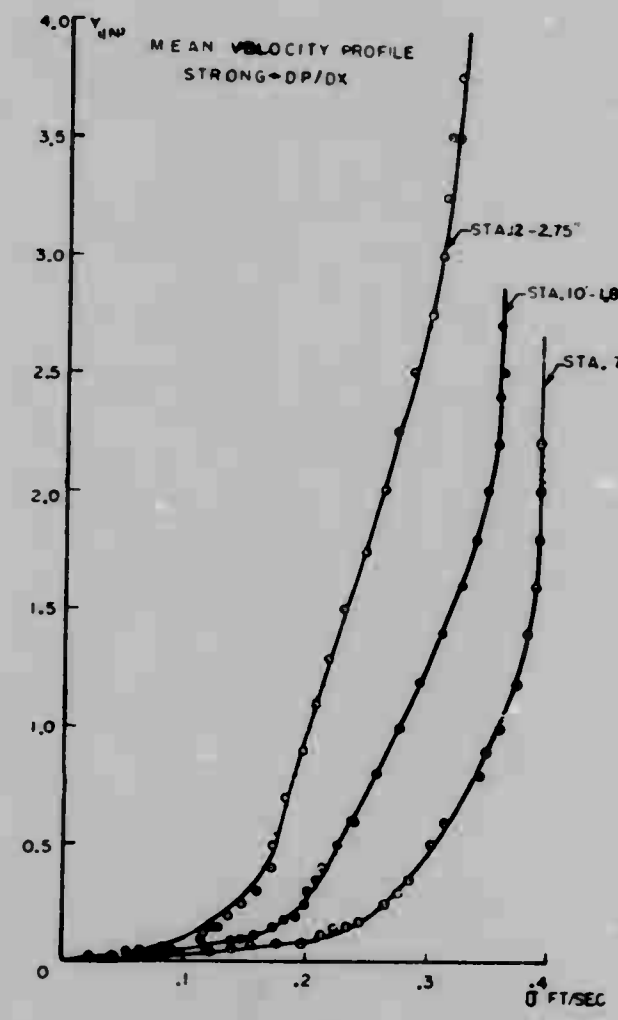

Fig. 3.13

Mean velocity profiles (u vs. y): strong positive pressure gradient flow.

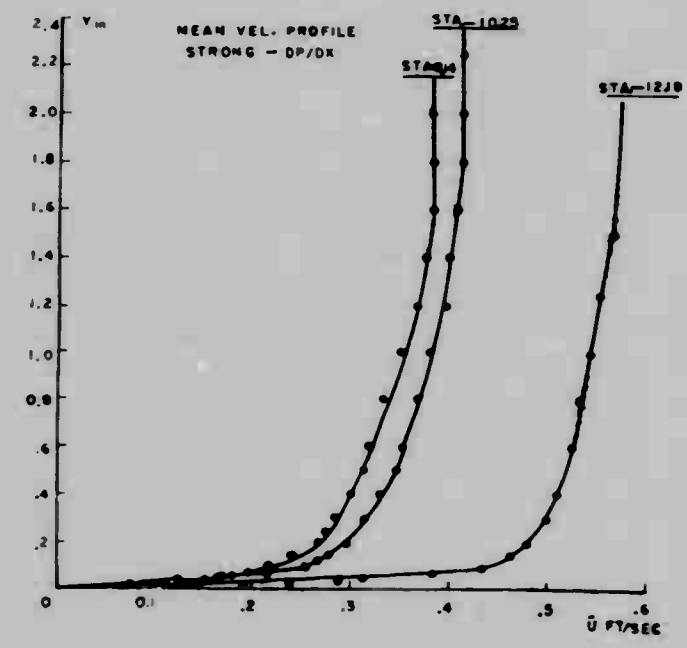

Fig. 3.14

Mean velocity profiles (u vs. y): strong negative pressure gradient flow.

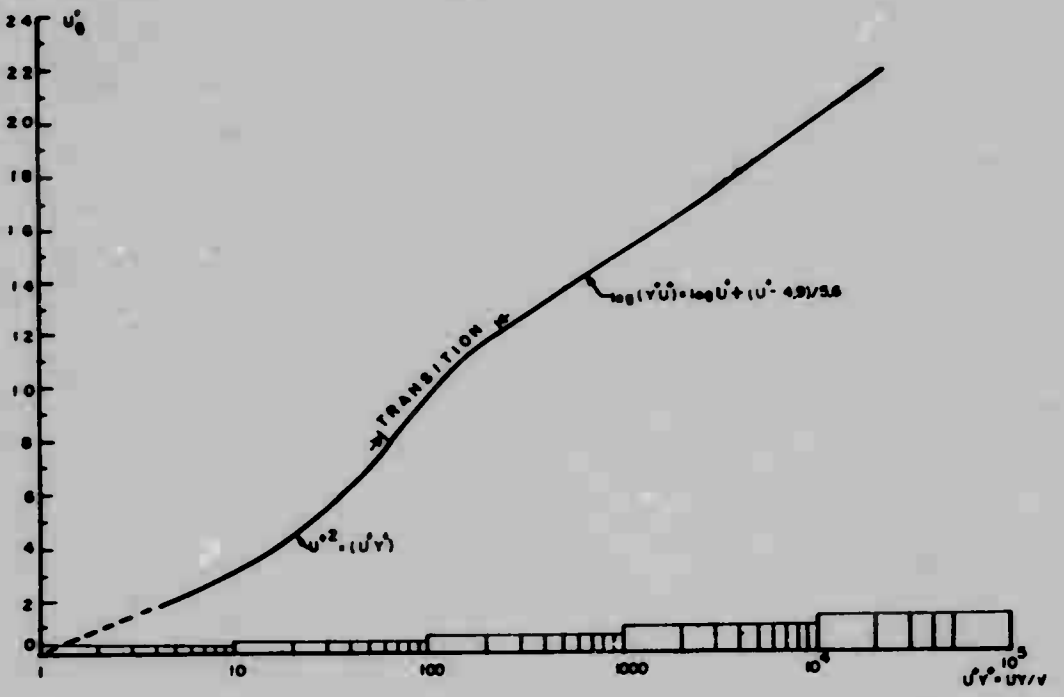

Fig. 3.15a Universal relation derived from the law of the wall.

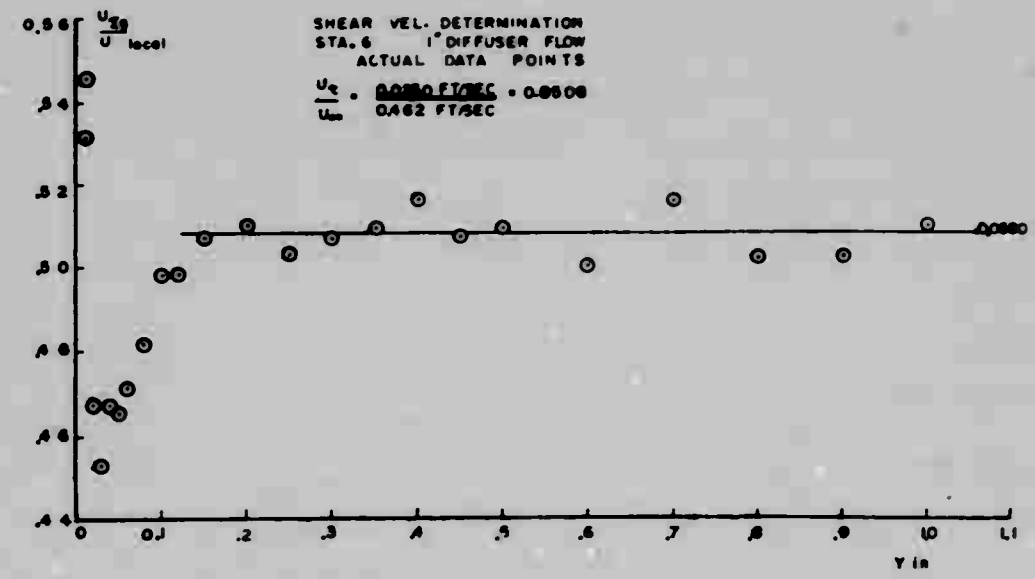

Fig. 3.15b u_τ determined by region of constant $u_{\tau g}$

Fig. 3.15 Wall shear velocity determination by method of cross-plotting data to match logarithmic part of velocity profile.

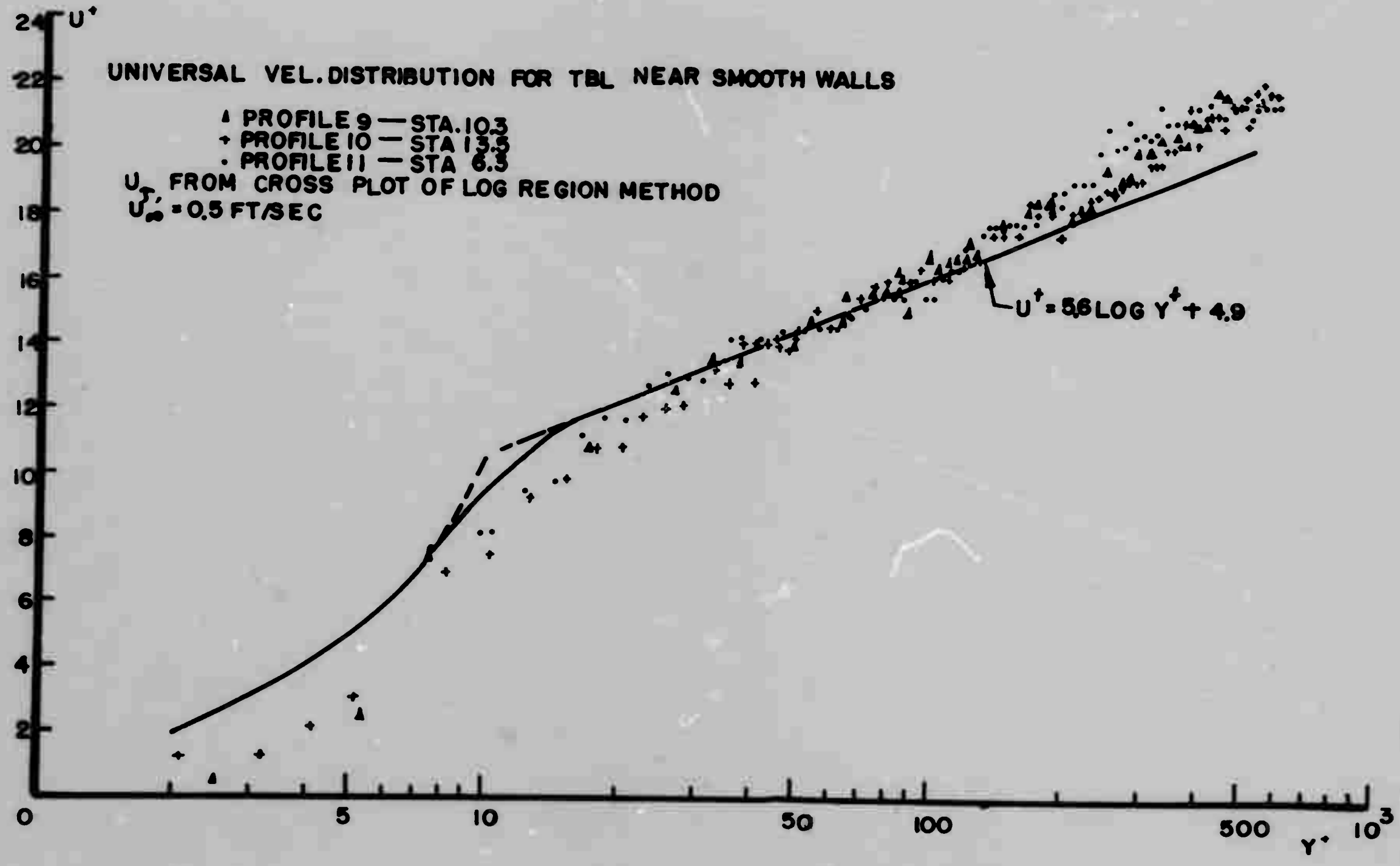

Fig. 3.16 u^+ vs. log y^+ non-dimensional mean velocity profiles: dp/dx = 0 flow.

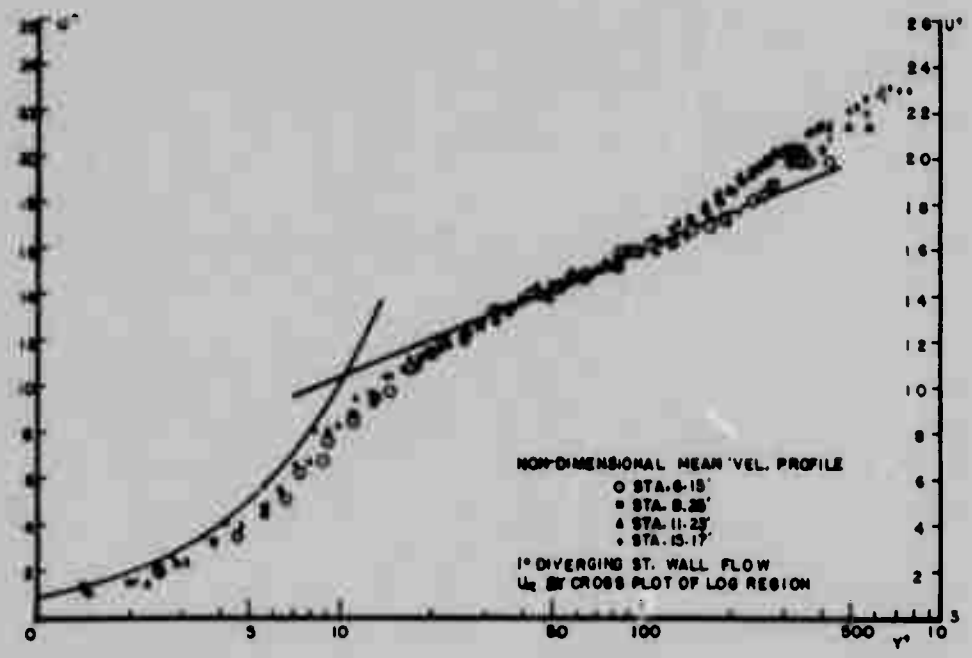

Fig. 3.17a u^+ vs. log y^+ non-dimensional mean velocity profiles: mild + dp/dx flow. u_τ by cross plot of log region method.

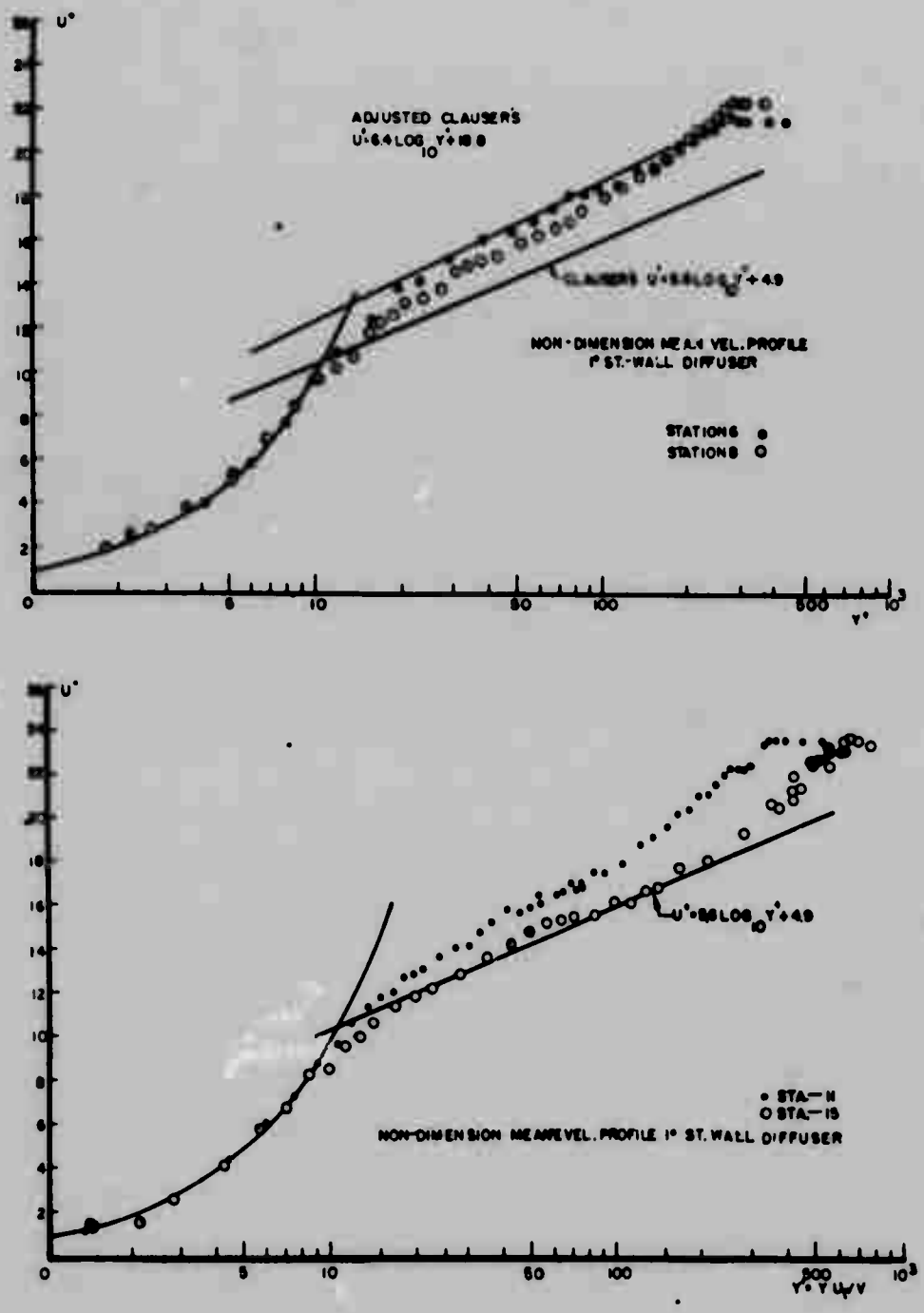

Fig. 3.17b u^+ vs. log y^+ non-dimensional mean velocity profiles: mild + dp/dx flow. u_τ by wall slope method.

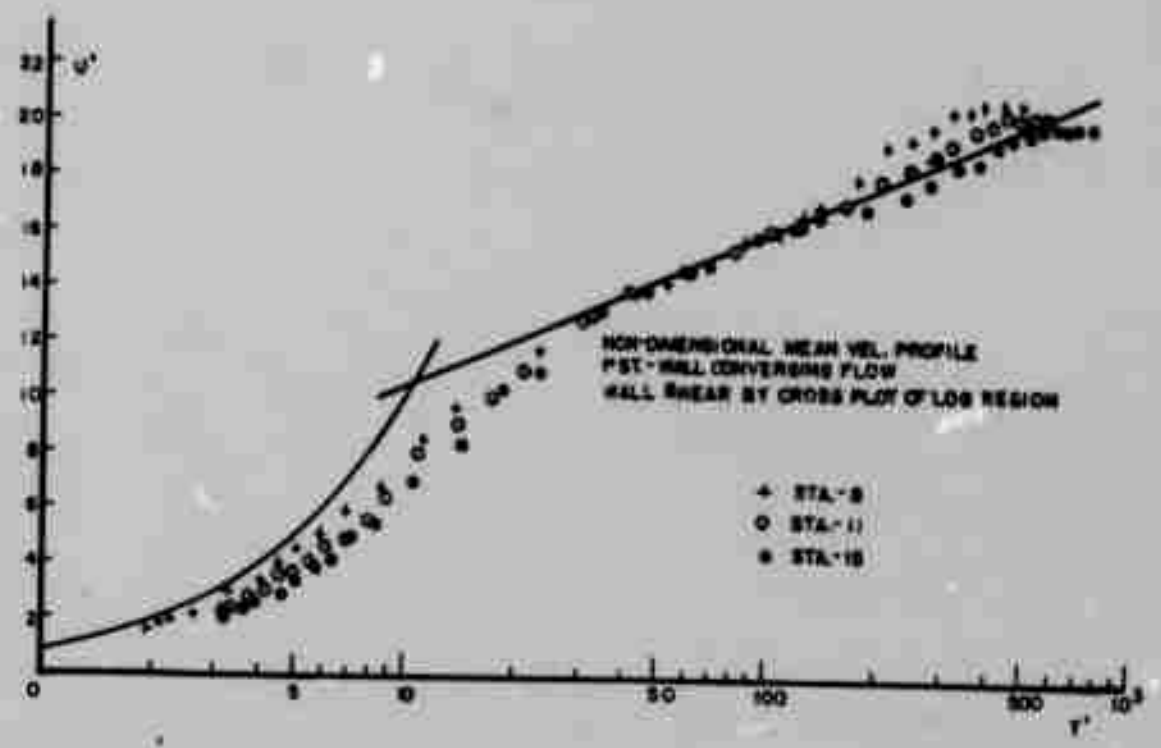

Fig. 3.18a u^+ vs. log y^+ non-dimensional mean velocity profiles: mild - dp/dx flow. u_τ by cross plot of log region.

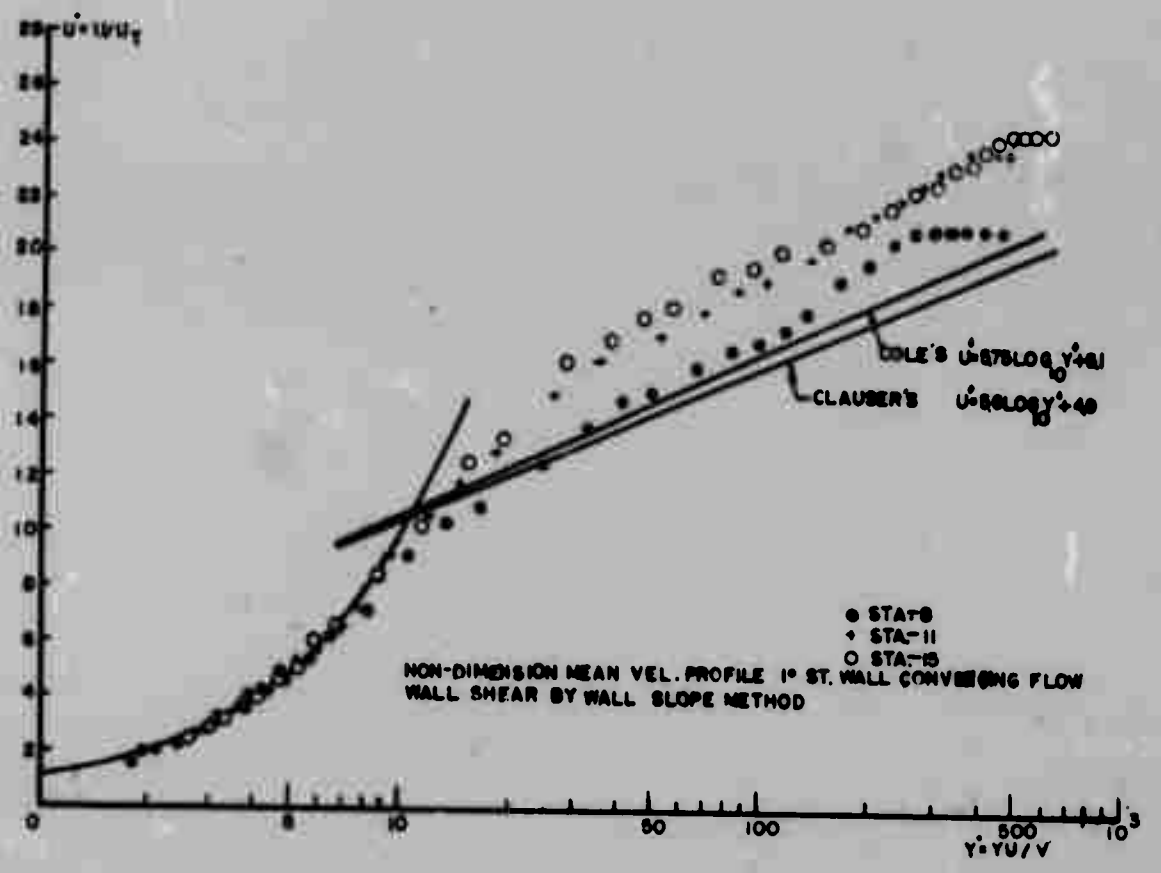

Fig. 3.18b u^+ vs. log y^+ non-dimensional mean velocity profiles: mild - dp/dx flow. u_τ by wall slope method.

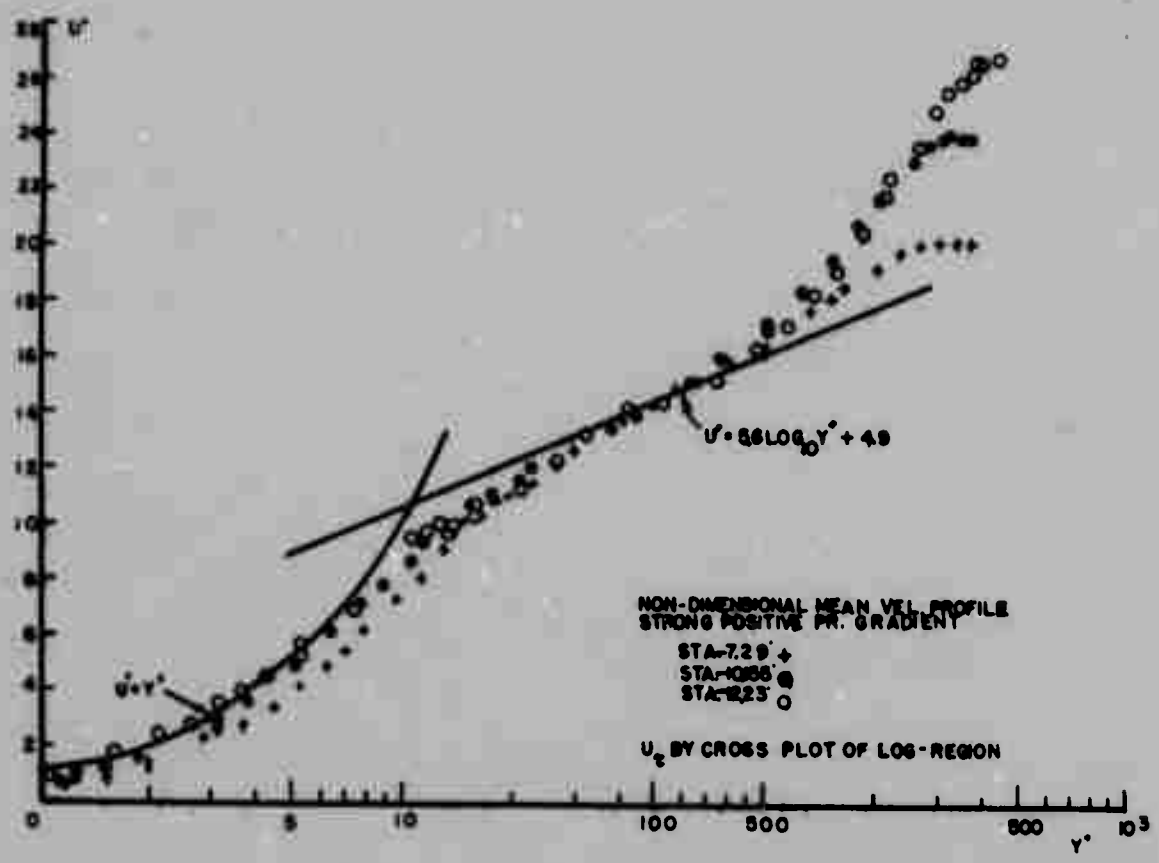

Fig. 3.19a u^+ vs. log y^+ non-dimensional mean velocity profiles: str + dp/dx flow. u_τ by cross plot of log region.

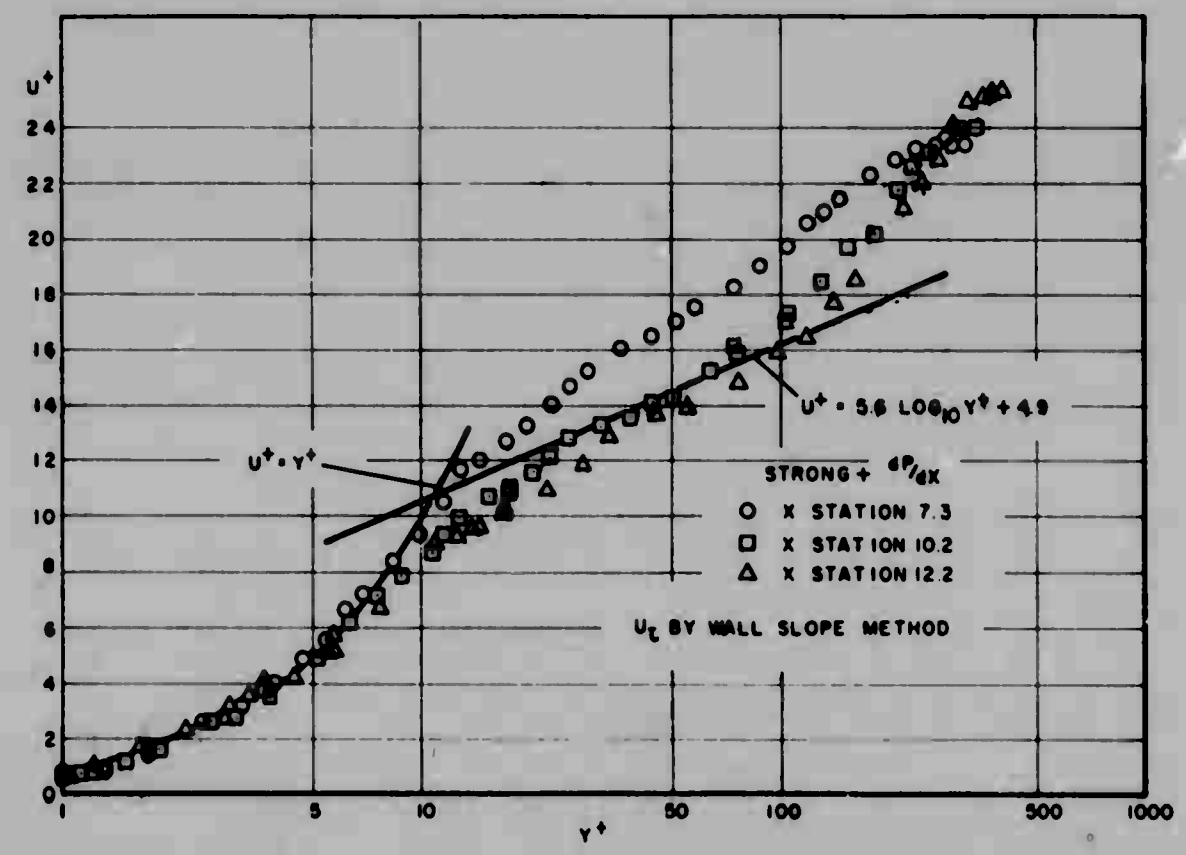

Fig. 3.19b u^+ vs. log y^+ non-dimensional mean velocity profiles: str + dp/dx flow. u_τ by wall slope method.

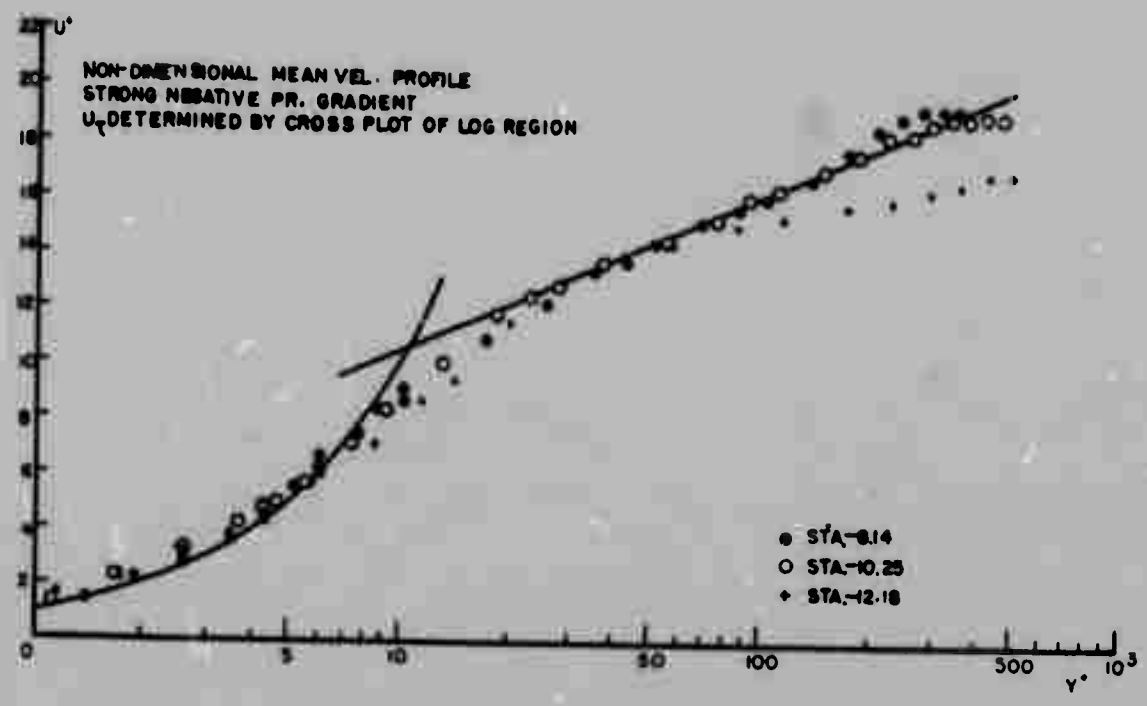

Fig. 3.20a u^+ vs. log y^+ non-dimensional mean velocity profiles: str - dp/dx flow. u_τ by cross plot of log region.

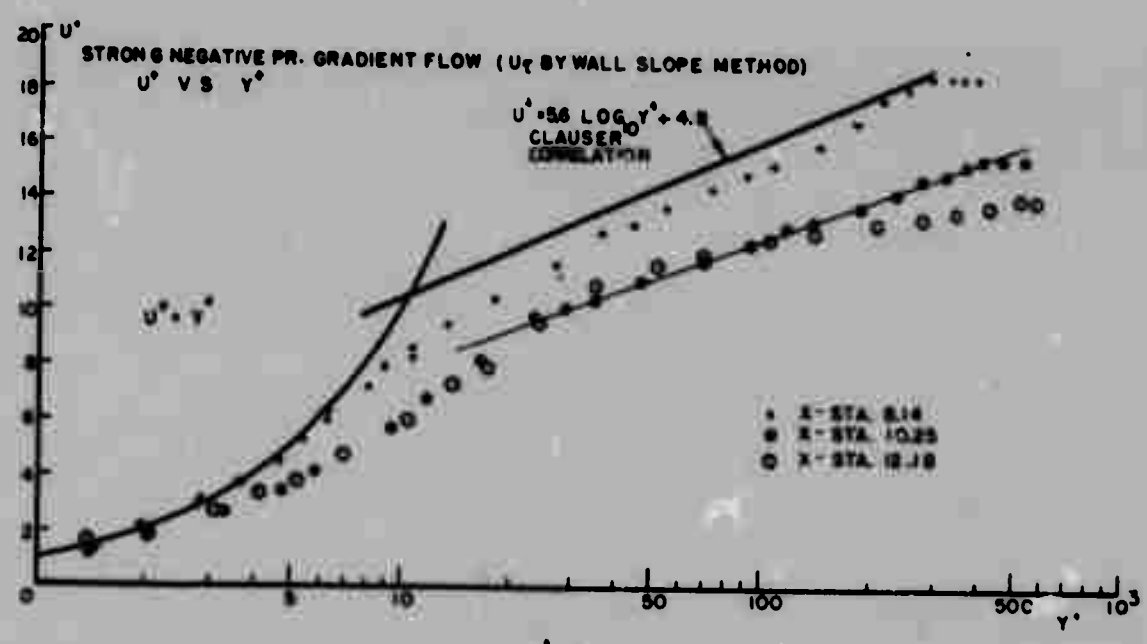

Fig. 3.20b u^+ vs. log y^+ non-dimensional mean velocity profiles: str - dp/dx flow. u_τ by wall slope method.

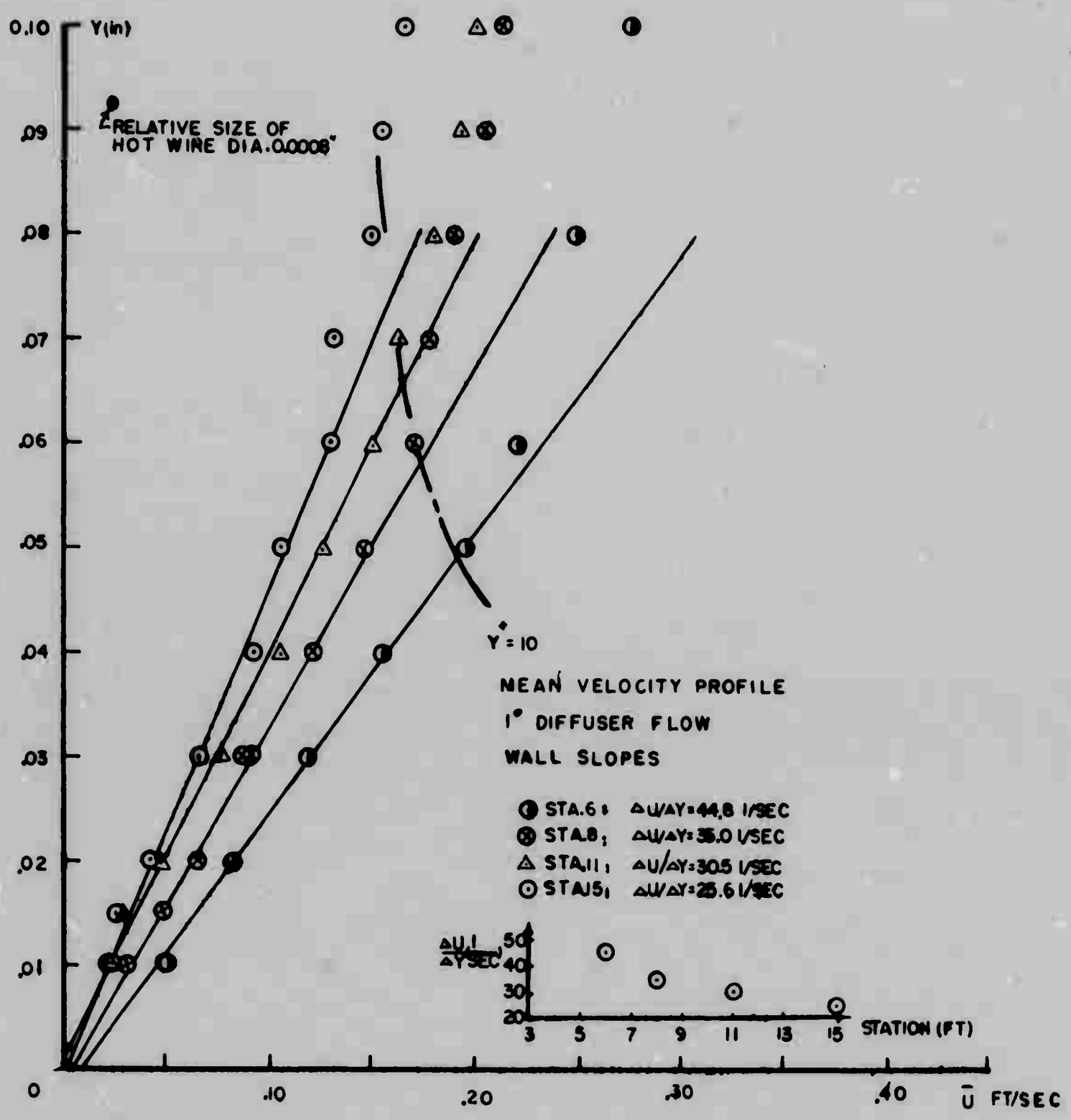

Fig. 3.21 Mean velocity profiles very near the wall: wall slope method of wall shear determination.

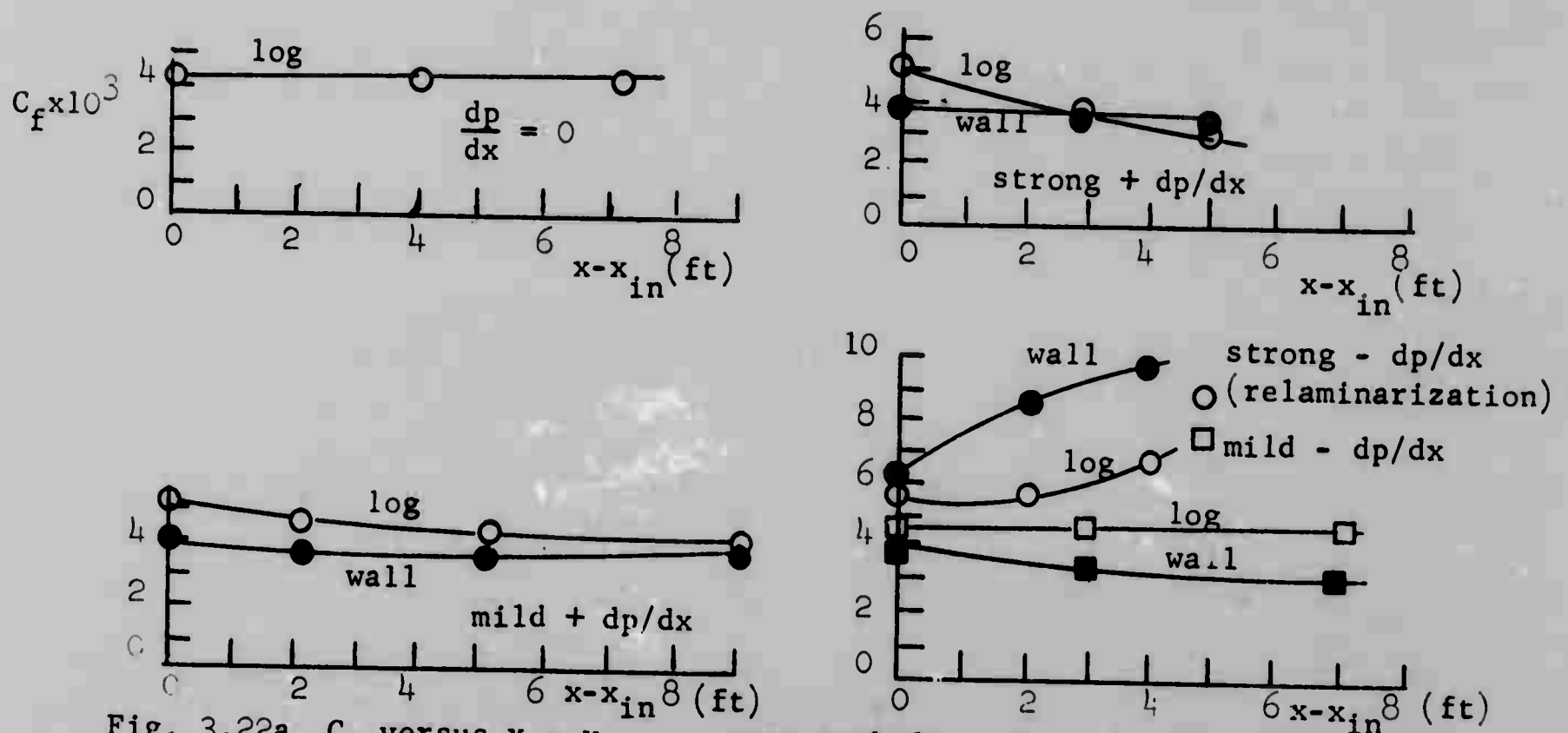

Fig. 3.22a C_f versus $x - x_{inlet}$; open symbols - shear by log cross plot, closed symbols - shear by wall slope method.

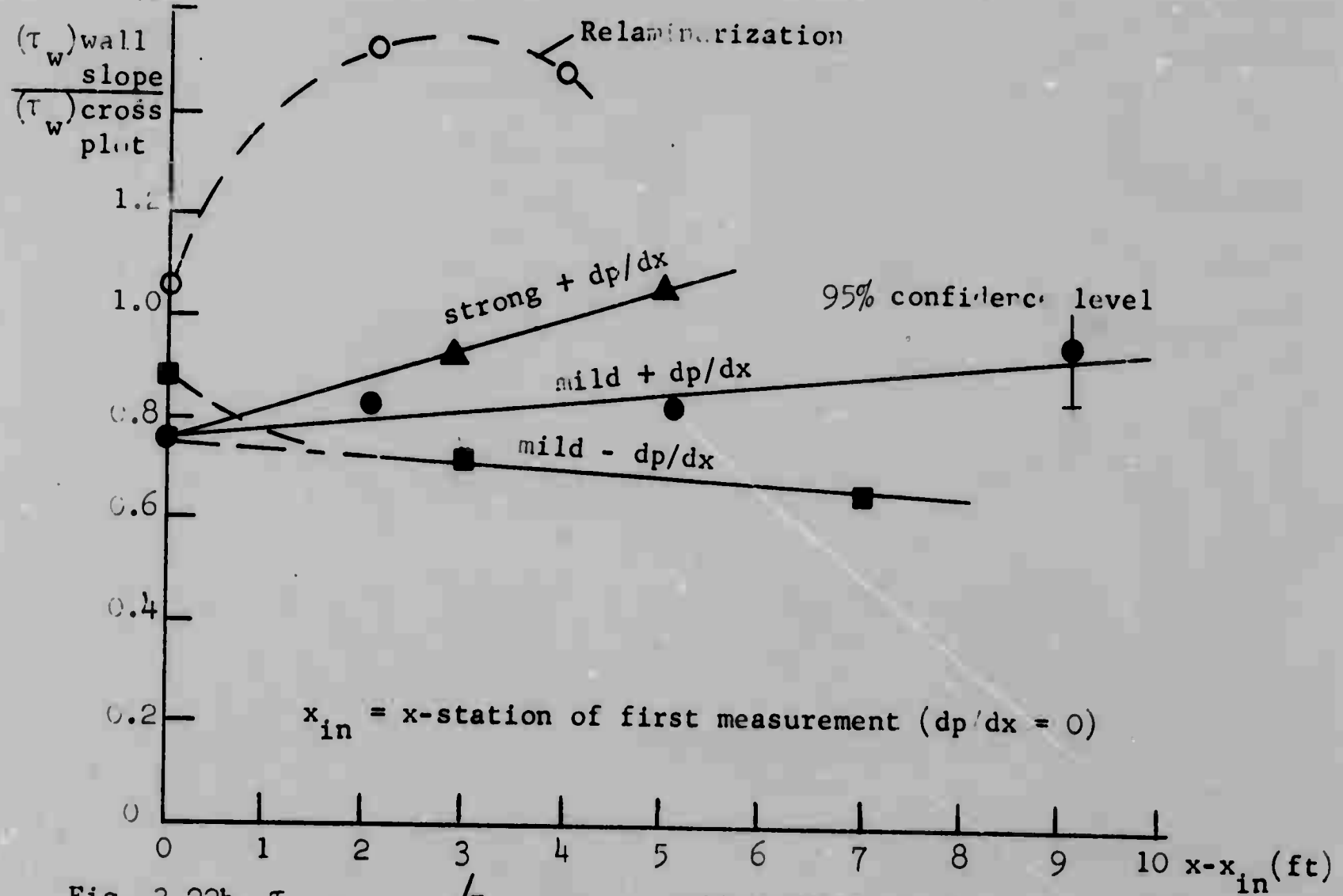

Fig. 3.22b $\tau_{wall\ slope}/\tau_{cross\ plot}$; illustrates the non-universality of the "law of the wall" in pressure gradient flows.

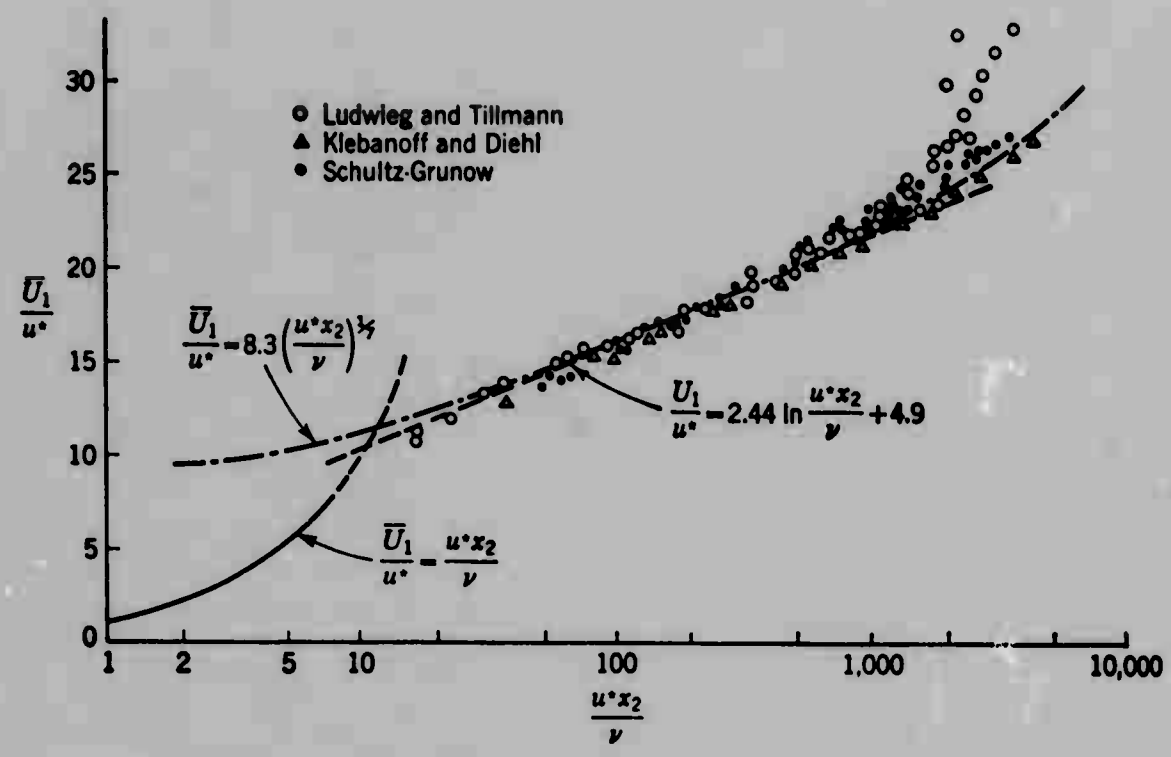

Fig. 3.23 Mean velocity distribution near smooth walls, early data; from Turbulence by Hinze, copyright 1959. Used by permission of McGraw-Hill Book Company.

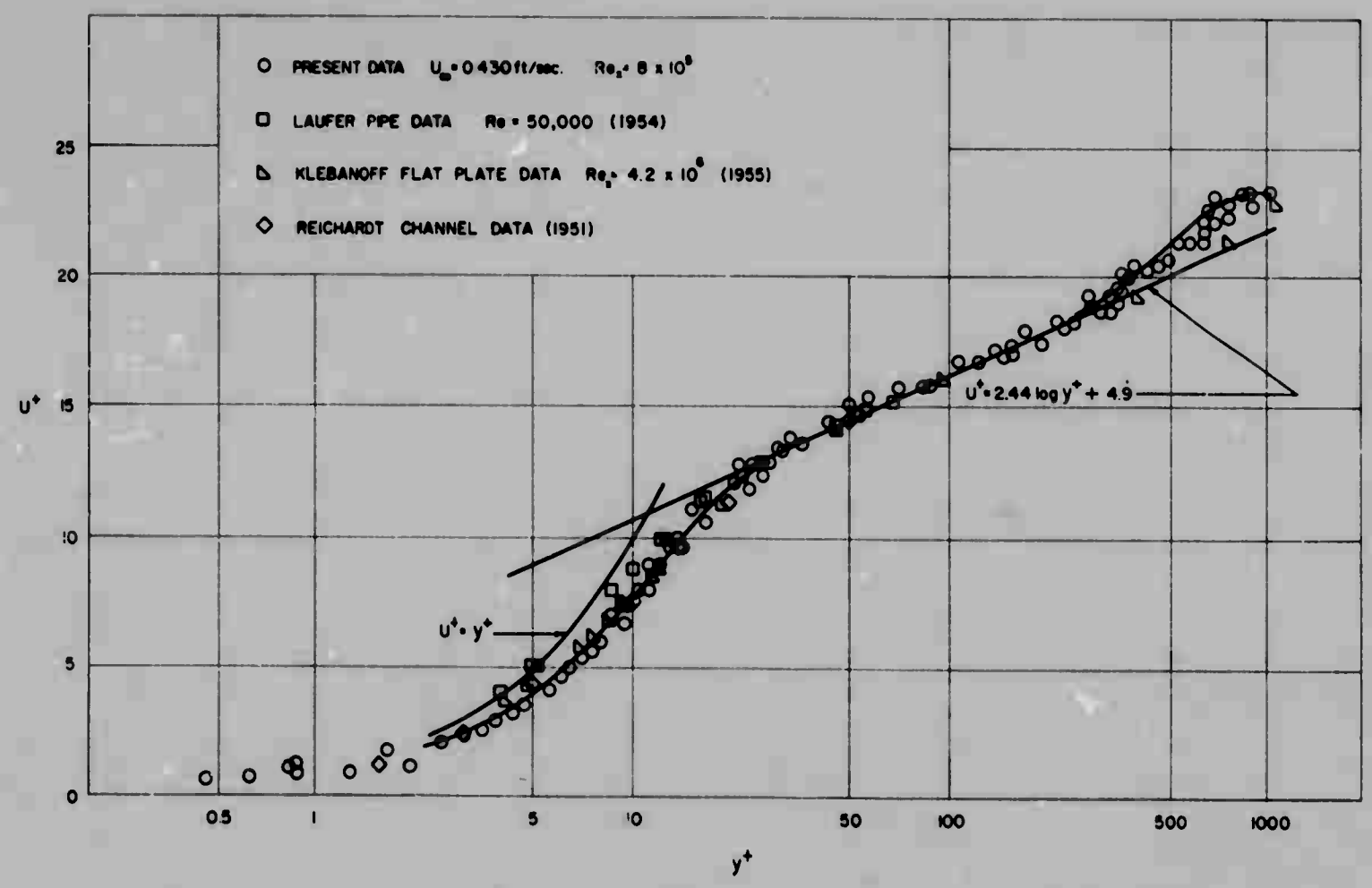

Fig. 3.24 Universal turbulent shear layer velocity profiles. Comparison data from Runstadler, et al [1963].

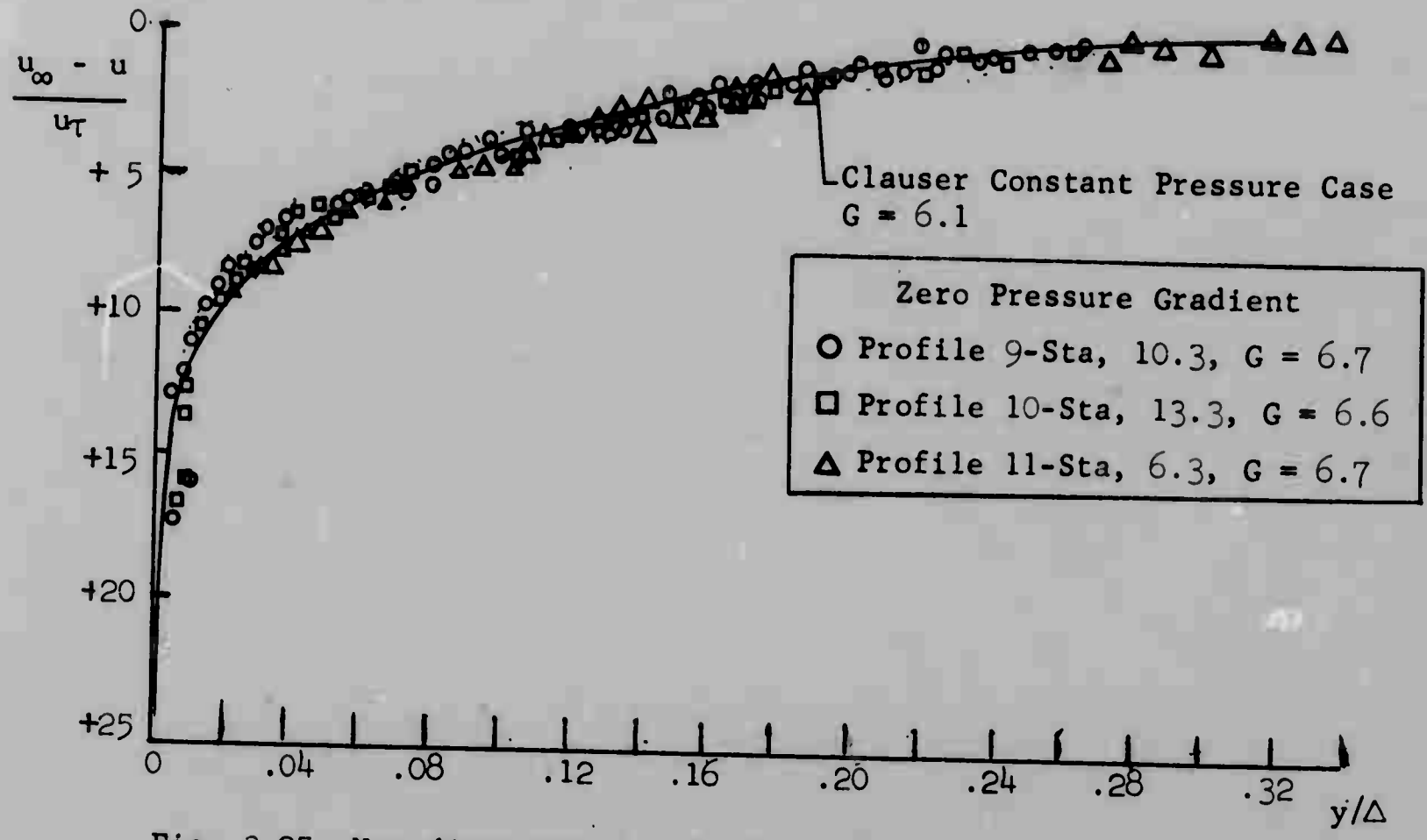

Fig. 3.25 Non-dimensional velocity-defect profiles: dp/dx = 0 flow

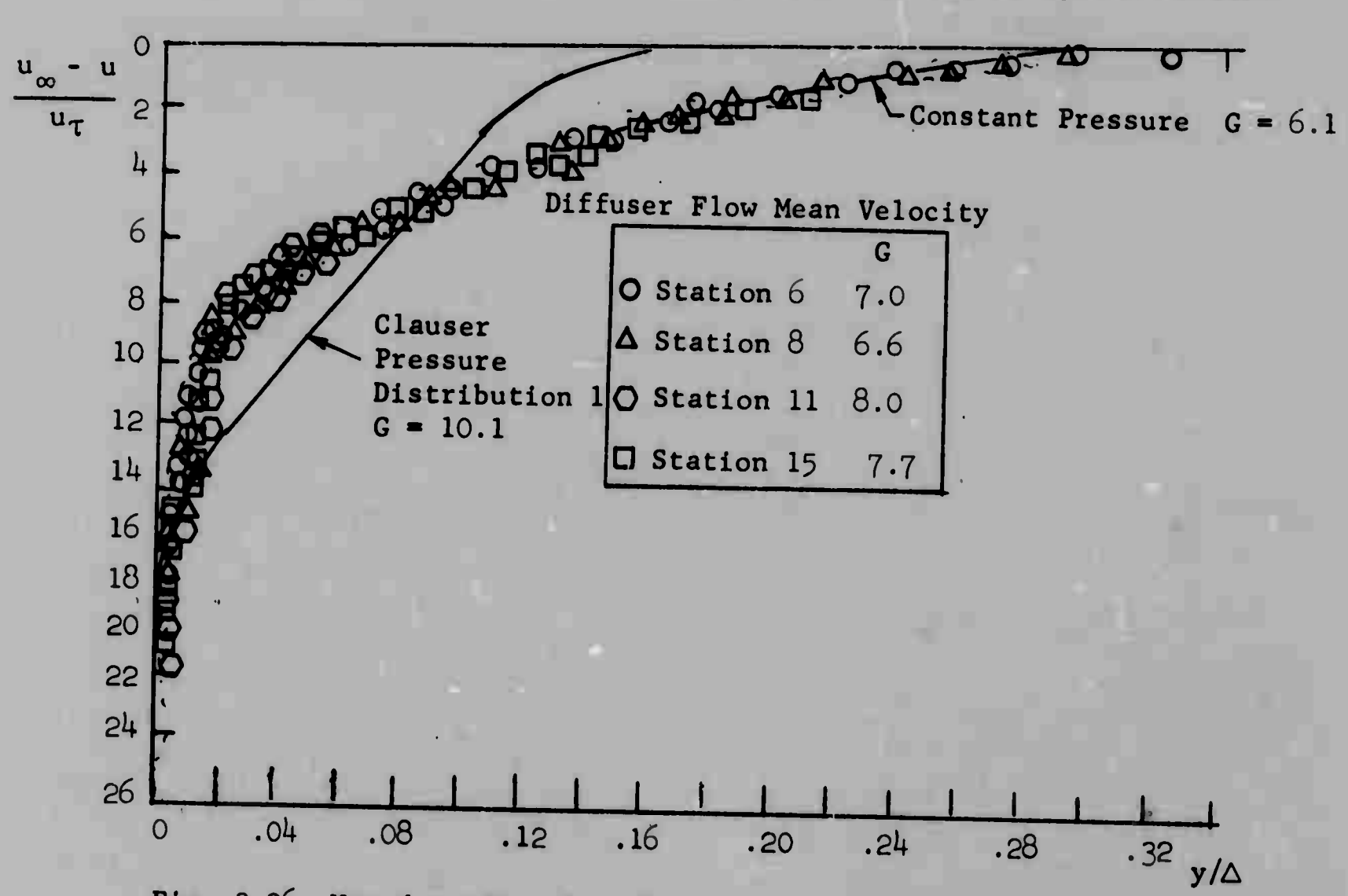

Fig. 3.26 Non-dimensional velocity-defect profiles: mild + dp/dx flow

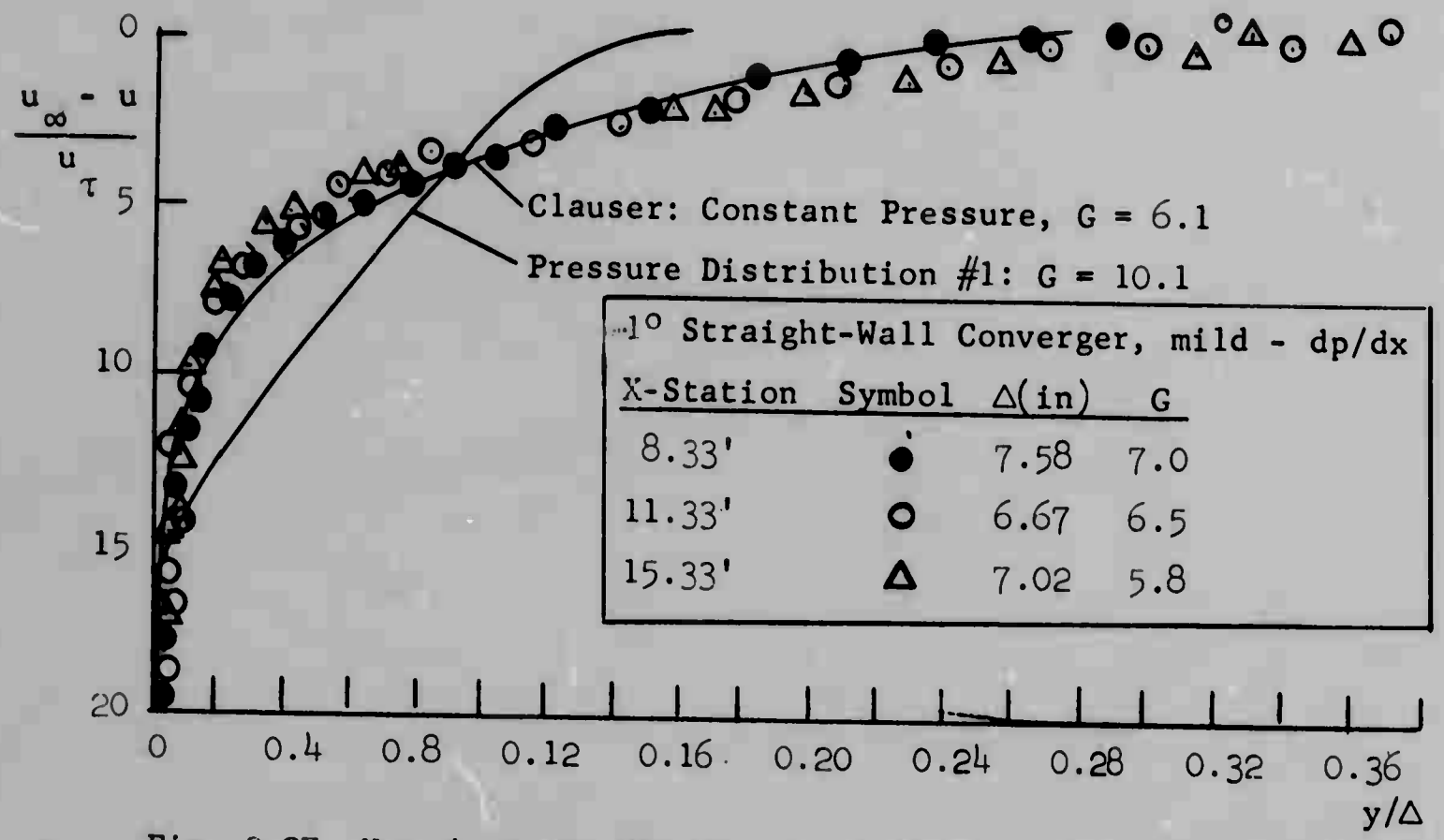

Fig. 3.27 Non-dimensional velocity-defect profiles: mild - dp/dx flow

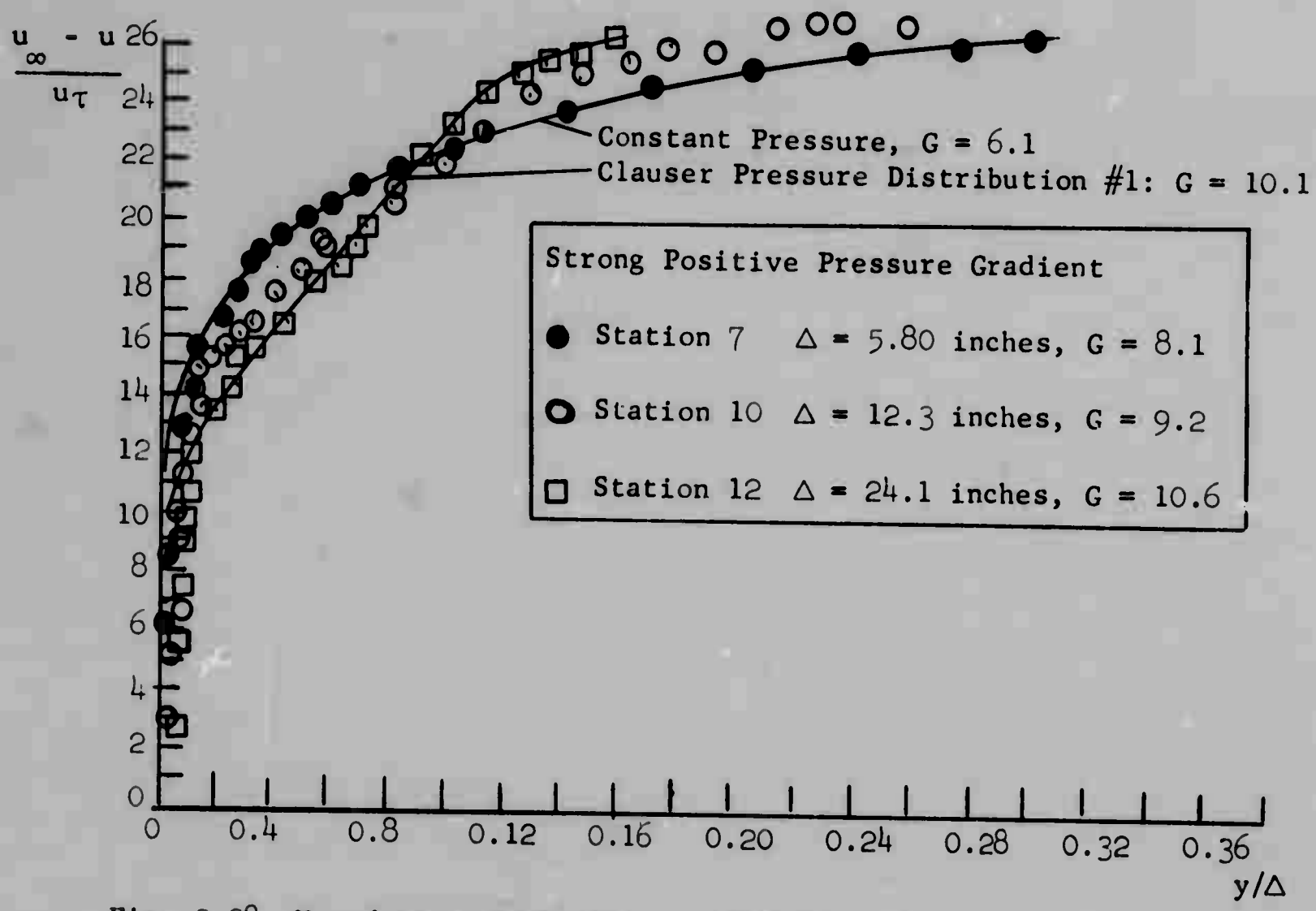

Fig. 3.28 Non-dimensional velocity-defect profiles: str + dp/dx flow

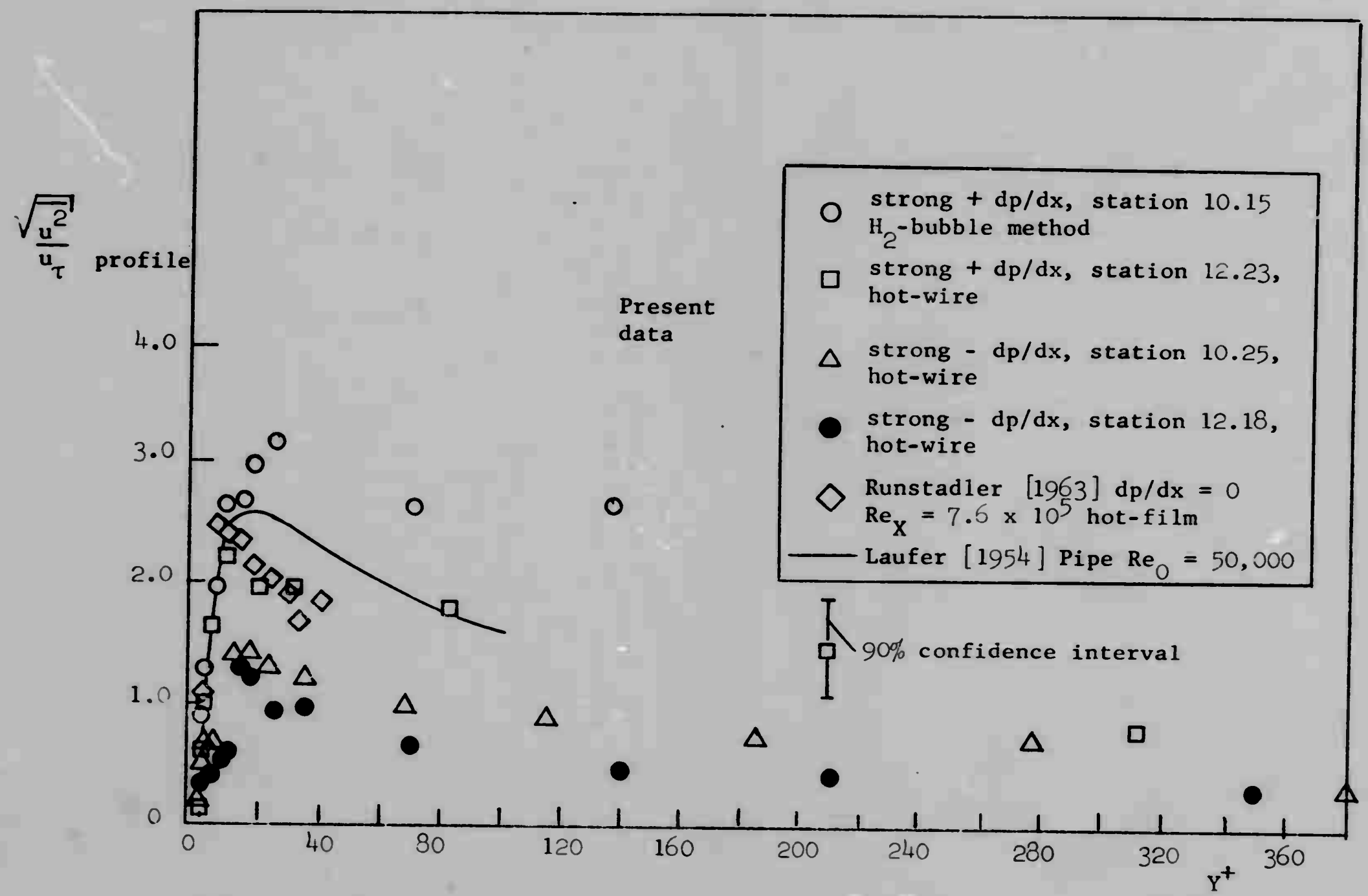

Fig. 3.29 Distribution of longitudinal component of velocity fluctuation.

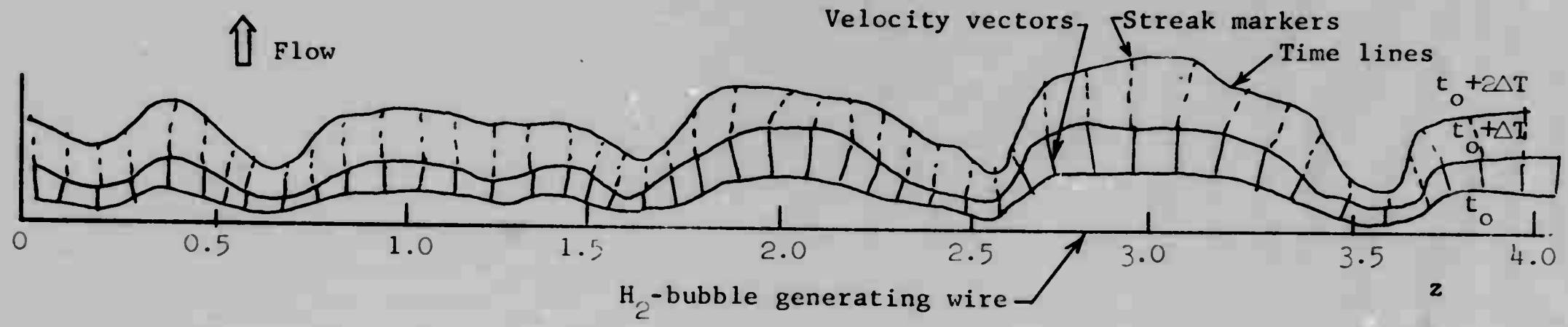

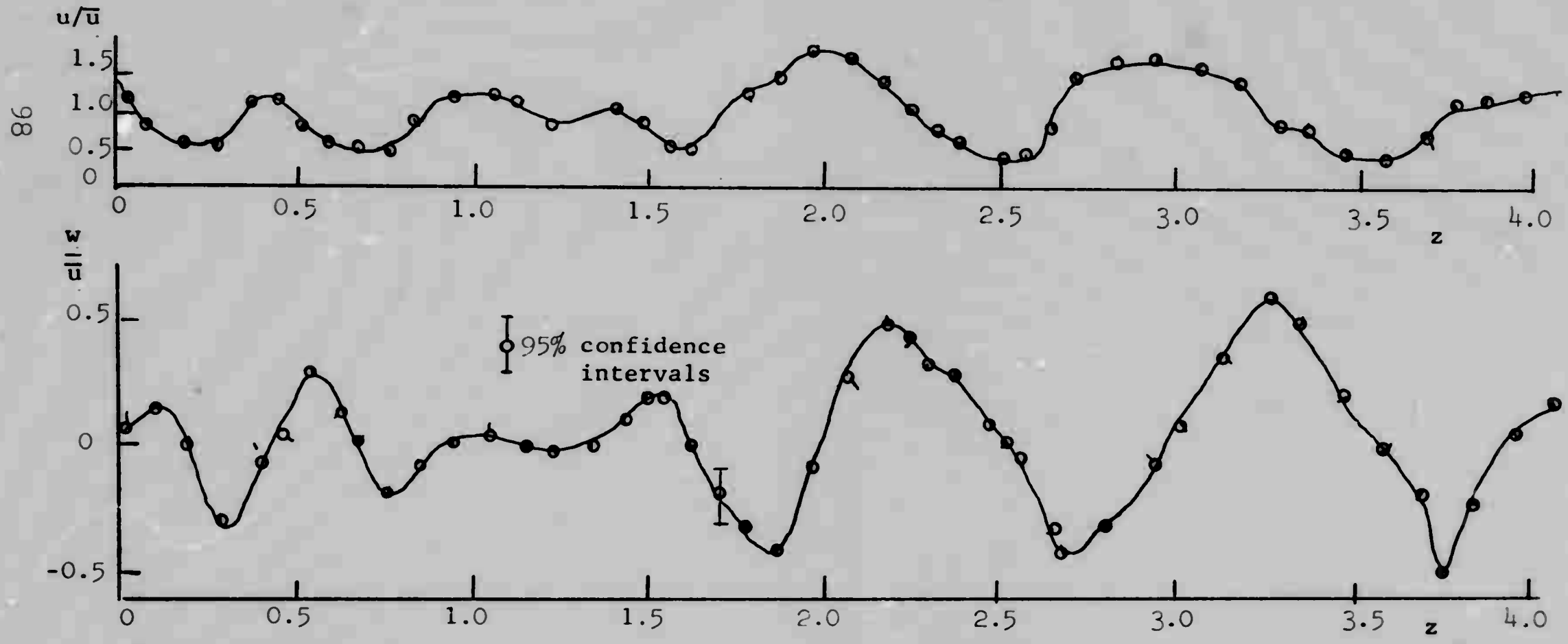

Fig. 3.30 Instantaneous u vs.z and w vs.z velocity profiles determined by H_2-bubble combined-time-streak marker method.

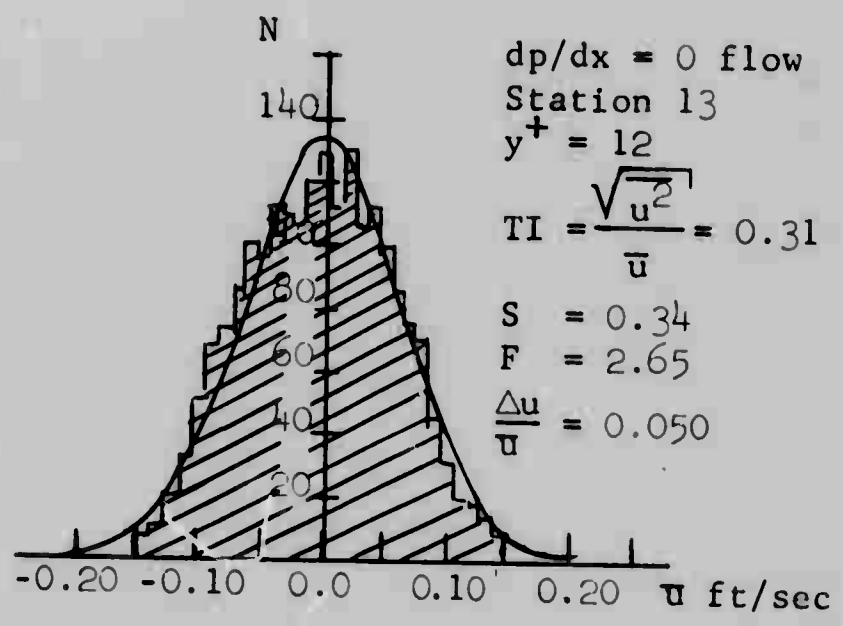

Fig. 3.31 Distribution of velocity values

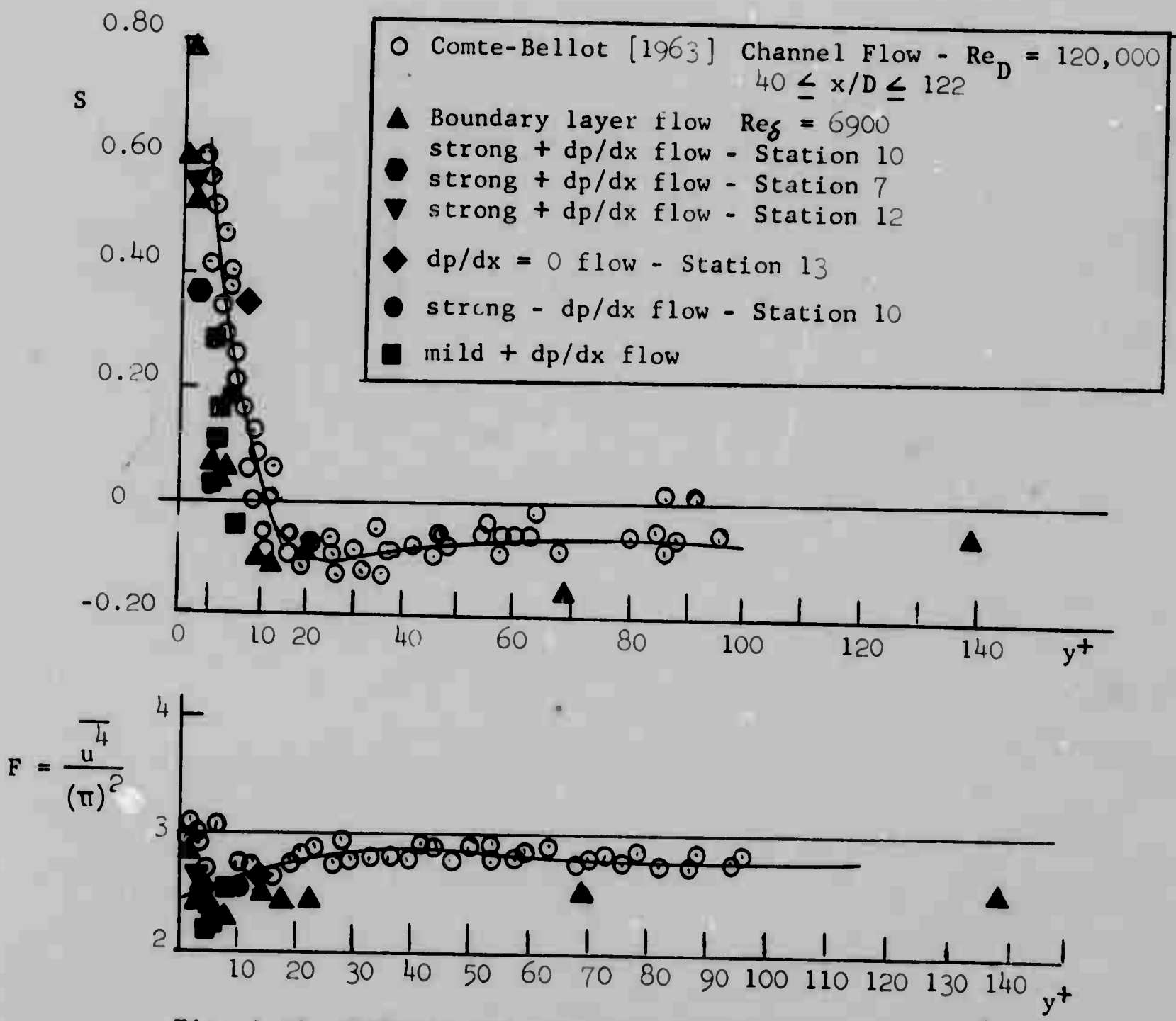

Fig. 3.32 Skewness and flatness distributions with y^+.

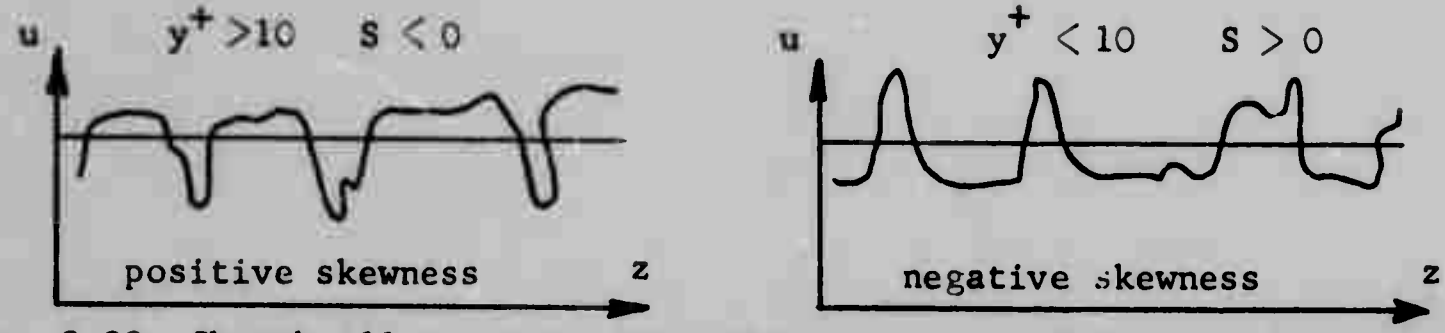

Fig. 3.33 Sketch illustrating the relative extent of low-speed regions corresponding to positive and negative skewness of the velocity fluctuation distribution in the wall region.

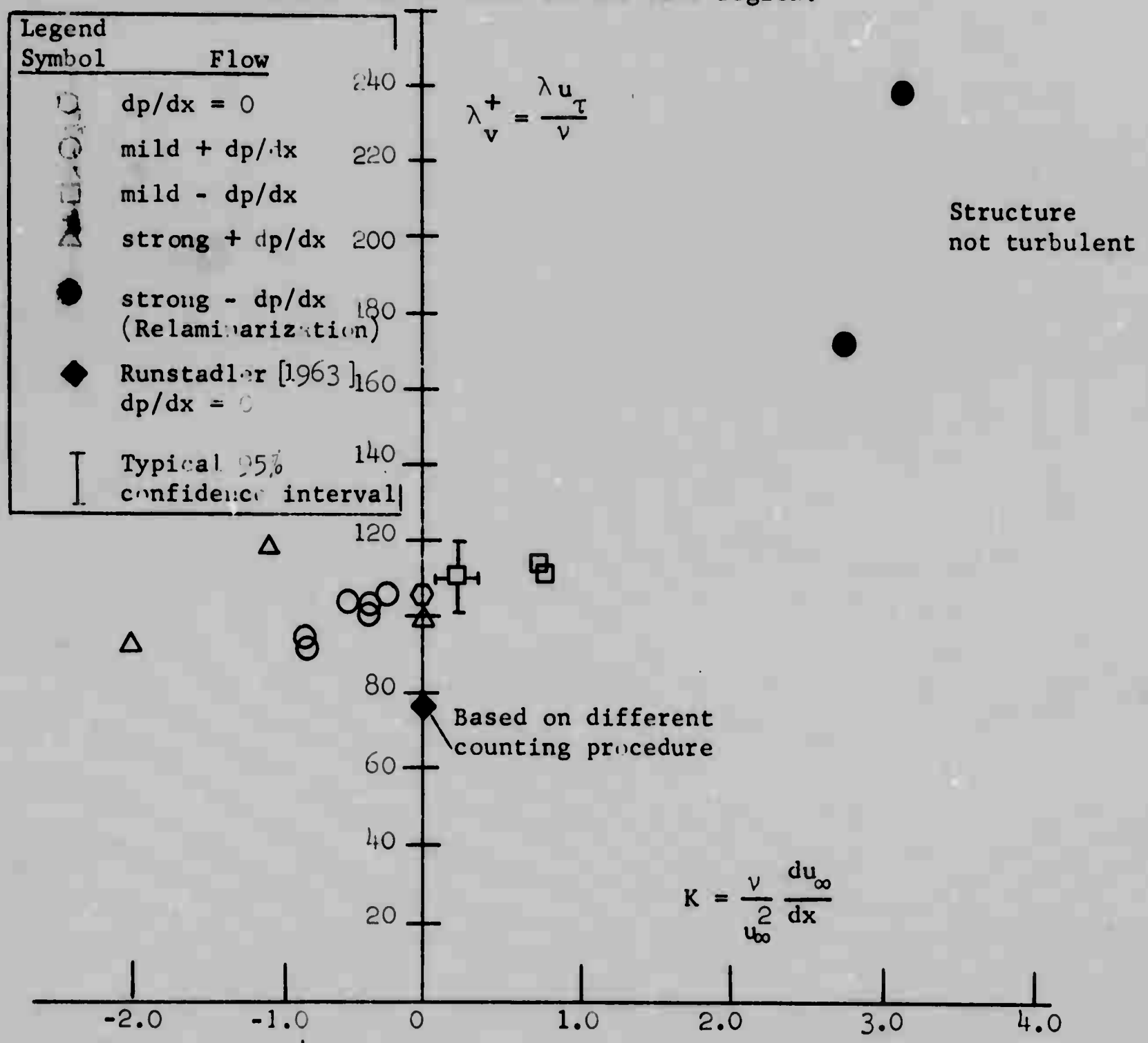

Fig. 3.34 versus K (Pressure gradient parameter)

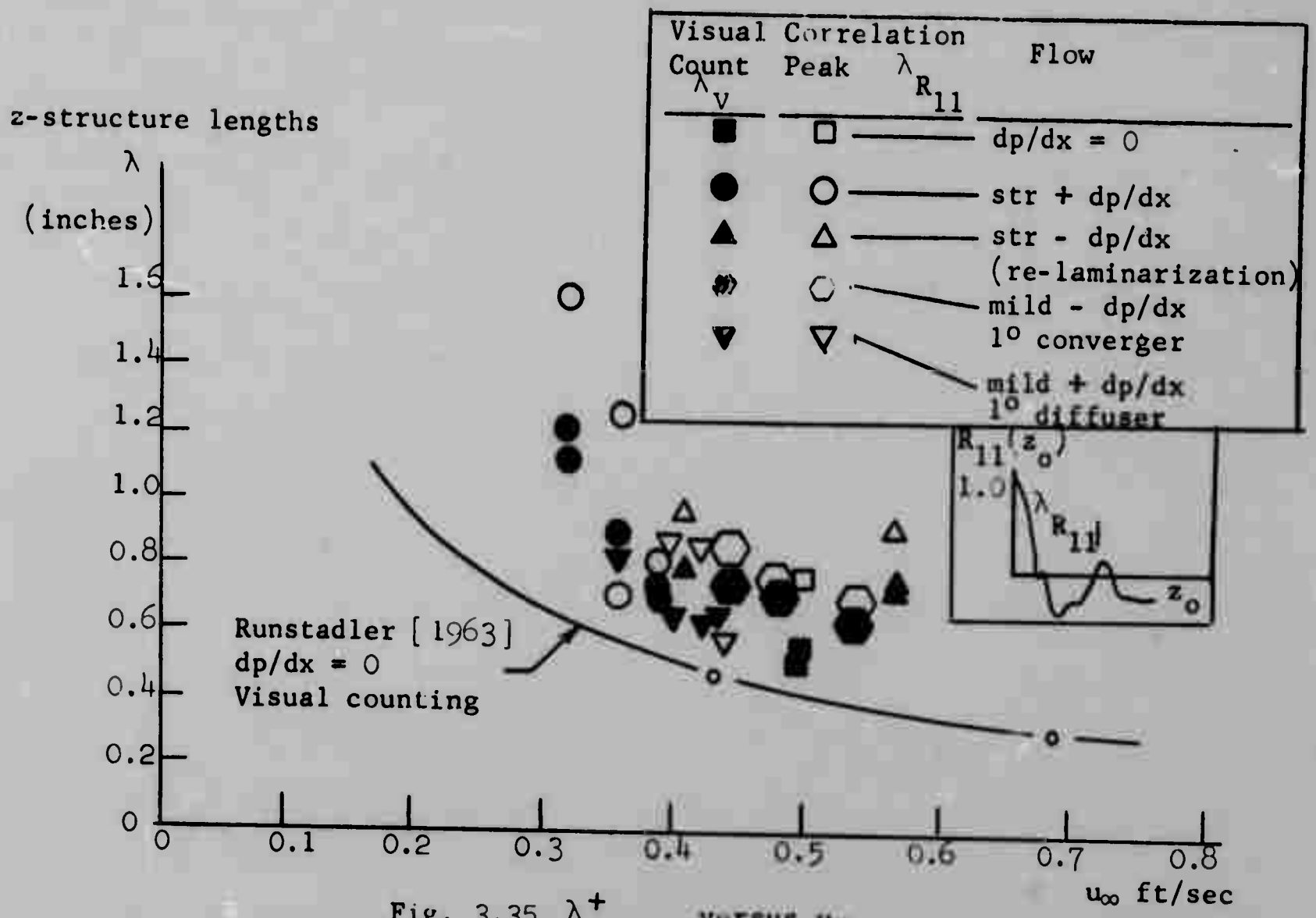

Fig. 3.35 λ^+_{visual} versus u_∞

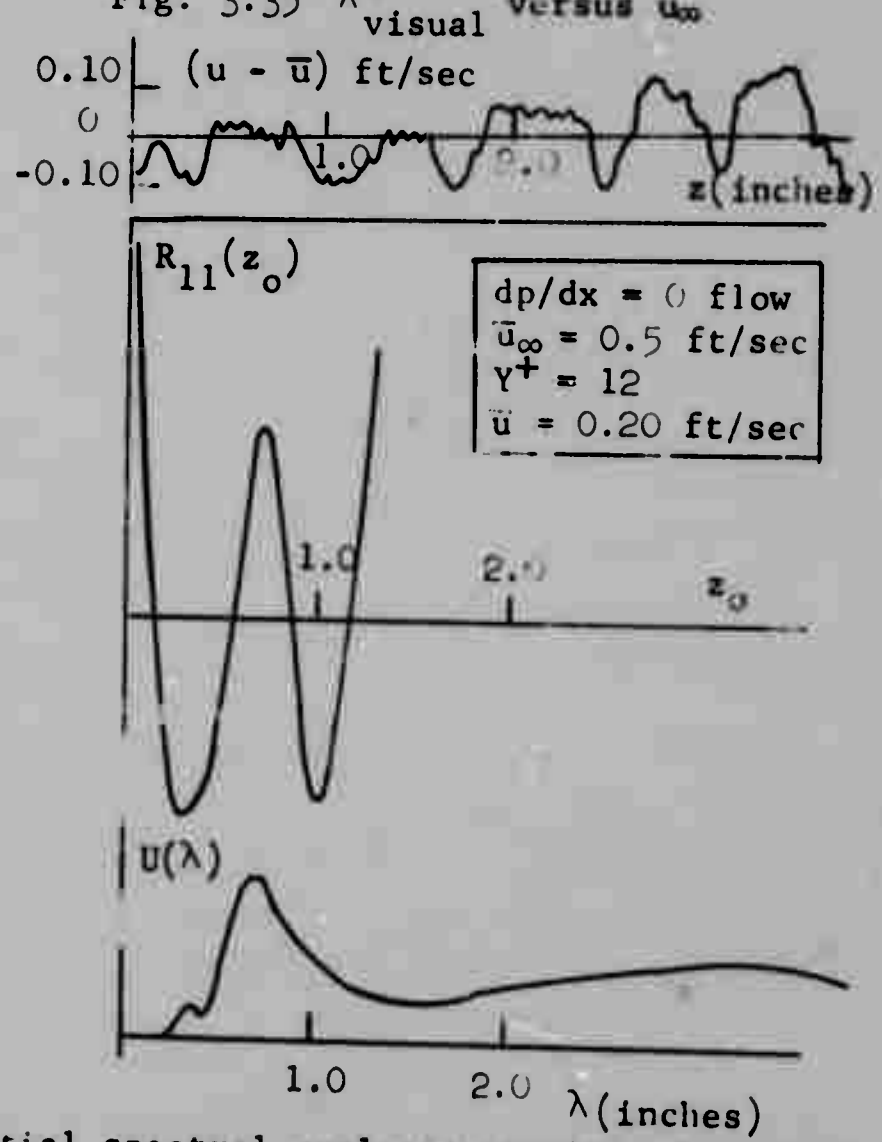

Fig. 3.36 Spatial spectral analysis results of a single movie frame.

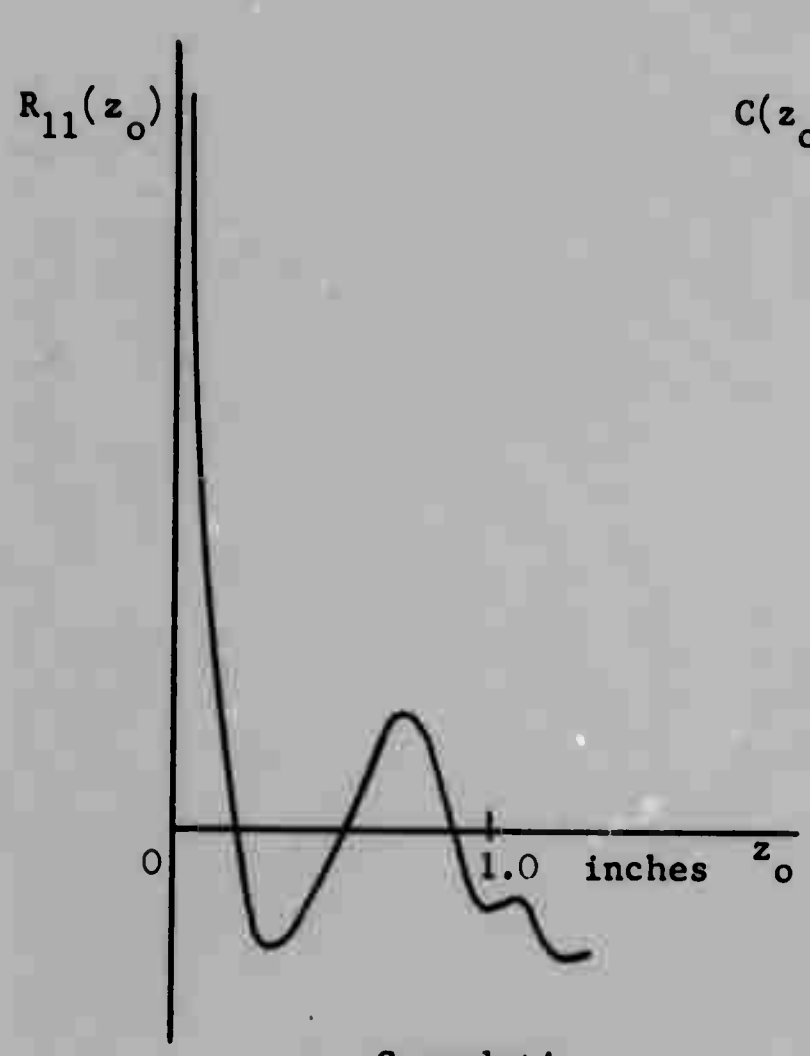

a. Correlation

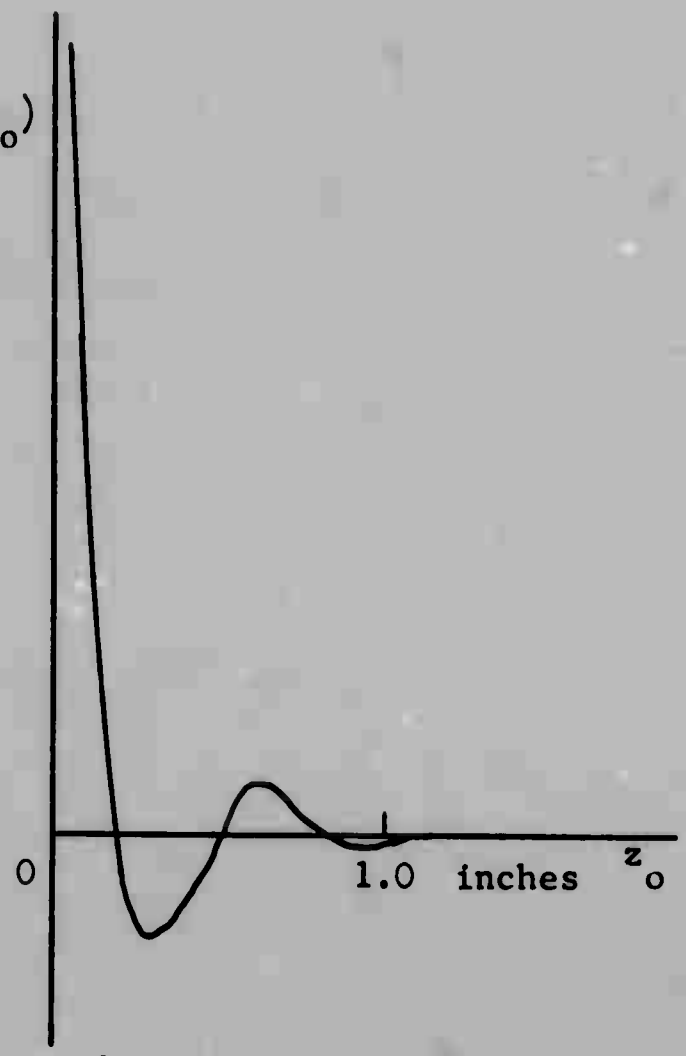

b. Weighted correlation

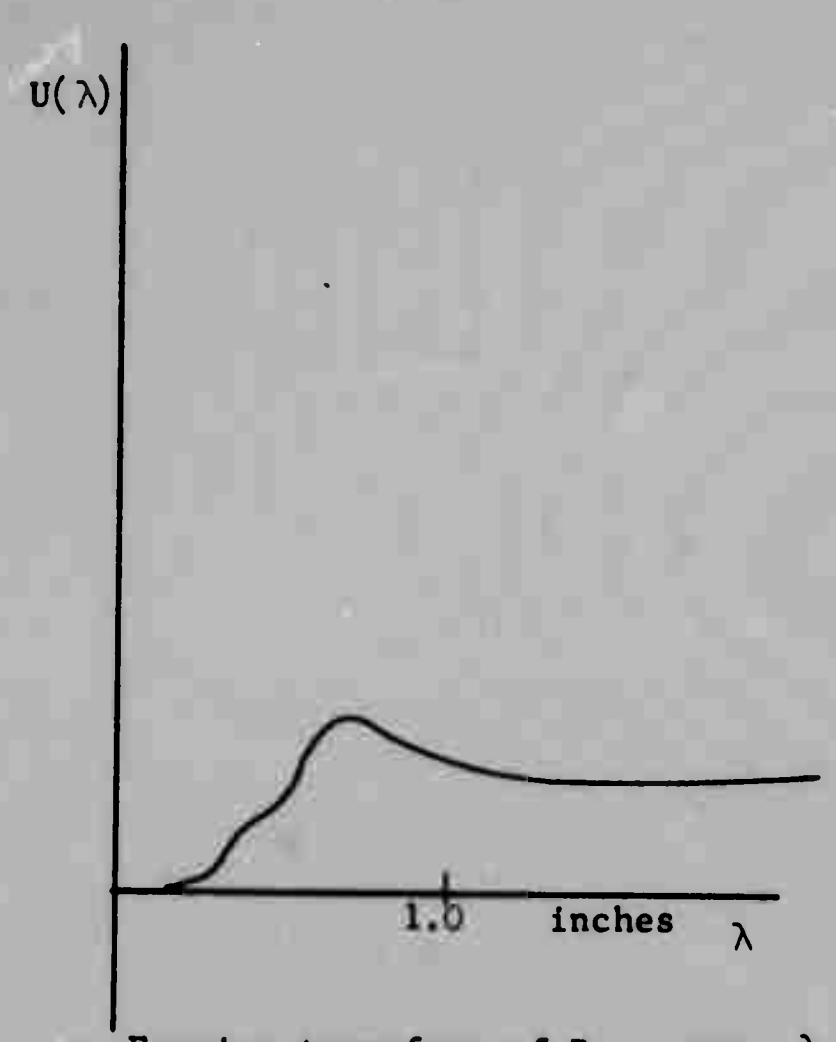

c. Fourier transform of R_{11} versus λ

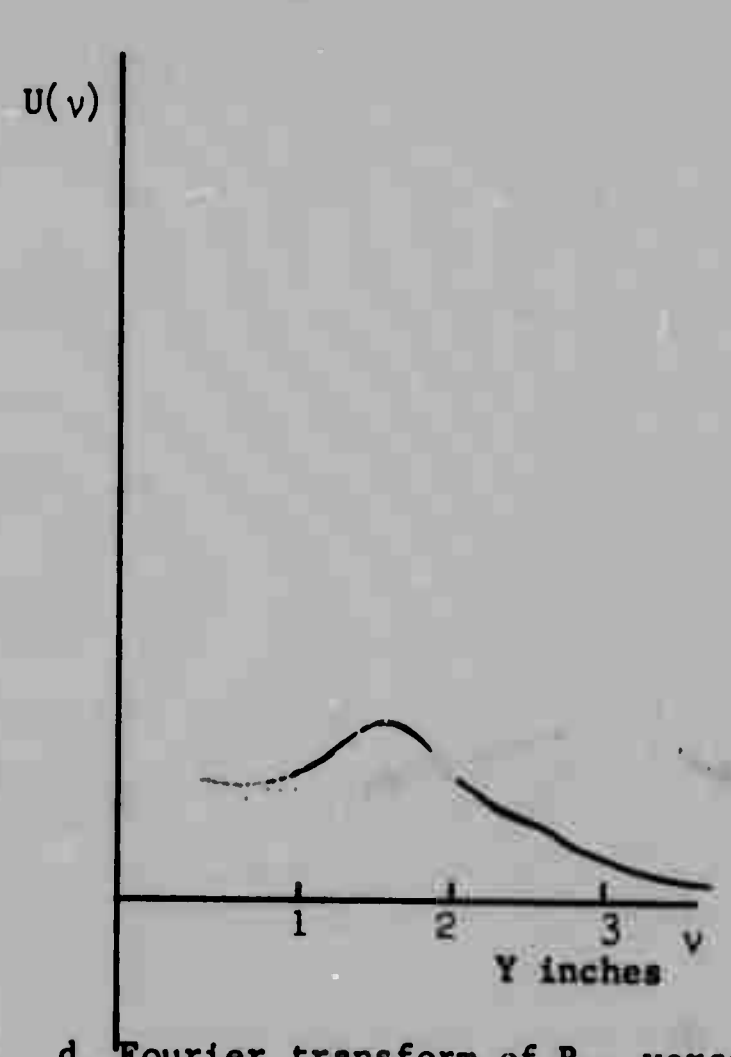

d. Fourier transform of R_{11} versus ν

Fig. 3.37 Spatial spectral analysis results from 6 frames; dp/dx = 0, station 13, u_∞ = 0.5 flow at y^+ = 12 .

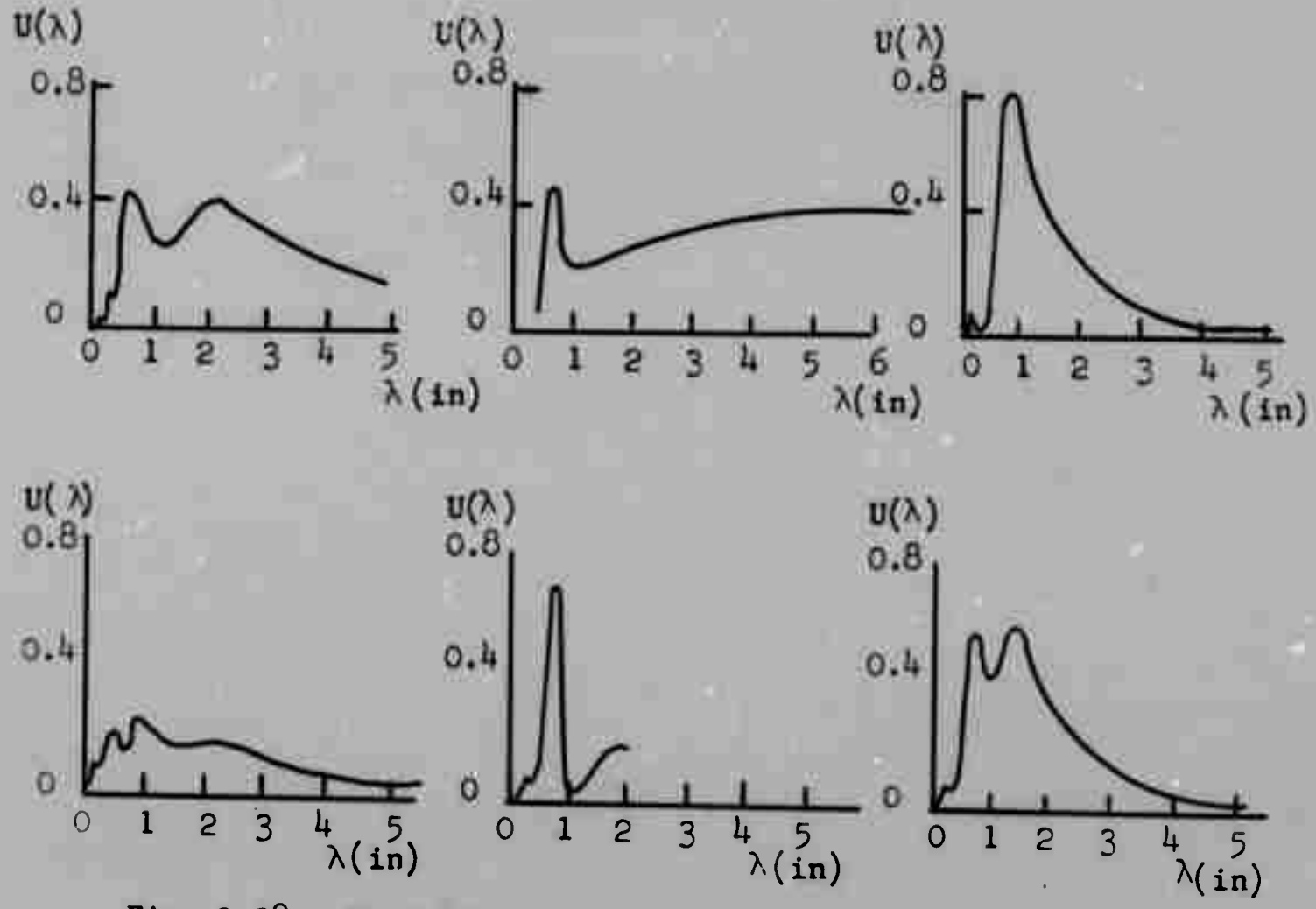

Fig. 3.38a Typical samples of individual frame spectrums
str + dp/dx, Station 10

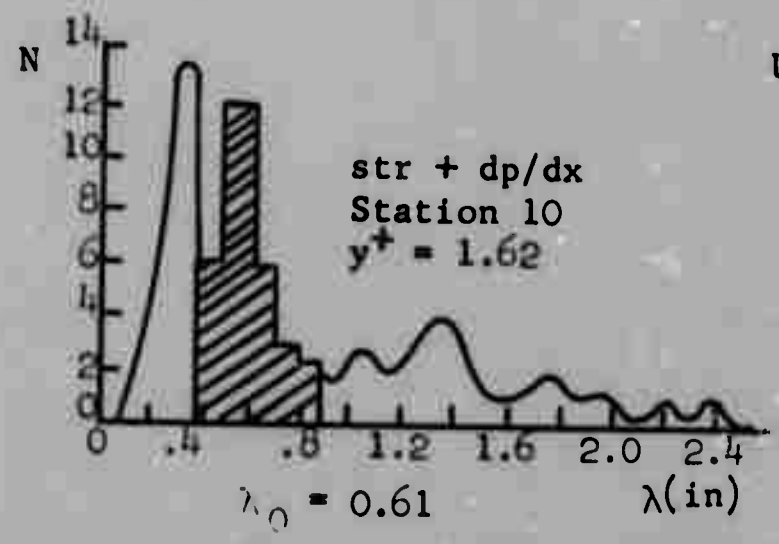

Fig. 3.38b Distribution of peaks from 31 individual frame spectrums:
str + dp/dx, Station 10

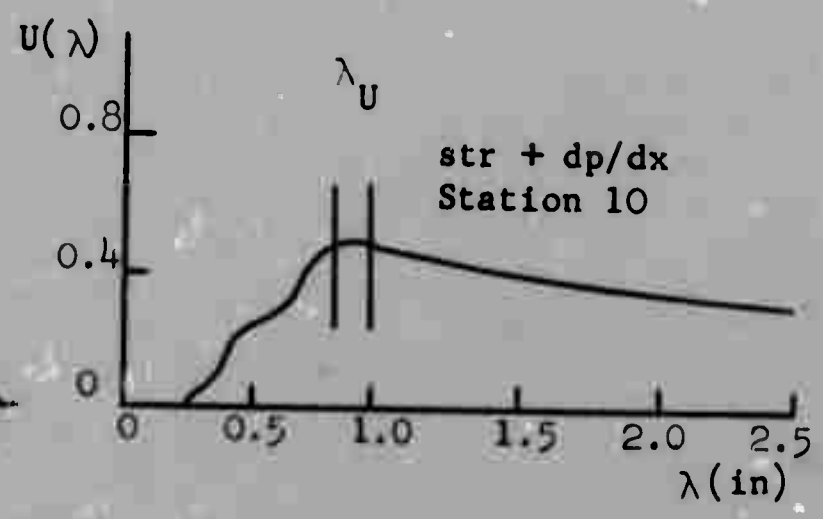

Fig. 3.38c Ensemble-spectrums from 31 frames:
str + dp/dx, Station 10

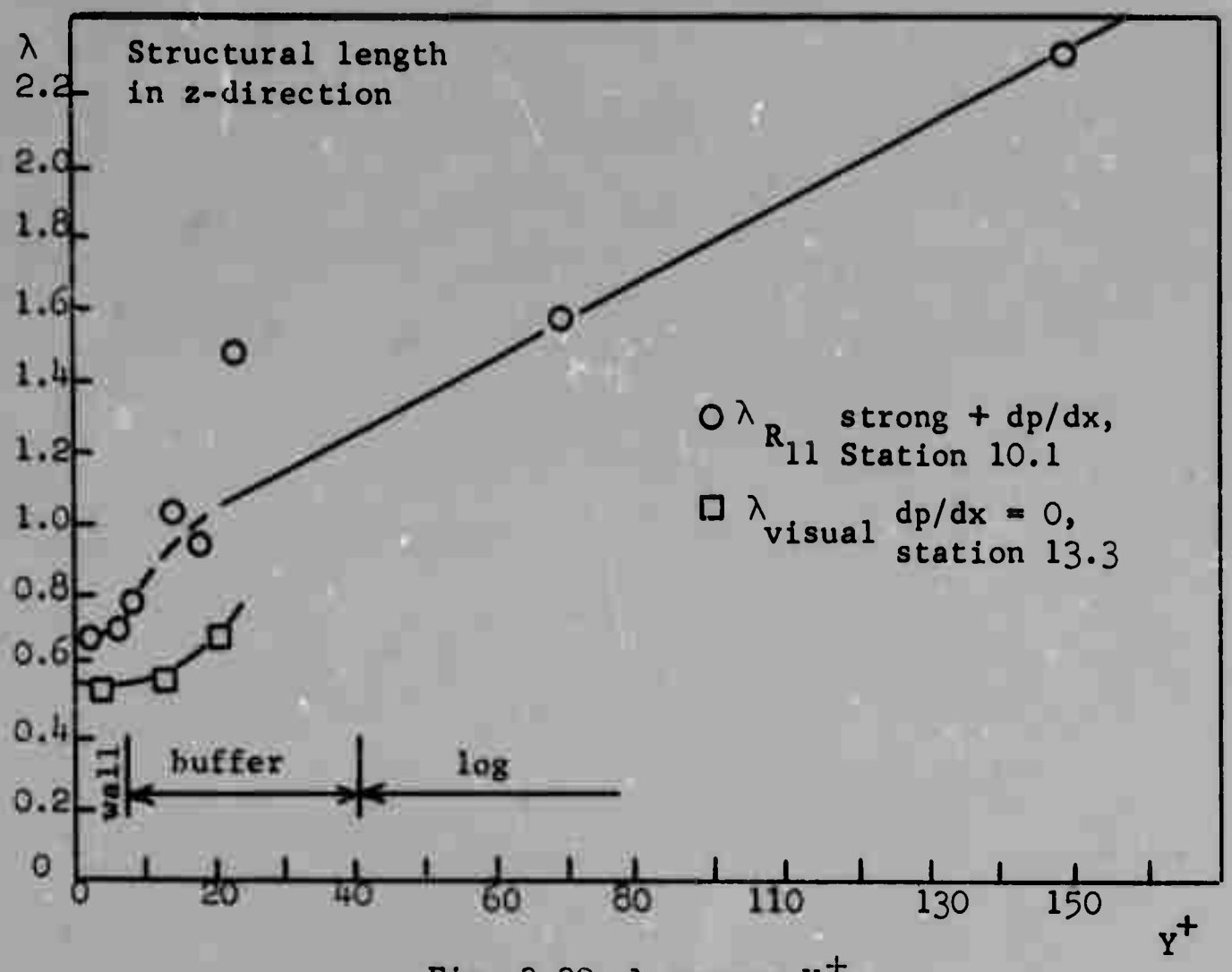

Fig. 3.39 λ versus Y^+

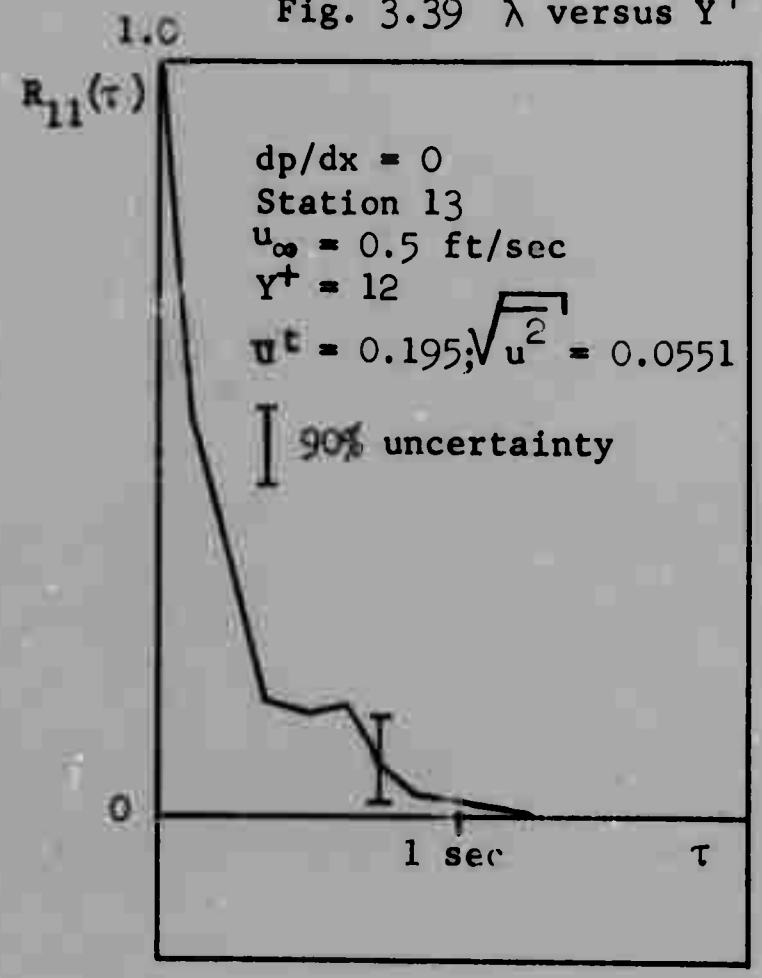

Fig. 3.40 Temporal correlation coefficient versus time lag for dp/dx = 0 flow; u_∞ = 0.5 ft/sec, Y^+ = 12 .

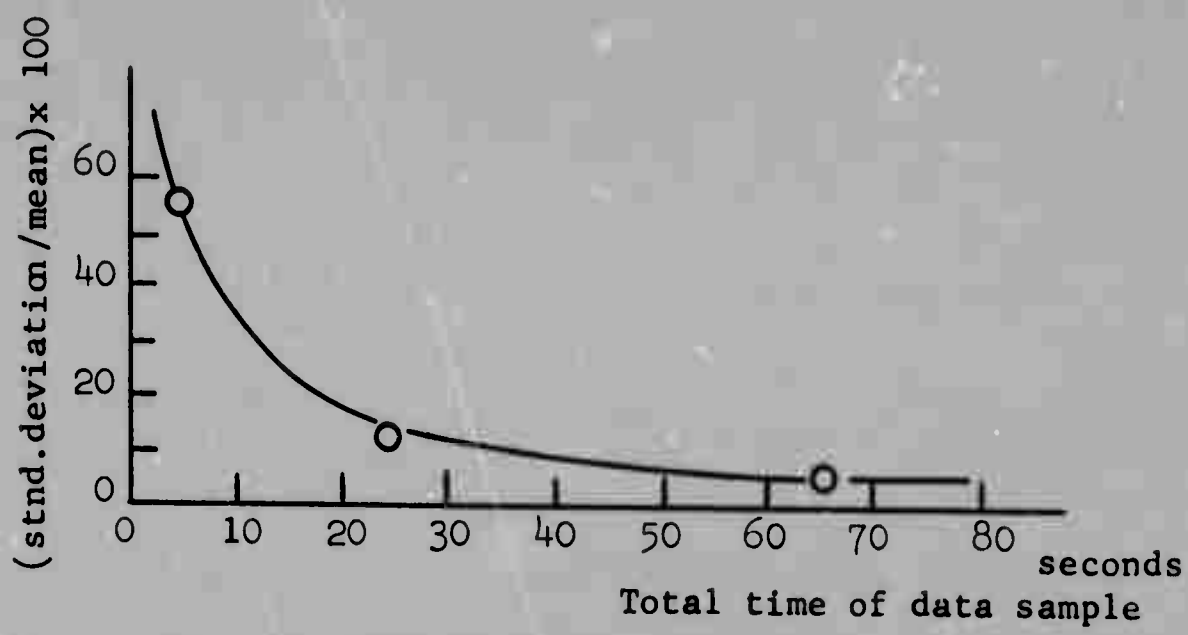

Fig. 3.41a Standard deviation of spatial distribution of low-fluid-velocity streaks versus sample time.

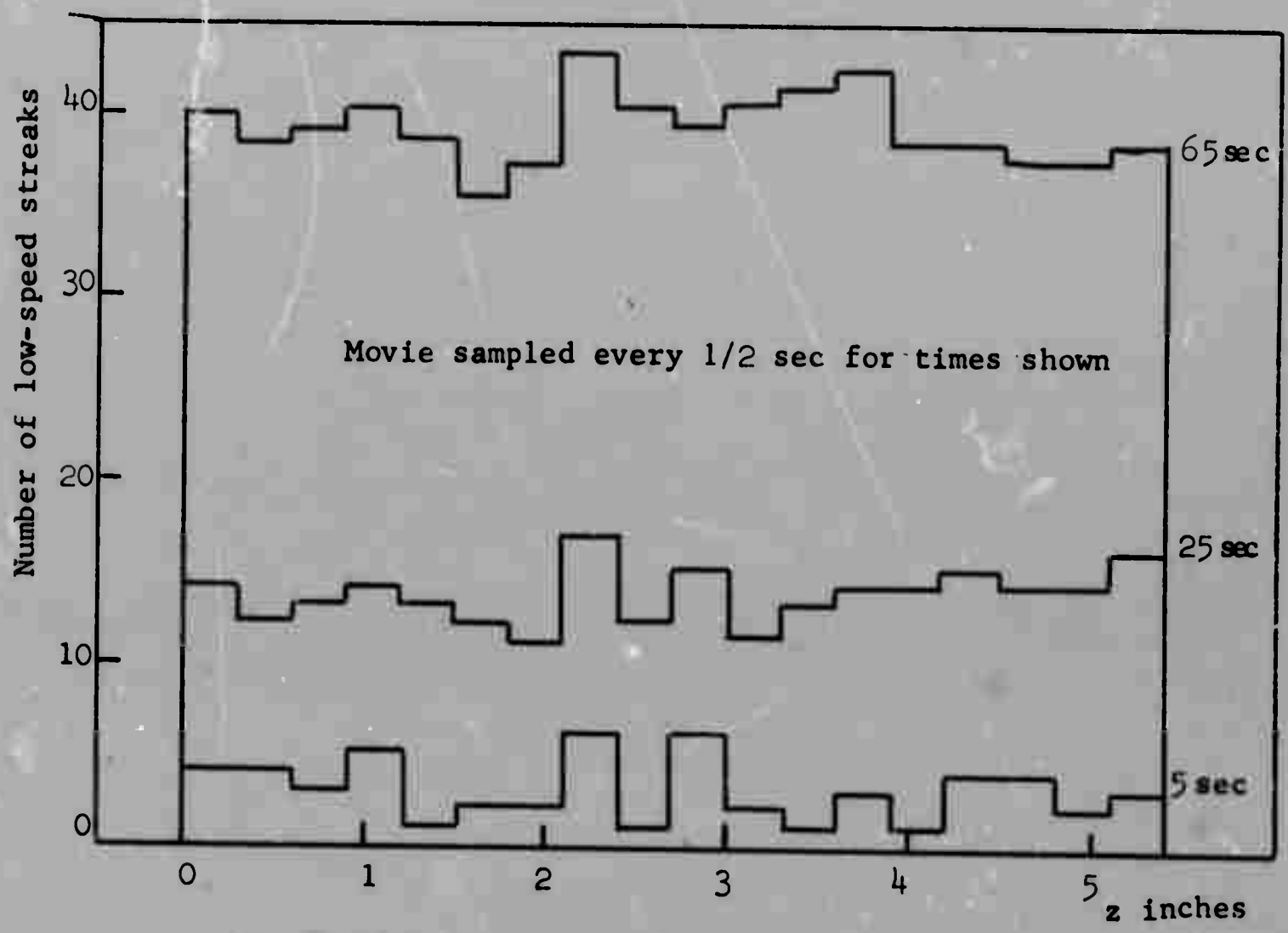

Fig. 3.41b Histogram of spatial distribution of low-speed streaks - zero pressure gradient u_∞ = 0.5 ft/sec

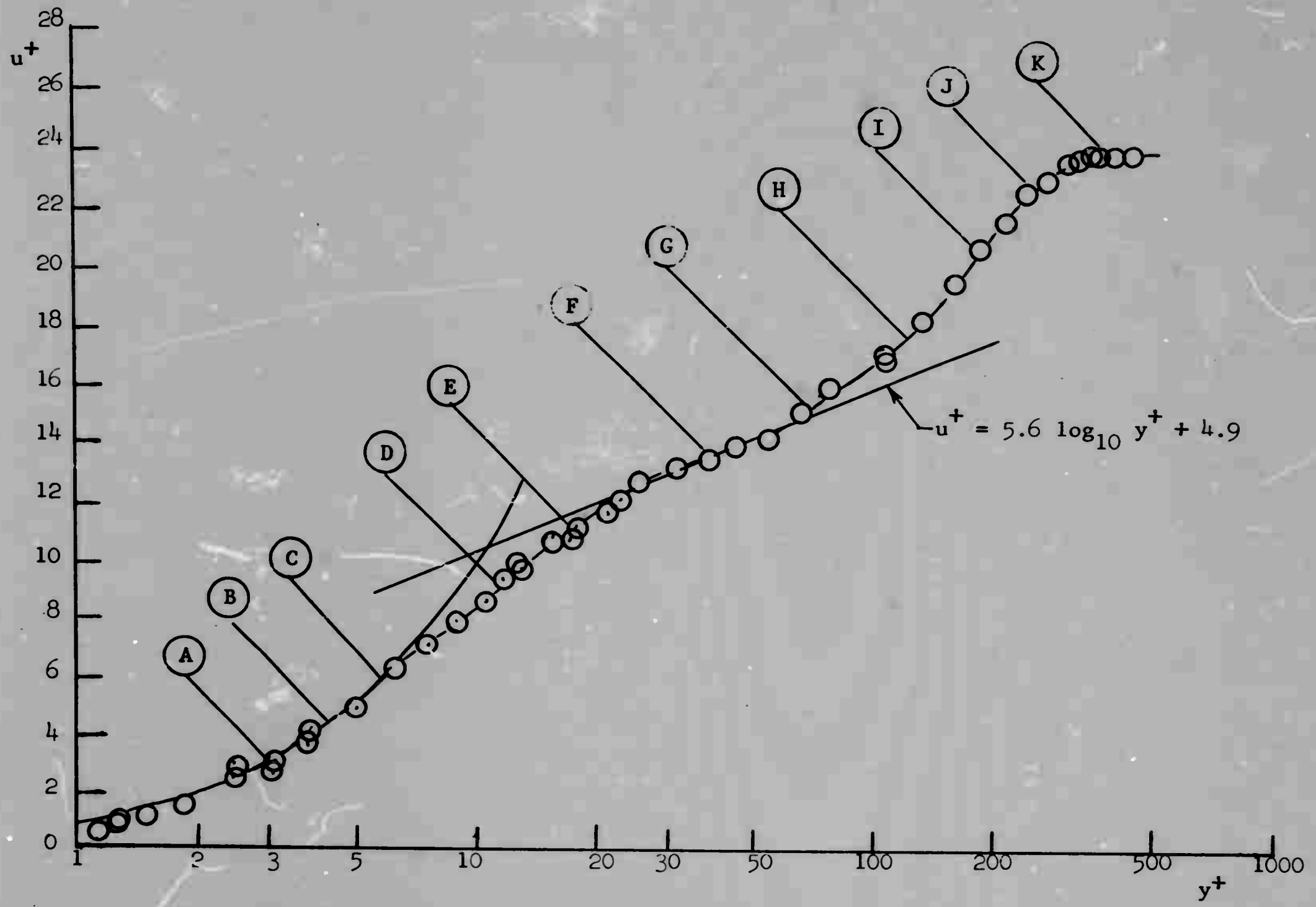

Fig. 3.42 Pictorial structure survey; str + dp/dx, x-station 10.2; relation of pictures to velocity profile.

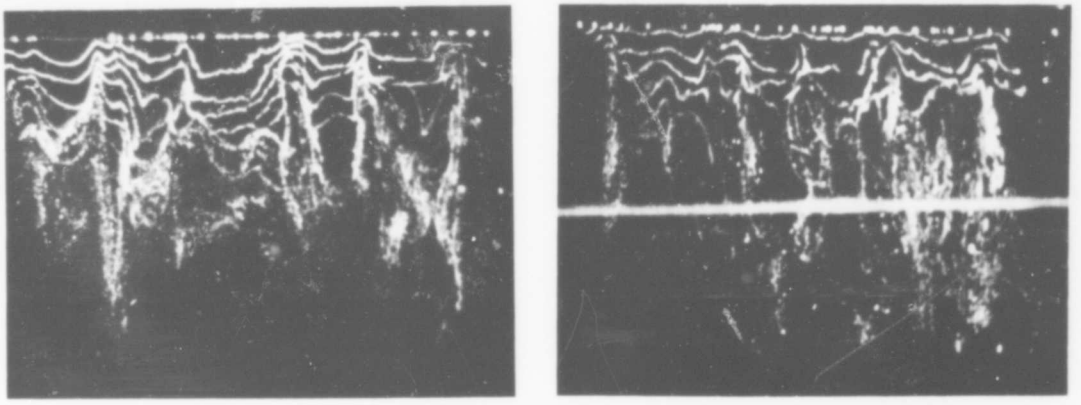

A B

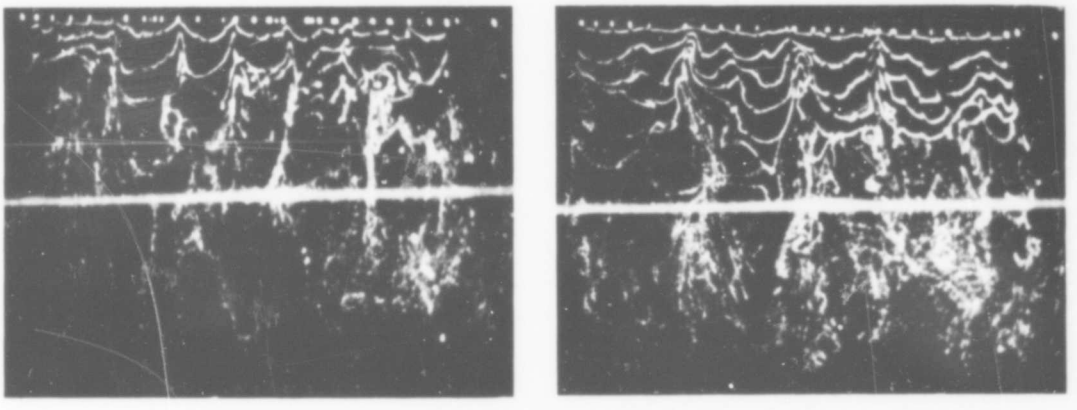

C D

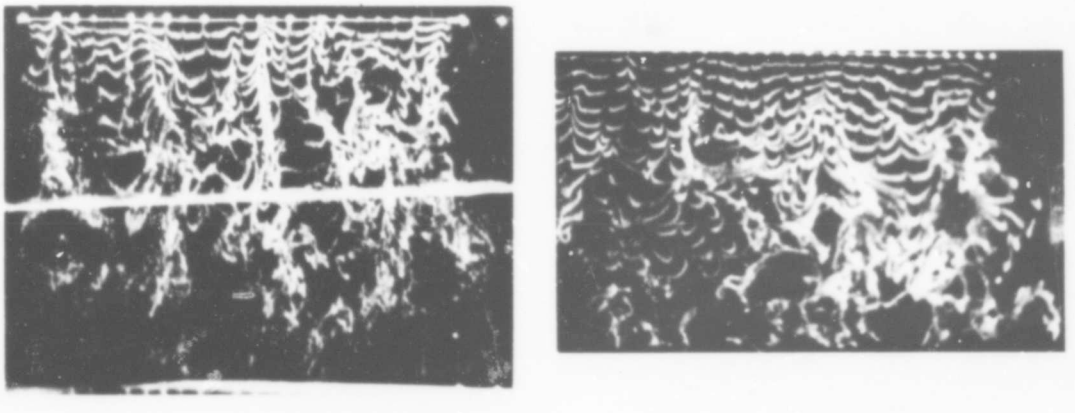

E F

Fig. 3.42 Pictorial structure survey: str + dp/dx, x-station 10. (continued).

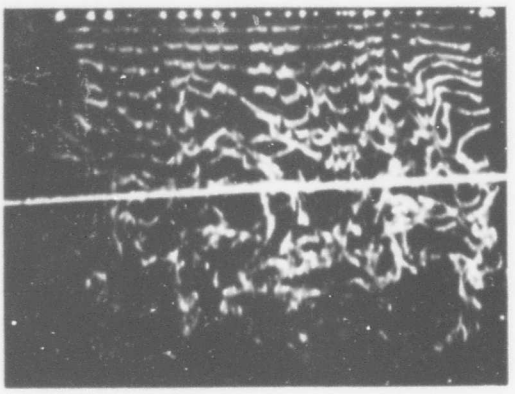

G

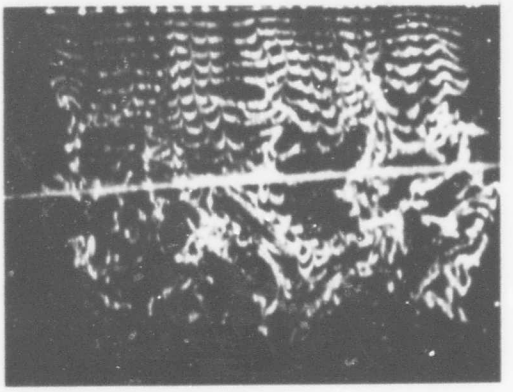

H

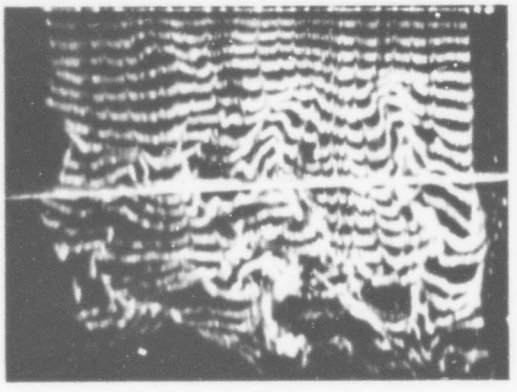

I

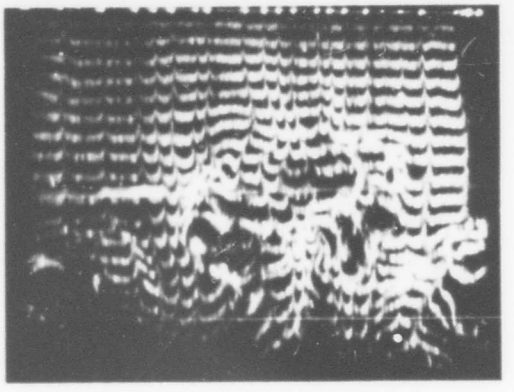

J

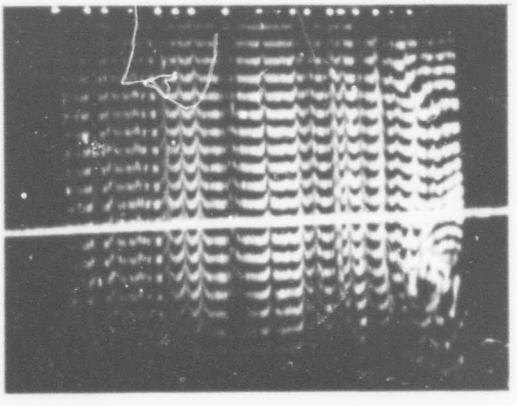

K

Fig. 3.42 Pictorial structure survey: str + dp/dx, x-station 10. (concluded).

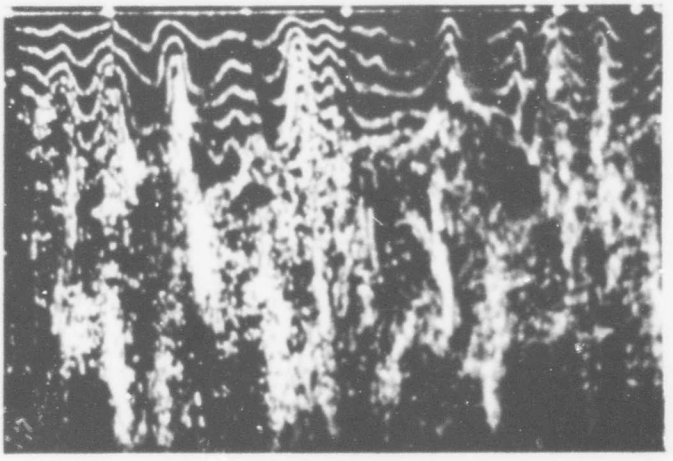

$\frac{dp}{dx} = 0$

$y^+ = 6$

$K = 0$

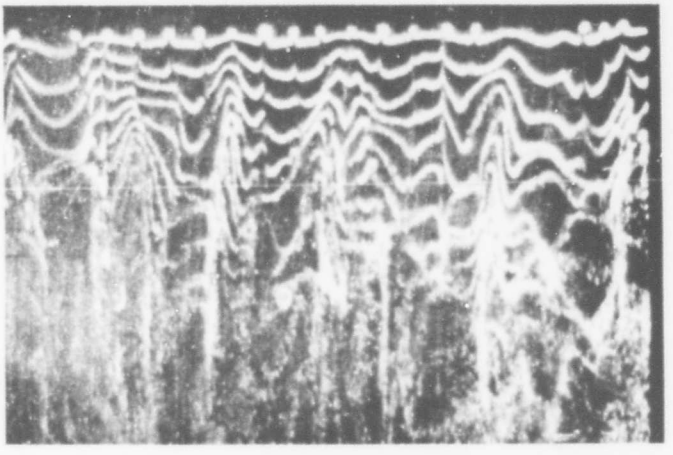

$\frac{dp}{dx} < 0$

$y^+ = 6.5$

$K = 0.79$

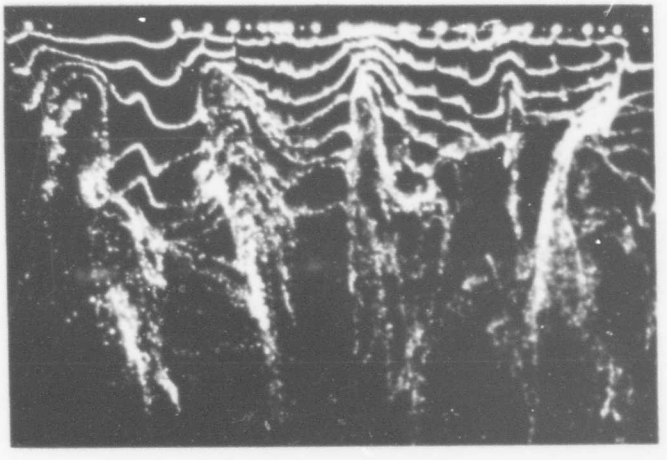

$\frac{dp}{dx} > 0$

$y^+ = 6.1$

$K = -1.05$

Fig. 3.43 Comparison of structure in wall layers for zero, positive, and negative pressure gradient flows. Field of view is 5" x 4", flow is top to bottom.

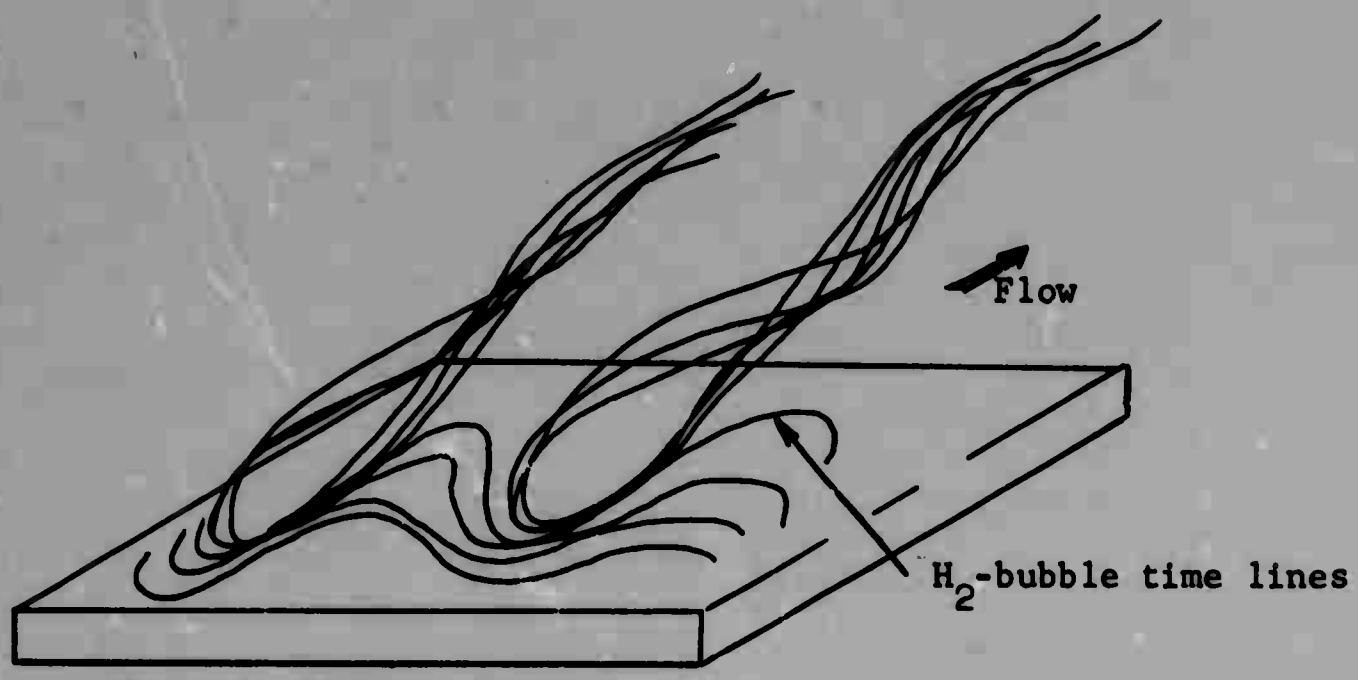

Typical oblique view

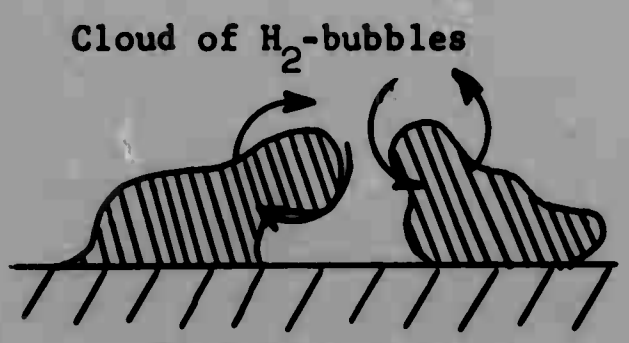

Typical end views
Horizontal bubble wire
Flow out of paper

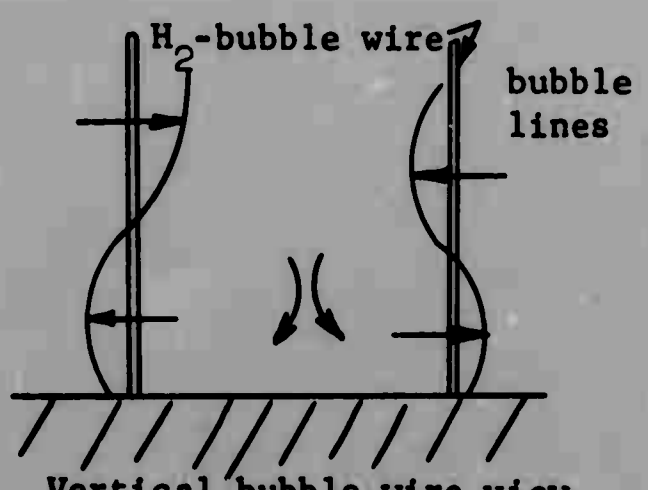

Vertical bubble wire view
Flow out of paper

Fig. 3.44 Sketches of ejection process as illuminated with various H_2-bubble techniques.

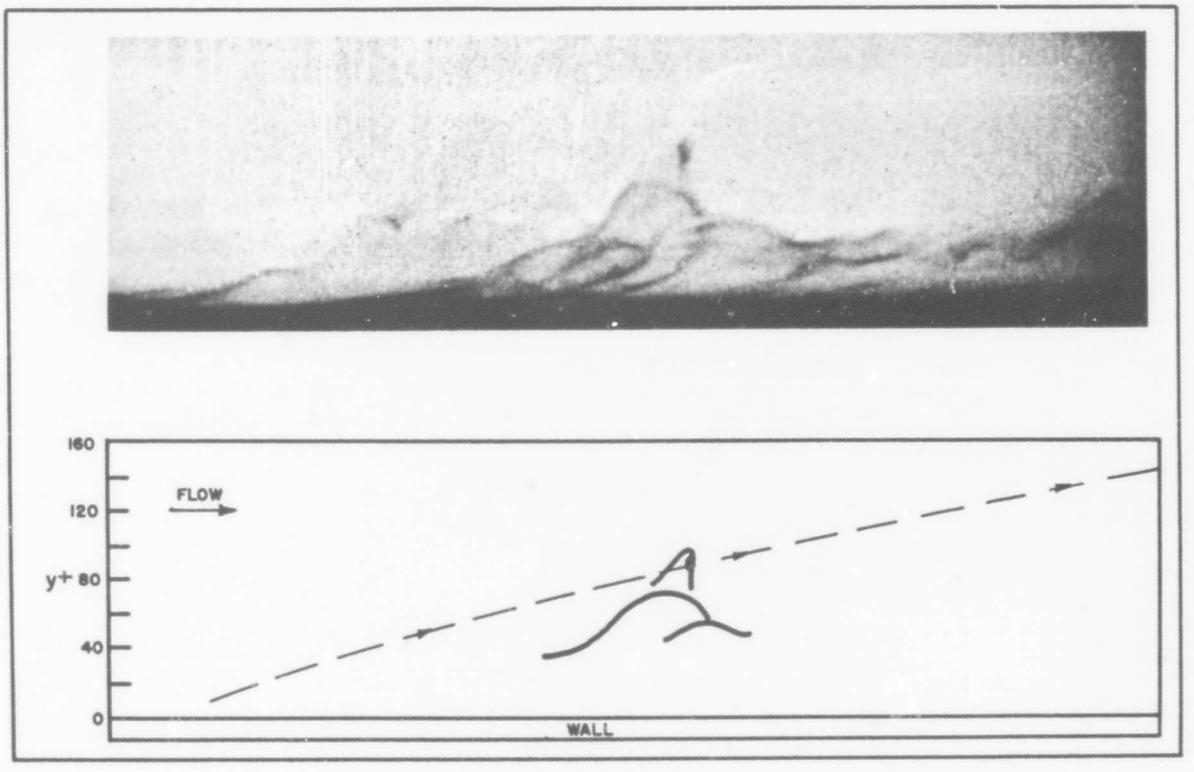

Fig. 3.45 Side view photograph of dye streaks ejected away from the wall layer flow. u_∞ = 0.291 ft/sec., y^+ scale shown on figure. dp/dx = 0 ; Runstadler [1963].

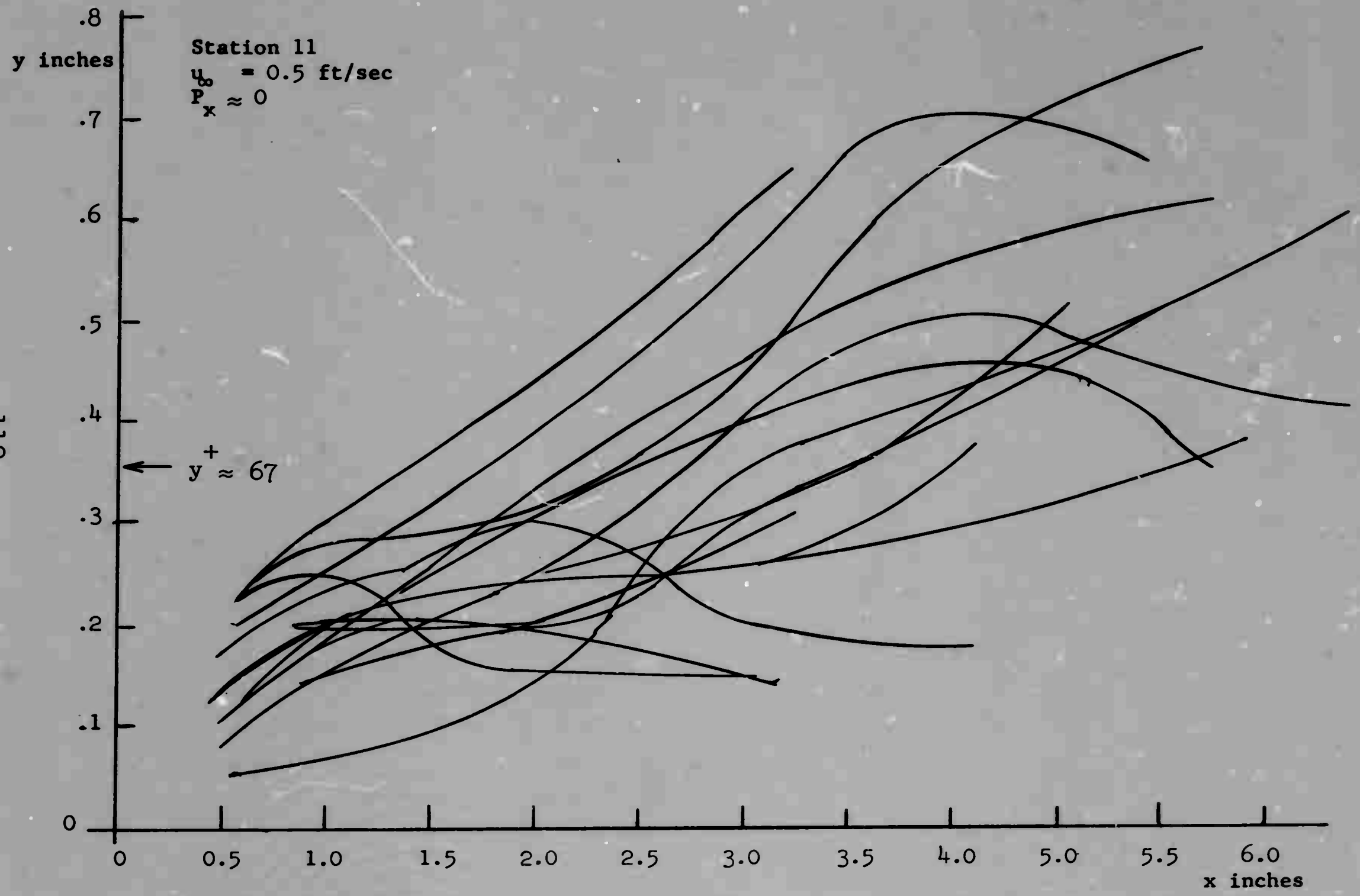

Fig. 3.46 Sample trajectory paths, illustrating wide variation of trajectories.

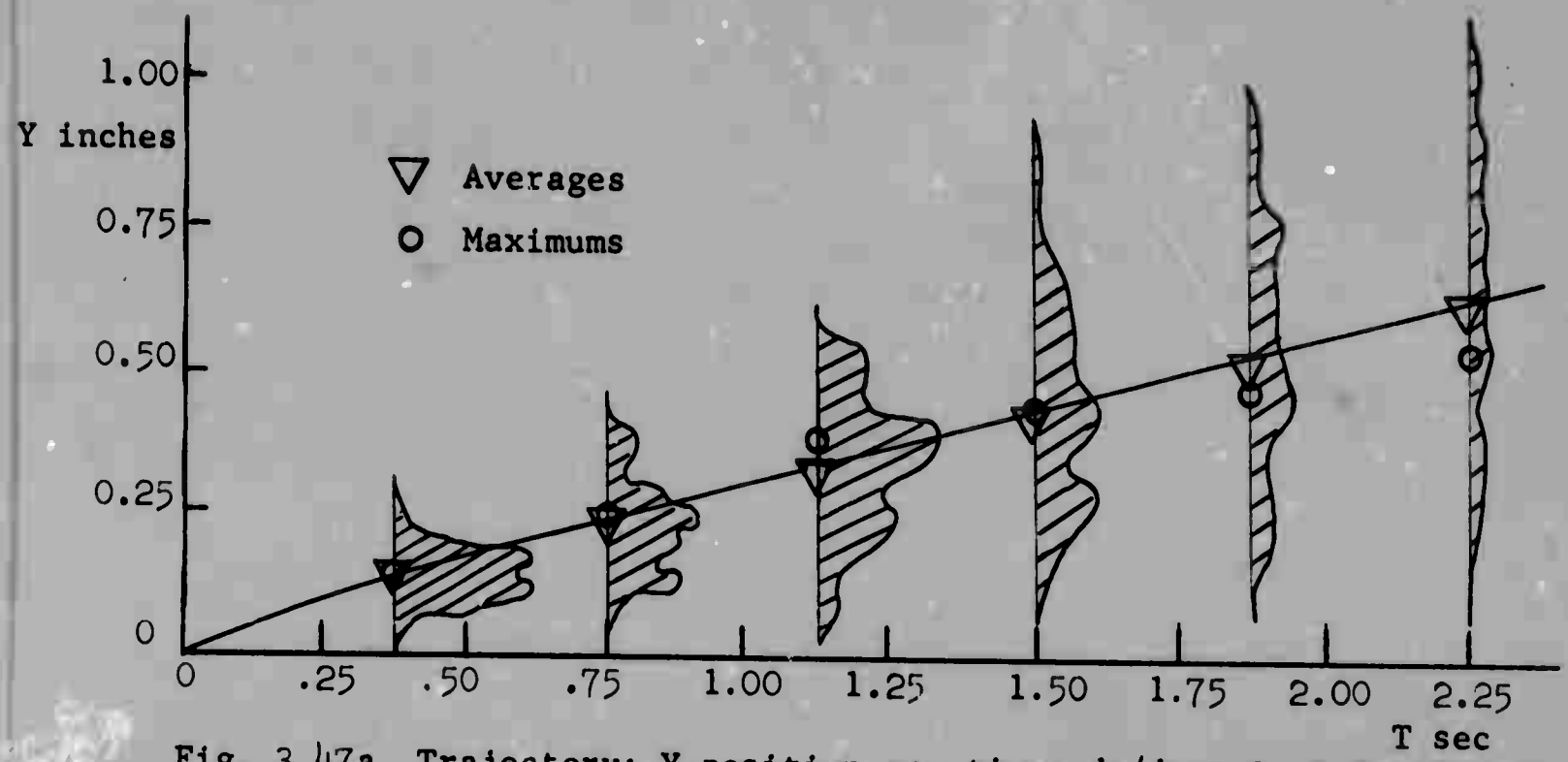

Fig. 3.47a Trajectory: Y-position vs. time; dp/dx = 0, X-Station 10.

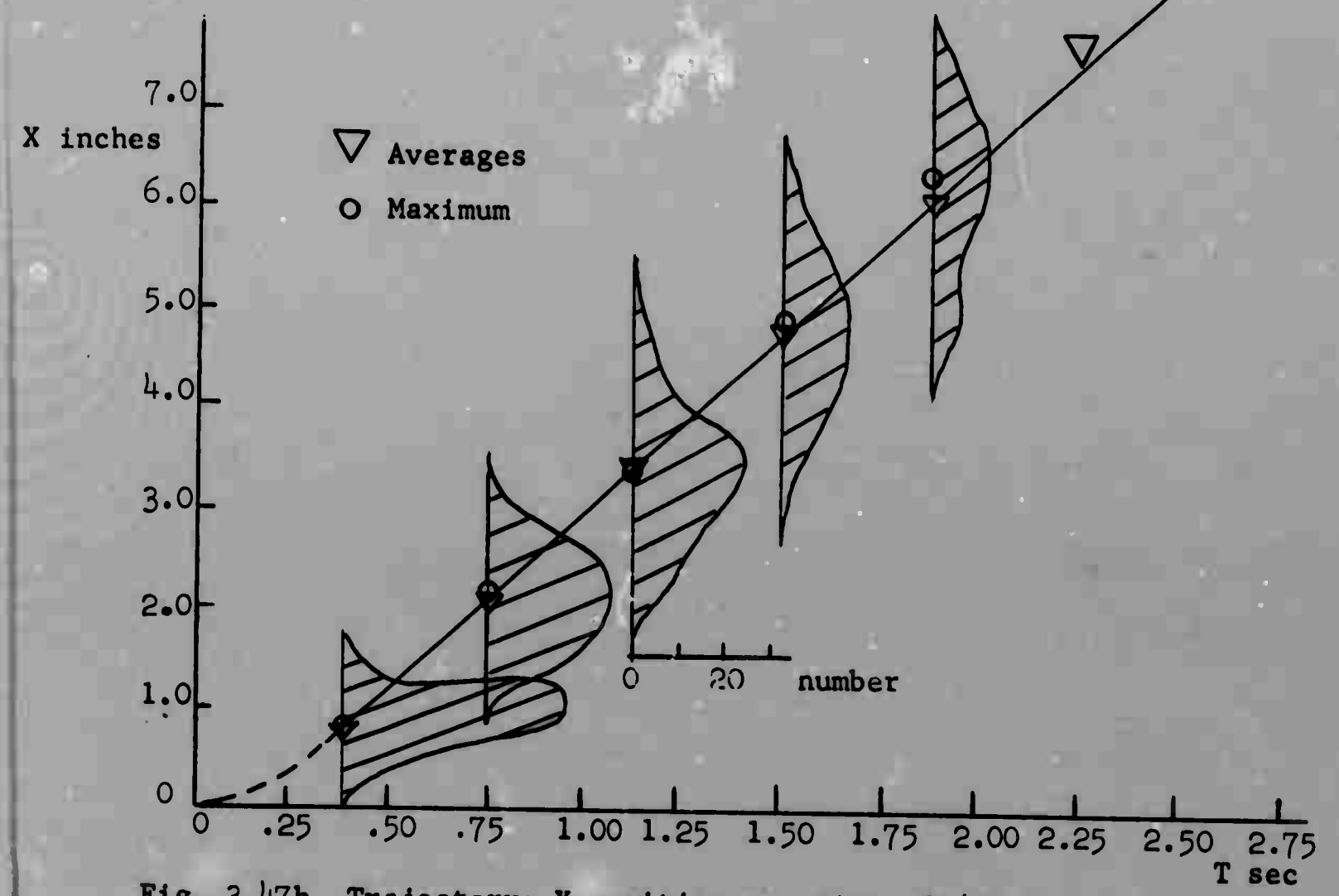

Fig. 3.47b Trajectory: X-position vs. time; dp/dx = 0, X-Station 10.

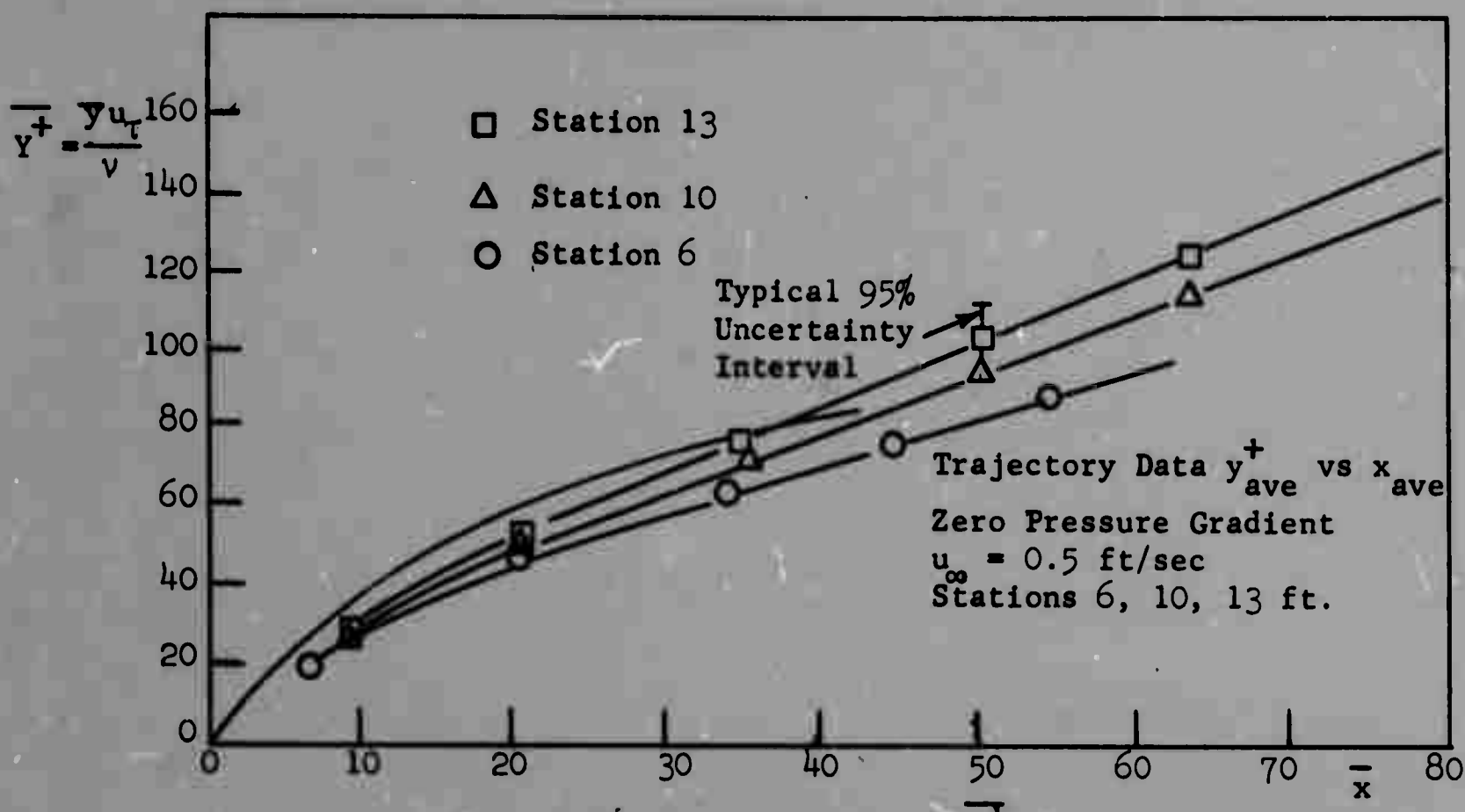

Fig. 3.48 Trajectory path $\overline{Y}^+$ vs. $\overline{x}$

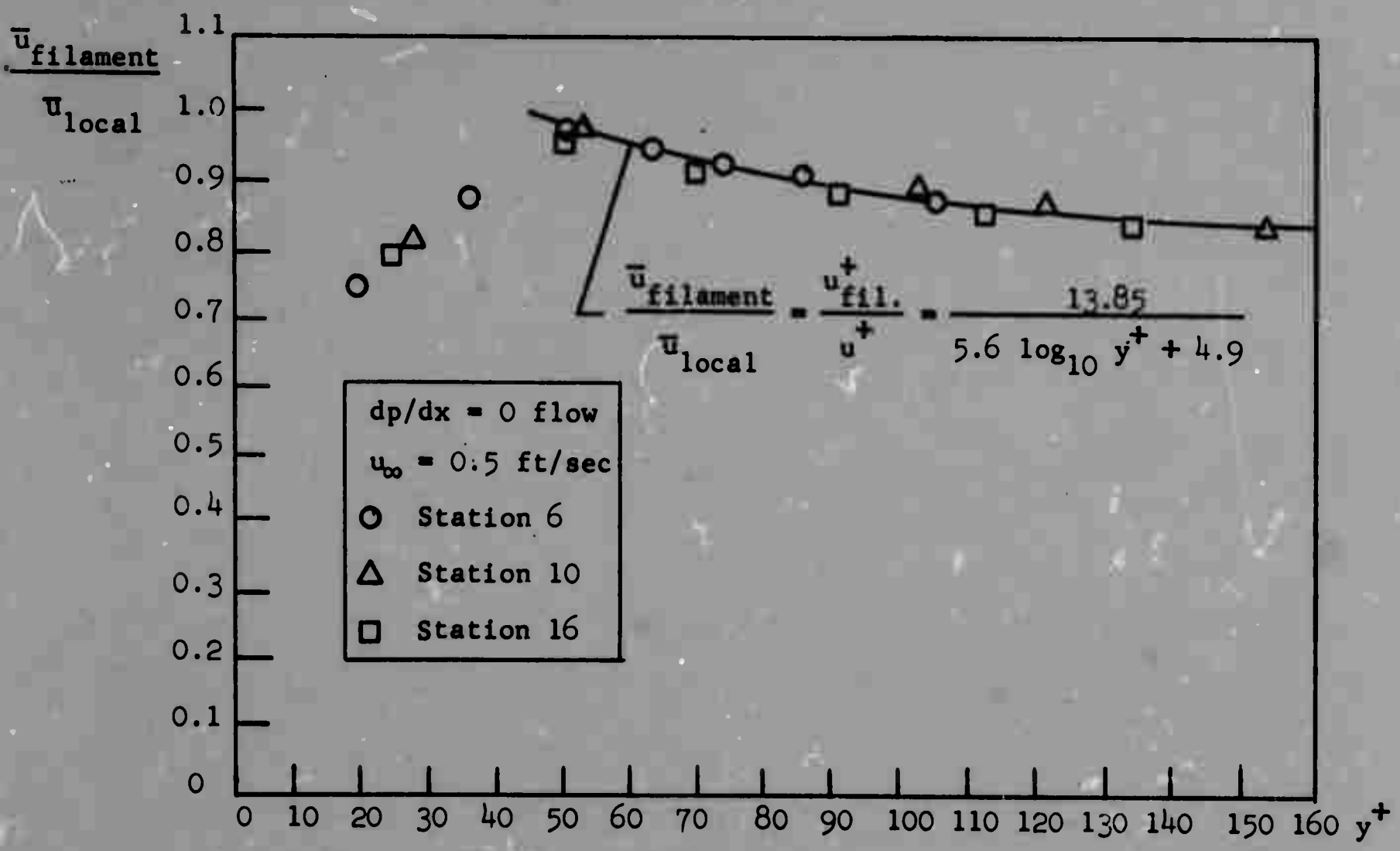

Fig. 3.49 Average ejected filament x-component of velocity vs y^+ .

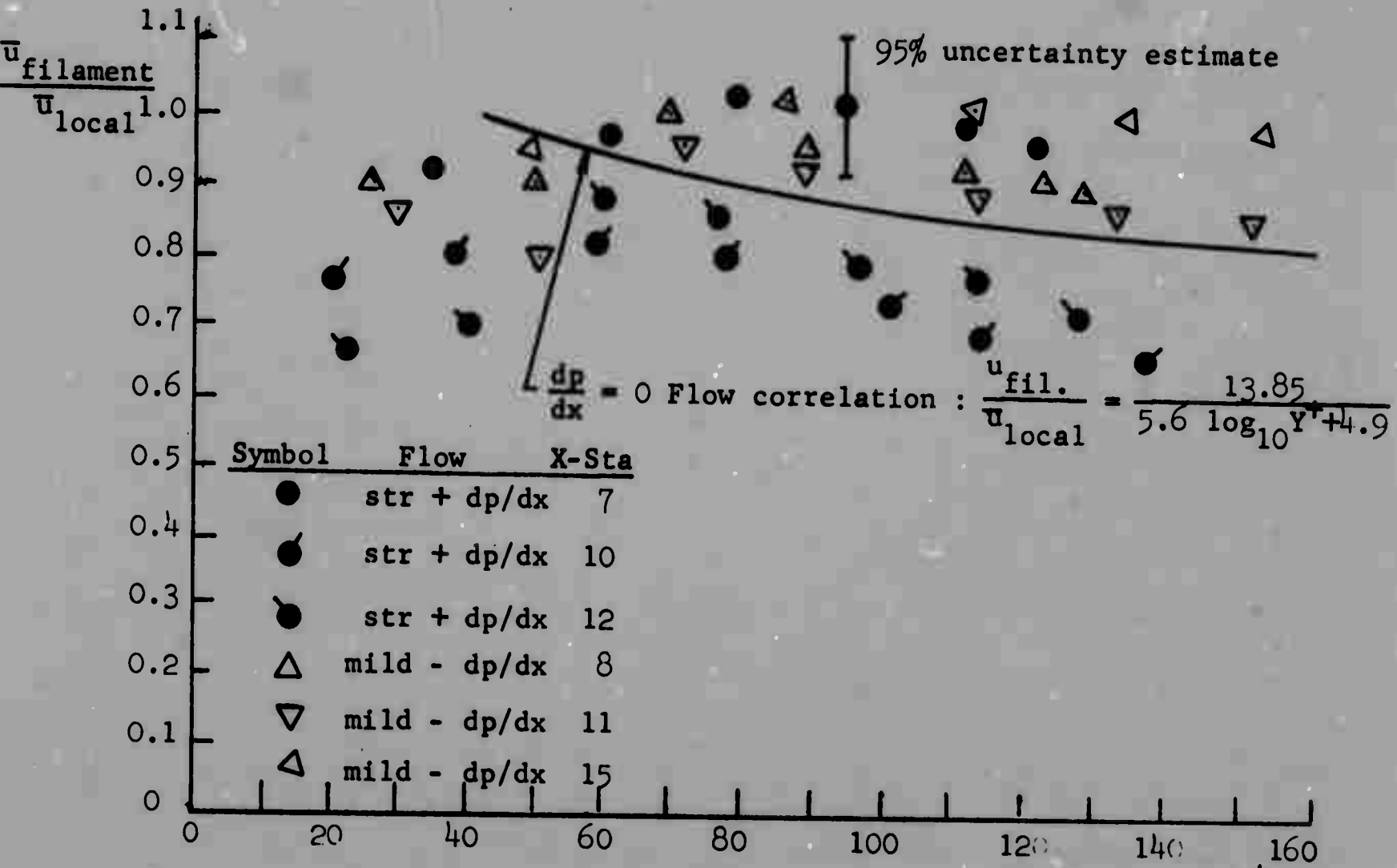

Fig. 3.51 Ejected filament average x-component of velocity vs. Y^+ pressure gradient flows.

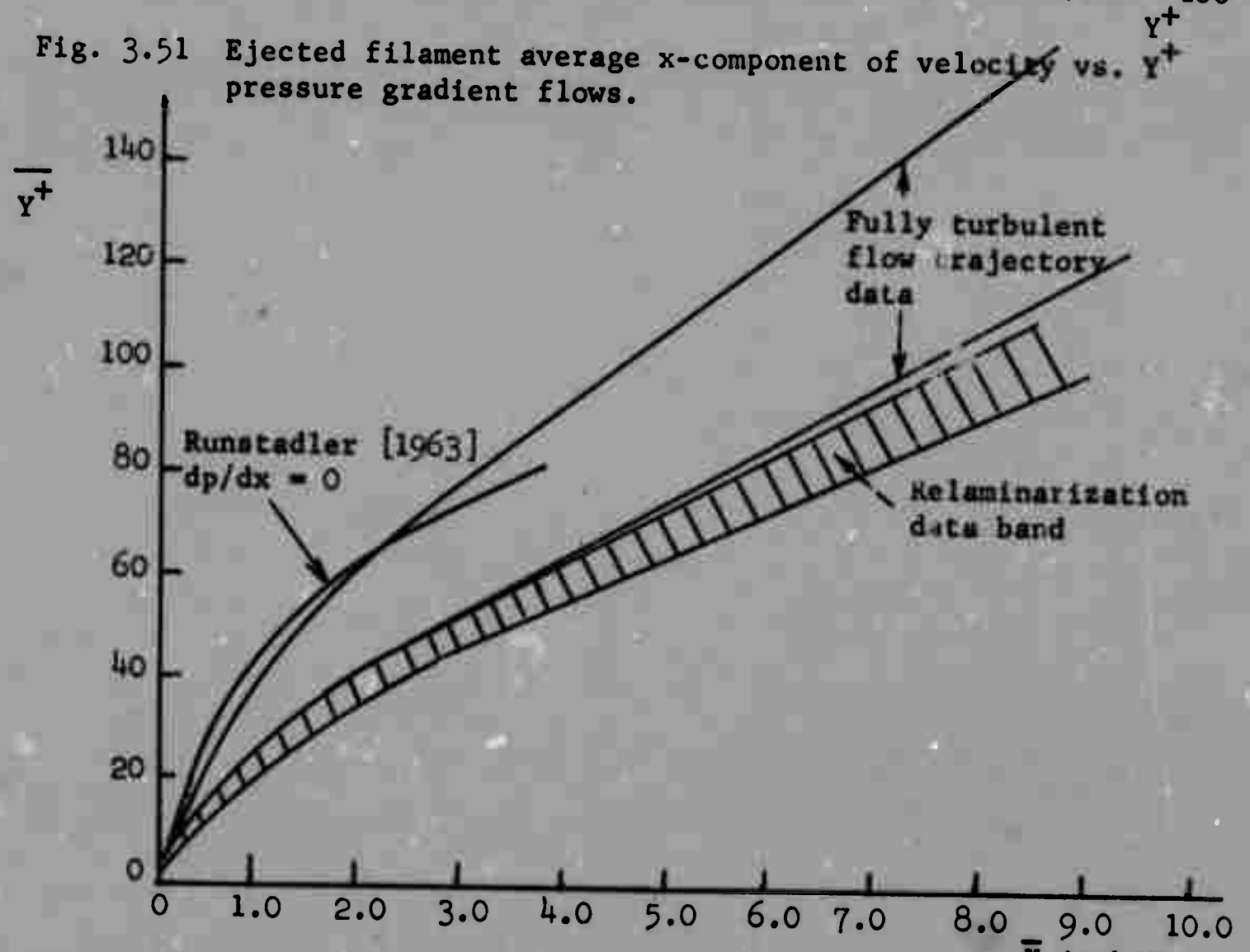

Fig. 3.50 Trajectory data Y^+ vs. X for pressure gradient flows.

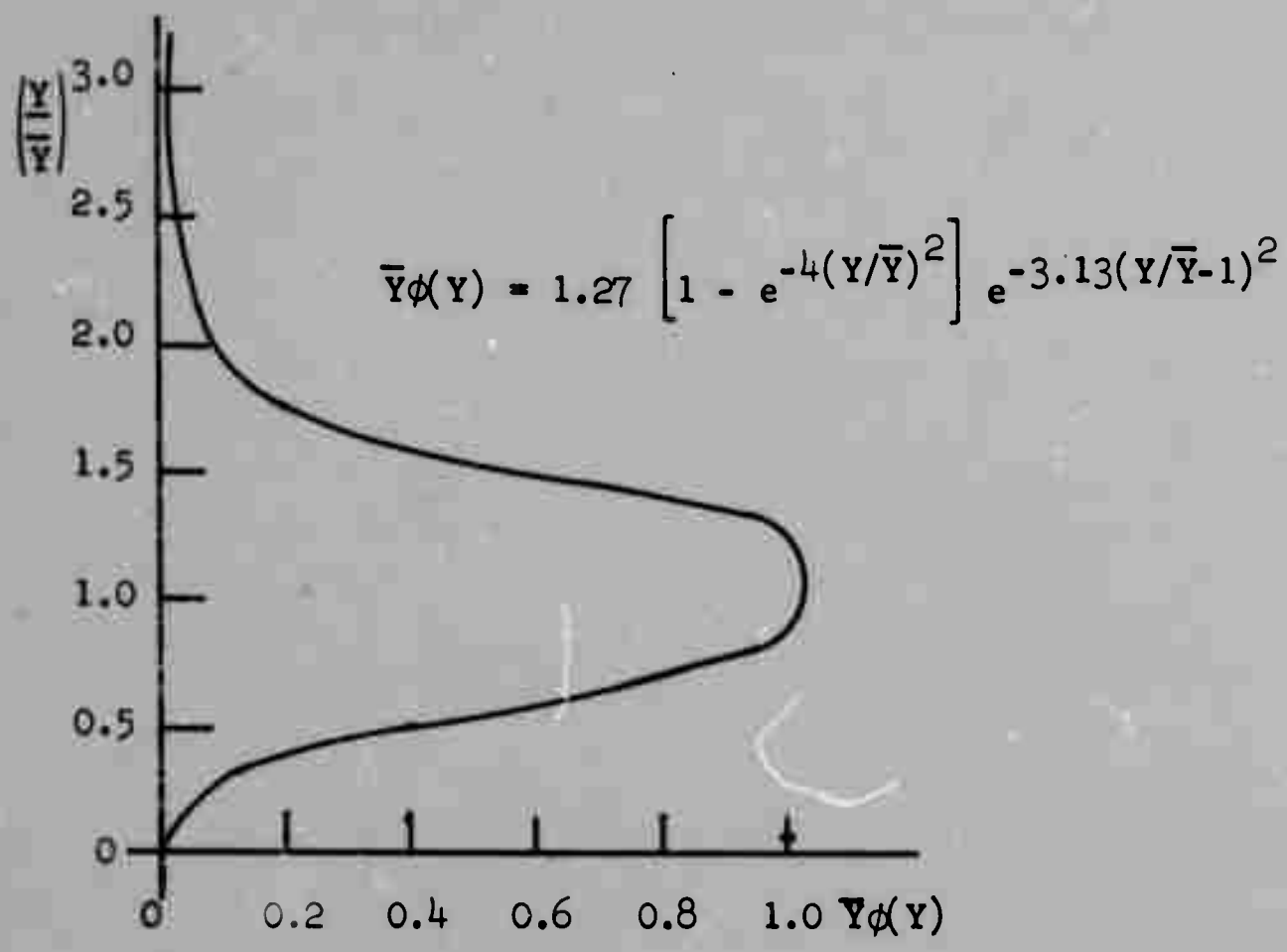

Fig. 3.52a Trajectory distribution model.

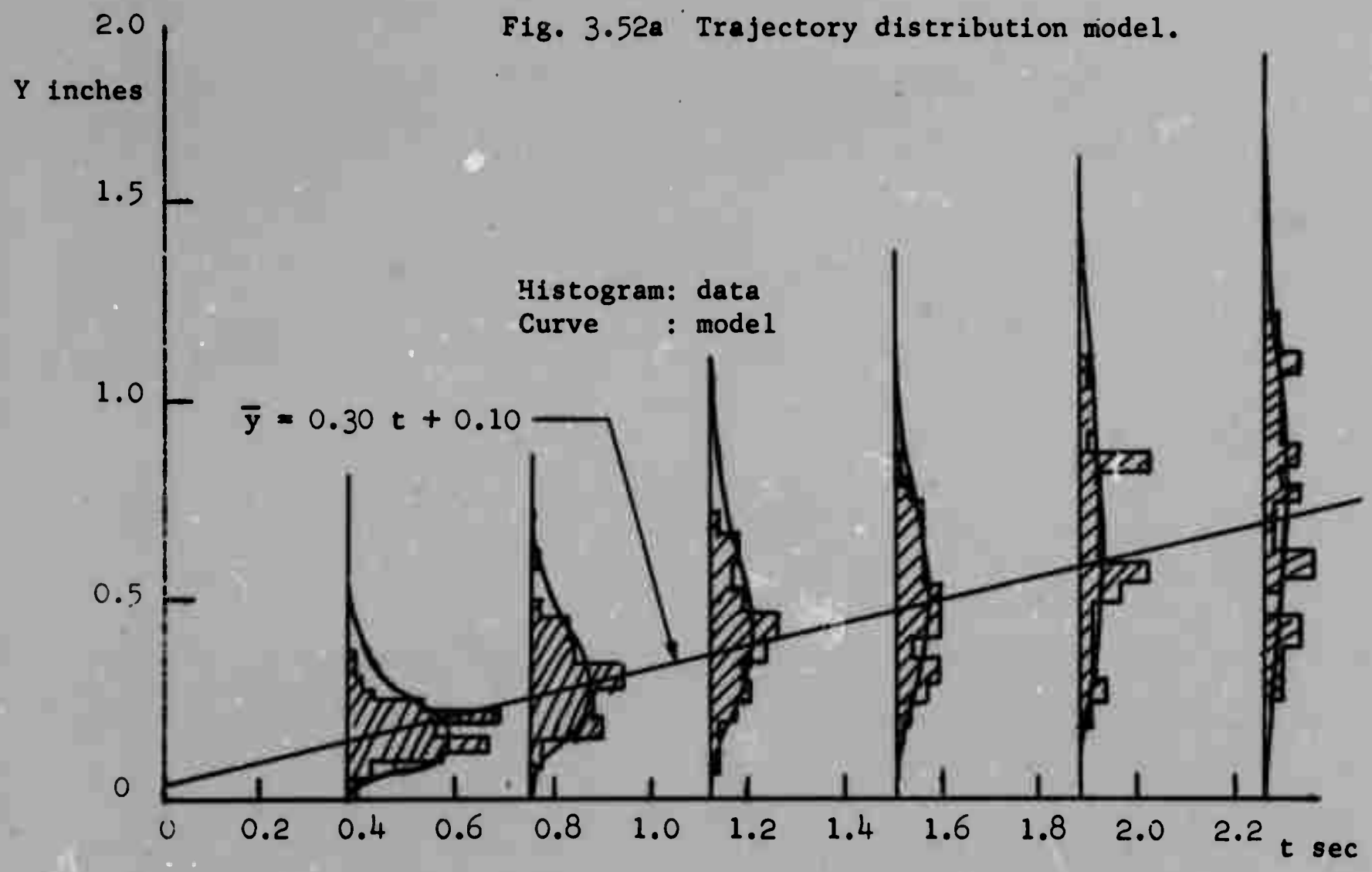

Fig. 3.52b Trajectory distribution: comparison of data to model dp/dx = 0 flow, x-station 10.1 ft.

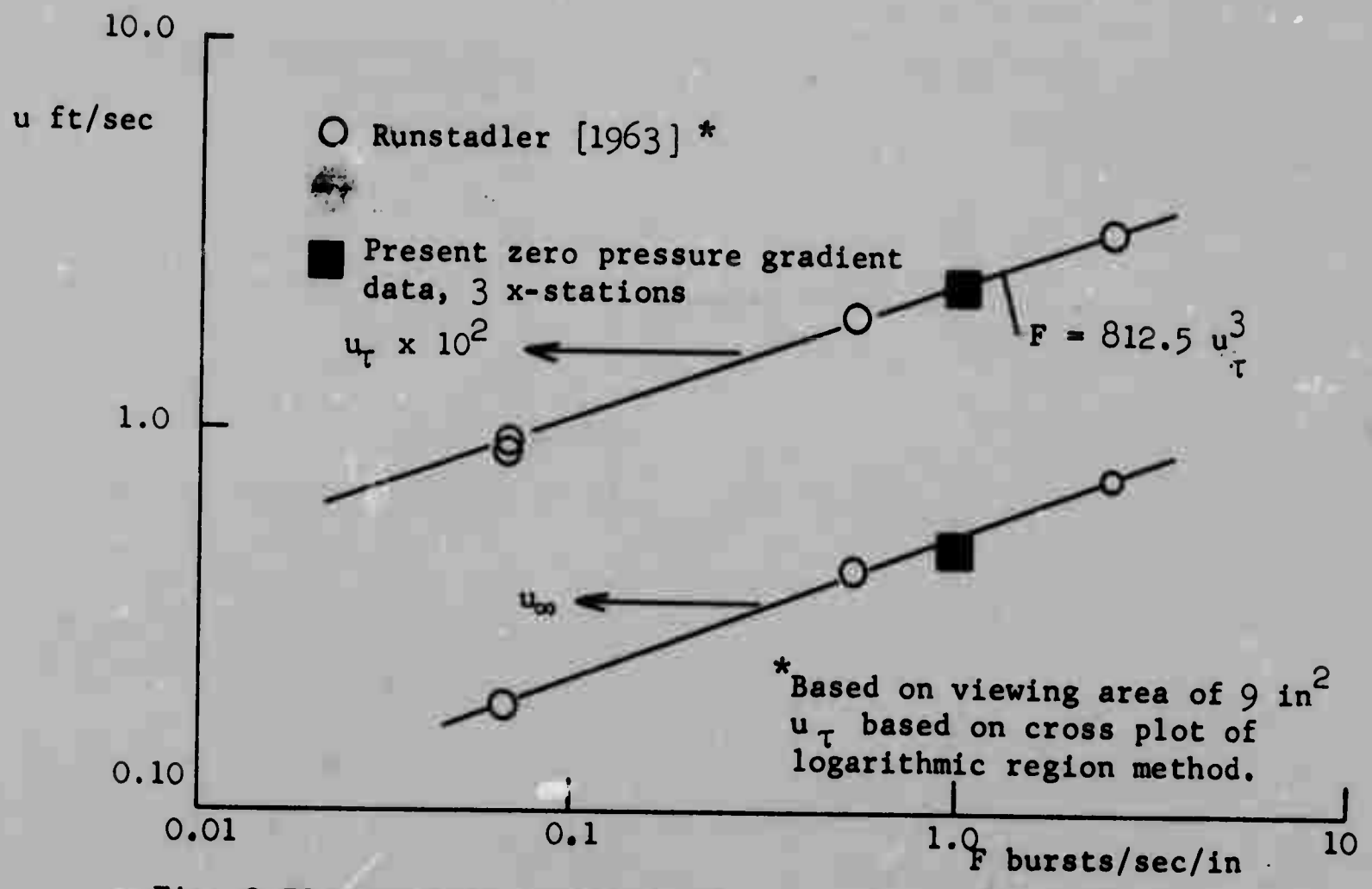

Fig. 3.53 Burst rate data for zero pressure gradient flow: F vs. u_∞ , F vs. u_τ

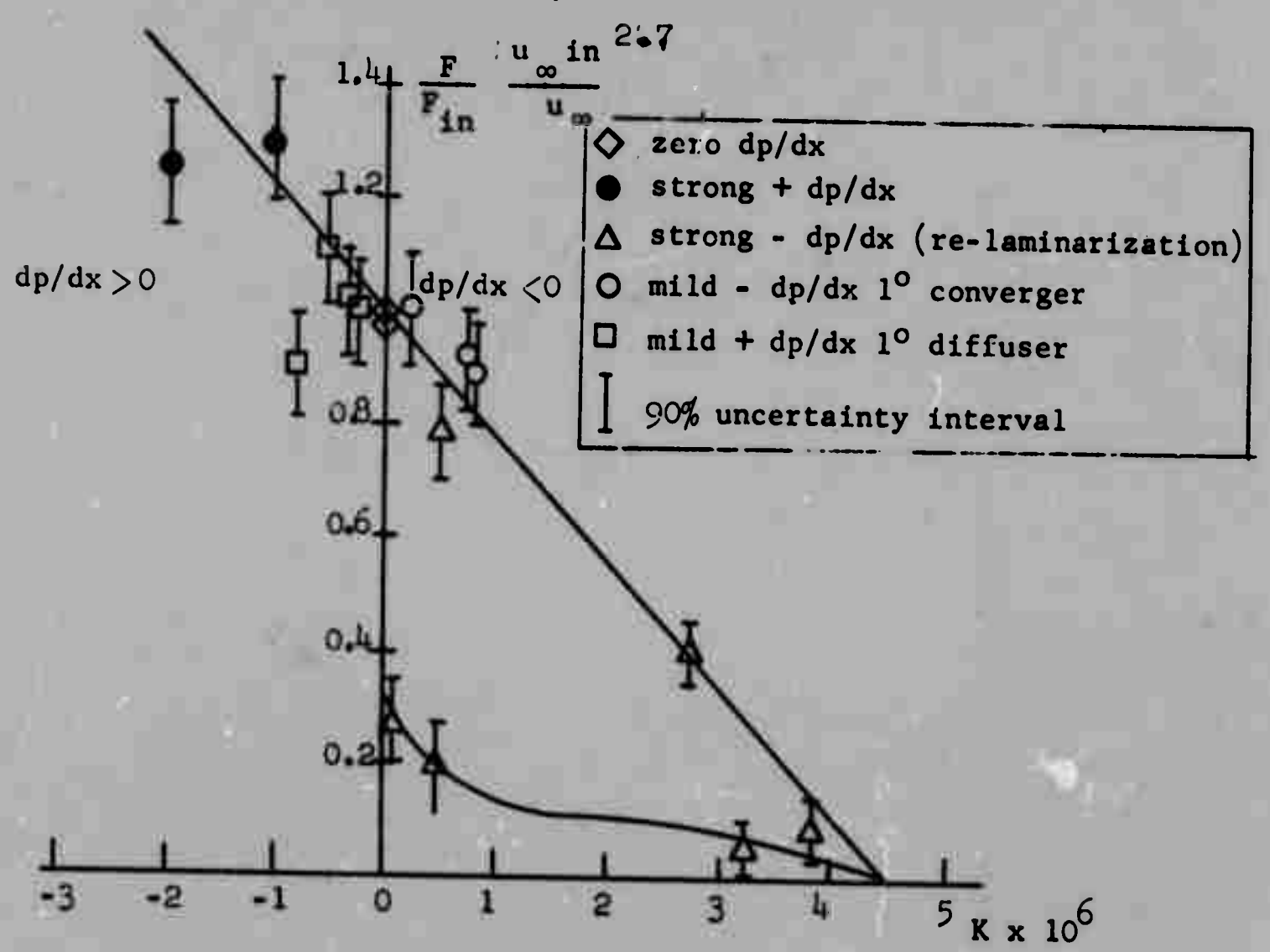

Fig. 3.54 Effect of pressure gradient on burst frequency from wall layer.

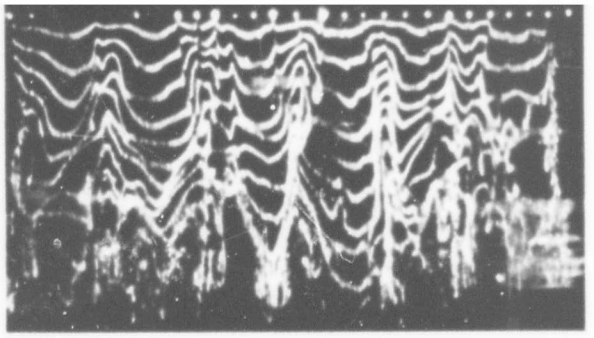

A

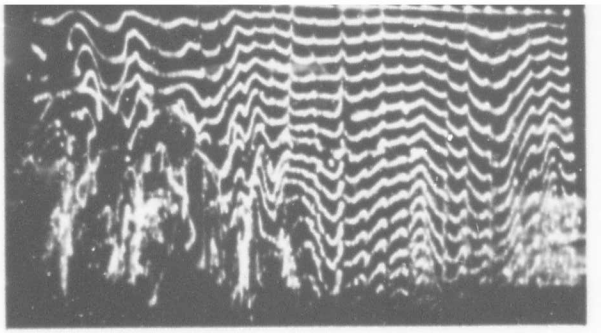

B

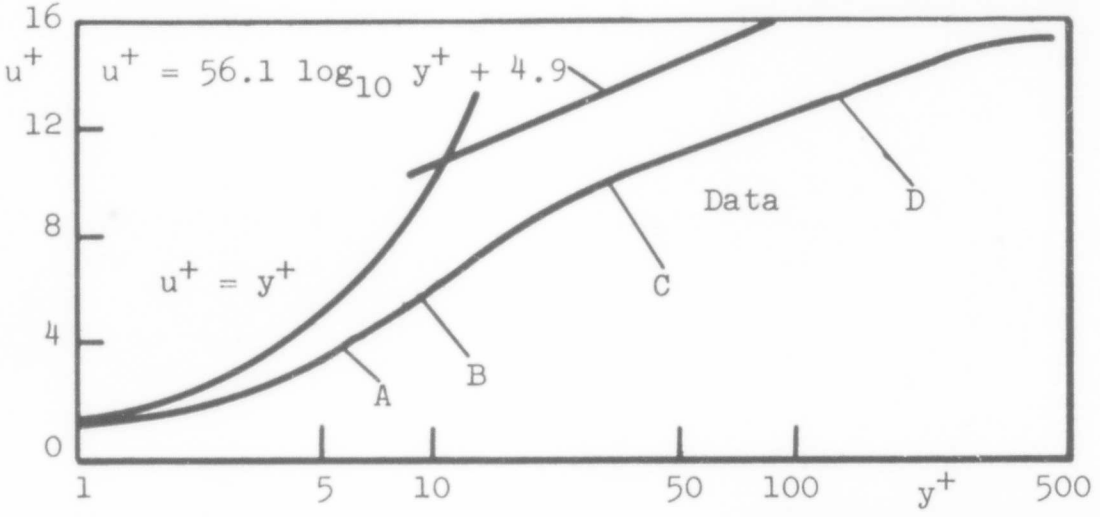

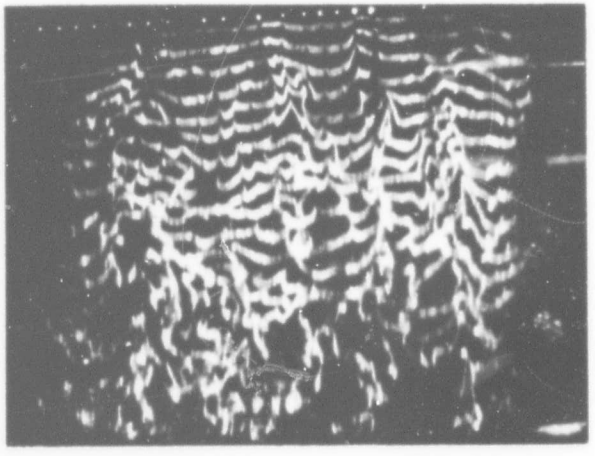

C

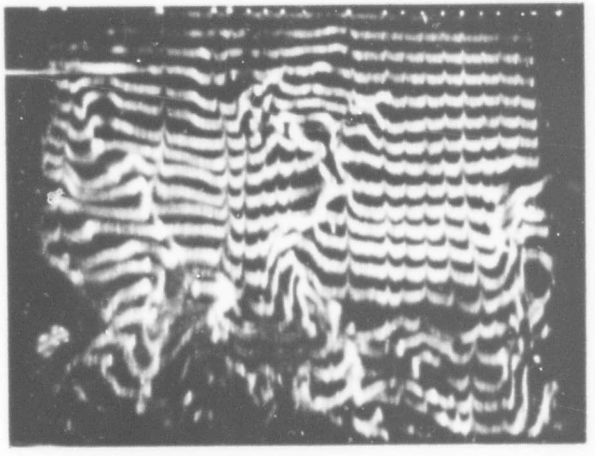

D

Fig. 3.55 Pictorial survey of laminarescent flow layer:
str - dp/dx flow, x-station 10.25; flow is top to bottom.

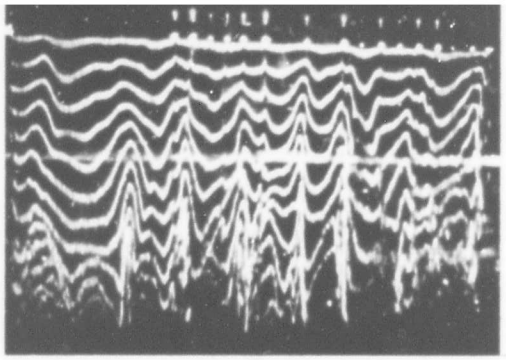

A

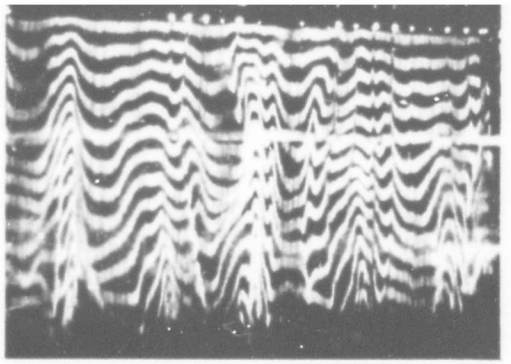

B

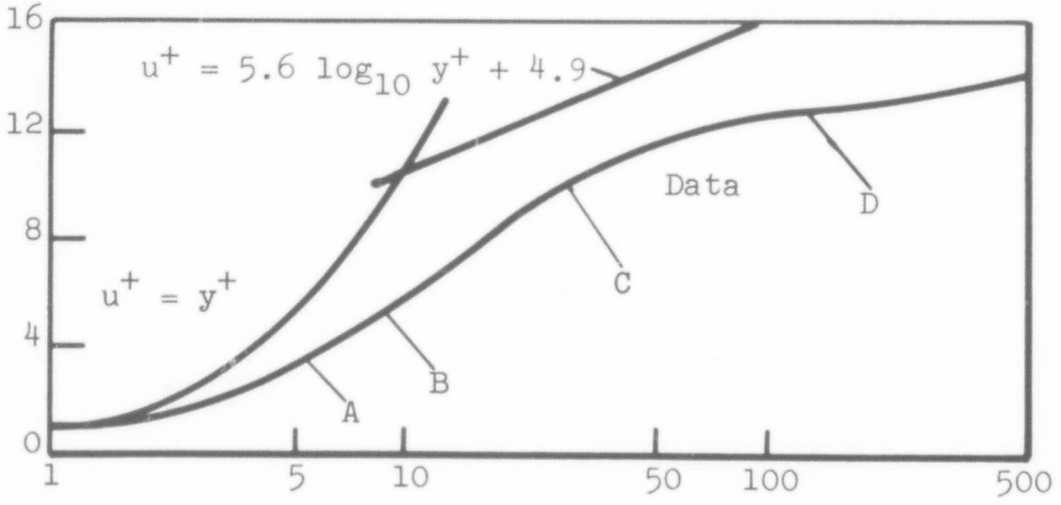

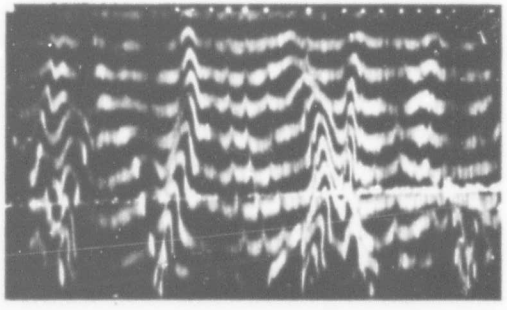

C

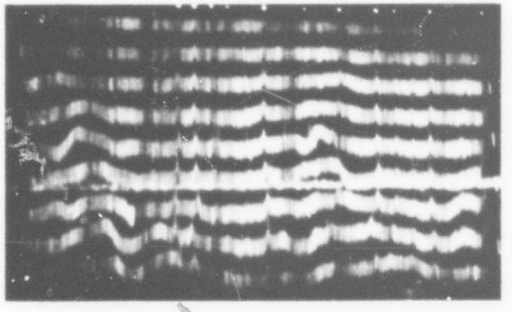

D

Fig. 3.56 Pictorial survey of laminarescent flow layer:
str - dp/dx flow, x-station 12.2; flow is top to bottom.

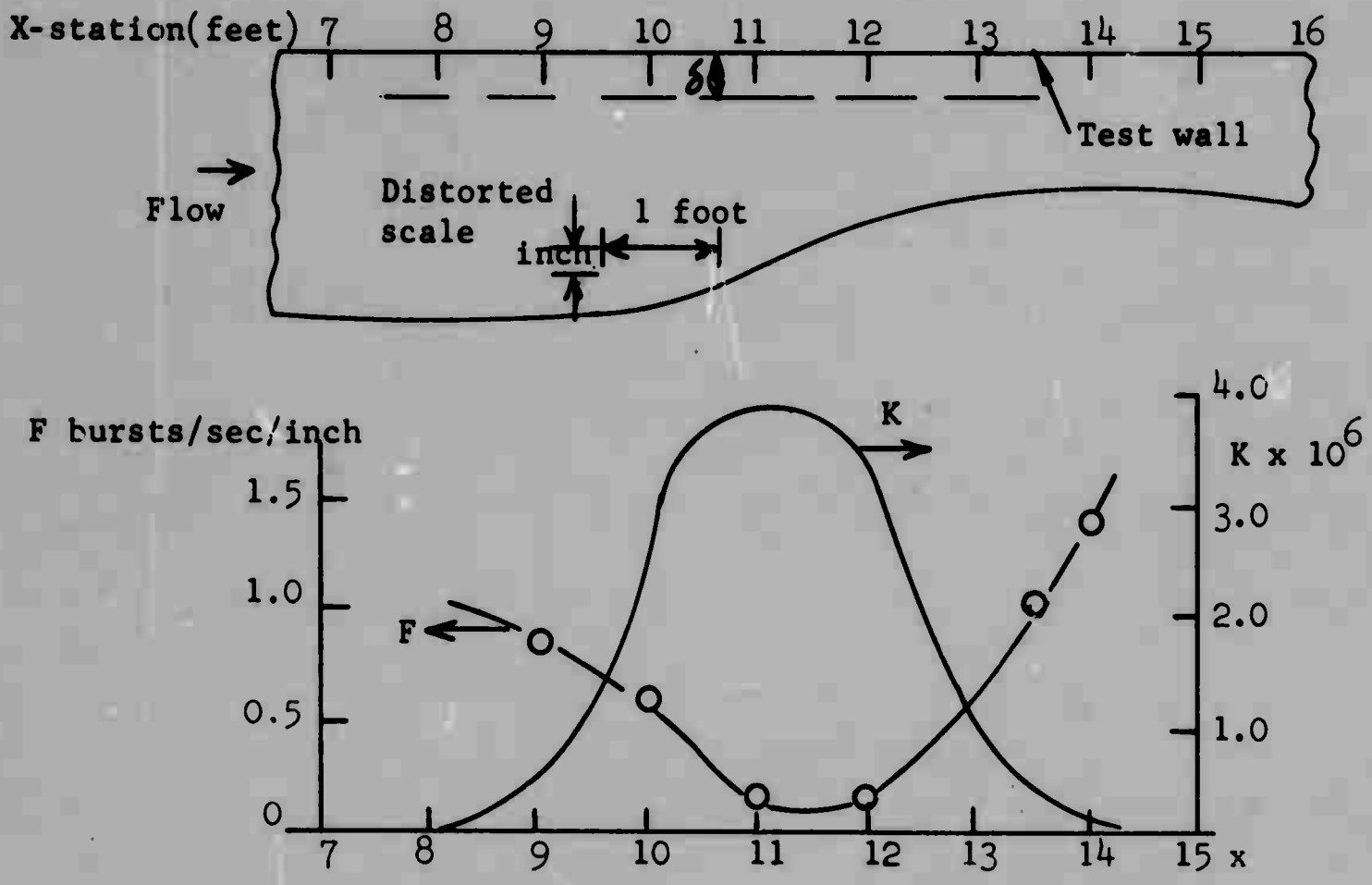

Fig. 3.57 Burst rate and K as functions of x ; relaminarization flow.

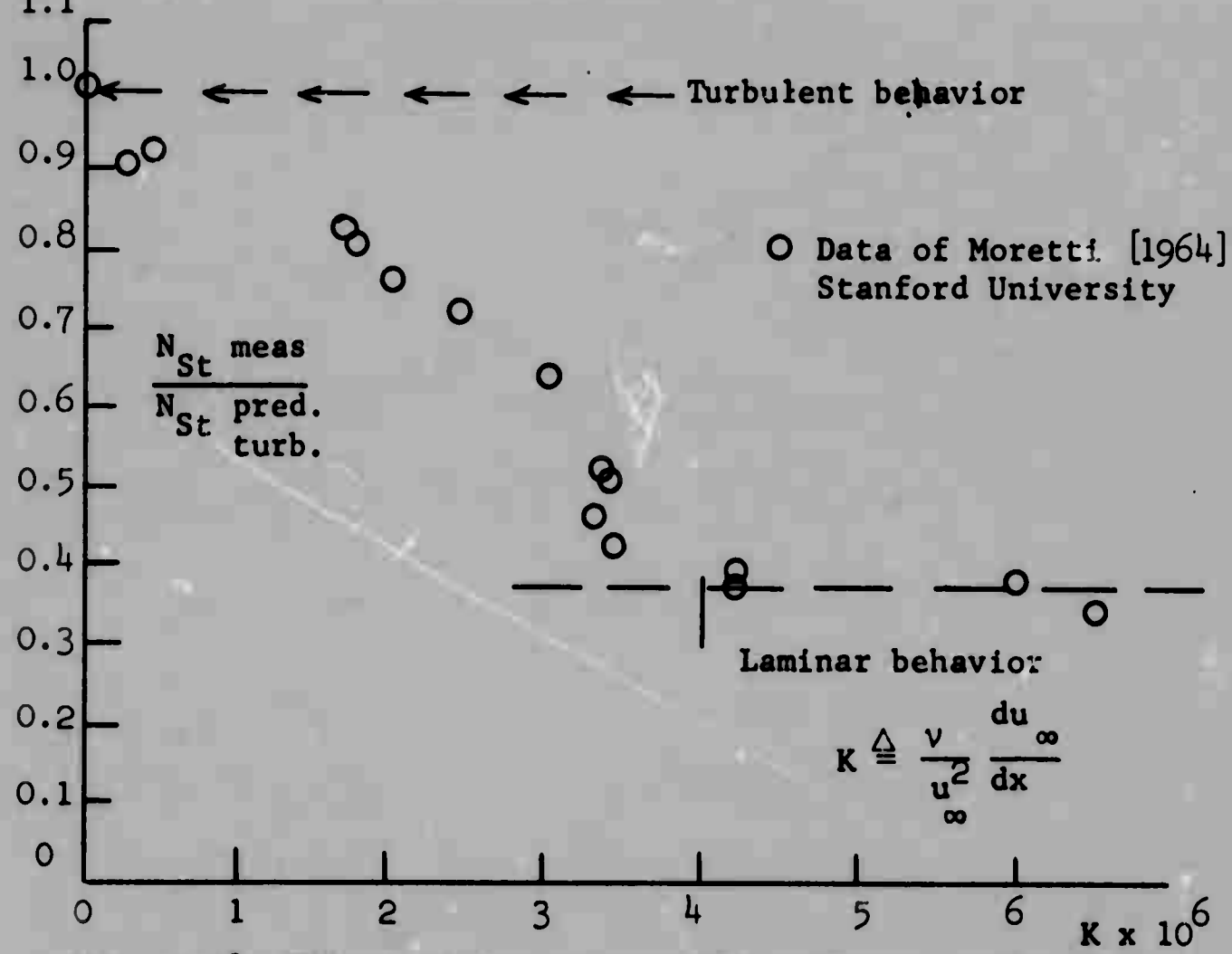

Fig. 3.58 Effect of severe negative pressure gradients on turbulent heat transfer.

Table 3.1 Summary of Parameters which Describe Experimental Flow Conditions at Each Test Station.

Flow Type	x-sta ft	u_∞ ft/sec	$\delta_{.99}$ inch	δ^* inches	θ inches	u_τ profile near wall ft/sec	u_τ cross plot log region ft/sec	K x 10^6	Re_θ	$H = \frac{\delta^*}{\theta}$	$\sigma_{c.p.}$	x 10^3 C_f wall pro.	x 10^3 C_f log. c.p.	$\frac{\delta^*}{\tau_w}\frac{dp}{dx}$ pro
dp/dx = 0	6.30	0.50	2.175	.337	.233	insufficient data	.0233	0	1000	1.45	6.67	-	4.34	0
	10.30	0.50	2.25	.362	.263	"	.0231	0	1080	1.43	6.63		4.26	0
	13.50	0.50	2.75	.442	.320	"	.0228	0	1325	1.38	6.76	-	4.15	0
mild+dp/dx	6.15	.44	1.38	.248	.172	.0195	.0223	-.25	566	1.44	7.02	3.92	5.14	.106
	8.25	.43	1.58	.294	.201	.0188	.0205	-.53	590	1.46	6.56	3.82	4.56	.238
	11.24	.40	2.20	.398	.264	.0168	.0185	-.83	778	1.50	7.98	3.54	4.27	.547
	15.24	.36	4.20	.798	.542	.0154	.0157	-.36	1680	1.47	7.65	3.66	3.80	.485
mild-dp/dx	8.33	.45	2.05	.362	.242	.0202	.0215	0.21	885	1.50	7.0	4.04	4.57	-.139
	11.33	.49	2.17	.362	.224	.0202	.0237	0.79	920	1.46	6.5	3.48	4.78	-.612
	15.33	.54	2.42	.346	.246	.0217	.0264	0.75	1160	1.40	5.8	3.23	4.78	-.829
str+dp/dx	7.25	0.39	1.53	0.287	0.173	0.0167	.0193	0	588	1.65	8.1	3.66	4.90	0
	10.15	.36	2.30	0.518	0.319	.0148	.0150	-2.0	957	1.63	9.2	3.38	3.48	1.76
	12.23	.32	3.40	0.898	0.540	.0124	.0120	-1.05	1560	1.66	10.6	3.00	2.82	1.95
str-dp/dx	8.14	.38	1.48	0.259	0.176	.0209	.0198				$\sigma_{c.p.}$ σ_{pro}			
	10.25	.41	1.60	0.252	0.171	.0268	.0216	0	586	1.47	6.17 5.80	6.03	5.42	0
	12.18	.57	1.60	0.159	0.115	.040	.033	2.8	615	1.47	6.08 4.90	8.53	5.56	-.576
Runstadler dp/dx = 0	19	0.430	5.0	0.70	.505	.0157	.0190	3.2	567	1.35	4.5 3.70	9.64	6.70	-.552
								0	2060	1.38	6.2			

Flow Type	x-sta ft	u_∞ ft/sec	$\delta_{.99}$ inch	δ^* inches	θ inches	u_τ profile near wall ft/sec	u_τ cross plot log region ft/sec	K x 10^6	Re_θ	$H = \frac{\delta^*}{\theta}$	$\sigma_{c.p.}$	x 10^3 C_f wall pro.	x 10^3 C_f log. c.p.	$\frac{\delta^*}{\tau_w}\frac{dp}{dx}$ pro
dp/dx = 0	6.30	0.50	2.175	.337	.233	insufficient data	.0233	0	1000	1.45	6.67	-	4.34	0
	10.30	0.50	2.25	.362	.263	"	.0231	0	1080	1.43	6.63	-	4.26	0
	13.50	0.50	2.75	.442	.320	"	.0228	0	1325	1.38	6.76	-	4.15	0
mild+dp/dx	6.15	.44	1.38	.248	.172	.0195	.0223	-.25	566	1.44	7.02	3.92	5.14	.106
	8.25	.43	1.58	.294	.201	.0188	.0205	-.53	590	1.46	6.56	3.82	4.56	.238
	11.24	.40	2.20	.398	.264	.0168	.0185	-.83	778	1.50	7.98	3.54	4.27	.547
	15.24	.36	4.20	.798	.542	.0154	.0157	-.36	1680	1.47	7.65	3.66	3.80	.485
mild-dp/dx	8.33	.45	2.05	.362	.242	.0202	.0215	0.21	885	1.50	7.0	4.04	4.57	-.139
	11.33	.49	2.17	.362	.224	.0202	.0237	0.79	920	1.46	6.5	3.48	4.78	-.612
	15.33	.54	2.42	.346	.246	.0217	.0264	0.75	1160	1.40	5.8	3.23	4.78	-.829
str+dp/dx	7.25	0.39	1.53	0.287	0.173	0.0167	.0193	0	588	1.65	8.1	3.66	4.90	0
	10.15	.36	2.30	0.518	0.319	.0148	.0150	-2.0	957	1.63	9.2	3.38	3.48	1.76
	12.23	.32	3.40	0.898	0.540	.0124	.0120	-1.05	1560	1.66	10.6	3.00	2.82	1.95
str-dp/dx	8.14	.38	1.48	0.259	0.176	.0209	.0198				$\sigma_{c.p.}$ σ_{pro}			
	10.25	.41	1.60	0.252	0.171	.0268	.0216	0	586	1.47	6.17 5.80	6.03	5.42	0
	12.18	.57	1.60	0.159	0.115	.040	.033	2.8	615	1.47	6.08 4.90	8.53	5.56	-.576
Runstadler dp/dx = 0	19	0.430	5.0	0.70	.505	.0157	.0190	3.2	567	1.35	4.5 3.70	9.64	6.70	-.552
								0	2060	1.38	6.2			

Table 3.2 Trajectory Data

dp/dx = 0 flow

x-sta(ft)	T,sec	$\bar{x}$,in	$\bar{y}$,in	$s_x/\bar{x}$	$s_y/\bar{y}$	no.counted
	0	0	0	-	-	88
	0.25	0.677	0.107	0.380	0.405	88
	0.50	1.502	0.192	0.276	0.346	88
6.1	0.75	2.402	0.270	0.208	0.342	88
	1.00	3.410	0.339	0.191	0.362	86
	1.25	4.412	0.394	0.172	0.394	43
	1.50	5.450	0.459	0.172	0.394	43
	1.75	6.568	0.556	-	-	14
	0	0	0	-	-	84
	0.375	0.935	0.149	0.276	0.380	84
10.1	0.750	2.183	0.266	0.229	0.387	84
	1.125	3.565	0.371	0.188	0.370	83
	1.500	5.026	0.477	0.174	0.424	70
	1.875	6.394	0.585	0.128	0.438	50
	2.250	7.993	0.706	0.113	0.403	21
	0	0	0	-	-	73
	0.375	0.877	0.151	0.301	0.380	73
13.1	0.750	2.080	0.289	0.231	0.400	73
	1.125	3.450	0.409	0.189	0.400	70
	1.500	5.057	0.562	0.163	0.401	63
	1.875	6.352	0.658	0.118	0.360	27
	2.250	8.143	0.833	0.111	0.312	11

Table 3.2 Trajectory Data (continued)

mild + dp/dx flow: 1° diffuser

x-sta(ft)	T,sec	$\bar{x}$,in	$\bar{y}$,in	$s_x/\bar{x}$	$s_y/\bar{y}$	no.counted
	0	0	0	-	-	52
	.375	1.23	.304	0.312	0.455	52
	.750	2.80	.443	0.195	0.324	52
8.1	1.125	4.52	.577	0.160	0.292	52
	1.50	6.39	.715	0.147	0.288	49
	1.875	8.04	.810	0.109	0.314	35
	2.250	9.41	1.065	0.114	0.267	12
	2.625	10.38	1.061			4
	0	0	0	-	-	50
	.38	.858	.205	0.312	0.367	50
	.75	1.95	.377	0.248	0.357	50
11.1	1.13	3.31	.530	0.179	0.351	50
	1.50	4.73	.653	0.166	0.311	48
	1.88	6.31	.752	0.129	0.280	31
	2.25	7.76	.833	0.151	0.213	13
	2.63	8.38	.883	0.164	0.193	5
	0	0	0	-		27
	.38	0.77	0.27	0.338	0.337	27
	.75	1.83	0.43	0.250	0.340	27
15.1	1.13	3.03	0.57	0.203	0.294	27
	1.50	4.23	0.69	0.187	0.271	25
	1.88	5.39	0.79	0.152	0.284	20
	2.25	6.92	0.93	0.111	0.210	16
	2.62	8.14	1.03	0.110	0.210	8

Table 3.2 Trajectory Data (continued)

mild - dp/dx flow: 1° converger

x-sta(ft)	T,sec	$\bar{x}$,in	$\bar{y}$,in	$s_x/\bar{x}$	$s_y/\bar{y}$	no.counted
	0	0	0	-	-	29
	.392	.910	.147	0.276	0.445	29
	.784	2.17	.280	0.166	0.425	29
	1.176	3.57	.402	0.138	0.337	29
8.1	1.57	5.12	.513	0.108	0.362	29
	1.96	6.74	.642	0.098	0.280	25
	2.35	8.23	.704	0.065	0.345	20
	2.74	9.67	.733	0.036	0.340	11
	0	0	0	-	-	30
	.392	1.03	0.147	0.290	0.336	30
	.784	2.40	0.252	0.191	0.384	30
11.1	1.176	3.84	0.355	0.170	0.452	30
	1.57	5.37	0.448	0.152	0.420	28
	1.96	6.94	0.563	0.132	0.411	23
	2.35	8.83	0.659	0.104	0.446	21
	2.74	9.98	0.758	0.091	0.416	12
	0	0	0	-	-	25
	0.392	1.662	.216	0.212	0.266	25
15.1	0.784	3.62	.374	0.138	0.302	25
	1.176	5.63	.491	0.123	0.367	25
	1.96	7.65	.587	0.094	0.340	23
	2.35	9.58	.668	0.094	0.337	17
	2.74	11.80	.790	-		4
		-	-			0

Table 3.2 Trajectory Data (continued)

str + dp/dx flow

x-sta(ft)	T,sec	$\bar{x}$,in	$\bar{y}$,in	$s_x/\bar{x}$	$s_y/\bar{y}$	no.counted
	0	0	0	-	-	42
	0.50	1.34	0.228	.266	.266	42
	1.00	2.93	0.394	.105	.304	42
7.1	1.50	4.75	0.517	.095	.294	42
	2.00	6.77	0.622	.087	.301	42
	2.50	8.88	0.730	.071	.326	28
	3.00	10.50	0.80	-	.290	9
	3.50	-	-	-	-	
	0	0	0	-	-	32
	0.50	0.70	0.170	0.272	0.160	32
	1.00	1.61	0.329	0.215	0.270	32
10.1	1.50	2.68	0.488	0.188	0.225	32
	2.00	3.84	0.653	0.147	0.296	31
	2.50	5.03	0.850	0.164	0.255	22
	3.00	6.06	0.956	0.110	0.250	9
	3.50	7.00	1.150	-	-	3
	0	0	0	-	-	44
	0.75	0.80	0.234	0.377	0.513	44
12.1	1.50	1.85	0.435	0.261	0.439	44
	2.25	3.06	0.630	0.225	0.446	44
	3.00	4.38	0.812	0.194	0.515	43
	3.75	5.88	1.018	0.174	0.506	37
	4.50	7.52	1.145	0.164	0.422	21
	5.25	8.76	1.342	0.141	0.521	8

Table 3.2 Trajectory Data (concluded)

str - dp/dx flow

x-sta(ft)	T,sec	$\bar{x}$,in	$\bar{y}$,in	$s_x/\bar{x}$	$s_y/\bar{y}$	no.counted
	0	0	0	-	-	26
	0.375	0.98	0.179	.281	.311	26
8.1	0.750	2.01	0.336	.190	.309	26
	1.125	3.30	0.476	.172	.285	26
	1.500	4.64	0.583	.128	.323	24
	1.875	6.10	0.740	.111	.250	22
	2.250	7.58	0.842	.108	.311	18
	2.625	8.30	1.082	-	-	4
	0	0	0			19
	0.375	0.86	0.130	(not determined)		19
	0.750	1.84	0.229			19
9.1	1.125	3.03	0.314			19
	1.500	4.32	0.368			19
	1.875	5.78	0.433			18
	2.250	6.89	0.549			10
	2.625	8.23	0.632			5
	0	0	0	-		37
	0.375	1.08	0.140	.266	.310	37
	0.750	2.34	0.241	.179	.334	37
10.1	1.125	3.76	0.336	.147	.377	37
	1.500	5.30	0.407	.122	.427	36
	1.875	7.07	0.458	.108	.397	33
	2.250	8.37	0.557	.093	.354	15
	2.625	8.55	0.555	-	-	2

Table 3.3 Burst Rate Data

Flow	x-sta ft	u_∞ ft/sec	K -	u_τ ft/sec	F burst/sec/in
dp/dx = 0					
Runstadler [1963]	19	0.197	0	0.00918	0.0652 †
	19	0.434	0	0.0188	0.530 †
	19	0.750	0	0.0311	2.48 †
dp/dx = 0 flow	6	0.50	0	0.0233	1.00
	10	0.50	0	0.0231	0.99
	13	0.50	0	0.0228	0.98
mild + dp/dx flow	6	0.440	-0.25	0.0223	1.02
	8	0.425	-0.53	0.0205	1.04
	11	0.396	-0.83	0.0185	0.70
	15	0.361	-0.36	0.0157	0.61
mild - dp/dx flow	8	0.450	0.21	0.0215	0.66
	11	0.485	0.79	0.0237	0.71
	15	0.536	0.75	0.0264	0.96
str + dp/dx flow	7	0.390	0	0.0193	0.84
	10	0.341	-2.00	0.0150	0.73
	12	0.308	-1.05	0.0120	0.57
str - dp/dx flow	8	0.382	0	0.0198	1.07
Relaminarization	9	0.386	0.50	0.020 ‡	0.86
	10	0.427	2.75	0.0216	0.58
	11	0.507	3.85	0.626 ‡	0.18
	12	0.602	3.25	0.633	0.19
	13.5	0.272	0.56	0.037 ‡	1.05
	14	0.683	0	0.038	1.42

† Based on estimated view area of 9 in^2 .

‡ Extrapolated; based on smooth C_f variation with x .

IV. SUMMARY AND CONCLUSIONS

A. Summary

The summary falls naturally into four categories:

1. The influence of moderate pressure gradients upon the flow structure of a turbulent boundary layer.
2. New information on the "basic" turbulent structure.
3. Relaminarization of turbulent boundary layers.
4. New experimental techniques.

1. The influence of moderate pressure gradients upon the flow structure of turbulent boundary layers

a. Similarities to zero gradient structure

For moderate streamwise pressure gradients: $-2 \times 10^{-6} \leq K \leq 0.5 \times 10^{-6}$ †, no changes in the qualitative appearance of the flow structure occur from that observed for zero gradient flow (Runstadler [1963]). The flow structure consists of three distinct regions: wall layer, fully turbulent core, and outer or wake region; and these structural regions coincide with distinct parts of the mean velocity profile in u^+, y^+ coordinates: linear sublayer, logarithmic, and defect or wake.‡ For example, still photographs at 11 y-positions across a layer under a positive pressure gradient (figure 3.42) show the same qualitative features in each profile region as similar structure surveys in zero pressure gradient flows. (Runstadler [1963]) These results are typical of many observed in this study, but not exhibited in detail.

The spanwise spacing between low u-velocity streaks in the sublayer indicate that λ^+ is constant for moderate pressure gradient as well as zero gradient flows (figure 3.34). The average trajectories of ejected fluid from the wall layer bursts falls within the scatter of the zero gradient data (figure 3.50)

---

† K is pressure gradient parameter.

‡ The extent (% of layer thickness) of the logarithmic and wake regions are pressure gradient dependent; but this dependence was not studied in detail here. The wall region extends $0 \leq y^+ \leq 8$.

when the $\bar{y}$ coordinate is normalized as a y^+ ($y^+ = yu_\tau/\nu$). That is, streak spacing and burst trajectory correlate on the wall parameter, u_τ, rather than on external parameters such as u_∞ for example.

b. Points of difference between pressure gradient structure and zero gradient structure

While the qualitative similarity between the structures is pronounced, some details of the flow structure appear to be pressure gradient dependent.

The present data indicates that the so-called "law of the wall" is pressure gradient dependent and not completely universal (as shown in profiles in figure 3.16 - 3.20). With wall shear determined by matching the linear profile near the wall to $u^+ = y^+$, no single (universal) curve correlates the present data. The degree and direction of deviation from the universal relation proposed by Clauser [1956] is pressure gradient dependent (figure 3.22b).

The rate of turbulent bursting from the sublayer region is somewhat pressure gradient dependent (figure 3.54). A rise in bursting rate (over that expected by the zero gradient correlation) is observed for $\frac{dp}{dx} > 0$. Conversely, $\frac{dp}{dx} < 0$ flows show decreases in bursting; if the applied negative gradient is severe, the burst rate will be decreased to zero--indicating relaminarization.

2. New information on basic flow structure

The great similarity between the moderate pressure-gradient flow and zero-gradient flow turbulent boundary layers makes discussion of a common "basic" flow structure expedient. In the course of investigating the effects of pressure gradients, some new information was revealed about the basic structure.

The improved H_2-bubble technique (see Schraub, et al [1964]) made instantaneous u-velocity traces across the flow

(z-direction) available as a function of time at discrete y-positions (figure 3.30). This profile data made possible various statistical analyses of the structure. Velocity probability density distributions (figure 3.31) were evaluated. The second, third, and fourth moments were evaluated (figure 3.32) and shown to be consistent with those evaluated by other investigators.† For example, the non-dimensional third moment, skewness, is positive in the sublayer and negative in the buffer and log regions (figure 3.32). This statistical result collaborates the physical flow patterns observed in these regions (figure 3.33).

Spatial spectral analysis procedures are applied to the u versus z data. The shape of the resulting correlation coefficients (figure 3.36) show the well-ordered structure of the sublayer region. Peaks in the Fourier transforms of the two-point velocity correlation coefficients are compared to λ_{visual}. The agreement (to about 20%) between the objective statistical procedures and the somewhat subjective visual counting procedures strongly supports the proposition that λ is a fundamental structural scale of the wall layer region. The flat distribution of spacing indicates the scale is best considered as a band of spatial wave lengths rather than a single value for λ.

The spectral analysis could also be applied to velocity profiles (u versus z) outside the wall region where the underlying structural scales are not obvious to the human eye. λ versus y (figure 3.39) shows a sharp rise in λ in the buffer region and then suggests a more gradual increase in scale proportional to the distance from the wall in the logarithmic region.

A simple model for the rate of sublayer bursting based

†The uncertainty in the bubble data is higher, but a greater range of information and improved understanding is obtained.

on the assumption that the volume ejected per unit area is a constant, for the $dp/dx = 0$ case, predicts that the burst rate should be proportional to u_τ^3. For $dp/dx = 0$, u_τ is proportional to $u_\infty^{0.9}$, so F should be proportional to $u_\infty^{2.7}$. This relation was shown to correlate the zero gradient burst data very well (figure 3.53).

The shape of the trajectory path of ejected low-momentum fluid was investigated in greater detail than heretofore. The average path ($\bar{y}$ vs $\bar{x}$) is shown to consist of two parts: a parabolic path (initial acceleration in the buffer region) just after ejection; and then a linear relation for the remainder of the path which could be observed (figures 3.47 and 3.48). The distribution of ejected fluid as a function of y at points downstream from the ejection station are well represented by a proposed universal analytical model (figure 3.52).

The present data (for example see figure 3.42) indicates that the y-position at which the mean velocity profile deviates from the log portion of the profile (u^+ versus log y^+ co-ordinates) is not the point where intermittency begins. Intermittency appears to begin at the point of inflection in the s-shaped wake profile instead. In the $dp/dx = 0$ flow, these two points are so close together, that a distinction was not possible in the data of Runstadler, et al [1963].

3. Relaminarization of turbulent boundary layers

For severe negative pressure gradient flows a fundamental change in the turbulent boundary layer structure away from the "basic structure" occurs. A "laminarescent" structure develops: the mean profiles are distorted (figure 3.20); the burst rate decreases below the turbulent correlation (figure 3.57); λ^+ rises rapidly above the turbulent correlation (figure 3.34); and the structure generally takes on a non-turbulent appearance (figure 3.50). A three-stage relaminarization process is suggested which somewhat parallels the

stages of natural transition. These results are consistent with the heat transfer studies of Moretti and Kays [1964], but further studies of relaminarization are still needed for complete understanding.

4. New experimental techniques

a. H_2-bubble development

A contribution to the development of the H_2-bubble combined-time-streak marker method of flow visualization was made as part of this work (see also: Schraub, Kline, et al [1964]). The method makes possible continuous quantitative determination of velocity over a large area for any surface which contains the velocity vector at the marking station. Either steady or time-dependent velocity fields can be studied. No other known method provides equivalent information. The statistical analyses of this investigation are made possible by the success of the combined-time-streak marker hydrogen bubble method and the associated data reduction techniques.

B. Conclusions

THE STRUCTURE PICTURE FOUND BY RUNSTADLER, ET AL [1963] FOR $dp/dx = 0$ FLOW HAS BEEN CONFIRMED, FURTHER VERIFIED AND EXTENDED.

This general conclusion is reached as the result of a study of turbulent flow in a turbulent boundary layer on a flat plate with and without longitudinal pressure gradients. Flow Reynolds numbers (based on momentum thickness) ranged from 560 to 1700 and the pressure gradient parameter $K = \frac{\nu}{u_\infty^2} \frac{du_\infty}{dx}$ ranged from -2.0×10^{-6} to 4.0×10^{-6}.

CONFIRMED

(a) Turbulent boundary layer consists of three zones: wall, fully turbulent, and wake regions.

(b) Structure of each zone agrees with descriptions of Runstadler.

(c) One to one correspondence exists between each zone and the distinct portions of mean velocity profile in u^+, y^+ coordinates.

(d) Average wall layer streak spacing λ yields a constant value of $\lambda^+ = \lambda u_\tau / \nu$.

(e) No evidence in contradiction to the "Hypothesis and Description" of Runstadler was found.

FURTHER VERIFIED

(a) Wall layer streaky pattern is shown beyond any reasonable doubt to be due to somewhat regular spanwise variations of the x-component of velocity.

(b) The wall streaks are conclusively shown to be randomly positioned over the wall and not fixed in space when viewed for long times.

(c) Statistical analysis of spanwise wall layer velocity profiles verify the existence of λ as fundamental structural scale, but indicate a band of spacings better describes the structure than a single spatial wave length.

(d) The bursts from the wall layer region arise from spreading of high speed regions in the wall layer with concomittant ejection of fluid from the low-speed regions in the form of filaments stretched in the longitudinal direction. The cause of this action is still not known.

(e) The bursting is an essential feature for the existence of turbulent flow; the absence of bursting indicates non-turbulent flow.

EXTENDED

(a) The structure under moderate pressure gradients is <u>not significantly changed from the zero pressure gradient case</u> as long as the layer is turbulent.

(b) <u>Relaminarization</u> occurs for strong negative pressure gradients; $K \geq 3 \times 10^{-6}$. A laminarescent layer does not exhibit the features of a turbulent layer. The most obvious change is the <u>cessation of turbulent bursting</u> from the sublayer region upon relaminarization, making burst rate a means of detecting relaminarization.

(c) True universality of the <u>"law of the wall" is doubted</u> for pressure gradient flows. Systematic differences from a single u^+, y^+ mean velocity profile are observed as a function of applied pressure gradient. A linear ($u^+ = y^+$) region in time average mean flow is always observed at the wall, but the constants in the logarithmic relation outside the linear region are pressure gradient dependent when the wall shear is determined from the linear region (wall slope method).

(d) The mean <u>trajectory path</u> of ejected fluid (bursts) is typically made up of a parabolic acceleration path near the wall and a very nearly linear path further from the wall.

The <u>distribution</u> of position of ejected fluid about the mean path is given by a universal function for the $dp/dx = 0$ case.

(e) The burst rate is proportional to u_τ^3 or to $u_\infty^{2.7}$ for $dp/dx = 0$ flow. A marked influence of pressure gradient on the correlation is shown although a general correlation was not obtained.

(f) The hydrogen-bubble combined-time-streak marker visualization method is very useful for quantitative measurement and an excellent supplement to the hot wire anemometer.

REFERENCES

Back, L. H. [1962], "Heat transfer to turbulent boundary layers with variable free-stream velocity", Ph.D. Dissertation, University of California at Berkeley, 1962.

Back, L. H., P. F. Massier, and H. L. Gier [1964], "Convective heat transfer in a convergent-divergent nozzle", Int. Jour. of Heat and Mass Transfer, May, 1964.

Blackman, R. B. and J. W. Tukey [1958], The Measurement of Power Spectra, Dover Publications, Inc., New York, 1958.

Clauser, F. H. [1954a], "Turbulent boundary layers in adverse pressure gradients", Journal of the Aeronautical Sciences, February 1954.

Clauser, F. H. [1956], "The turbulent boundary layer", Advances in Applied Mechanics, Volume IV, 1956.

Coles, D. [1956], "The law of the wake in the turbulent boundary layer", Journal of Fluid Mechanics, Vol. I, Part 2, July 1956.

Comte-Bellot, G. [1963], "Coefficients de dessymétrie et d'aplatissement, spectres et corrélations en turbulence de conduite", Journal de Méchanique, Vol. II, No. 2, June 1963.

Craemer, Harold [1955], The Elements of Probability Theory, John Wiley and Sons, 1955.

Dryden, H. L., G. B. Schubauer, W. C. Mock, Jr. and H. K. Skramstad, NACA TN 581, 1937.

Einstein, H. A. and H. Li [1956], "The viscous sublayer along a smooth boundary", A.S.C.E. Proc. 82, 1956.

Emmons, H. W. [1951], "The laminar-turbulent transition in a boundary layer", Part I, Journal of Aeronautical Sciences, Vol. 18, No. 7, p. 490, 1951.

Grant, H. L. [1958], "The large eddies of turbulent motion", Journal of Fluid Mech., Vol. 4, Part 2, June 1958.

Hinze, J. O. [1959], Turbulence, McGraw-Hill Book Co., Inc., New York, 1959.

Jenkins, G. M. [1961], "General Considerations in the Analysis of Spectra", Technometrics, Vol. 3, No. 2, May 1961.

Klebanoff, P. S. and Z. W. Diehl [1951], "Some features of artificially thickened fully developed turbulent boundary layers", NACA TN 2475, 1951.

Klebanoff, P. S. [1954], "Characteristics of turbulence in a boundary layer with zero pressure gradient", NACA TN 3178, 1954; also Rept. 1247, 1955.

Kline, S. J. [1959], "On the Nature of Stall", Journal Basic Engrg., Vol. 81, Series D, No. 3, September 1959.

Kline, S. J. and F. A. McClintoch [1953], "The description of uncertainty in single sample experiments", Mech. Engrg., January 1953.

Laufer, J. [1953], "The structure of fully developed pipe flow", NACA Rept. 1174, 1954 or TN 2954, 1953.

Launder, B. E. [1963], "The turbulent boundary layer in a strongly negative pressure gradient", Gas Turbine Lab Report No. 71, M.I.T., 1963.

Lin, C. C. [1959], Statistical theories of turbulence, Princeton University Press, 1959.

Ludwieg, H. and W. Tillman [1949], Ingr. Arch, 17, 288, 1949.

Lumley, J. L. [1962], "The constant temperature hot-thermister anemometer", ASME Symposium On Measurements in Unsteady Flow, 1962.

Lumley, J. L. and H. A. Panofsky [1964], The Structure of Atmospheric Turbulence, John Wiley and Sons, New York, 1964.

Mellor, G. L. and D. M. Gibson [1963], Equilibrium Turbulent Boundary Layers, Mech. Engrg. Dept., Princeton University, FLD No. 13, 1963.

Meyer, K. A. and S. J. Kline [1961], "A visual study of the flow model in the later stages of laminar-turbulent transition on a flat plate", Report MD-7, Thermosciences Division, Mech. Engrg. Dept., Stanford University, 1961.

Moretti, P. M. and W. M. Kays [1964], "Heat transfer through an incompressible turbulent boundary layer with varying free-stream velocity and varying surface temperature", Rept. No. P6-1, Thermosciences Division, Mech. Engrg. Dept., Stanford University, 1964.

Parzen, E. [1960], Modern Probability Theory and its Applications, John Wiley, 1960.

Parzen, E. [1963], "On Statistical Spectral Analysis", Tech. Rept. No. 49, Applied Math. and Statistics Lab., Stanford University, June 1963.

Prandtl, L. [1933], "Recent results of turbulence research", NACA Tech. Memo. 720, 1933.

Raven, F. H. [1961], Automatic Control Engineering, McGraw-Hill Book Co., Inc., New York, 1961; Appendix III: "Obtaining the frequency response from the transient response."

Sabin, C. M. [1963], "An analytical and experimental study of the plane, incompressible, turbulent free shear layer with arbitrary velocity ratio and pressure gradient", Report MD-9, Thermosciences Division, Mech. Engrg. Dept., Stanford University, 1963.

Schlichting, H. [1960], Boundary Layer Theory, McGraw-Hill Book Co., Inc., New York.

Schraub, F. A., S. J. Kline, et al [1964], "Use of hydrogen bubbles for quantitative determination of time dependent velocity fields in low speed water flows", Report MD-10, Thermosciences Division, Mech. Engrg. Dept., Stanford University, 1964; also Jour. of Basic Engrg., Trans. ASME, Series D, Vol. 87, 1965.

Schultz-Grunow, F. [1940], "Luftfahit-Forsch", 17, 239, 1940.

Sergienko, A. A. and V. K. Gretsov [1959], "Transition from a turbulent into a laminar boundary layer", Soviet Physics "Doklady", Vol. 4, Number 1, August 1959. (A translation of the "Physics Sections" of the Proceedings of the Academy of Sciences of the USSR, Russian Original Vol. 124, Nos. 1-6, published by the American Institute of Physics, Inc.)

Sibulkin, M. [1962], "Transition from turbulent to laminar pipe flow", Physics of Fluids 5, March 1962.

Smith, D. W. and J. H. Walker [1957], "Skin-friction measurements in incompressible flow", NACA TN 4231, Dec. 1957.

Smith, A. M. O. and N. Gamberom [1956], "Transition, Pressure Gradient and Stability Theory", Rept. No. ES 26388, Douglas Aircraft Co., August 1956.

Sneddon, I. N. [1951], Fourier Transforms, McGraw-Hill Book Co., Inc., New York, 1951.

Sternberg, J. [1954], "The transition from a turbulent to a laminar boundary layer", U.S. Army Bal. Res. Lab. Rept. 906, Arberdeen, May 1954.

Taylor, G. I. [1938], Proc. Roy. Soc. London, 164A, 1938.

Townsend, A. A. [1956], The Structure of Turbulent Shear Flow, Cambridge University Press, 1956.

Uzkan, T. [1964], "Corrections to hot wire readings due to finite length of wires", Internal report of Thermosciences Division, Dept. of Mech. Engrg., Stanford University, 1964.

APPENDIX A

HOT-WIRE ANEMOMETER DYNAMIC FREQUENCY RESPONSE TEST

The hot-wire anemometer used for this study is a new instrument and a test of the frequency response was appropriate.

An estimate of the dynamic frequency response of the <u>entire</u> anemometer-probe system is obtained using a simple test of the transient response suggested by Lumley [1962]. A step change in Peclet number $\left(\text{Peclet No.} \triangleq \left(\frac{\text{wire length}}{\text{wire diameter}} \cdot \frac{k_{probe}}{k_{fluid}}\right)^2\right)$ was obtained by plunging the probe through the interface between kerosene and water at the same temperature. $\left(\frac{k_{kerosene}}{k_{water}} = 0.25\right)$ Figure A.1 shows the apparatus used and typical results obtained by photographing the anemometer output on a CRT oscilloscope. The platinum wire was 0.0008 inches in diameter, 0.2 inches long, and was moving 31.3 inches/sec as it passed through the interface.

The "break-off frequency", ω_o, is defined as that frequency at which the output of the anemometer first drops 2.5 db below the DC response when subjected to a <u>sinusoidal</u> input. An estimate of ω_o is given by $\omega_o = 1/2\pi\tau$ where τ is defined by figure A.2. This expression is exact for a first order system - i.e., one governed by the 1st order differential equation: $\tau \frac{dy}{dt} + y = y_o$, where y is output, t is time, and y_o is an exact-step forcing function (see eq., Raven [1961]). However, this value is not exact because (1) the system is not simply first order; (2) the forcing function or change in K_{fluid} around the wire is not a perfect step function. This is because the wire takes a finite time to pass through the interface (about 0.13 τ) and there is a boundary layer transient time or fluid entrainment which also tends to make the step less sharp.

These effects and the fact that the probe is still accelerating at the interface are all felt to give a high value for τ and thus a conservatively low value of ω_o.

The break-off frequency, ω_o , thus determined was 800 cps, and so "flat" frequency response is expected from this hot-wire system up to at least 800 cps. See sample response curve in figure A.3.

The upper limit for ω_o is 1000 cps; it is determined by the frequency response of the plug-in operational amplifiers used in the anemometer amplifier.

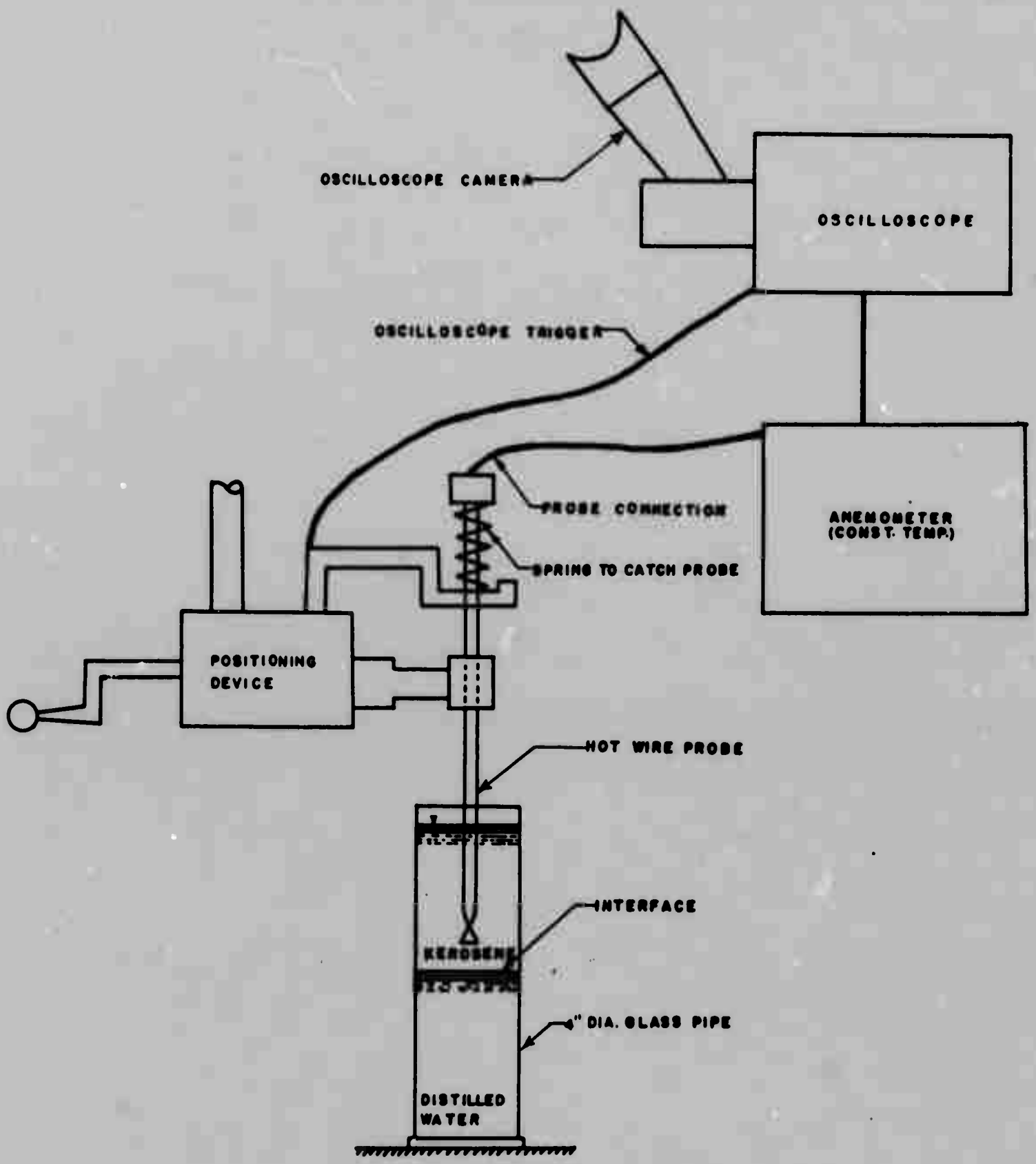

Fig. A.1 Schematic of apparatus for hot-wire frequency response test.

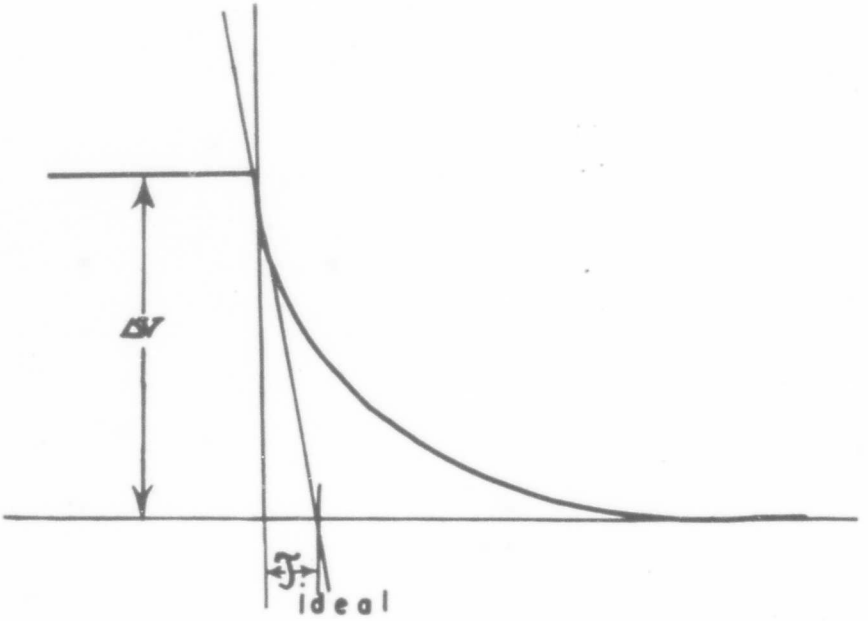

Fig. A.2 Idealized response of hot-wire to step change in power.

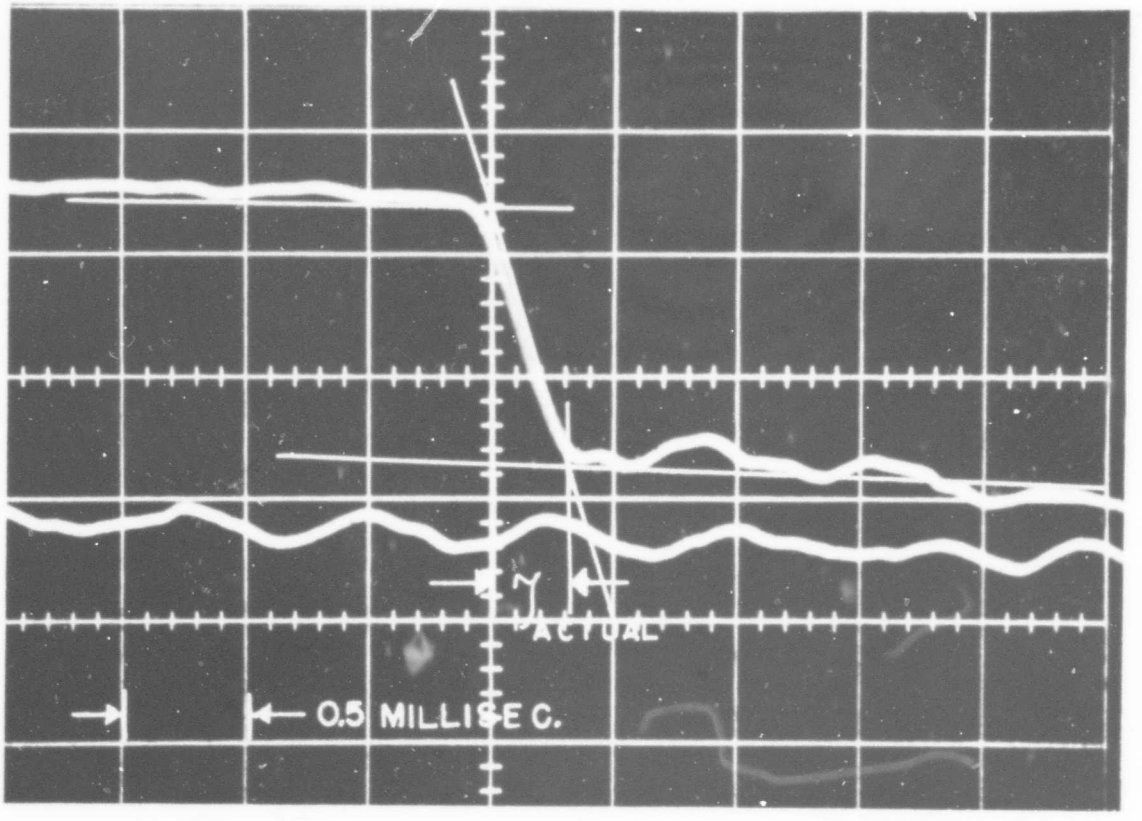

Fig. A.3 Photograph of typical CRT oscilloscope trace of hot-wire anemometer system response to step power output.

APPENDIX B
CORRECTIONS TO HOT-WIRE MEASUREMENTS

The following possible sources of error in velocity measurements are considered:

A. Velocity Fluctuations of Large Amplitude
   1. Fluctuations normal to wire and normal to streamwise direction
   2. Fluctuations along the finite wire length

B. Wall Effects
   1. Thermal conduction to wall
   2. Flow field distortion by wire near wall.

The hot-wire probe is calibrated in the free-stream external to the boundary layer where turbulence intensity is approximately 1%. The calibration thus accounts for probe geometry and all constants of the circuitry but does not include the factors mentioned above which are encountered in measurements in turbulent boundary layer flows.

A. Velocity Fluctuations of Large Amplitude

1. Fluctuations normal to wire

The hot-wire is sensitive to the absolute value of the total velocity vector normal to the wire. Thus when large velocity components in directions other than the direction of the mean component being measured are present, the probe output is not entirely due to the component being measured.

The absolute value of the total velocity vector is P and

$$P = [(\bar{u} + u)^2 + (\bar{v} + v)^2 + (\bar{w} + w)^2]^{1/2} \qquad (A\text{-}1)$$

where $\bar{u}$, $\bar{v}$, $\bar{w}$ are the x, y, z mean velocity components and u, v, w the corresponding fluctuating components.

Consider the common situation for this study: in order to measure $\bar{u}$, the wire is placed perpendicular to the x-flow direction and parallel to the wall and to the z-direction;

for a two-dimensional boundary layer, $\overline{v}$ and $\overline{w}$ are zero and the effect of w may be neglected compared to v and u because the heat transfer coefficient for flow parallel to the wire is small in comparison to that perpendicular to the wire and so the anemometer is not sensitive to the v and w velocity components.

With these assumptions,

$$P = [(\overline{u} + u)^2 + v^2]^{1/2}$$

or

$$\frac{P}{\overline{u}} = \left[1 + \frac{2u}{\overline{u}} + \frac{u^2 + v^2}{\overline{u}^2}\right]^{1/2} \qquad \text{(A-2)}$$

Now for finite $\overline{u}$ and for fluctuations which are not excessively large, so that $\left(\frac{2u}{\overline{u}} + \frac{u^2 + v^2}{\overline{u}^2}\right) < 1$, $\frac{P}{\overline{u}}$ is approximately given by

$$\frac{P}{\overline{u}} = 1 + \frac{1}{2}\left[\frac{2u}{\overline{u}} + \frac{u^2+v^2}{\overline{u}^2}\right] - \frac{1}{8}\left[\frac{2u}{\overline{u}} + \frac{u^2+v^2}{\overline{u}^2}\right]^2 + \frac{1}{16}\left[\frac{2u}{\overline{u}} + \frac{u^2+v^2}{\overline{u}^2}\right]^3 - \cdots \qquad \text{(A-3)}$$

expanding and neglecting terms of 4th order or higher in fluctuations,

$$\frac{P}{\overline{u}} \approx 1 + \frac{u}{\overline{u}} + \frac{v^2}{2\overline{u}^2}\left(1 - \frac{u}{\overline{u}}\right) \qquad \text{(A-4)}$$

The mean velocity determined by the anemometer is $\overline{P}$. Averaging the above expression,

$$\overline{P} \cong \overline{u} + \frac{\overline{v^2}}{2\overline{u}} \qquad \left(\text{neglecting } \frac{v^2 u}{2\overline{u}}\right) \qquad \text{(A-5)}$$

Therefore, a better estimate of the true mean x-component of velocity is given by subtracting a correction of $\overline{v^2}/2\overline{u}$ from the velocity given by the anemometer output calibration curve, i.e.,

$$\overline{u}_{true} = \overline{P}_{\substack{anem. \\ calibration}} - \frac{\overline{v^2}}{2\overline{u}} \qquad (A\text{-}6)$$

Turbulence Intensity may be calculated by

$$\frac{TI}{100} = \frac{\left[\overline{P^2} - (\overline{P})^2\right]^{1/2}}{\overline{P}}$$

Application of the above expressions for P yield:

$$\frac{TI_{true}}{TI_{\substack{anem. \\ calib.}}} = \frac{1 + \overline{v^2}/2\overline{u^2}}{1 - \left(\overline{v^2}/2\overline{u^2}\right)^2} = \frac{1}{1 - \overline{v^2}/2\overline{u^2}} \qquad (A\text{-}7)$$

as the approximate relation between the true TI of x-component and the value calculated when y-components are present.

The precent error in mean velocity in the x-direction due to y-direction velocity fluctuations as a function of $\frac{\left(\overline{v^2}\right)^{1/2}}{\overline{u}} \times 100$ is given in figure A.4.

For the data of this study, the correction may be approximated using the data of Klebanoff [1954] for $\left(\overline{v^2}\right)^{1/2}/\overline{u}$ across a turbulent boundary layer on a flat plate. For the region of highest y-fluctuations, $0 \leq y^+ \leq 50$, Klebanoff shows a nearly constant value of $\left(\overline{v^2}\right)^{1/2}/\overline{u} = 0.06$. The pipe data of Laufer [1953] confirms this value. Thus, the mean velocity data in this region as determined by the anemometer is at most 0.4% high due to this effect. Since this correction is less than 1/5 of the basic uncertainty in the mean velocity measurements, no correction of this type will be made to the data.

2. Velocity fluctuations along finite hot-wire length

Uzkan [1964]† has estimated the errors introduced into hot-wire mean velocity measurements in water due to the temperature fluctuations along the finite length of the wire associated with local velocity fluctuations. The results of this analysis are applied here to the hot-wire and flow conditions used in this study.

Where the hot-wire has been calibrated under low turbulence conditions, but measurements are desired for high turbulence levels, a correction factor K_o^2 gives the ratio $\frac{\bar{u}_{true}}{\bar{u}_{calib.}} = K_o^2$ where

$$1/K_o = 1 + \frac{\overline{q^2}}{\overline{u^2}} \left[- g_1 + g_2 \int_o^1 (1 - z/\ell) R_{11}(z/\ell) d\, z/\ell \right] \quad (A\text{-}8)$$

$\overline{q^2}/\overline{u^2}$ is the turbulence intensity squared at the point of measurement; assuming the wire is not sensitive to ω. I.e., $\overline{q^2} = \overline{u^2} + \overline{v^2}$. $R_{11}(z/\ell)$ is the correlation coefficient in the direction of the wire. I.e.,

$$R_{11}(z/\ell) \triangleq \frac{\overline{u\left|\frac{z'}{\ell}\right| \; u\left|\frac{z'}{\ell} + \frac{z}{\ell}\right|}}{\overline{u^2}} \quad (A\text{-}9)$$

ℓ is the wire length, d = wire diameter. g_1, g_2 are constants dependent upon wire diameter, wire material, overheat temperature difference and local mean velocity.

A sample correction will be calculated for conditions typical for the measurements of this study, e.g., for $y^+ \approx 10 - 15$ in buffer layer where such a correction is expected to be maximum.

For ℓ = 0.20 inch, d = 0.0008 inch, platinum wire, $\Delta T_{overheat}$ = 30°F, $\bar{u}$ = 0.20 ft/sec: $g_1 = 0.143$ and $g_2 = 0.123$

†Similar (but different) error estimates are given in the literature; see e.g. Dryden [1937].

$R_{11}(z)$ has been determined in this study by H_2-bubble techniques in the outer sublayer and may be approximated by:

$$R_{11}(z) = e^{-\left(\frac{2z}{\lambda}\right)^2} \cdot \cos \frac{2\pi z}{\lambda}$$

where λ is the characteristic length of the sublayer structure in the z-direction. $\lambda \approx 0.4 - 1.0"$ for the velocity range of this study so that a conservatively small value of $\lambda = 2\ell$ will be chosen to give a conservatively small value of I for $\lambda = 2\ell$: $R_{11}(z) = e^{-(z/\ell)^2} \cdot \cos \frac{\pi z}{\ell}$ and the value of the integral expression in $1/K_o$ is 0.37. So that:

$$1/K_o = 1 + \frac{\overline{q^2}}{\overline{u^2}} (- 0.097)$$

and

$$\bar{u}_{true} = \frac{1}{\left(1 - 0.097 \frac{\overline{q^2}}{\overline{u^2}}\right)^2} \cdot \bar{u}_{calib.} \qquad (A\text{-}10)$$

Typical highest values of $\left(\overline{q^2}\right)^{1/2}/\bar{u}$ in the buffer region are 40% (Klebanoff [1954]) which gives $\bar{u}_{true} = 1.03\ \bar{u}_{calib.}$ or the $\bar{u}$ determined by the hot-wire procedure determines a mean value which is, at most, 3.0% too low when measuring in a flow with 40% turbulence intensity.

Figure A.5 shows the per cent error in mean velocity due to fluctuations along the wire as a function of $\left(\overline{q^2}\right)^{1/2}/\bar{u}$.

So a conservative estimate of this type of error in the mean velocity under the most extreme conditions shows that the error is no higher than the inherent uncertainty of the hot-wire system. No such corrections have been applied to the data.

B. Wall Effects

The effects of thermal conduction to a lucite wall from a hot-film probe are discussed by Runstadler [1963] and assumed small (less than 3%) because the thermal conductivity of lucite is very nearly that of water ($K_{lucite}/K_{water} \approx 0.31$ while by comparison for air flow over steel plates, $K_{steel}/K_{air} \approx 1670$). The same very small effect is expected for hot wires. If there were an effect, it would present a reduction in heat transfer over that where no wall is present and hence indicate too low a velocity.

When a probe is brought very near a solid wall the probe produces a flow disturbance which tends to increase the heat transfer and indicate too high a velocity. The hot-film produces a larger disturbance than the hot-wire due to its larger size. Hot-film data further than 0.025 inches from the wall are felt to be not influenced by flow blockage (this corresponds to $y^+ \approx 5$ for data taken with hot-film). For hot-wire data no flow blockage effect is expected since the wire is never closer than 10 wire diameters from the wall.

In summary, none of the corrections discussed and approximated above indicate the need for corrections which are greater than the inherent scatter of the systems ($\pm$ 5% for hot-film and $\pm$ 2.5% for hot-wire). Since different corrections require corrections in opposite directions and since all corrections are just approximations indicating order of magnitude, no corrections will be applied to the velocity data.

In some cases a correction to the zero-position of the hot-wire is made where the mean velocity clearly indicates a linear trend near the wall but does not pass through $y = 0$. Where this correction is made, it will be clearly indicated; no such correction greater than $\pm$ 0.003 inches was made. This correction is made necessary because the wire could be placed with reference to the wall to only $\pm$ 0.002 inches.

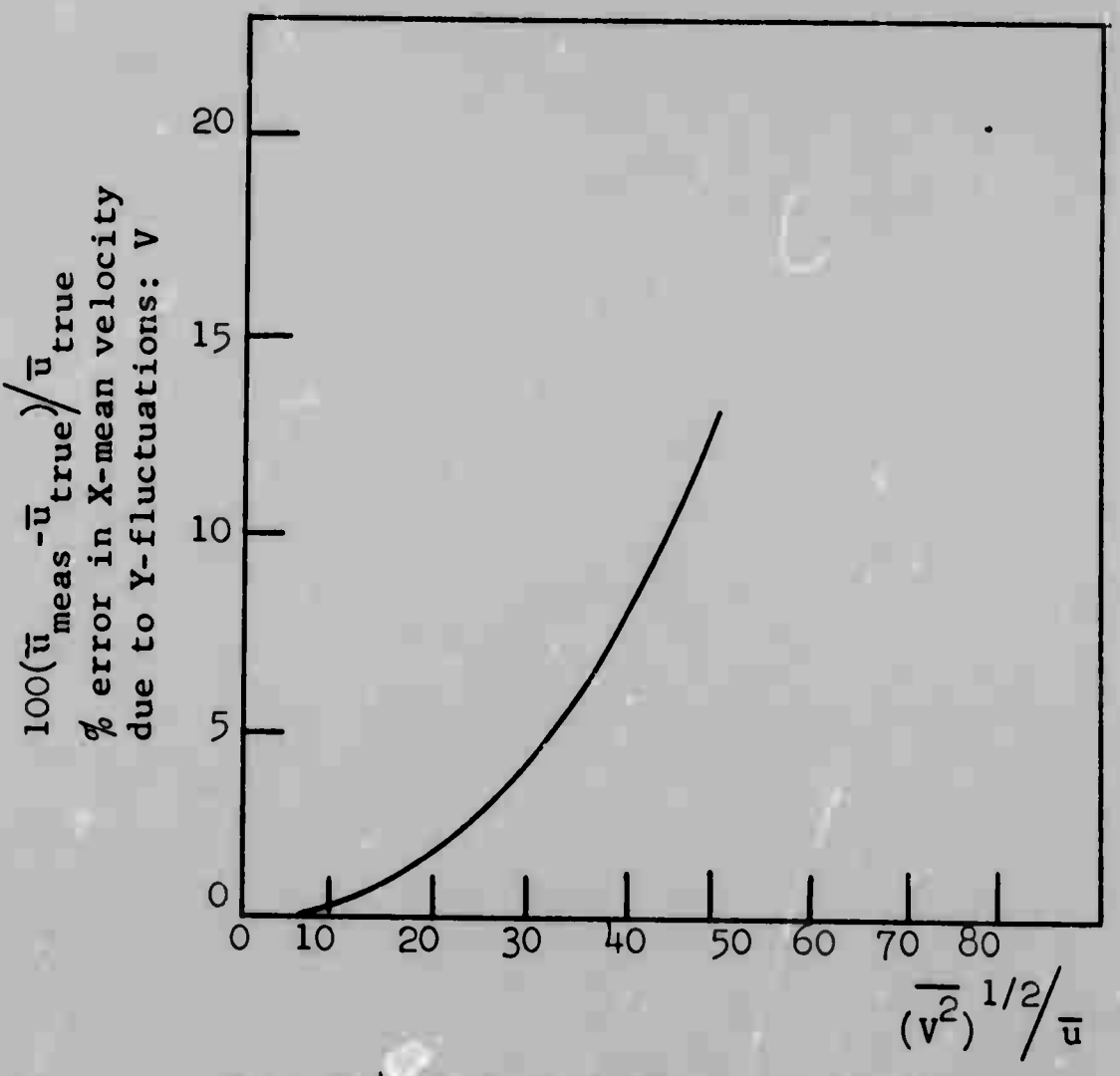

Fig. A.4 Hot-wire error due to transverse velocity fluctuations.

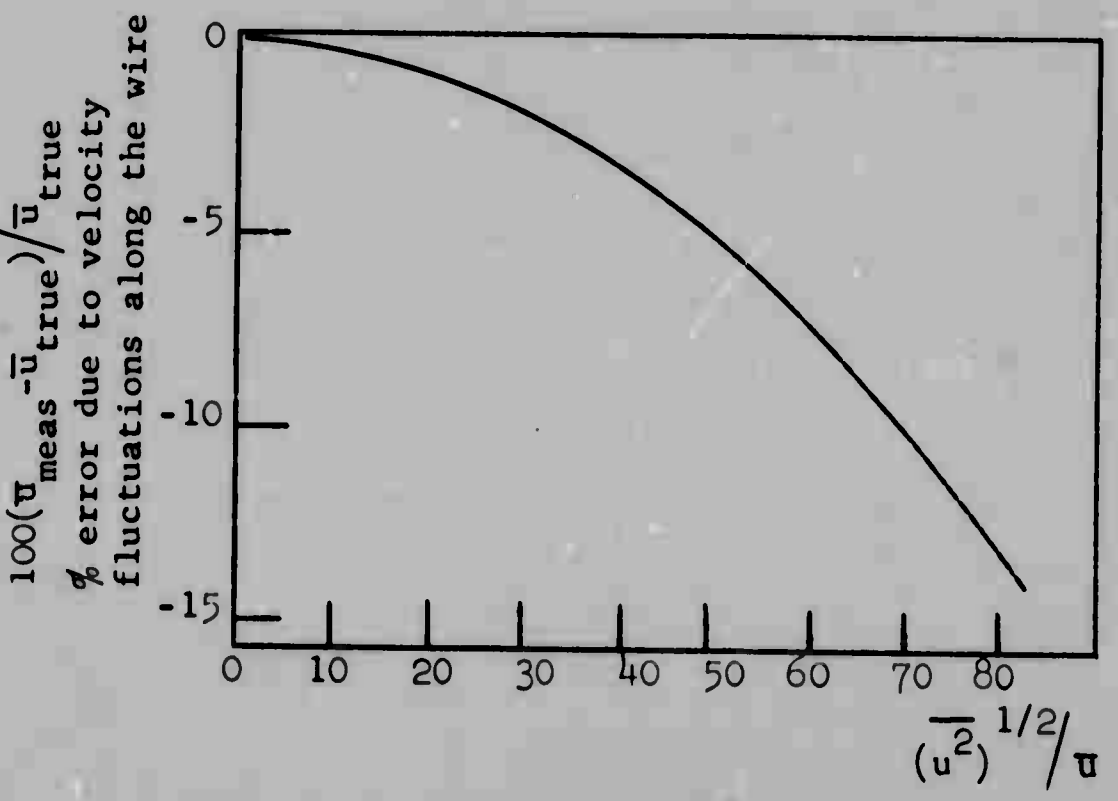

Fig. A.5 Errors in hot-wire mean velocity due to large turbulent fluctuation level.

APPENDIX C
UNCERTAINTY CONSIDERATIONS

When a large number of samples of a given experimental variable may be obtained, the expected value of that variable is given by the sample mean. The "uncertainty" in the sample mean is due to the finiteness of the data sample. This uncertainty is expressed by a confidence interval calculated at a certain significance level using a standard statistical distribution test; (see standard statistics book, such as Parzen [1960]).

Such "usual" statistical procedures were employed where possible in this study. For example, in the estimate of mean velocity using the H_2-bubble method, several thousand samples of velocity could be taken and then the uncertainty between the sample mean and the "true" mean was calculated as above.

However, where an estimate of the uncertainty in any <u>single</u> sample (e.g., a single specific velocity sample out of a thousand samples) is desired, the usual statistics are not applicable.

The procedure for estimating single sample uncertainties to be used here is that given by Kline and McClintoch [1963]. When the uncertainty in a result, R , is desired where $R = R(V_1, V_2 \ldots V_n)$, then a very good approximation of the uncertainty in R may be expressed as:†

$$W_R = \left[\left(\frac{\partial R}{\partial V_1} \cdot W_1\right)^2 + \left(\frac{\partial R}{\partial V_2} \cdot W_2\right)^2 + \ldots \left(\frac{\partial R}{\partial V_n} \cdot W_n\right)^2\right]^{1/2}$$

where $W_1, W_2 \ldots W_n$ are the uncertainty intervals in $V_1 , V_2 \ldots V_n$. The uncertainty intervals are the estimated confidence intervals about the expected value of each variable given at some specific odds such as 20:1.

---

†Provided $V_1, V_2 \ldots V_n$ are independent and the experiment is under control such that the statistical distributions of $V_1, V_2 \ldots V_n$ have a single peak. If the distributions are normal in $V_1, V_2 \ldots V_n$ then the expression given is exact.

The results of uncertainty estimates, as well as the sources of the uncertainty, are summarized below for the various measured and calculated variables of this study.

A. Velocity by H_2-Bubble Combined-time-streak Marker Technique

Since the use of combined-time-streak markers for quantitative velocity measurements is a new technique, a very detailed uncertainty analysis has been made. This analysis was of sufficient general interest to warrant separate publication (see Schraub, et al [1964]). General formulae are worked out using the single sample procedures and the numerical example chosen is the determination of velocity in the sublayer region of the turbulent boundary layer from the present study.

For local mean velocity of 0.20 $\pm$ ft/sec, with near optimum† measurement interval of 0.083 seconds, the various sources of uncertainty considered gave the following result at 20:1 odds:

1.	Measurement	2.5%
2.	Averaging (due to Eulerian velocity determination using a LaGrangian method. Value depends on data reduction method.)	1.1 or 2.2%
3.	Bubble displacement out of measurement plane including that due to bubble rise.	2.5%
4.	Response of bubbles to fluctuations.	Negligible
5.	Resolution restricts observable fluctuations to about 50 cps and below.	
6.	Velocity defect behind generating wire negligible where "proper" procedures employed.	

†The criterion for optimum measurement interval is one result of the uncertainty analyses (see Schraub, et al [1964]).

Total uncertainty is obtained by combining these independent sources of uncertainty by the square propagation law yielding 3.8 to 4.3% uncertainty at 20:1 odds depending on the exact method of data reduction (see Schraub, et al [1964] for details). Thus, any single velocity determination by the H_2-bubble method is felt ot be accurate within about $\pm$ 4%.

B. Mean Velocity by Constant Temperature Anemometer

Mean velocity is given by: $\bar{u}(y_o) = E_{30}(T) \cdot u(E_{30})$ where $E_{30}(T) = \frac{30}{T}\int_o^T e_{anem.}\,dt$ and $\bar{u}(E_{30})$ is the (linear) calibration function obtained for 30 second integration time. $e_{anem.}$ is the voltage output from the anemometer.

The uncertainty in $E_{30}(T)$ was kept less than 1/2% by making integration times as long as necessary. For mean velocity profiles integration times varied from 2 minutes to 5 minutes.

$$\left.\frac{W\bar{u}(E_{30})}{\bar{u}(E_{30})}\right]_{\text{hot film}} \approx 4\%$$

$$\left.\frac{W\bar{u}(E_{30})}{\bar{u}(E_{30})}\right]_{\text{hot wire}} \approx 2.5\%$$

So the estimate of uncertainty in mean velocity by hot-wire is 2.5% and by hot-film, 4% at 20:1 odds.

C. Y-Position in Boundary Layer

Zero (wall) location of measurement probes was ascertained using an optical-comparison system to $\pm$ 0.0015 inches. Thereafter, movement with respect to this zero point was determined by a dial indicator which read to $\pm$ 0.0002 inches.

Thus, $\left.W_y/y\right]_{\text{uncorrected}} \approx 0.0015/y$

However, very near the wall a correction was sometimes

applied to the zero point by requiring the linear mean velocity profile near the wall to intersect $y = 0$ for $u = 0$.

$$W_y/y\Big]_{corrected} \approx 0.0005/y$$

D. Wall Shear

1. By velocity profile at the wall:

$$\tau_W = \mu \left.\frac{\Delta u}{\Delta y}\right]_W = \mu\, s_w$$

$W_\mu < 1/5\, W_{s_W}$ and is neglected.

s_W is actually determined not just at the wall but over the linear portion of the velocity profile of the sublayer which extends over about 0.025 to 0.040 inches depending on the flow conditions.

$$\frac{W_s}{s} = (W^2_{\Delta u} + W_{\Delta y})^{1/2} = \frac{W_{\tau_W}}{\tau_W}$$

$W_{\Delta u}$ must be given a larger estimate than that given in Section B because for the low velocities in this region at the wall, no method of calibration is available and an extrapolation is necessary between the lowest calibration points and $u = 0$ (the hot-wire anemometer is calibrated such that $e = 0$ at $u = 0$).

$W_u/\bar{u} \approx 5\%$ is estimated for this region.

Therefore

$$W_{\Delta u}/\Delta u = \sqrt{2}\ 5\% = 5.7\%$$

$$W_{\Delta y}/\Delta y = \frac{\sqrt{2}\ (0.0002)}{\Delta y} = 1.4\% \quad \text{for typical} \quad \Delta y = 0.033".$$

Therefore

$$\frac{W_{\tau_W}}{\tau_W} = \left[(5.7)^2 + (1.4)^2\right]^{1/2} \approx 6\%$$

2. By the cross-plot of logarithmic region

This method (see Chapter II for details) consists of forcing the mean velocity data points in the logarithmic part of the u^+, y^+ non-dimensional velocity profile to fit a specific "universal" $u^+ = A \log y^+ + B$ curve. The primary uncertainty is that associated with the applicability of the "universal" curve to the experimental data. If the data could be shown by some other information to exactly fit the universal curve used, then the technique for finding τ_w will yield uncertainties of just 4% (estimate).

See Chapter III for discussion of extent to which the data of this study are felt to obey a single "universal" mean velocity profile.

E. Integral Profile Parameters

Displacement thickness: δ^* is evaluated by a numerical integration scheme:

$$\delta^* = \sum_{i=1}^{N} (1 - u/u_\infty)\, \Delta y_i \qquad \Delta y_i = \delta/N$$

Since only a single velocity profile is available for the δ^* determination, the single sample uncertainty procedure yields:

$$\frac{W_{\delta^*}}{\delta^*} = \sqrt{2}\, \frac{\delta}{\delta^*}\, \frac{1}{N} \left\{ \sum_{i=1}^{N} \left[\left(\frac{u_i}{u_\infty} \right) \left(\frac{Wu_i}{u_i} \right) \right]^2 \right\}^{1/2}$$

For $Wu_i/u_i \approx 2.5\%$ and $\delta^*/\delta = 0.20$, a typical integration yields $W\delta^*/\delta^* = \pm 6.6\%$ at 20:1 odds.

Momentum thickness: similarly for momentum thickness:

$$\frac{W_\theta}{\theta} = \sqrt{2} \left(\frac{\delta}{\theta} \right) \left(\frac{W_u}{u} \right) \frac{1}{N} \left\{ \sum_{i=1}^{N} \left[\frac{u_i}{u_\infty} \left(1 - 2\, \frac{u_i}{u_\infty} \right) \right]^2 \right\}^{1/2}$$

$\frac{W_\theta}{\theta} = \pm 8.2\%$ at 20:1 odds for $\frac{Wu_i}{u_i} = \text{const} = 2.5\%$ at 20:1 odds.

F. Streak Spacing by Visual Counting

The uncertainty is of three types:

1. Counting rules: The decision of the observer in deciding what are "low-speed streaks" and what are not is based upon a set of "rules" used for interpreting the structure pictures. Without careful consultation, different observers count somewhat differently and differences of up to 50% in λ are sometimes obtained. It is absolutely necessary in comparing structure spacing data of different observers to have a common set of rules. With well-defined "rules", different observers are able to obtain λ to within 10% of each other.

2. Reading, accidental, scale factor, and other inherent uncertainties in visual counting account for about $\pm$ 9% uncertainty.

3. The finiteness of the data sample accounts for additional uncertainty in the sample mean λ which is estimated by the usual statistical procedures. The distribution of sample spacings about λ was shown to be very nearly normally distributed with standard deviation of about 30%. 450 samples then make λ within $\pm$ 5% of the true mean at 5% significance level.

These uncertainties combine to make the total uncertainty in λ_{visual} about $\pm$ 11% for a specified set of counting rules.

G. Burst Trajectory

Sources of uncertainty in trajectory data: (at 20:1 odds)

1. Scale factors: $\pm$ 1%
2. Film reading equipment: $\pm$ 2%
3. Finiteness of data sample: for 50 samples, where standard deviation is about 30%, the uncertainty in $\bar{y}$ and/or $\bar{x}$ will be about $\pm$ 7% (t-statistic test).
4. Framing rate: $\pm$ 0.6%

Total uncertainty is thus about 8% (at 20:1 odds).

H. Burst Rate: F

Sources:

1. As with visual counting of low-speed streaks, a well-defined set of rules must be adopted for consistent results; different rules account for ± 25% variations.
2. Inability of observer to distinguish individual bursts: ± 6% .
3. Framing rate: 0.6% .
4. Inconsistency in counting even with consistent rules: ± 5% .

Total uncertainty ± 8% at 20:1 odds with a consistent set of counting rules.

I. Turbulence Intensity

Turbulence intensity uncertainty when determined from velocity values from hydrogen bubble combined-time-streak marker technique arises from:

1. Single sample uncertainty (uncertainty in single velocity determination is evaluated using methods of Kline and McClintock [1953]. Where evaluated numerically

$$TI = \left\{ \frac{1}{N} \sum_{i=1}^{N} \left(\frac{u_i^2}{\bar{u}^2} - 1 \right) \right\}^{1/2}$$

$$\frac{W_{TI}}{TI} \approx \frac{1}{(TI)^2 \sqrt{N}} \left(\frac{W u_i}{\bar{u}_i} \right) \quad \text{for large } N$$

so that (typically) for dp/dx = 0 flow station 13:

$$N = 1934, \ \bar{u} = 0.192 \text{ ft/sec}, \ TI = 0.31 \ \frac{W_u}{u} = 4\%$$

$$\frac{W_{TI}}{TI} \approx 1\%$$

2. Finite data sample: at 20:1 odds TI calculated (using x^2 test statistic test) for above example is 5% at 5% significance level. (Craemer [1961].)

So total uncertainty is about 5.5% to 20:1 odds.

J. Uncertainty in Spectral Analysis

The following approximate formula (Blackman and Tukey [1958]) was employed in estimating the resolution and uncertainty bands in the spatial spectral analyses.

Where p separate pieces of data (e.g., u(z)) are analyzed:

$$EBW = 1/L_M$$

$$\frac{VAR[U(\nu)]}{[U(\nu)^2]} = L_M/L_N' \quad \text{where} \quad L_N' = L_N - p/3\ L_M$$

L_N is total length of all data samples. L_M is the lag length over which the correlation coefficient is calculated prior to determining its Fourier transform (the spectrum). EBW is the "equivalent band-width" which is a measure of the extent to which the spectrum is "smeared" over a range of frequencies near the frequency of interest. $\frac{VAR[U(\nu)]}{(U(\nu)]^2}$ is the estimated variance in the distribution of magnitude of $U(\nu)$.